

Dynamical Effects in Heavy-Fermion Systems

Dissertation
zur
Erlangung des Doktorgrades (Dr. rer. nat.)
der
Mathematisch-Naturwissenschaftlichen Fakultät
der
Rheinischen Friedrich-Wilhelms-Universität Bonn

von
Marvin Lenk
aus
Bergisch Gladbach

Bonn, June 2024

Angefertigt mit Genehmigung der Mathematisch-Naturwissenschaftlichen Fakultät der Rheinischen
Friedrich-Wilhelms-Universität Bonn

Gutachter / Betreuer: Prof. Dr. Johann Kroha
Gutachter: Prof. Dr. Simon Trebst
Tag der Promotion: 18.09.2024
Erscheinungsjahr: 2025

Abstract

When atoms in solids have unfilled d - or f -orbitals, local Coulomb interaction often becomes non-negligible due to the strongly localized nature of those orbitals. A hallmark effect of such systems is the formation of a set of localized states at the Fermi energy due to the local nature of the Kondo effect. If the so-formed Kondo singlets become lattice coherent, a heavy Fermi liquid is formed. A long-standing open question is the fate of individual crystal (electric) field (CEF) states involved in this process. Lattice coherence of different CEF states could, in principle, occur at different temperatures and extents.

This is the case in YbRh_2Si_2 , for which scanning tunneling microscopy (STM) revealed a puzzling picture. The Kondo effect leads to a dip in the STM spectrum. Below temperatures where the dip was already clearly pronounced, a peak close to the minimum of the dip arose, which was attributed to the formation of lattice coherence. Simultaneously, additional peaks at the CEF energies arose, hinting towards lattice coherence in all states.

In this thesis, I present a comprehensive overview of lattice coherence in heavy fermion systems, from the basics of quantum particles in periodic potentials to methods for interacting systems and how to modify them to include CEF states and methods for solving such systems with quantum field theory and numerically. I construct a minimalistic model for YbRh_2Si_2 , including all four CEF states of the $\text{Yb}^{3+} 4f^{13}$ configuration. With this, I present results confirming the observed behavior qualitatively. The Kondo dip and the coherence peak are reproduced faithfully. The first excited CEF level shows clear signs of lattice coherence, and higher excited CEF states show weaker signs of coherence.

The non-Fermi liquid behavior in two-channel Kondo heavy-fermion systems is explored as a second topic. Intriguingly, such behavior was experimentally observed in $\text{PrV}_2\text{Al}_{20}$, whereas $\text{PrTi}_2\text{Al}_{20}$ showed regular heavy Fermi liquid behavior. It was proposed that the former sits closer to a putative quantum-critical point. While this could explain the observed behavior, another possible explanation can be formulated. The two-channel Kondo effect gives rise to a local non-Fermi liquid behavior. If this picture translates to the lattice case, it could fully explain the experimentally observed scaling.

This option is explored as the second main subject of this thesis. I present a model incorporating the relevant CEF states of the $\text{Pr}^{3+} 4f^2$ configuration and using *ab initio* band structure data. While including only the CEF ground state already leads to non-Fermi liquid behavior in the lattice model, the stark deviation from the experimentally observed magnetic susceptibility necessitates the inclusion of the first excited CEF state as well. This is shown to improve the scale of the onset of non-Fermi liquid behavior and reproduce the qualitatively correct scaling of the magnetic susceptibility, confirming the alternative explanation for the experimentally observed behavior.

Acknowledgements

I would like to express my honest and utmost gratitude towards the people without whom this work would not have been possible.

First and foremost, my beloved wife Sabine, who has accompanied me for almost half my life¹, ever supporting, comforting, open-hearted and last but not least, loving (whenever I deserve it). Without her, my life would have probably taken many wrong turns by now, and I can not thank her enough. I also want to thank my sweet daughter Fiona for her overwhelming love and for being the light in our life that shines brighter every day.

I always considered myself especially lucky. This luck started with my parents, Andrea and Rainer, who provided a safe space at home and always took me for what I was. Their support was and still is without limits, and I am extremely grateful to be their son. To my brother Florian: I would like to express my gratitude for the invaluable time we've spent together. Thank you for everything we share and for all our differences.

Every day, I realize more how much every single member of my family, be it close or remote, and every close and long-time friend plays an invaluable role in the play that is my life. The list of names would be much too long, and I would never forgive myself if any one of those names were missed by accident. I would, therefore, love to thank all of my family, without a single exception, from the bottom of my heart!

My scientific journey so far has given me the opportunity to meet plenty of good people throughout the years. One of those people turned out to play a major role in my scientific career: Thank you, Hans, for leading and accompanying me on my journey through quantum thermalization and the infinitely deep well of knowledge and understanding that is the Kondo effect. I consider it more than just a lucky chain of events that led to me staying for my Master's thesis, discovering my love for the rich physics of correlated matter and especially the Kondo effect in all of its facets. I look forward to exploring many more aspects of heavy fermion physics with you and your group.

Speaking of which, I want to express a special thanks to the colleagues and friends who contributed to this scientific journey. In no particular order, I would first like to thank Francisco Meirinhos, Michael Kajan, and Michael Turaev. Our combined efforts in disentangling the complex machinery that is the non-crossing approximation and the dynamical mean-field theory were very much enjoyable and extremely fruitful. Our discussions, sometimes heated and sometimes puzzling to all participants, were a great deal of fun and helped me understand physics and much more in a way that I would never be able to by myself.

Equally, I would like to thank Qiwei Li, with whom I went deeper into the gloomy forest of lattice coherence than I would have ever dared by myself. In the first half of our common project, I was

¹ Actually precisely 5955 days on the day this thesis was handed in, but who even counts that...

unable to dedicate as much time to you as you would have deserved, and I am very grateful for the help from Michael Turaev, who made sure we were on track to finish the project in time.

A special dedication goes to Andriy Nevidomskyy, who initiated the $\text{PrV}_2\text{Al}_{20}$ project and made an essential contribution to understanding the involved physics. I am grateful for the opportunity to work on this topic with such excellent researchers and for the great hospitality he extended to me during my brief visit to Houston. Additionally, I want to express my gratitude to Fei Gao, who contributed substantial parts to the $\text{PrV}_2\text{Al}_{20}$ project and briefly introduced me to crystal fields, a topic in which I developed a special interest in the late stages of this project.

I want to also thank Ammar Nejati for always asking the right questions to open up a journey of deep understanding, Soroush Arabi for his excellent work on the topological Kondo insulators and for sharing his knowledge with me, Tim Bode for our discussions and for exploring the wide world of small bosonic systems with me, Arkadeep Mitra and Sayak Biswas who were invaluable partners in further explorations of quantum thermalization and the limits of the fluctuation-dissipation relation in small systems, and Lukas Köbbing for his excellent work on the quantum thermalization of fermionic systems.

Additionally, I would like to thank all the present and past colleagues and friends in our group: Sayak Ray, Ulli Pohl, Krzysztof Wójcik, Haixin Qiu, Aya Abouelela, Fabiola Neumann, Roman Kramer, Julian Schwingel, Marcel Schindler, Mohamed Elhabib Saadi, Paul Züge, Bastian Havers, Christopher Lietmeyer, Zhong Yuan Lai and all others that are not listed here.

Lastly, I want to thank Prof. Dr. Simon Trebst for reviewing my Master's thesis and now also this dissertation, and Prof. Dr. Simon Stellmer and Prof. Dr. Thomas Bredow for being part of my doctoral committee.

Contents

1	Preface	1
2	Atomic Lattices and Lattice Coherence	5
2.1	Particles in Periodic Potentials	7
2.1.1	Electronic Bands and Their Connection to Electrical Conductivity	9
2.1.2	Wannier Functions	10
2.1.3	Uniqueness of Wannier Functions / Lattice Coherence	11
2.1.4	Heavy Quasiparticles and Itinerant Electrons	12
2.1.5	Understanding Localization in Lattices from the Kronig-Penney Model	12
2.2	The Resonant-Level Model	14
2.2.1	Block-Matrix Inversion in the Context of Green Functions	14
2.2.2	Solutions via Self-Energies and T -Matrices	15
2.2.3	Local Density of States	17
2.2.4	Spectrum of the Green Function Trace / Lattice Density of States	20
2.2.5	The Problem of a Lattice-Momentum Dependent Spectrum	22
2.3	The Two-Band Hybridization Model	24
2.3.1	Band Gap	25
2.3.2	Density of States	27
2.3.3	Green Functions	28
3	Heavy Fermions and Interacting Models	29
3.1	Hubbard's Model for Electrons in s -Orbitals	31
3.2	Hubbard Operators	32
3.3	Anderson's Single-Impurity Model	33
3.3.1	Spectrum of the SIAM I	34
3.3.2	Parameter Regimes of the SIAM	35
3.3.3	Spectrum of the SIAM II	37
3.4	The s - d Model and Kondo's Treatment	39
3.4.1	Resistivity and Conductivity via Boltzmann's Equation	41
3.4.2	T -Matrix Perturbation Theory in J	43
3.4.3	The Kondo Temperature	45
3.4.4	Screening of Local Moments and the Kondo Cloud	46
3.5	Impurity Lattice Models	46
3.5.1	The Kondo Lattice Model and the Large- N Limit	47
3.5.2	The Fate of the Fermi Surface	48

3.5.3	The Periodic Anderson Impurity Model	49
4	Modeling Realistic Materials	51
4.1	Orbital Angular Momentum	52
4.2	Spin-Orbit Interaction and Hund's Rules	52
4.2.1	The Addition of Angular Momenta	53
4.2.2	Hund's Rules	54
4.3	Crystal Fields and Group Theory	56
4.3.1	Representations of Groups and their Character	57
4.3.2	Examples for the Reduction of Symmetry	60
4.3.3	Clebsch-Gordan Coefficients for Point Groups	62
4.3.4	Crystal-Field States in Quantum Field Theory	63
5	Methods and Approximations	65
5.1	Auxiliary Particles	66
5.1.1	Constructing Auxiliary-Particle Representations	67
5.1.2	Fixing the Operator Constraint $\hat{Q} = 1$	70
5.1.3	The Single-Impurity Anderson Model with Auxiliary Particles	71
5.2	The Luttinger-Ward Functional	71
5.3	The Non-Crossing Approximation	74
5.3.1	Conduction-Electron Self-Energy	75
5.3.2	Impurity Green Function	78
5.3.3	Auxiliary-Particle Self-Energies	80
5.3.4	Fixing the Auxiliary-Particle Energy Scale	87
5.3.5	Addressing the Diverging Boltzmann Factor via Tilde Functions	88
5.3.6	The NCA Loop	91
5.3.7	Two Limits: Infinite U and Infinite ε^d	92
5.4	Dynamical Mean-Field Theory	94
5.4.1	Electrons in Infinite Dimensions / Suppression of Non-Local Self-Energies	94
5.4.2	Dynamical Mean-Field Theory for the Periodic Anderson Model	95
6	Lattice Coherence of CEF States in YbRh₂Si₂	101
6.1	Experimental observation of lattice coherence	101
6.2	Minimalistic Microscopic Model	103
6.3	The Fano-Lineshape in the Conduction-Electron Density of States	105
6.4	Numerical Results and Interpretation	106
6.4.1	Density of States	107
6.4.2	Conduction-Electron Density of States and q -Factor	108
6.4.3	Dip Depth and Peak Heights	111
6.4.4	Spectral Function and Orbitally Selective Lattice Coherence	112
6.5	Conclusion	115
7	The non-Fermi liquid behavior in PrV₂Al₂₀	117
7.1	Crystal Field States of Pr ³⁺ in PrV ₂ Al ₂₀	120
7.2	An Effective Periodic Anderson Model for PrV ₂ Al ₂₀	121

7.3	Conduction Electrons in the Effective Model	123
7.4	Dynamical Mean-Field Theory and Non-Crossing Approximation for the Model	125
7.5	Results for the Single CEF-State Model	128
7.6	Results for the Two CEF-State Model	130
7.7	Conclusion	133
8	Summary and Outlook	135
A	Lattice-Momentum Discretization	139
B	Simplifying the T-Matrix Equation of the Resonant-Level Model	141
C	Transformations, Tricks, and Algorithms	145
C.1	Integrals over Lorentzians	145
C.2	Inversion of Tilde Green-Function Matrices	146
C.3	Efficient Calculation of the Cubic Density of States in Arbitrary Dimensions	147
C.4	Transforming Between Local T -Matrices and Self-Energies	148
D	Expressing $\varepsilon^a \rightarrow \infty$ NCA Equations via $U \rightarrow \infty$ Equations	149
E	Details of the $\text{PrV}_2\text{Al}_{20}$ Model	153
E.1	Representation of Selected CEF States in Total Angular Momentum States for $\text{PrV}_2\text{Al}_{20}$	153
E.2	CEF Multiplet Hybridization Matrix Elements	154
E.3	Details of the Structure factor	156
E.4	Details about the Numerical Treatment of the Magnetic Susceptibility	158
	Bibliography	159
	List of Figures	175
	List of Tables	181

Preface

Condensed matter physics has played an integral role in understanding the physics of *naturally observable* phenomena. From its early inception as a connection between the chemistry of solids and physical phenomena like optical reflectivity (color) and electric conductivity to modern-day superconductivity, topological insulators, semi-metals, and Majorana fermions, only naming a few, it has always been at the forefront of innovation on a fundamental level.

Historically, the quantum theory of solids seemed to have reached an insurmountable barrier: The non-negligible Coulomb interaction and the seemingly non-applicability of the theory of free Fermi gases to electrons in solids. In contrast, experimental data seemingly confirmed the applicability of the aforementioned theory. This conundrum was solved by Landau's Fermi liquid theory [1], in which he was able to attribute (free) particle-like behavior to excitations close to the Fermi energy in an interacting system, just with a renormalized mass m^* , which could be many times larger than the electron mass m_e .

Prototypical interacting systems are those with partially filled d - or f -orbitals. Typically, such electrons are tightly bound to the ion. Due to the strong localization of such orbitals, the Coulomb repulsion between occupying electrons is strong and often non-negligible. This leads to a strong exchange coupling in which the spins of localized electrons are effectively coupled to itinerant electrons via a simple spin exchange. In the simplest case, often realized in Cerium materials, a single electron in the f -shell is the system's ground state. If the interaction is strong enough to effectively remove the double occupancy from the dynamics and the temperature is low enough, the f -electron will act like a localized spin. The exchange interaction gives rise to a coherent spin-scattering of localized- and itinerant electrons, resulting in the formation of spin-singlets in the antiferromagnetic case. This effect was first described by Kondo in 1964 [2], in which only a single localized spin was considered. If a material contains a large concentration of such localized spins, a Kondo lattice in the extreme case, the local singlets can be considered the ground state to which the hopping of the itinerant electrons acts as a perturbation. Since the large Coulomb interaction gives rise to the singlet formation, the perturbation of de-localization can be considered small. This leads to a Fermi liquid of quasiparticles, which are mostly localized and only perturbatively de-localized. Their dispersion is flat compared to the itinerant electrons. Consequently, their effective mass is very large, resulting in a *heavy Fermi liquid*.

A prominent example of a *localizing* effect is the Ruderman-Kittel-Kasuya-Yosida (RKKY) interaction [3-5], which is a long-range interaction stemming from a second-order process in the

local exchange coupling including an intermediate itinerant electron. This interaction can lead to magnetic order, effectively localizing the spins. Hence, it directly competes with the Kondo effect, which was shown to give rise to Fermi liquid behavior. The resulting phase diagram was pioneered by Doniach [6] in 1977. A strong local spin interaction favors the heavy Fermi liquid phase, whereas a weak coupling favors long-range order.

It is this competition between two effects stemming from the same interaction that makes this problem so intriguing. The dynamical generation of lattice coherence in a temperature-dependent way is another interesting, open question. Originating in the (local) Kondo effect, it is not clear if lattice coherence of the heavy band is generated on the same scale, the Kondo temperature, or if it can be controlled by other parameters [7–11]. It seems that one can influence the two scales by external parameters such that they separate. A simple method is just controlling the chemical potential and, by that, the band filling [11].

Theoretical investigations in the matter were so far limited to the standard formulations of the Kondo lattice model or the periodic Anderson model. The ground state of such systems in the strong-coupling parameter regime is already known to be a heavy Fermi liquid. If one is interested in comparing involved temperature scales and crossover regimes, a model that is still valid on *those* scales has to be used. While the difference between the Kondo- and Anderson models will likely not influence the intermediate temperature results much, another scale enters the picture, which, in some cases, can be crucial in describing the physics of intermediate temperatures: crystal field splitting.

Ions in lattices are *not* in a fully rotationally invariant environment. The discrete lattice structure imposes a discrete rotational symmetry on each localized ion. As such, the atomic orbitals of each ion, after being treated by *LS*-coupling and split by the spin-orbit interaction, are further split into eigenstates of the discrete rotational symmetry. This splitting is typically of the order $\Delta/k_B \approx \mathcal{O}(10 - 100 \text{ K})$. Hence, the discussion of materials at temperatures compatible with the crystal (electric) field (CEF) splitting should not be limited to the CEF ground state.

In this thesis, the matter of lattice coherence of different CEF states is discussed in the context of YbRh_2Si_2 , where experimental data [12] suggest individual lattice-coherent heavy bands stemming from the Yb^{3+} CEF states. A theoretical description in terms of a minimalistic model and a numerical treatment via dynamical mean-field theory and the non-crossing approximation reveal fascinating (theoretical) scale separations between the coherence of different CEF states.

Another aspect of the competition between localization and de-localization in Kondo materials is the emergence of a quantum critical point separating the RKKY-induced magnetically ordered phase and the Kondo-effect-induced heavy Fermi liquid phase at zero temperature. Phase transitions are usually associated with diverging thermal fluctuations near the phase boundary. Here, the abrupt change of ground state depending on the strength of the local spin interaction leads to a phase transition driven by quantum fluctuations, which persist down to absolute zero temperature. The phase boundary of such a quantum phase transition narrows down to a single point, the quantum critical point (QCP). At finite temperatures, the behavior of a material near this QCP will be of a non-Fermi liquid type, where thermodynamic properties are governed by unconventional power-law behavior.

Typically, stoichiometric materials under normal conditions do not sit close to such a QCP, and reaching the NFL region can only be achieved by tuning external parameters like doping, pressure, or magnetic field. The emergence of non-Fermi liquid behavior in the 1-2-20 material $\text{PrV}_2\text{Al}_{20}$, in contrast to the Fermi liquid behavior of $\text{PrTi}_2\text{Al}_{20}$, has led to the conclusion that the former sits close

to a QCP [13]. There is a subtlety to both materials in that they host an unconventional *quadrupolar two-channel* Kondo effect. There, two independent conduction-electron baths compete to screen the same impurity degree of freedom. In this case, the electronic spin acts as a conserved scattering channel to screen a twofold quadrupole moment. Hence, the Doniach phase diagram [6] of the aforementioned competition between Kondo and RKKY has to be modified to incorporate quadrupolar ordering.

Several experimental results support the hypothesis of proximity to a QCP. Both materials show quadrupolar order at low temperatures, where the ordering temperature is lower, and the effective mass of the heavy band is larger in $\text{PrV}_2\text{Al}_{20}$ compared to $\text{PrTi}_2\text{Al}_{20}$. This indicates a weaker hybridization in $\text{PrV}_2\text{Al}_{20}$. Consequently, extrapolating the ordering temperature and assuming a QCP at the vanishing point of the phase, indeed $\text{PrV}_2\text{Al}_{20}$ would sit closer to this QCP than $\text{PrTi}_2\text{Al}_{20}$.

Alternatively, the observed non-Fermi liquid behavior could be attributed to the two-channel Kondo effect alone. In dilute two-channel Kondo systems, a local non-Fermi liquid arises due to the degeneracy of the ground state—the singlet can be formed in either channel. Although the lattice extension of this has not been exactly solved so far, it can be expected that the NFL behavior carries over to the lattice case in the same way as the Fermi-liquid behavior carries over in “conventional” Kondo systems. If so, the NFL behavior in $\text{PrV}_2\text{Al}_{20}$ could be explained with the two-channel Kondo effect alone. Compatibility of the scaling of different thermodynamic quantities with the known results for dilute two-channel Kondo systems strengthens this alternative hypothesis.

As a second main part of this thesis, the non-Fermi liquid behavior arising from the two-channel Kondo effect alone is explored in terms of a dynamical mean-field theory calculation with underlying *ab initio* band structure provided by Fei Gao and Andriy H. Nevidomskyy. In addition to the persisting non-Fermi liquid behavior in the lattice, the addition of the first excited crystal field state for the faithful description of the magnetic susceptibility is also discussed.

The structure of the thesis is as follows. In Chapter 2, the basics of quantum particles in periodic lattices are presented, along with a discussion of the resonant-level model and a two-band hybridization model. Motivated by the strongly interacting nature of localized electrons in atomic *d*- and *f* orbitals, Chapter 3 introduces models that incorporate such interactions, including the Hubbard model, *s-d* model, single-impurity Anderson model, and periodic Anderson impurity model. Chapter 4 addresses how such models can be constructed respecting the reduced rotational symmetry of realistic materials. This is done in terms of group theory, and the resulting states are represented by Hubbard operators. Chapter 5 details treating strongly interacting models via auxiliary particles, the non-crossing approximation, and dynamical mean-field theory. Utilizing these concepts, Chapter 6 discusses lattice coherence in YbRh_2Si_2 . Lastly, a reduced DFT+DMFT treatment of the two-channel Kondo effect in $\text{PrV}_2\text{Al}_{20}$, with an emphasis on the emerging non-Fermi liquid behavior, is presented in Chapter 7.

I often set $\hbar = k_B = 1$ throughout the thesis unless stated otherwise. It will be clear from the context when this is not the case.

Atomic Lattices and Lattice Coherence

Solving the many-body Schrödinger equation exactly for atoms more complex than isolated hydrogen is an insurmountable task. Bringing multiple such atoms close enough that the Coulomb interaction is non-negligible is an even more challenging, impossible-to-solve theory puzzle.

Conveniently, real-life matter often, yet not always, tends to arrange itself in either a diffuse statistical arrangement (typical gases under normal conditions) or a stiff (semi-)periodic arrangement (crystalline matter). When arranging atoms in a rigid and repetitive pattern forming a lattice, an immediate simplification comes to mind: discrete translational symmetry and, by Fourier-transform, the well-defined lattice momentum. Finite-sized lattices lead to discretized lattice-momentum, which becomes continuous in infinitely large lattices¹. Each atom in such a lattice can be viewed as a two-component object: the nucleus and the electrons. The large energy scales involved in the intrinsic physics of nuclei place the internal degrees of freedom firmly outside the scope of most real-world applications. Additionally, nuclei are orders of magnitude heavier than electrons, leaving them spatially mostly unaffected under interaction with the light electrons. A reasonable approximation is, therefore, leaving the heavy nuclei fixed (and mostly out of the picture of dynamics) to concentrate on the much lighter electrons with their less localized wave functions. They tend to become de-localized in the lattice, giving rise to a series of electronic states that are now a feature of the lattice and not the localized atoms only.

Those states form bands with typical bandwidths of order eV. Due to Pauli's exclusion principle, low-lying bands are completely filled with electrons, which is illustrated in Fig. 2.1. At zero temperature, this is true up to the Fermi-energy E_F . For an excitation of energy E to happen, there must be a pair of an occupied and an unoccupied state with energy difference E available in the material (orange arrows in Fig. 2.1). Since all low-lying bands are filled, the chance of finding such a pair significantly increases around the Fermi energy.

At finite temperature T , this is softened up in a region of width $k_B T$ around E_F . Close to room temperature $O(k_B T) = 10$ meV, which is typically much smaller than the bandwidth.

The following sections will explore the rich landscape that opens up from these concepts, starting with a general theoretical description of delocalized states in lattices, followed by the Hubbard model

¹ For an example, see Appendix A. This is different from, and should not be confused with, the discretization of the reciprocal lattice.

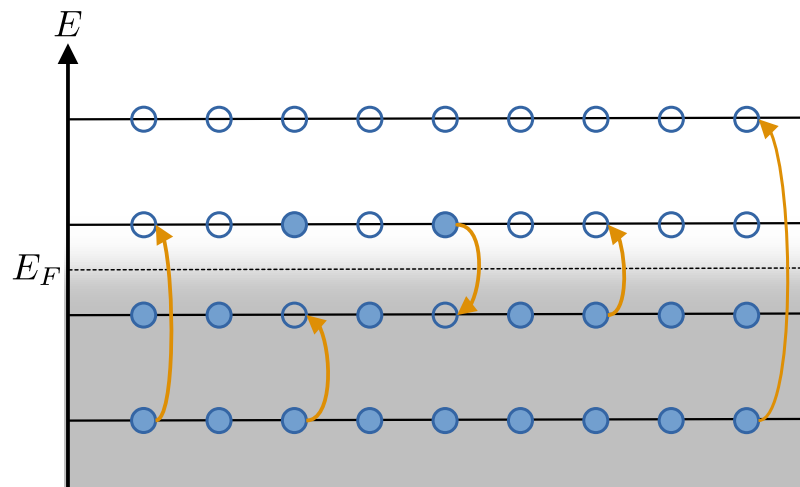


Figure 2.1: Illustration of the filling of bands. The shaded area represents the Fermi distribution function, gray areas are fully filled, white areas are unfilled. Full horizontal lines represent bands, the dashed horizontal line indicates the Fermi energy. Blue circles illustrate states in bands, filled blue circles signal an occupied state. The vertical distance between bands represents excitation energies. Orange arrows highlight a selection of possible transitions.

for s -orbitals and the extension to other orbitals via Hubbard operators. This is followed by a discussion of the group-theoretical aspects of angular momenta, which is then used in the following sections about the coupling of angular momenta and the reduced rotational symmetry imposed by the presence of crystal fields. The mostly empirical rules for determining the ground-state electron configuration in atoms considering LS -coupling are used in both sections to determine relevant states that can later be used to set up minimalistic yet faithful models.

The chemical potential is often omitted in the following.

2.1 Particles in Periodic Potentials

Whenever a particle is subject to a periodic potential of the form $V(\vec{x} + n \cdot \vec{a}) = V(\vec{x})$, where $n \in \mathbb{Z}$, Bloch's theorem applies [14, 15]². It states that the wavefunction of a particle in a periodic potential is given by

$$\psi_{n\vec{k}}(\vec{r}) = u_{n\vec{k}}(\vec{r}) \cdot \exp(i\vec{k} \cdot \vec{r}), \quad (2.1)$$

where n is a band index, $u_{n\vec{k}}(\vec{r})$ has the same spatial periodicity as the potential, and the exponential is a plane wave. This form originates from the definition of the discrete translation operator in terms of its generators, where \vec{k} is a momentum associated with the *discrete* translations by lattice vectors.

Typically, real-life solids are three-dimensional arrangements of atoms³. Their crystalline structure allows for the definition of lattice vectors \vec{a}_i , $i \in \{1, 2, 3\}$, such that an offset of the lattice potential $V(\vec{r})$ by any integer combination of those vectors remains invariant:

$$V(\vec{r} + u_1\vec{a}_1 + u_2\vec{a}_2 + u_3\vec{a}_3) = V(\vec{r}) \quad | \quad u_i \in \mathbb{Z} : i \in \{1, 2, 3\}. \quad (2.2)$$

If any two *equivalent*⁴ points can be mapped onto each other by this translation, the vectors \vec{a}_i are called *primitive* lattice vectors. The smallest building block of a lattice, the primitive unit cell, is defined via those vectors. The whole lattice can be filled without gaps by starting at any lattice point and filling space with such cells only shifted by a lattice vector $\vec{R} = \sum_i u_i \vec{a}_i$. Larger unit cells are sometimes used if that choice more easily visualizes a specific symmetry. Due to their convenience, those cells are usually called *conventional* unit cells.

The periodic nature of the potential naturally calls for Fourier analysis. A periodic function in real-space $f(\vec{r}) = f(\vec{r} + \vec{R})$, with \vec{R} defined above, has the following Fourier representation:

$$f(\vec{r}) = \sum_{\vec{G}} f_{\vec{G}} e^{i\vec{G} \cdot \vec{r}} = \sum_{\vec{G}} f_{\vec{G}} e^{i\vec{G} \cdot (\vec{r} + \vec{R})} = f(\vec{r} + \vec{R}), \quad (2.3)$$

$$\Rightarrow e^{i\vec{G} \cdot \vec{R}} = 1 \Rightarrow \vec{G} \cdot \vec{R} = 2\pi n, \quad (2.4)$$

where $n \in \mathbb{Z}$. The vector \vec{G} is called *reciprocal* lattice vector. Using the definition of \vec{R} via \vec{a}_i , one can define \vec{G} in terms of reciprocal vectors \vec{b}_i that satisfy $\vec{b}_i \cdot \vec{a}_j = 2\pi\delta_{ij}$ as $\vec{G} = \sum_i v_i \vec{b}_i$, where $v_i \in \mathbb{Z}$. The Fourier modes are therefore countable, hence the sum instead of an integral in Eq. (2.3). The primitive unit cell⁵ of the reciprocal lattice is called the first Brillouin zone. Due to its periodic nature, it is sufficient to address the physics within this zone.

Returning to the problem at hand, the Schrödinger equation of a particle in a periodic potential itself is not necessarily periodic in the same way. The kinetic energy term is continuous in Fourier space, whereas the potential term was shown to be discrete. Hence, one would not expect the solution to have the periodicity of the lattice. Let's construct a minimal example closely following [15] to

² I will closely follow Kittel's book [15] in the following since it is modern standard literature and the notation convenient. I will however, inspired by [16], replace the lattice-vector \vec{T} by \vec{R} and the Wannier functions $w_{n\vec{k}}$ by $\phi_{n\vec{k}}$ for convenience.

³ Not going into detail about the different possible crystal structures, which are especially well addressed and explained in the standard literature by Ashcroft and Mermin [17], the generalized picture suffices for this section.

⁴ Equivalent means that the infinite lattice looks identical from both points.

⁵ It is actually the primitive Wigner-Seitz-Cell, but that does not matter here.

understand the steps that need to be taken. A minimal, stationary, 1D Schrödinger equation is

$$\left(-\frac{1}{2m} \frac{d^2}{dx^2} + V(x) - E\right) \psi(x) = 0, \quad (2.5)$$

where we assume $V(x) = V(x + R)$ as discussed before. We can now express $\psi(x)$ and the potential in terms of their Fourier components, where its Fourier representation is discrete due to the exact periodicity of the potential.

$$\psi(x) = \int dk e^{ikx} C(k), \quad V(x) = \sum_G V_G e^{iGx} \quad (2.6)$$

$$\Rightarrow 0 = \left(-\frac{1}{2m} \frac{d^2}{dx^2} + \sum_G V_G e^{iGx} - E\right) \int dk e^{ikx} C(k) \quad (2.7)$$

$$= \int dk \left(\frac{1}{2m} k^2 + \sum_G V_G e^{iGx} - E\right) e^{ikx} C(k) \quad (2.8)$$

$$= \int dk \left(\frac{1}{2m} k^2 e^{ikx} C(k) + \sum_G V_G e^{i(G+k)x} C(k) - E e^{ikx} C(k)\right) \quad (2.9)$$

By analyzing the different coefficients of the plane waves, one can see that

$$\left(\frac{k^2}{2m} - E\right) C(k) + \sum_G V_G C(k - G) = 0. \quad (2.10)$$

So, for any fixed k , one only needs to solve for a discrete (yet infinite) set of coefficients $C(k - G)$.

From Eq. (2.10), it can also be seen that—in principle—multiple k -dependent solutions are possible. The associated energy eigenvalues are labeled by n . If the energy eigenvalues are smoothly parametrized by k , they are called a *band*. Of course, multiple bands are generally possible, and crossings can occur.

We can now also re-write the Fourier transform (2.6) of the wave function in terms of the first Brillouin zone and a sum over reciprocal lattice vectors G ⁶

$$\psi_n(x) = \int dk e^{ikx} C_n(k) = \int_{\text{BZ}} dk \sum_G e^{i(k-G)x} C_n(k - G) \quad (2.11)$$

$$= \int_{\text{BZ}} dk e^{ikx} \sum_G e^{-iGx} C_n(k - G) = \int_{\text{BZ}} dk \psi_{nk}(x). \quad (2.12)$$

Since the sum over G is infinite, this is exact. The term in the sum is invariant under translations by a lattice vector since it only depends on position via $\exp(iGx)$. We can therefore identify the function

⁶ I want to express my gratitude towards Prof. Föll for addressing this matter very concisely in his online lecture notes about Semiconductors [18].

$u_{nk}(x)$ in Eq. (2.1) as

$$u_{nk}(x) = \sum_G e^{-iGx} C_n(k - G). \quad (2.13)$$

After all of this, what have we gained? We started from the Schrödinger equation of a particle in a periodic potential (2.5) and represented it in Fourier-space via Eq. (2.6). For each momentum k , we derived equation (2.10) for the Fourier-coefficient $C(k)$ in terms of all other $C(k - G)$ that are shifted by a reciprocal lattice vector. This is a closed set of equations for all $C(k - G) \forall G$. By partitioning the Fourier integral in a suitable way, we were able to express the position-space wave function of a given band in terms of an integral over a plane wave $\exp(ikx)$ times a lattice-periodic function $u_{nk}(x)$. This process was beneficial in two ways. First, we understood a lot about the structure of a wave function describing a particle in a periodic potential. Second, we reduced the complexity from solving the full Schrödinger equation to solving a much simpler, algebraic equation (2.10) for each k . The corresponding Hamiltonian in the eigenvalue equation for the periodic function is called *Bloch Hamiltonian*.

Density of States

A convenient concept in this context is the density of states (DOS), which provides information about the number of states available at any given energy. It is, therefore, used to describe the ability of a system to absorb or emit a given portion of energy, which is crucial for calculations of macroscopic observables. Consequently, the DOS provides an interface between microscopic band theory and larger-scale observables such as electrical resistivity, photon absorption and emission, and specific heat.

The DOS is defined as

$$\rho(E) = \sum_n \int \frac{d^d k}{(2\pi)^d} \delta(E - E_{n\vec{k}}), \quad (2.14)$$

where δ is the Dirac delta-distribution. Alternatively, the discrete version (without normalization to the volume) is often used:

$$\rho(E) = \sum_{n,\vec{k}} \delta(E - E_{n\vec{k}}). \quad (2.15)$$

The density of states can be used to transform a *high-dimensional* momentum integral of objects that only depend on momentum via the dispersion into a *one-dimensional* energy integral.

2.1.1 Electronic Bands and Their Connection to Electrical Conductivity

It is worth taking a physical detour before moving on to another theoretical construction. In real-world solids, the aforementioned framework of bands and Bloch wavefunctions is used to describe electrons in the ionic potential of a lattice that forms a solid. Electrons are naturally spin- $1/2$ particles and—as such—obey Pauli's exclusion principle. At zero temperature, their distribution function is a Heaviside step function in energy. All bands are filled up to a threshold energy—the Fermi energy E_F .

One possibility is that E_F crosses one or more bands. If an electric field is applied, it causes the electrons to drift by applying a force proportional to the applied electric field. To realize this transition, an electron needs to be in a state that has an unoccupied state close by (in terms of momentum *and* energy). This is not possible within a fully filled band. Fully filled bands below E_F are called valence bands; partially filled or empty bands are called conduction bands.

If this leads to a situation where no band crosses E_F , all bands below are *completely* filled, whereas all bands above are *completely* empty. In this case, the solid will be an insulator. If the chemical potential resides in the gap, exchanging particles with the system is not possible due to the lack of unoccupied states available at the corresponding energy. As an example, the situation illustrated in Fig. 2.1 would lead to an insulator at an appropriately low temperature. If one or more bands would get tilted to cross the Fermi energy, it would lead to a metal.

2.1.2 Wannier Functions

Despite the Bloch wavefunctions being a perfect choice for solving the Schrödinger equation in a periodic potential, switching from a de-localized wavefunction to a localized one is sometimes desirable. This feat is achieved by Wannier functions [19], which, for a given band n , form an orthonormal basis in \vec{R} in the same way that Bloch wavefunctions form an orthonormal basis in \vec{k} . They are given by

$$\phi_{n\vec{R}}(\vec{r}) = \frac{1}{(2\pi)^d} \int_{\text{BZ}} d^d k e^{-i\vec{k}\vec{R}} \psi_{n\vec{k}}(\vec{r}), \quad (2.16)$$

where the integral is over the first Brillouin zone. Although this looks like a Fourier transform, it is not conventional since we originally used a phase-factor $e^{i\vec{k}\vec{r}}$ to transform from real- to reciprocal space. Here, we used the conjugate factor for the same conceptual “direction”. The reason becomes clear when inspecting the integrand:

$$\phi_{n\vec{R}}(\vec{r}) = \frac{1}{(2\pi)^d} \int_{\text{BZ}} d^d k e^{-i\vec{k}\vec{R}} u_{n\vec{k}}(\vec{r}) e^{i\vec{k}\vec{r}} \quad (2.17)$$

$$= \frac{1}{(2\pi)^d} \int_{\text{BZ}} d^d k e^{i\vec{k}(\vec{r}-\vec{R})} \sum_{\vec{G}} e^{-i\vec{G}\vec{r}} C(\vec{k}-\vec{G}) \quad (2.18)$$

By shifting $\vec{r} \rightarrow \vec{r} + \vec{R}'$ one gets

$$\phi_{n\vec{R}}(\vec{r} + \vec{R}') = \frac{1}{(2\pi)^d} \int_{\text{BZ}} d^d k e^{i\vec{k}(\vec{r}+\vec{R}'-\vec{R})} \sum_{\vec{G}} e^{-i\vec{G}(\vec{r}+\vec{R}')} C(\vec{k}-\vec{G}) \quad (2.19)$$

The second exponential is—by construction—invariant under any lattice translation \vec{R}' . The only difference is, therefore, in the first exponential. If we now also shift \vec{R} by the same vector \vec{R}' , the shift exactly cancels in the first exponential, and we get

$$\phi_{n\vec{R}}(\vec{r}) = \phi_{n(\vec{R}+\vec{R}')}(\vec{r} + \vec{R}'), \quad (2.20)$$

i.e. Wannier functions are invariant under simultaneous translations by a lattice vector in both their arguments. Hence, they can only depend on the difference $\vec{r} - \vec{R}$. This is a highly desirable feature. Determining the Wannier functions inside a single unit cell is sufficient to get the behavior throughout the full lattice. We can now also analyze the physical significance of those functions.

Wannier functions can be understood as the equivalent of local atomic wavefunctions in a lattice. They are localized at each lattice site (each ion in the lattice) and have a spatial dependence relative to the ion's position. This dependence *can* stretch to neighboring ions and—in principle—have an overlap with Wannier functions on remote sites, which naturally leads to the tight-binding model [20].

The Bloch wavefunctions are given in terms of Wannier functions as

$$\psi_{n\vec{k}}(\vec{r}) = \sum_{\vec{R}} e^{i\vec{k}\vec{R}} \phi_{n\vec{R}}(\vec{r}). \quad (2.21)$$

2.1.3 Uniqueness of Wannier Functions / Lattice Coherence

Bloch wavefunctions are eigenfunctions of a hermitian operator $\hat{H}_{\vec{k}}$ and, as such, are only defined up to a global phase.

$$\hat{H}_{\vec{k}} e^{i\varphi_{n\vec{k}}} \psi_{n\vec{k}}(\vec{r}) = E_{n\vec{k}} e^{i\varphi_{n\vec{k}}} \psi_{n\vec{k}}(\vec{r}) \quad (2.22)$$

The phase $\varphi_{n\vec{k}}$ heavily influences the Wannier functions, since it nontrivially enters the Fourier transform that connects Wannier functions and Bloch functions.

$$\phi_{n\vec{R}}(\vec{r}) = \sum_{\vec{k}} e^{-i\vec{k}\vec{R}} e^{i\varphi_{n\vec{k}}} \psi_{n\vec{k}}(\vec{r}) \quad (2.23)$$

Therefore, Wannier functions are not unique, and fitting them from Bloch wavefunctions can be tedious. Once the phase of the Bloch functions is fixed, the Wannier functions have a known, fixed phase relation dictated by their periodicity, c.f. Eq. (2.20). So if lattice-momentum \vec{k} is a *good quantum number* of the Hamiltonian, the Wannier functions obtain a fixed phase relation. If position \vec{R} is a *good quantum number*, working in Bloch basis does not make sense, which would be maximally degenerate in the worst case (fully localized states). Therefore, individual local wavefunctions are a good description of the system. Their phase relation is not fixed by a periodicity condition. Hence, they are not *lattice coherent*.

One could, therefore, define lattice coherence in the following way:

Definition: Lattice coherence

If parts of a system with discrete translational invariance can be described fully by only a set of fully localized Hamiltonians, the respective eigenstates are localized and have independently undetermined phases, so they show no lattice-coherence.

If this is not the case and the eigenstates are therefore *not* fully localized, de-localized Bloch states are eigenstates of the Hamiltonian which imprint a fixed phase-relation onto the localized Wannier states, so they show lattice-coherence.

2.1.4 Heavy Quasiparticles and Itinerant Electrons

It is often beneficial to use the concept of *quasiparticles* instead of physical particles. They are particle-like excitations of an (interacting) system. This will be especially relevant in the context of heavy-fermion materials, which are the focus of this thesis. Being a particle-like collective excitation of the system, a quasiparticle can be assigned a mass that is not restricted to the physical mass of the physical, real particles. The definition of this mass is not unique and depends on the context.

Canonically, the mass is proportional to the inverse of the curvature ($\partial^2 \varepsilon / \partial k^2$) of the dispersion. In terms of band structure, we can understand this as a straight band (weakly \vec{k} -dependent) corresponding to a large mass and a curvy (strongly \vec{k} -dependent, higher order polynomial) band corresponding to a light mass.

Additionally, an effective quasiparticle velocity can be assigned, which is proportional to the slope of the dispersion ($\partial \varepsilon / \partial k$). A perfectly flat band, therefore, describes infinitely heavy, spatially static (standing-wave) particles, whereas a strongly \vec{k} -dependent band describes—relatively—light, itinerant particles.

2.1.5 Understanding Localization in Lattices from the Kronig-Penney Model

If we look at a single, perfectly localized state, its Fourier transform will be fully momentum-independent. Its energy therefore has no notion of spatial extend so that the dispersion will appear as a perfectly flat band in the spectrum. This is still true for a periodic set of perfectly localized states, as can be seen from the Kronig-Penney model [21] with delta-potentials, arranged equally spaced with distance a on an $2N + 1$ -site, 1D chain, i.e. from $x_{\min} = -a \cdot N$ to $x_{\max} = a \cdot N$. The potential is

$$V(x) = \sum_{n=-N}^N -V_0 \delta(x - n \cdot a). \quad (2.24)$$

The basis vector of the reciprocal lattice, defined just below Eq. (2.4), is $b = 2\pi/a$. The Fourier representation of the potential is

$$V_G = \frac{1}{\mathcal{V}} \int dx e^{-iGx} V(x) = -\frac{V_0}{\mathcal{V}} \sum_{n=-N}^N e^{-iGx} \delta(x - n \cdot a) \quad (2.25)$$

$$= -\frac{V_0}{\mathcal{V}} \sum_{n=-N}^N e^{-inG \cdot a} = -\frac{V_0}{\mathcal{V}} \sum_{n=-N}^N \quad (2.26)$$

$$= -\frac{V_0}{a}, \quad (2.27)$$

with the volume $\mathcal{V} = 2N \cdot a$. This is no longer N -dependent, so the limit $N \rightarrow \infty$ is well defined. Inserting this into Equation (2.10) leads to

$$EC(k) = \frac{k^2}{2m} C(k) - \frac{V_0}{a} \sum_G C(k - G) \quad (2.28)$$

Making the Ansatz $C(k) = C \neq 0$ and using $\sum_G = 2\pi/\mathcal{V}$ for one dimension, we get

$$E = \frac{k^2}{2m} - 2\pi \frac{V_0}{a\mathcal{V}}. \quad (2.29)$$

Since k is limited to the first Brillouin zone, the energy E will be less k -dependent the larger V_0 becomes. In the limit $V_0 \rightarrow \infty$, E becomes practically constant. The wave function for a bound state in a single delta-potential of infinite depth V_0 is infinitely localized on the position of the potential. The periodic part of the wavefunction is

$$u_{nk} = \sum_G e^{-iGx} C = \sum_n e^{-i\frac{2\pi nx}{a}} C = C \frac{2\pi}{\mathcal{V}} \sum_n \delta\left(\frac{2\pi x}{a} - 2\pi n\right) \quad (2.30)$$

$$= C \frac{2\pi}{\mathcal{V}} \frac{a}{2\pi} \sum_n \delta(x - n \cdot a), \quad (2.31)$$

where C can now be used to fix the normalization. Therefore, the full wave function is a plane-wave times a series of delta-distributions located at each site. The infinitely bound case leads to a superposition of perfectly localized wavefunctions and a flat dispersion.

The other limit is $V_0 \rightarrow 0$, resulting in the free-electron dispersion $E(k) = k^2/2m$, for which we know the solutions are just plane waves in real space. They extend throughout the whole volume of the system and, as such, are perfectly non-local. The dispersion wraps around at the band edges and creates a gapless band structure, shown in Fig. 2.2. Although the lattice constant a is kept here, it will be effectively set to unity $a = 1$. Also, note that the choice of a is somewhat arbitrary in the case of a vanishing potential.

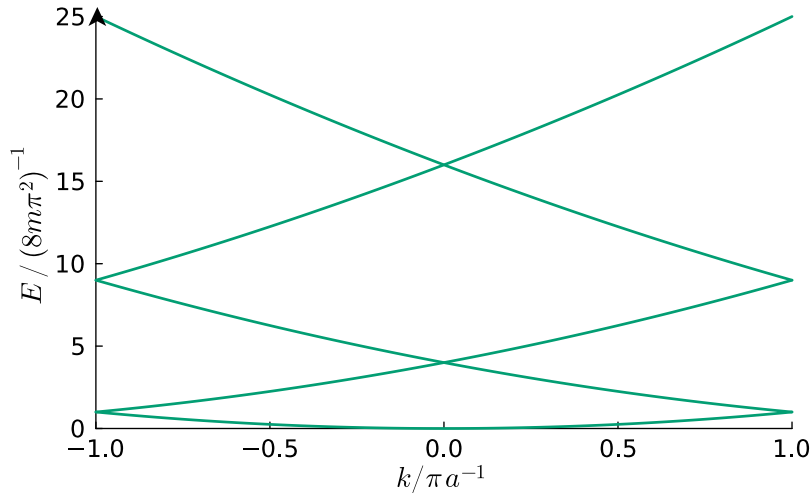


Figure 2.2: Dispersion of a free particle folded into the first Brillouin zone.

2.2 The Resonant-Level Model

Picking up the discussion of Section 2.1.4, we can now construct a minimal model that describes a localized state (at site $i = 0$) embedded in a host of itinerant electrons, i.e. with a dispersive band.

$$H_{\text{RLM}} = \sum_{\vec{k}, \sigma} \varepsilon_{\vec{k}}^c c_{\vec{k}\sigma}^\dagger c_{\vec{k}\sigma} + \sum_{\sigma} \varepsilon^d d_{\sigma}^\dagger d_{\sigma} + \sum_{\sigma} \left(V c_{i=0, \sigma}^\dagger d_{\sigma} + h.c. \right) \quad (2.32)$$

$$= \sum_{\vec{k}, \sigma} \varepsilon_{\vec{k}}^c c_{\vec{k}\sigma}^\dagger c_{\vec{k}\sigma} + \sum_{\sigma} \varepsilon^d d_{\sigma}^\dagger d_{\sigma} + \sum_{\vec{k}, \sigma} \left(V c_{\vec{k}\sigma}^\dagger d_{\sigma} + h.c. \right) \quad (2.33)$$

This is a simple version of the “resonant-level model” in arbitrary dimensions, which is a model describing the potential scattering of itinerant electrons with an impurity. It is a quadratic model and can, therefore, be solved exactly. The problem can be approached in many different ways, but in anticipation of later chapters, I will use a matrix representation of the Hamiltonian, which can then be diagonalized exactly.

$$H_{\text{RLM}} = \sum_{\sigma} \begin{pmatrix} d_{\sigma}^\dagger & c_{\sigma}^\dagger \end{pmatrix} \begin{bmatrix} \varepsilon^d & \mathbf{V}^\dagger \\ \mathbf{V} & \boldsymbol{\varepsilon}^c \end{bmatrix} \begin{pmatrix} d_{\sigma} \\ c_{\sigma} \end{pmatrix} \quad (2.34)$$

$$\mathbf{V} = \left(V, V, V, \dots \right)^\top \quad (2.35)$$

$$\mathbf{c}_{\sigma} = \left(c_{\vec{k}_1 \sigma}, c_{\vec{k}_2 \sigma}, \dots \right)^\top \quad (2.36)$$

$$\boldsymbol{\varepsilon}^c = \begin{bmatrix} \varepsilon_{\vec{k}_1}^c & 0 & 0 \\ 0 & \varepsilon_{\vec{k}_2}^c & 0 & \dots \\ 0 & 0 & \varepsilon_{\vec{k}_3}^c & \\ \vdots & & & \ddots \end{bmatrix} \quad (2.37)$$

I will refer to this representation as the *flavor*-representation⁷ in which the nature of the particles, i.e. itinerant c or local d , is the “flavor”. Note that the matrices \mathbf{V} and \mathbf{c} are $N \times 1$ matrices, where N enumerates the momentum. Additionally, conduction electrons have a momentum quantum number, so the matrix elements are two momenta and two spins. Since spin is conserved at each point, its quantum number can be dropped in the description. This would ideally be diagonalized to find the eigenenergies.

2.2.1 Block-Matrix Inversion in the Context of Green Functions

A more general formulation of the problem is useful at this point so that the solution can be utilized at a later point in this thesis. Let’s consider the matrices \mathbf{A} , \mathbf{B} , \mathbf{C} of size $\{N \times N\}$, $\{N \times M\}$, and

⁷ People often use the name “Nambu representation” or “Nambu space”, which is mathematically probably even correct but physically heavily dressed with expectations of Superconductivity or Majorana physics. Similarly, transformations in this space are sometimes called Bogoliubov-like transformations. Again, this is heavily dressed, and neither shall be used in this thesis for an unbiased and clear picture.

$\{M \times M\}$, where we assume that A and D are invertible. The block matrix of interest is

$$\mathcal{M} = \begin{bmatrix} A & B \\ B^\dagger & C \end{bmatrix}. \quad (2.38)$$

The problem can—in principle—be made even more general, but it's not necessary in the context of this thesis. Generally, block-diagonalization is a challenging problem; not much can be done without assumptions. However, constructing the inverse Green function can be done exactly. The Green function is the operator-inverse of the Schrödinger operator $i\partial_t - H$. In the language of quantum field theory, it is an appropriately constructed expectation value of two field operators, details of which are not important here but can be found in any standard textbook.

Using the equations of motion for frequency-dependent equilibrium Green functions [22] as the solution of the inverse Hamiltonian in operator space (i.e. the flavor-representation from before)

$$G(\omega) [\omega \mathbb{1} - H] = \mathbb{1}. \quad (2.39)$$

This equation can be used for Matsubara-, retarded- or advanced Green functions equally by substitution of ω by $i\omega_n$ or $\omega \pm i\eta$ and $\eta \rightarrow 0^+$ respectively. The frequency part $\omega \mathbb{1}$ can be absorbed in A and C , assuming the resulting matrices remain invertible. This is specifically true in the cases of interest; their inverses are just the free Green functions. The inverse is then

$$\begin{bmatrix} A & B \\ B^\dagger & C \end{bmatrix}^{-1} = \begin{bmatrix} (A - B C^{-1} B^\dagger)^{-1} & 0 \\ 0 & (C - B^\dagger A^{-1} B)^{-1} \end{bmatrix} \begin{bmatrix} \mathbb{1} & -B C^{-1} \\ -B^\dagger A^{-1} & \mathbb{1} \end{bmatrix}. \quad (2.40)$$

Most quantities of interest (like the density of states) involve tracing over flavor space, elevating the importance of the diagonal elements.

2.2.2 Solutions via Self-Energies and T -Matrices

Combining equations (2.34) and (2.40) we can now immediately write down the Green functions for the flavors d and c as

$$[G^d]_{\sigma}^{-1}(\omega) = \omega - \varepsilon^d - \sum_{\vec{k}} \frac{|V|^2}{\omega - \varepsilon_{\vec{k}}^c}, \quad \text{and} \quad (2.41)$$

$$[G^c]_{\vec{k}\vec{k}'\sigma}^{-1}(\omega) = (\omega - \varepsilon_{\vec{k}}^c) \delta_{\vec{k},\vec{k}'} - \frac{|V|^2}{\omega - \varepsilon^d}, \quad (2.42)$$

where the last part of the second equation is independent of \vec{k} and \vec{k}' and is therefore maximally filled in lattice-momentum space. This makes the first equation simply diagonalizable, whereas the second is much more challenging. The mixture of the non-local part ($\varepsilon_{\vec{k}}^c$) and the singular local hybridization, breaking translation invariance, makes neither position nor lattice-momentum a good quantum number. Physically, the problem lies in mixing itinerant electrons with a singular localized state, creating a distinct point in the lattice that differs from the rest. In contrast, the lattice has non-local elements in the Hamiltonian, making the electrons itinerant. One should note that, since the off-diagonal Green

functions are non-zero, the diagonal Green functions are *not* representing the Green functions of the flavor-mixed field operators that solve the system, i.e. diagonalize the matrix Hamiltonian. The trace of the Green functions, on the other hand, is the physical solution to the system. It is independent of the chosen base and contains the spectral information required to describe the behavior of the system.

Utilizing the free Green functions

$$G_{\sigma}^{d(0)}(\omega) = (\omega - \varepsilon^d)^{-1}, \quad G_{\vec{k}\sigma}^{c(0)}(\omega) = (\omega - \varepsilon_{\vec{k}}^c)^{-1}, \quad \text{and} \quad G_{\text{loc},\sigma}^{c(0)}(\omega) = \sum_{\vec{k}} G_{\vec{k}\sigma}^{c(0)}(\omega), \quad (2.43)$$

the full Green functions (with the argument ω suppressed for readability) are

$$[G^d]_{\sigma}^{-1} = [G^{d(0)}]_{\sigma}^{-1} - |V|^2 G_{\text{loc},\sigma}^{c(0)}, \quad \text{and} \quad (2.44)$$

$$[G^c]_{\vec{k}\vec{k}'\sigma}^{-1} = [G^{c(0)}]_{\vec{k}\sigma}^{-1} \delta_{\vec{k},\vec{k}'} - |V|^2 G_{\sigma}^{d(0)}. \quad (2.45)$$

Multiplying from the left with the respective free Green function and from the right with the respective full Green function yields Dyson equations, where the self-energies are not *proper* self-energies in the sense that they stem from quadratic parts in the Hamiltonian.

$$G_{\sigma}^d = G_{\sigma}^{d(0)} + G_{\sigma}^{d(0)} |V|^2 G_{\text{loc},\sigma}^{c(0)} G_{\sigma}^d \quad (2.46)$$

$$G_{\vec{k}\vec{k}'\sigma}^c = G_{\vec{k}\sigma}^{c(0)} \delta_{\vec{k},\vec{k}'} + \sum_{\vec{k}''} G_{\vec{k}\sigma}^{c(0)} |V|^2 G_{\sigma}^{d(0)} G_{\vec{k}''\vec{k}'\sigma}^c \quad (2.47)$$

Simultaneous iteration of both equations to infinite order transforms them into the T -matrix equations

$$G_{\sigma}^d = G_{\sigma}^{d(0)} + G_{\sigma}^{d(0)} |V|^2 G_{\text{loc},\sigma}^c G_{\sigma}^{d(0)}, \quad \text{and} \quad (2.48)$$

$$G_{\vec{k}\vec{k}'\sigma}^c = G_{\vec{k}\sigma}^{c(0)} + G_{\vec{k}\sigma}^{c(0)} |V|^2 G_{\sigma}^d G_{\vec{k}'\sigma}^{c(0)}, \quad (2.49)$$

with $G_{\text{loc}}^c(\omega)$, the conduction-electron Green function at the position of the resonant level. It is readily calculated using the Fourier-transform of the lattice-momentum dependent Green function

$$G_{ij}^c(\omega) = \sum_{\vec{k},\vec{k}'} e^{-i\vec{k}\vec{r}_i} G_{\vec{k}\vec{k}'}^c(\omega) e^{i\vec{k}'\vec{r}_j} = \sum_{\vec{k},\vec{k}'} e^{i(\vec{k}'\vec{r}_j - \vec{k}\vec{r}_i)} G_{\vec{k}\vec{k}'}^c(\omega), \quad (2.50)$$

$$\Rightarrow G_{00}^c(\omega) = G_{\text{loc}}^c(\omega) = \sum_{\vec{k},\vec{k}'} G_{\vec{k}\vec{k}'}^c(\omega). \quad (2.51)$$

To proceed, we have to choose a representation of the Green functions since so far ω was just a placeholder. A convenient choice is $\omega \rightarrow \omega - i\eta$, i.e. advanced Green functions. Free Green functions can be described then by the same general formulation using the Sokhotski–Plemelj theorem under $\eta \rightarrow 0^+$,

$$G^{(0)}(\omega - i\eta, \varepsilon) = \frac{1}{\omega - \varepsilon - i\eta} \xrightarrow{\eta \rightarrow 0^+} \text{p.v.} \frac{1}{\omega - \varepsilon} + i\pi\delta(\omega - \varepsilon) = G^{(0),A}(\omega - \varepsilon), \quad (2.52)$$

where p.v. denotes the Cauchy principal value. From this, we can define

$$G_{\sigma}^{d(0),A}(\omega) = G^{(0),A}(\omega - \varepsilon^d), \quad (2.53)$$

$$G_{\vec{k}\sigma}^{c(0),A}(\omega) = G^{(0),A}(\omega - \varepsilon_{\vec{k}}^c), \quad (2.54)$$

where—in this case—both functions are spin-degenerate. From here on, I will drop the superscript A in favor of readability unless it is necessary for context.

As can be seen from comparing Eq. (2.48) to Eq. (2.44), directly inverting Dyson's equation is much preferable for the resonant-level part. The conduction electrons, on the other hand, are much better described by the T -matrix equation (Eq. 2.49) due to the lattice-momentum independence of their “self-energy” resulting in a fully filled matrix form, where each entry has identical values⁸. Due to the full spin-degeneracy of the solution, the subscript σ is dropped in the following.

There are a couple of objects that are now of interest:

1. The impurity density of states (DOS) $\rho^d(\omega) = \text{Im } G^d(\omega)/\pi$.
2. The local conduction-electron DOS at the impurity site $\rho_{\text{loc}}^c(\omega) = \sum_{\vec{k}, \vec{k}'} \text{Im } G_{\vec{k}\vec{k}'}^c(\omega)/\pi$.
3. The trace of the conduction-electron spectrum, which can be seen as the proper lattice conduction-electron DOS $\rho_0^c(\omega) = \sum_{\vec{k}} \text{Im } G_{\vec{k}\vec{k}}^c(\omega)/\pi$.
4. The lattice-momentum dependent spectrum.

2.2.3 Local Density of States

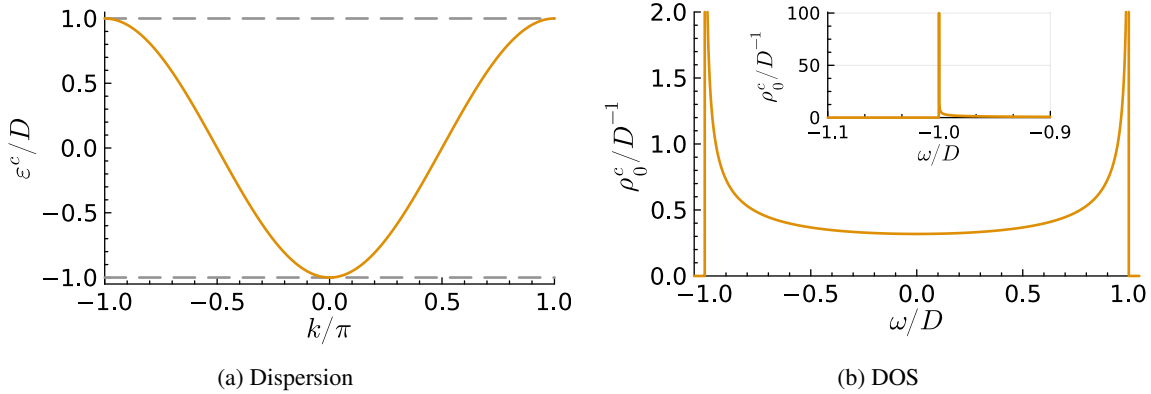


Figure 2.3: Dispersion and DOS of a 1D tight-binding lattice.

Although the largest part of the following will be fully general, I will discuss the case of a constant conduction-electron density of states and present results for the case of a 1-dimensional lattice with lattice spacing a in the tight-binding approximation. All energies in the example system are given in units of the half-bandwidth D , and lattice-momenta \vec{k} are given in units of $1/a$, making the first Brillouin zone for \vec{k} range from $-\pi$ to π . The dispersion is then just $\varepsilon_{\vec{k}}^c = -\cos(k)$, c.f. Fig. 2.3(a).

⁸ The problem persists and becomes arguably even worse for a lattice-momentum dependent hybridization.

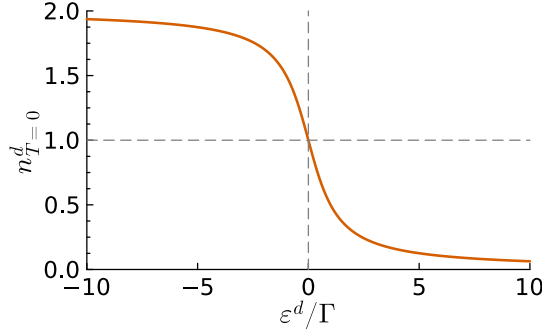


Figure 2.4: Occupation of the resonant level for $T = 0$ according to Eq. (2.57).

The density of states is flat around the band center and has van-Hove singularities at the band edges, c.f. Fig. 2.3(b). It can be calculated analytically (c.f. app. C.3) and is

$$\rho_{1D}^c(0) = \frac{1}{\pi} \frac{\Theta(1 - |\omega|)}{\sqrt{1 - \omega^2}}. \quad (2.55)$$

Its Hilbert transform is $0 \forall |\omega| < 1$ [23]. The band edges will often be neglected in further discussions when they are not essential for a physical understanding.

The first quantity we shall investigate is the resonant-level density of states. In the textbook-example of a flat conduction-electron DOS $\rho^c(0)(\omega) = \rho^c(0)$, the impurity DOS is analytically computable. This is a good approximation when the resonant-level position is well within the band, and the hybridization strength is small compared to the bandwidth. The imaginary part of the conduction-electron Green function is then just a constant, resulting in a vanishing real part via the Kramers-Kronig relation. By defining $\Gamma(\omega) = \pi|V|^2\rho^c(0)(\omega) = \pi|V|^2\rho^c(0)$ the resonant-level DOS is

$$\rho^d(\omega) = \frac{1}{\pi} \frac{\Gamma}{(\omega - \varepsilon^d)^2 + \Gamma^2}, \quad (2.56)$$

as can be easily derived from Eq. (2.44) by expanding the fraction with the complex conjugate of the denominator. The resonant-level spectrum thus picks up a width Γ and produces a Lorentzian line shape. The zero-temperature occupation of the resonant level (using Eq. (C.7) in Appendix C.1) is thus

$$n_{T=0}^d = 1 - \frac{2}{\pi} \arctan\left(\frac{\varepsilon^d}{\Gamma}\right), \quad (2.57)$$

where the overall factor of 2 is due to spin degeneracy. The occupation is plotted in Fig. 2.4.

In the case of arbitrary conduction-electron DOS, the resonant-level DOS is

$$\rho^d(\omega) = \frac{1}{\pi} \frac{\Gamma(\omega)}{[\omega - \varepsilon^d - |V|^2 \text{Re} G_{\text{loc}}^c(0)(\omega)]^2 + [\Gamma(\omega)]^2}, \quad (2.58)$$

where $\text{Re} G_0^c(0)(\omega)$ can be calculated via the Kramers-Kronig relation using only the free conduction-

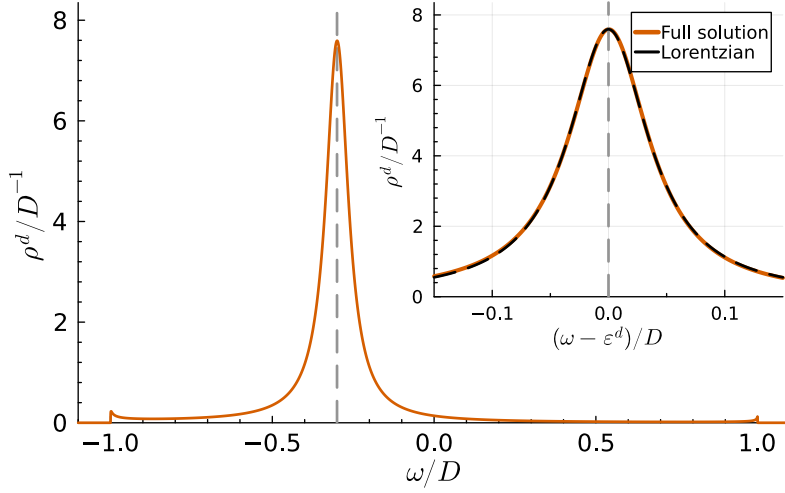


Figure 2.5: Resonant-level density of states.

electron density of states. In general, the peak position will thus also get renormalized. For ε^d well inside the band and a smooth c-electron DOS around it, the shape of the resonance can be expected Lorentzian-like around ε^d and $\propto \Gamma(\omega)/\omega^2$ far away. The results for a 1D lattice of conduction electrons are shown in Fig. 2.5. Since the real part also vanishes in this case, and due to the almost flat DOS for $\varepsilon^d \ll D$, the Lorentzian line shape can be well approximated by a constant $\Gamma(\omega) = \Gamma(\varepsilon^d)$ for conservative choices of parameters. The peak height is precisely $1/(\pi\Gamma(\varepsilon^d))$.

The local conduction-electron DOS can be calculated by Fourier-transforming the lattice-momentum-dependent Green function in Eq. (2.50) and (2.51).

$$\begin{aligned} G_{ij}^c(\omega) &= \sum_{\vec{k}, \vec{k}'} e^{-i\vec{k}\vec{r}_i} G_{\vec{k}\vec{k}'}^c(\omega) e^{i\vec{k}'\vec{r}_j} = \sum_{\vec{k}, \vec{k}'} e^{i(\vec{k}'\vec{r}_j - \vec{k}\vec{r}_i)} G_{\vec{k}\vec{k}'}^c(\omega) \\ \Rightarrow G_{00}^c(\omega) &= G_{\text{loc}}^c(\omega) = \sum_{\vec{k}, \vec{k}'} G_{\vec{k}\vec{k}'}^c(\omega) \end{aligned}$$

Using the T -matrix equation (2.49) it evaluates to

$$G_{\text{loc}}^c(\omega) = \sum_{\vec{k}, \vec{k}'} \left(G_{\vec{k}}^{c(0)}(\omega) \delta_{\vec{k}, \vec{k}'} + G_{\vec{k}}^{c(0)}(\omega) |V|^2 G^d(\omega) G_{\vec{k}'}^{c(0)}(\omega) \right) \quad (2.59)$$

$$= \sum_{\vec{k}} G_{\vec{k}}^{c(0)}(\omega) + |V|^2 G^d(\omega) \left(\sum_{\vec{k}} G_{\vec{k}}^{c(0)}(\omega) \right)^2 \quad (2.60)$$

$$= G_{\text{loc}}^{c(0)}(\omega) + |V|^2 G^d(\omega) \left(G_{\text{loc}}^{c(0)}(\omega) \right)^2, \quad (2.61)$$

$$\rho_{\text{loc}}^c(\omega) = \text{Im} G_{\text{loc}}^c(\omega) / \pi. \quad (2.62)$$

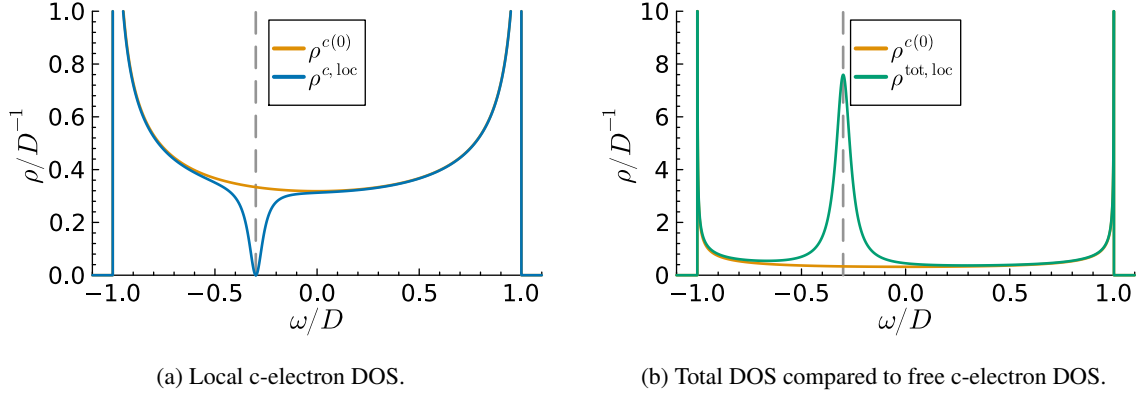


Figure 2.6: Local DOS of a 1D tight-binding lattice.

For a flat c-band again, the expression reduces to

$$\rho_{\text{loc}}^c(\omega) = \rho^{c(0)} \left(1 - \pi\Gamma \rho^d(\omega)\right) = \rho^{c(0)} \left(1 - \frac{\Gamma^2}{(\omega - \varepsilon^d)^2 + \Gamma^2}\right), \quad (2.63)$$

which exactly vanishes at $\omega = \varepsilon^d$. Results for the 1D system are shown in Fig. 2.6.

2.2.4 Spectrum of the Green Function Trace / Lattice Density of States

Another quantity used to get the canonical definition of the density of states of a system is the trace of the imaginary part of the Green function. Since the trace is just a sum, it commutes with the projection onto the imaginary axis. The trace of the Green function is

$$\sum_{\vec{k}} G_{\vec{k}\vec{k}}^c(\omega) = \sum_{\vec{k}} \left(G_{\vec{k}}^{c(0)}(\omega) + G_{\vec{k}}^{c(0)}(\omega) |V|^2 G^d(\omega) G_{\vec{k}}^{c(0)}(\omega) \right) \quad (2.64)$$

$$= G_{\text{loc}}^{c(0)}(\omega) + |V|^2 G^d(\omega) \sum_{\vec{k}} \left(G_{\vec{k}}^{c(0)}(\omega) \right)^2 \quad (2.65)$$

$$= G_{\text{loc}}^{c(0)}(\omega) + |V|^2 G^d(\omega) \int_{-\infty}^{\infty} d\varepsilon \rho^c(\varepsilon) \left(G^c(\omega - \varepsilon) \right)^2, \quad (2.66)$$

$$\text{Tr} G(\omega) = \sum_{\vec{k}} G_{\vec{k}\vec{k}}^c(\omega) + G^d(\omega) = G_{\text{loc}}^{c(0)}(\omega) + \Delta G^c(\omega). \quad (2.67)$$

The second part of Eq. (2.66) is notoriously hard to evaluate numerically if the c-electron DOS is not smooth enough. Analytically, it needs some massaging to allow for insight. Let's calculate the change

in the trace of the total Green function ΔG^c via a trick [24].

$$\frac{\partial}{\partial \omega} \ln \left(\omega - \varepsilon^d - |V|^2 \sum_{\vec{k}} G_{\vec{k}}^{c(0)}(\omega) \right) \quad (2.68)$$

$$= G^d(\omega) - G^d(\omega) \cdot |V|^2 \sum_{\vec{k}} \left(\frac{\partial}{\partial \omega} G_{\vec{k}}^{c(0)}(\omega) \right) = \Delta G^c(\omega) \quad (2.69)$$

The derivative can be calculated by analyzing the function for finite width η before sending it to zero.

$$\begin{aligned} \frac{\partial}{\partial \omega} G_{\vec{k}}^{c(0)}(\omega - i\eta) &= \frac{\partial}{\partial \omega} \frac{1}{\omega - \varepsilon_{\vec{k}}^c - i\eta} = -\frac{1}{(\omega - \varepsilon_{\vec{k}}^c - i\eta)^2} \\ &= -\left(G_{\vec{k}}^{c(0)}(\omega - i\eta) \right)^2 \xrightarrow{\eta \rightarrow 0^+} -\left(G_{\vec{k}}^{c(0),A}(\omega) \right)^2 \end{aligned} \quad (2.70)$$

Therefore,

$$\Delta G^c(\omega) = G^d(\omega) + G^d(\omega) \cdot |V|^2 \sum_{\vec{k}} \left(G_{\vec{k}}^{c(0)}(\omega) \right)^2, \quad (2.71)$$

which proves this substitution via a series of identities. Investigating Eq. (2.69) more thoroughly as

$$\Delta G^c(\omega) - G^d(\omega) = G^d(\omega) \cdot |V|^2 \int_{-\infty}^{\infty} d\varepsilon \rho^{c(0)}(\varepsilon) \left(\frac{\partial}{\partial \omega} G^{c(0)}(\omega - \varepsilon) \right) \quad (2.72)$$

$$= G^d(\omega) \cdot |V|^2 \frac{\partial}{\partial \omega} \int_{-\infty}^{\infty} d\varepsilon \rho^{c(0)}(\varepsilon) G^{c(0)}(\omega - \varepsilon) \quad | \tilde{\varepsilon} = \omega - \varepsilon \quad (2.73)$$

$$= G^d(\omega) \cdot |V|^2 \frac{\partial}{\partial \omega} \int_{-\infty}^{\infty} d\tilde{\varepsilon} \rho^{c(0)}(\omega - \tilde{\varepsilon}) G^{c(0)}(\tilde{\varepsilon}) \quad (2.74)$$

$$= G^d(\omega) \cdot |V|^2 \int_{-\infty}^{\infty} d\tilde{\varepsilon} \left(\frac{\partial}{\partial \omega} \rho^{c(0)}(\omega - \tilde{\varepsilon}) \right) G^{c(0)}(\tilde{\varepsilon}), \quad (2.75)$$

which works under the restrictions of the Leibniz integral rule. Therefore, it is not applicable for a highly singular $G^{c(0)}$. We can, however, circumvent this by sticking to the finite but small width η , ensuring the regularity of all functions (and their derivative) under the integral. This expression exactly vanishes for a constant c-electron density of states. In this case, the (lattice) density of states is just the original one, plus the local resonant-level DOS. Results for the 1D lattice are shown in Fig. 2.7.

Just as in the case of the local DOS, this still holds approximately true for a resonant-level well within the conduction band $|\varepsilon^d| \ll D$, obtaining a small width $\Gamma \ll D$. First, since we are interested in the imaginary part of the expression, we note that only cross-terms of the complex product of G^d and $G^{c(0)}$ contribute. One term is $\sim \text{Im} G^d(\omega) \text{Re} G^{c(0)}(\omega - \varepsilon)$, which we shall analyze in the intermediate result of Eq. (2.73). The real part of $G^{c(0)}$ gives a principal-value integral

$$\text{p.v.} \int_{-1}^1 d\varepsilon \frac{\rho^{c(0)}(\varepsilon)}{\omega - \varepsilon}, \quad (2.76)$$

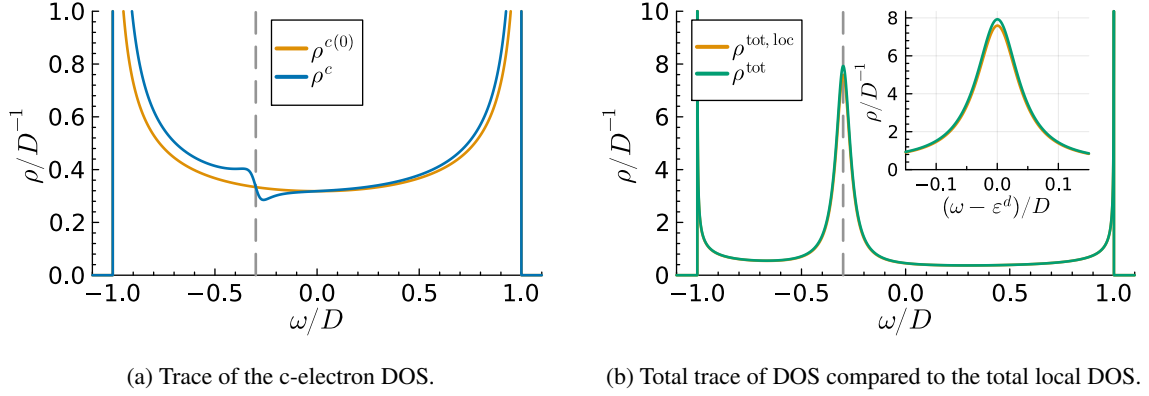


Figure 2.7: Trace of the DOS of a 1D tight-binding lattice.

which is just the negative real part of the free conduction-electron Green function $-\pi \text{Re } G^{c(0)}(\omega)$. For a flat enough conduction band in a region of width Γ around ε^d , this is just a constant, so the frequency derivative vanishes. Outside of that region, $\text{Im } G^d(\omega)$ is very small, suppressing the contribution from the other term. In our 1D example, the only case where this can not be argued is the band edges due to the van-Hove singularities. There, this correction is dwarfed by the divergence in $\rho^{c(0)}$, making it negligible.

The second contribution is the term $\sim \text{Re } G^d(\omega) \text{Im } G^{c(0)}(\omega - \varepsilon)$, where the integral collapses to the value $\varepsilon = \omega$ due to the delta distribution in the imaginary part of $G^{c(0)}$. The contribution, therefore, reduces to

$$\pi \text{Re } G^d(\omega) \cdot |V|^2 \frac{\partial}{\partial \omega} \rho^{c(0)}(\omega). \quad (2.77)$$

This again exactly vanishes if $\rho^{c(0)}$ is flat. Since $\text{Re } G^d(\omega) \sim \omega^{-1}$ for $\omega \gg \Gamma$ (in contrast to $\text{Im } G^d(\omega) \sim \omega^{-2}$), the contribution might be larger but also vanishes in the flat-band limit. Furthermore, the contribution will be slowly varying in the other case considered above.

Overall, it can be seen that the total (lattice) density of states, defined as the imaginary part of the trace of the full Green function, is mostly just the sum of the free conduction-electron DOS $\rho^{c(0)}$ and the renormalized, local resonant-level DOS $\rho^d(\omega)$. This is a crucial observation in that the local level only weakly, if at all, influences the conduction electron density of states when averaged over the whole lattice. This is obviously due to volume effects since the local level is a singular point in a much larger lattice. Locally, as seen in the previous section, the situation is much different.

2.2.5 The Problem of a Lattice-Momentum Dependent Spectrum

Finally, to wrap the discussion back around to the picture of lattice coherence, we would like to look at the lattice-momentum dependent spectra. Concretely, the momentum-diagonal elements of the full Green function. We can use the Dyson equation (Eq. (2.44)) for the resonant-level spectrum and the T-matrix equation (Eq. (2.49)) for the conduction electrons. Since the spectra are plotted in the basis of a bad quantum number, they do not reproduce the shape of Bloch bands. Instead, the resonant

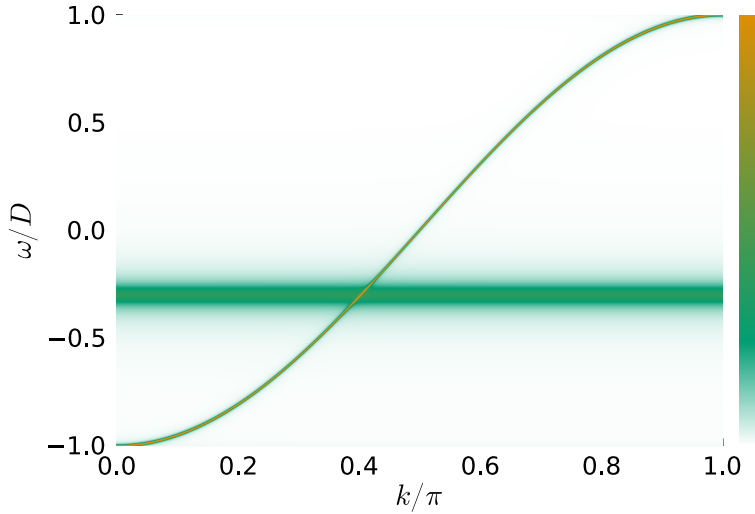


Figure 2.8: Illustration of a resonant-level model's expected lattice-momentum dependent spectrum. The resonant-level density of states is exactly reproduced at each momentum since it is perfectly localized. As discussed in the text, the conduction-electron band is modeled as just the free band. The free band was approximated by a Lorentzian of width $\eta/D = 10^{-3}$. The color corresponds approximately to strength, but the normalization is not meaningful due to the problems discussed in the text. The color bar, therefore, remains unlabeled. Here, k is dimensionless via the lattice constant $a = 1$.

level obtains a finite width, which can be deduced from Fig. 2.5 paired with the fact that this picture is reproduced for each value of \vec{k} maintaining normalization. The main problem is evaluating the T -matrix equation for the conduction electrons. Here, the occurrence of the free Green function poses a problem of being only defined under an integral, c.f. equation (2.52), i.e.

$$G^{(0)}(\omega - i\eta, \varepsilon) = \frac{1}{\omega - \varepsilon - i\eta} \xrightarrow{\eta \rightarrow 0^+} \text{p.v.} \frac{1}{\omega - \varepsilon} + i\pi\delta(\omega - \varepsilon) = G^{(0),A}(\omega - \varepsilon).$$

The goal of plotting the exact spectrum is, therefore, unachievable. If we think of the local scattering as introducing a phase shift to the conduction electrons, combined with the above definition of the free conduction-electron Green function, it becomes clear why we can not faithfully visualize the spectrum. An attempt at simplifying the equations, breaking them down to the product of $G^c{}^{(0)}$ and an analytically calculable object depending on G^d and the derivative of the free, local conduction-electron Green function $G_{\text{loc}}^c{}^{(0)}$ is presented in Appendix B.

We can, however, estimate how a spectrum would look like if measured. There, the conduction electrons will be influenced minimally by the resonant level, mostly via a phase shift, which will be reflected in the shift of weight *within* the band. Disregarding this redistribution of weight, an expected spectrum is shown in Fig. 2.8.

2.3 The Two-Band Hybridization Model

A fundamental “problem” of the resonant-level model is the broken discrete translation symmetry, resulting in momentum being a bad quantum number. The model is justified for dilute, localized resonant levels embedded in a metal. Increasing the concentration of the resonant levels will ultimately lead to one level at each lattice site, at which point the model is a periodic resonant-level model⁹

$$H_{PRLM} = \sum_{\vec{k}, \sigma} \varepsilon_{\vec{k}}^c c_{\vec{k}\sigma}^\dagger c_{\vec{k}\sigma} + \sum_{i, \sigma} \varepsilon^d d_{i\sigma}^\dagger d_{i\sigma} + \sum_{i, \sigma} \left(V c_{i\sigma}^\dagger d_{i\sigma} + h.c. \right). \quad (2.78)$$

This is the flat-band local hybridization limit of a two-band hybridization model

$$H_{2BHM} = \sum_{\vec{k}, \sigma} \varepsilon_{\vec{k}}^c c_{\vec{k}\sigma}^\dagger c_{\vec{k}\sigma} + \sum_{\vec{k}\sigma} \varepsilon_{\vec{k}}^d d_{\vec{k}\sigma}^\dagger d_{\vec{k}\sigma} + \sum_{\vec{k}\sigma} \left(V_{\vec{k}} c_{\vec{k}\sigma}^\dagger d_{\vec{k}\sigma} + h.c. \right). \quad (2.79)$$

Momentum is a good quantum number for this model, and the Hamiltonian becomes block-diagonal in \vec{k} -space with each block being a matrix in flavor-space.

$$H_{2BHM} = \sum_{\vec{k}, \sigma} \begin{pmatrix} d_{\vec{k}\sigma}^\dagger & c_{\vec{k}\sigma}^\dagger \end{pmatrix} \begin{bmatrix} \varepsilon_{\vec{k}}^d & V_{\vec{k}}^* \\ V_{\vec{k}} & \varepsilon_{\vec{k}}^c \end{bmatrix} \begin{pmatrix} d_{\vec{k}\sigma} \\ c_{\vec{k}\sigma} \end{pmatrix} \quad (2.80)$$

The system is solved by block-diagonalization of the Hamiltonian. As shown above, each block is a hermitian 2×2 matrix. The eigenenergies are

$$E_{\vec{k}, 1/2} = \frac{1}{2} \left[\varepsilon_{\vec{k}}^c + \varepsilon_{\vec{k}}^d \pm \sqrt{(\varepsilon_{\vec{k}}^c - \varepsilon_{\vec{k}}^d)^2 + 4|V|^2} \right]. \quad (2.81)$$

The eigenvectors are

$$\vec{v}_{\vec{k}, 1} = \begin{pmatrix} e^{i\phi_{\vec{k}}} \cos(\Theta_{\vec{k}}/2) \\ \sin(\Theta_{\vec{k}}/2) \end{pmatrix}, \quad \vec{v}_{\vec{k}, 2} = \begin{pmatrix} e^{-i\phi_{\vec{k}}} \sin(\Theta_{\vec{k}}/2) \\ \cos(\Theta_{\vec{k}}/2) \end{pmatrix}, \quad (2.82)$$

where $\phi_{\vec{k}}$ is defined via $V_{\vec{k}} = |V_{\vec{k}}| \cdot \exp(i\phi_{\vec{k}})$ and $\Theta_{\vec{k}} = \arccos(\varepsilon_{\vec{k}}^c - \varepsilon_{\vec{k}}^d) / (E_{\vec{k}, 1} - E_{\vec{k}, 2})$. Note that this decouples exactly for $V = 0$, which remains throughout the following discussion. The energies are finite for finite parameters and finite bandwidth of $\varepsilon_{\vec{k}}^c$ and $\varepsilon_{\vec{k}}^d$. Depending on the parameters, a gap can appear. This will be explored in the next section.

Results for the lattice-momentum dependent spectra for a 1D system with parameters $\varepsilon_{\vec{k}}^d = \varepsilon^d = -0.3$, $V_{\vec{k}}^2 = V^2 = 0.05$ and $V_{\vec{k}}^2 = V^2 = 0.2$ are shown in Fig. 2.9. The tendency of hybridizing bands to avoid points of degeneracy is well visible. This concept is known as *avoided crossing*. It will play an essential role in gauging the degree of lattice coherence in systems where localization competes with de-localization.

⁹ The name is an analogy to the periodic Anderson model, which will be discussed later in the thesis.

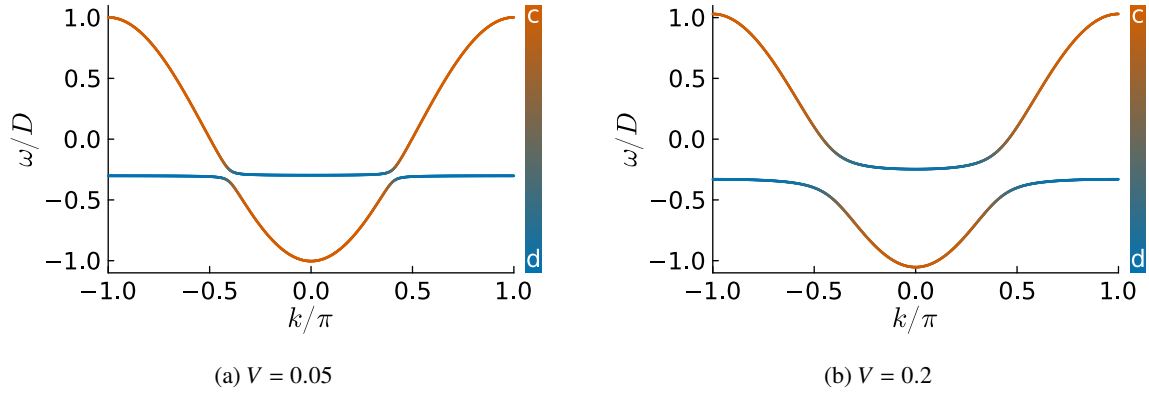


Figure 2.9: Spectral function of the 1D two-band hybridization model for two different V , where $\varepsilon_k^c = -\cos(k)$ and $\varepsilon^d = -0.3$. The coloring represents the flavor of the eigenvector in terms of c - and d electrons. Here, k is dimensionless via the lattice constant $a = 1$.

2.3.1 Band Gap

At this point, not much can be done without assuming details of the model. In an effort to restrict the validity of results as little as possible while still reducing the complexity enough to allow for analytical results, the assumption $\varepsilon_k^d = \varepsilon_0^d + \kappa \cdot \varepsilon_k^c$ is made, where κ is a real number. This includes the flat-band case $\kappa = 0$. The parameter κ can be restricted to $|\kappa| \leq 1$ without loss of generality. If $|\kappa| > 1$ the role of c - and d -electrons is just reversed and taking the ε_k^d as the reference, i.e. $\varepsilon_k^c = \varepsilon_0^c + \tilde{\kappa} \cdot \varepsilon_k^d$ leads to identical equations with a new $|\tilde{\kappa}| \leq 1$ and $c \leftrightarrow d$. This can also be done in the more general case, where one would then use the d -electron DOS to replace the momentum sum and write $\varepsilon_k^c = \varepsilon^c(\varepsilon_k^d)$. Furthermore, the parameter $|V|$ is assumed \vec{k} -independent and finite.

Under this assumption, the eigenenergies take the shape

$$E_{\vec{k},1/2} = \frac{1}{2} \left[\varepsilon_0^d + (1 + \kappa)\varepsilon_k^c \pm \sqrt{\left((1 - \kappa) \cdot \varepsilon_k^c - \varepsilon_0^d \right)^2 + 4|V|^2} \right], \quad (2.83)$$

$$\Rightarrow E_{1/2}(\varepsilon) = \frac{1}{2} \left[\varepsilon_0^d + (1 + \kappa)\varepsilon \pm \sqrt{\left((1 - \kappa) \cdot \varepsilon - \varepsilon_0^d \right)^2 + 4|V|^2} \right]. \quad (2.84)$$

Three values of κ are of special interest: $\kappa = -1, 0, 1$. Specifically, one wants to determine whether there is an energy gap $\Delta = \min [E_{\vec{k},1}] - \max [E_{\vec{k},2}]$ in the system.

- For $\kappa = 0$, the eigenenergies are

$$E_{\vec{k},1/2}^{\kappa=0} = \frac{1}{2} \left[\varepsilon_0^d + \varepsilon_k^c \pm \sqrt{\left(\varepsilon_k^c - \varepsilon_0^d \right)^2 + 4|V|^2} \right], \quad (2.85)$$

$$\Rightarrow \Delta = \frac{1}{2} \left(\sqrt{(D + \varepsilon_0^d)^2 + 4|V|^2} + \sqrt{(D - \varepsilon_0^d)^2 + 4|V|^2} \right) - D \geq 0, \quad (2.86)$$

which results in a gap for $|V| > 0$. Typically, and especially for generic cubic lattices, this gap is

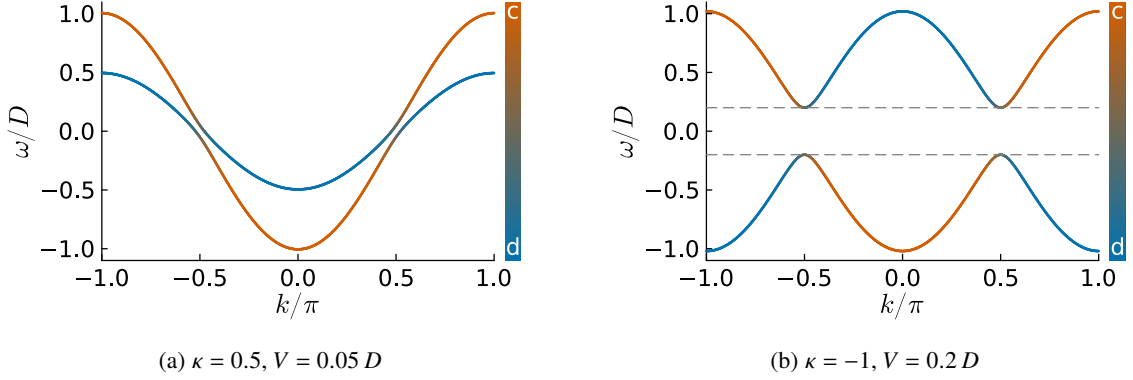


Figure 2.10: Spectral function of the two-band hybridization model for two sets of parameters a and V , where $\varepsilon_k^c = -\cos(k)$, $\varepsilon_k^d = \kappa \cdot \varepsilon_k^c + \varepsilon_0^d$, and $\varepsilon_0^d = -0.3D$. The coloring represents the flavor of the eigenvector in terms of c - and d electrons. The grey dashed lines in (b) are at the predicted gap edges $\omega = \pm|V|$. Here, k is dimensionless via the lattice constant $a = 1$.

indirect. Often, $|\varepsilon_0^d|, |V| \ll D$, leading to a small gap size. This can be nicely seen in Fig. 2.9 including the avoided crossing.

- The case $\kappa = 1$ gives

$$E_{k,1/2}^{\kappa=1} = \frac{1}{2} \left[\varepsilon_0^d + 2\varepsilon_k^c \pm \sqrt{(\varepsilon_0^d)^2 + 4|V|^2} \right] \quad (2.87)$$

$$= \varepsilon_k^c + \frac{1}{2} \left[\varepsilon_0^d \pm \sqrt{(\varepsilon_0^d)^2 + 4|V|^2} \right], \quad (2.88)$$

$$\Rightarrow \Delta = \sqrt{(\varepsilon_0^d)^2 + 4|V|^2} - 2D. \quad (2.89)$$

The bands are, therefore, just the original c -electron band shifted by a constant. If this shift is large enough to separate the bands, the system will be gapped. This requires $(\varepsilon_0^d)^2 + 4|V|^2 \leq 4D^2$. Typically, the conduction-electron bandwidth is the largest scale in such microscopic models; the case $\kappa = 1$ is, therefore, typically non-gapped. An example is shown in Fig. 2.10(a). Avoided crossing can also be seen around $k/\pi \approx \pm 0.5$, where the touching points get repelled. Due to the identical sign of slope, this does not lead to a gap.

- Finally, $\kappa = -1$ yields

$$E_{k,1/2}^{\kappa=-1} = \frac{1}{2} \left[\varepsilon_0^d + \pm \sqrt{(2\varepsilon_k^c - \varepsilon_0^d)^2 + 4|V|^2} \right] \quad (2.90)$$

$$\Rightarrow \Delta = 2|V|. \quad (2.91)$$

This case, therefore, leads to a gapped system with a gap size $2|V|$. An example is shown in Fig. 2.10(b). The avoided crossing is nicely visible and leads to a clear gap.

2.3.2 Density of States

The lattice density of states, which is also the local density of states due to translational invariance, can be calculated using the canonical definition

$$\rho(\omega) = \sum_{\vec{k}} \delta(\omega - \varepsilon_{\vec{k}}), \quad (2.92)$$

replacing the dispersion $\varepsilon_{\vec{k}}$ by the eigenenergies $E_{\vec{k},i}$ for $i = 1, 2$. This is—in general—still a demanding calculation. For the more specific case $\varepsilon_{\vec{k}}^d = \varepsilon^d(\varepsilon_{\vec{k}}^c)$ the momentum sum can be replaced by an integral over the conduction-electron dispersion via their free DOS. The resulting expression is

$$\rho_i(\omega) = \sum_{\vec{k}} \delta(\omega - E_{\vec{k},i}) \quad (2.93)$$

$$= \int d\varepsilon \rho^c(\varepsilon) \delta(\omega - E_i(\varepsilon)) \quad (2.94)$$

$$= \int d\varepsilon \rho^c(\varepsilon) \sum_j \frac{\delta(\varepsilon - \nu_j)}{|E'_i(\nu_j)|} \quad (2.95)$$

$$= \sum_j \frac{\rho^c(\nu_j)}{|E'_i(\nu_j)|}, \quad (2.96)$$

where ν_j are the roots of $\omega - E_i(\varepsilon)$ in ε and $E'_i(\nu_j)$ is the derivative $\partial E_i(\varepsilon)/\partial \varepsilon$ at $\varepsilon = \nu_j$. Typically, the bands are of finite bandwidth; therefore, the eigenenergies E_i are finite, leading to $\rho_i(\omega)$ also being of finite bandwidth. Within the approximation $\varepsilon_{\vec{k}}^d = \varepsilon_0^d + a \cdot \varepsilon_{\vec{k}}^c$, as defined in the previous section, the roots of $\omega - E_i(\varepsilon)$ can be determined exactly. First, we can evaluate the derivative

$$\frac{\partial E_{1/2}(\varepsilon)}{\partial \varepsilon} = \frac{1}{2} \left[1 \pm (\varepsilon - \varepsilon^d) / \sqrt{(\varepsilon - \varepsilon^d)^2 + 4|V|^2} \right] \quad (2.97)$$

For $a = 0$, the solution is simply

$$\nu_{1/2}^{a=0} = \left(\omega - \frac{|V|^2}{\omega - \varepsilon_0^d} \right) \Theta \left(\pm(\omega - \varepsilon_0^d) \right) \Big|_{\omega \neq \varepsilon_0^d}. \quad (2.98)$$

The theta-function is necessary since the solution produces a term like $\pm\sqrt{x^2} = \pm|x|$, which is only a solution to the problem if the sign in front of the square-root is identical to the sign of x . This solution produces a gap around $\omega = \varepsilon_0^d$, which can be seen in Fig. 2.11 for the same parameters as in Fig. 2.9. The avoided crossing leads to singularities at the gap boundaries.

The other cases are much harder to solve for arbitrary parameters. The significantly increased complexity of this calculation is disproportionate to the physical insight gained. Thus, it is omitted in this discussion. Generally speaking, calculating the density of states is straightforward and efficient if one knows the roots of $\omega - E_i(\varepsilon)$ either analytically or numerically.

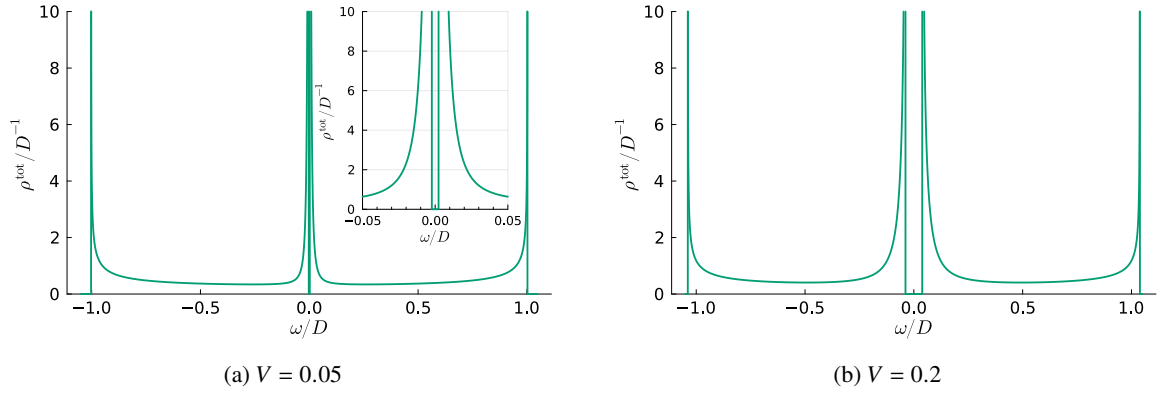


Figure 2.11: Density of states of the 1D two-band hybridization model for two different V , where $\varepsilon_k^c = -\cos(k)$ and $\varepsilon^d = -0.3$.

2.3.3 Green Functions

Equivalently, the system could have been solved using the Green function equation of motion technique, just as in the case of the resonant lattice model. Due to translational symmetry, full Green functions are diagonal in \vec{k} -space. The Dyson equations (with the argument ω suppressed for readability) are

$$[G^d]_{\vec{k}\sigma}^{-1} = [G^{d(0)}]_{\vec{k}\sigma}^{-1} - |V_{\vec{k}}|^2 G_{\vec{k},\sigma}^c, \text{ and} \quad (2.99)$$

$$[G^c]_{\vec{k}\sigma}^{-1} = [G^{c(0)}]_{\vec{k}\sigma}^{-1} - |V_{\vec{k}}|^2 G_{\vec{k}\sigma}^d. \quad (2.100)$$

Iteration to infinite order yields the T -matrix equations

$$G_{\vec{k}\sigma}^d = G_{\vec{k}\sigma}^{d(0)} + G_{\vec{k}\sigma}^{d(0)} |V_{\vec{k}}|^2 G_{\vec{k}\sigma}^c G_{\vec{k}\sigma}^d, \text{ and} \quad (2.101)$$

$$G_{\vec{k}\sigma}^c = G_{\vec{k}\sigma}^{c(0)} + G_{\vec{k}\sigma}^{c(0)} |V_{\vec{k}}|^2 G_{\vec{k}\sigma}^d G_{\vec{k}\sigma}^c. \quad (2.102)$$

The self-energy equations are most useful here since they are diagonal in all quantum numbers, are numerically more stable, and maintain analyticity. Again, as with the resonant-level model, the problem of using free Green functions is also present here. It is, therefore, much preferred to diagonalize the Hamiltonian, if possible.

Heavy Fermions and Interacting Models

Despite the simplicity of the models discussed in the previous chapter they already allowed for deep physical insight into the competition between itinerant and localized electrons and, more generally, the interplay of non-orthogonal bands. The next logical step is to include the Coulomb interaction between two or more electrons. This adds higher-order terms to the Hamiltonian, prohibiting an exact solution except in special cases. With this, multiple different models arise.

As a first step, one can consider the local interaction of itinerant electrons in the Hubbard model, which brings about another realization of the competition between localization and de-localization. Prototypical examples for more localized electrons are systems of d - or f -orbital electrons, which are typically confined to the vicinity of the host ion in contrast to s - or p -orbital electrons that tend to become de-localized throughout the lattice. Specifically, for strongly localized electrons, the overlap between electrons on neighboring sites is small, while the density of such electrons on the same site overlaps strongly, resulting in a large Coulomb interaction. This is the narrow-band limit of the Hubbard model.

The Anderson impurity model, on the other hand, incorporates the hybridization of localized, interacting electrons with itinerant, typically non-interacting electrons into the picture, leading to yet another realization of the aforementioned competition by attributing the two extremes of localization to different particles. The low-energy limit of the Anderson impurity model in the local moment regime (impurity occupation pinned to one) is the Kondo model, in which the interaction is reduced to a local Heisenberg-like spin interaction between itinerant and localized electrons. The hallmark feature of the Kondo effect is the screening of this localized spin by the conduction electrons for antiferromagnetic coupling below the so-called Kondo temperature T_K . At first glance, the singlet ground state appears to be a strongly localized object but turns out to lead to an extended region of screening, the Kondo cloud. The finite energy ($k_B T_K$) required to break up the singlet leads to a characteristic time scale over which the electrons can move while still participating in the screening, leading to the aforementioned effect. Surprisingly, the low-energy state is locally describable with a Fermi liquid, where the ground state is the local singlet, and conduction-electron hopping is considered a weak perturbation to this state.

Extending those local models to the lattice case opens up the possibility for a much richer phase space. The local Fermi-liquid picture can be immediately extended to the lattice case, leading to heavy quasiparticles at the Fermi energy. These heavy quasiparticles are the defining feature of a whole class of materials known as heavy-fermion metals, which exhibit unique electronic properties

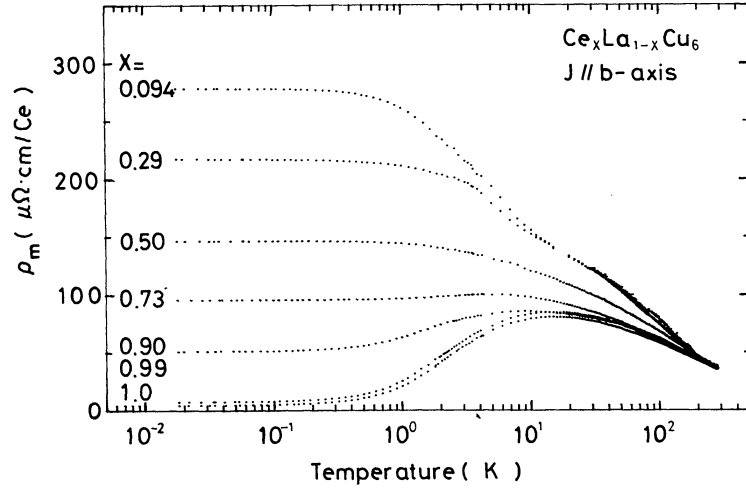


Figure 3.1: Resistivity measurement on $\text{Ce}_x \text{La}_{1-x} \text{Cu}_6$ with varying Cerium concentration, extracted from [25]. The lines are of increasing Ce concentration from top to bottom. A low concentration leads to the expected results for dilute magnetic impurities, whereas a large concentration leads to Fermi liquid behavior.

and complex magnetic behaviors. Most notably, resistivity in the single-impurity case was found to increase when approaching T_K and reach a plateau at temperatures well below, whereas the formation of a Fermi liquid leads to a vanishing resistivity. The transition from localized to itinerant physics has been observed several times by now, of which an early example is shown in Fig. 3.1. Additionally, magnetic ordering can occur via long-distance conduction-electron-mediated spin interaction. Since both originate from the same local spin interaction, their competition is an ongoing field of research. One of the most intriguing features of this competition is the appearance of a quantum-critical point between the magnetically ordered phase and the heavy Fermi liquid.

This chapter explores the physics of such interacting systems with competition between localization and de-localization. Starting with the Hubbard model for interacting electrons in s -orbitals, which allows investigation of the transition from metallic to insulating behavior in narrow-band systems and still proves a formidable challenge until today. This is followed up by an extensive discussion of the s - d model and Kondo's treatment of the single-spin version (the Kondo model) focusing on the energy scales, electrical resistivity, and magnetic susceptibility. Although one might be tempted to consider Kondo's model to be much different from Hubbard's model, there is a connecting link, which is discussed immediately after: the Anderson impurity model. There, a local impurity is modeled by an interacting theory in the same way as the interaction in the Hubbard model was modeled. This impurity is coupled to a free conduction-electron sea and leads to a much more promising description of local impurities than just the resonant-level model. Finally, the extension to the lattice case of the two local models is presented.

3.1 Hubbard's Model for Electrons in s -Orbitals

While the previously discussed models in chapter 2 allow for a deep insight into simple metals at high temperatures, the fermionic nature of the conduction electrons paired with the Coulomb interaction between charged particles allows for a straightforward and seemingly simple extension of free electronic bands that can describe a broader range of systems at lower temperatures. This is achieved by the Hubbard model [26, 27], which was originally designed for s -orbital bands but can also describe other bands in the case of sufficiently large Coulomb repulsion.

The restrictions to s -orbitals stem from the problem of representing fermionic many-body states with field operators. This will be explored more in the next section. For now, let's restrict the discussion to s -orbitals as Hubbard originally did. The bands are described by a usual quadratic Hamiltonian as before, which, in real space, is typically well approximated by a tight-binding model. The Coulomb repulsion, in the lowest non-vanishing order, will act locally when two electrons reside on the same site (but with different spin).

$$H_{\text{HM}} = \sum_{i,j,\sigma} (T_{i-j} - \mu\delta_{ij}) c_{i\sigma}^\dagger c_{j\sigma} + U \sum_i c_{i\uparrow}^\dagger c_{i\uparrow} c_{i\downarrow}^\dagger c_{i\downarrow} \quad (3.1)$$

$$= \sum_{\vec{k},\sigma} (\varepsilon_{\vec{k}}^c - \mu) c_{\vec{k}\sigma}^\dagger c_{\vec{k}\sigma} + U \sum_i \hat{n}_{i\uparrow} \hat{n}_{i\downarrow} \quad (3.2)$$

$$U = \iint_{\mathbb{R}^d \otimes \mathbb{R}^d} d^d r d^d r' \phi^*(\vec{r}) \phi^*(\vec{r}') \frac{e^2}{|\vec{r} - \vec{r}'|} \phi(\vec{r}') \phi(\vec{r}) \quad (3.3)$$

Here, $\phi(\vec{r})$ are the Wannier functions of the conduction electrons. The chemical potential is now included, which was unaccounted for in the previous sections. The hopping term T de-localizes the electrons, whereas U acts locally and emphasizes local effects. The interaction term brings about a rich field of phases. Most notably, when $U \rightarrow \infty$ and $\mu < D$, where D is the bandwidth, the system potentially undergoes a phase transition to a Mott insulator. This phase is characterized by the restriction $\sum_\sigma \langle \hat{n}_{i\sigma} \rangle = 1 \forall i$. For finite U , this can happen at a finite temperature but depends a lot on the details of the system. Inherently, the competition between (non-commuting) non-local and local terms is of great importance to the phase diagram of any given Hubbard model.

Free electrons are naturally paramagnetic; interactions can, however, lead to a more intricate magnetism. According to Stoner [28], a system of itinerant electrons with exchange interaction can develop a spin-polarized state. Exchange interactions are naturally present in fermionic systems, where Coulomb interaction is considered, e.g. the Hubbard model. Pauli's principle does not allow for double occupation of the same spin at any given site. Therefore, Coulomb repulsion between electrons of the same spin orientation is much reduced since they are kept apart. Opposite orientations are, however, not influenced by the exclusion principle, and therefore, the Coulomb interaction between different spins is, on average, much larger. Therefore, from this perspective, it is energetically favorable to spin-polarize the system, leading to ferromagnetism. Although this argument is only exactly correct for $T = 0$ (mean-field Hubbard model), it is an excellent example of how interactions influence fermionic systems.

Depending on the band filling, the large- U limit can be shown to lead to the t - J -model [29] or the Heisenberg model [30], emphasizing the importance of exchange interaction in interacting models.

For completeness, attractive interaction leads to BCS-superconductivity.

3.2 Hubbard Operators

Although originally designed for atomic s -orbitals exclusively, the Hubbard model has since been applied to more realistic cases in which bands contain combinations of multiple orbitals. Considering s -orbitals enables focusing on the electronic spin as the only local quantum number. This makes the model nice and simple to write down. Degeneracies are often broken in real-world solids since *exact* degeneracy typically needs to be protected by a strong symmetry to survive through higher-order approximations. It is, therefore, not too far-fetched to use the Hubbard model for Bloch bands in solids. However, the cases where symmetries are not broken need a bit more treatment than the original Hubbard model. In his second paper about this subject [27], Hubbard discussed extensions to degenerate models, specifically addressing atomic orbitals with $L > 0$. Electrons in such orbitals can be characterized by the field operators $c_{m\sigma}$, where m represents the orbital quantum number and σ spin. The quadratic part of the Hamiltonian is now generalized straightforwardly, typically maintaining diagonality in all quantum numbers. The interaction term, though, even when only considering the lowest (quartic) order, now includes all allowed combinations of m and σ

$$H_{\text{HM2}} = \sum_{\vec{k}, m, \sigma} (\varepsilon_{m, \vec{k}}^c - \mu) c_{\vec{k}m\sigma}^\dagger c_{\vec{k}m\sigma} + U \sum_i \sum_{\substack{m, m' \\ \sigma, \sigma'}} (1 - \delta_{mm'} \delta_{\sigma\sigma'}) \hat{n}_{im\sigma} \hat{n}_{im'\sigma'}. \quad (3.4)$$

The field theory for such a model now includes many different combinations of field operators due to the highly mixed interaction term. This inspired Hubbard to group field operators together such that $X_{ab} = c_{\sigma_1}^\dagger \dots c_{\sigma_n}^\dagger c_{\sigma_1} \dots c_{\sigma_m} \equiv |a\rangle \langle b|$ connects two many-body states. A direct consequence of this definition is $X_{ab} X_{cd} = \delta_{b,c} X_{ad}$, from which the Hubbard-operator superalgebra

$$[X_{ab}, X_{cd}]_{\pm} = \delta_{b,d} X_{ad} \pm \delta_{a,d} X_{bc} \quad (3.5)$$

directly follows. Despite the advantages, working with such operators in a field-theoretical context is impractical since Wick's theorem does not hold due to the non-canonical (anti-)commutation relation.

Despite the apparent impracticality, Hubbard operators have been quite useful in special cases. Most notably, they allow for a faithful representation of the $U \rightarrow \infty$ case, in which the Hubbard term can be discarded, and only empty and singly-occupied Hubbard operators remain in the model¹. Another case is back-engineering models for systems of highly localized electrons and crystal field splitting (c.f. Section 4.3) in which a single valence configuration is split into several multiplets. Such states can not be straightforwardly represented with fermionic field operators.

¹ Although I am not aware of any papers explicitly using Hubbard operators for this case, the slave-boson approach by Kotliar and Ruckenstein [31] implicitly relies on that picture.

3.3 Anderson's Single-Impurity Model

In an effort to describe the physics of dilute localized magnetic moments in metals (c.f. [32]), Anderson argued that a description that only includes potential scattering is not well motivated for cases where the magnetic moments stem from inner-shell electrons. The standard example at that time was the $s - d$ case, where conduction electrons of the metallic host were modeled as itinerant s -orbital electrons, and local moments were attributed to strongly localized d -shell electrons. A description in terms of single-particle models (c.f. the resonant-level model in Section 2.2) would always lead to a de-localization of the originally localized state. The description is also oblivious to spin structure, leading to incompatibility with the experimentally observed temperature dependence of local magnetic moments. Anderson argued that the coulomb interaction of the strongly localized atomic d -shell states is non-negligible and, therefore, must be included in a faithful description.

In 1961 [32], he thus proposed a model for a single magnetic impurity embedded in a dilute metallic host. The model Hamiltonian is comparably simplistic but surprises by providing rich physics. Its base is a free conduction-electron theory

$$H_c = \sum_{\vec{k}, \sigma} \left(\epsilon_{\vec{k}}^c - \mu \right) c_{\vec{k}\sigma}^\dagger c_{\vec{k}\sigma}, \quad (3.6)$$

which could, for example, be a tight-binding model with nearest-neighbor hopping in combination with a chemical potential. The impurity is modeled by a single localized level like in the resonant-level model of Section 2.2 but with an additional term accounting for the non-negligible Coulomb interaction on-site

$$H_d = \sum_{\sigma} \left(\epsilon^d - \mu \right) d_{\sigma}^\dagger d_{\sigma} + U n_{\uparrow}^d n_{\downarrow}^d, \quad (3.7)$$

where $n_{\sigma}^d = d_{\sigma}^\dagger d_{\sigma}$ is the density operator of the impurity electron with spin σ . Here, U is defined in the same way as in Eq. (3.3) just for the Wannier functions of the impurity instead of the conduction electrons². This is, again, an idealized picture. Those impurity states typically are d - or f -shell electrons with potentially complex structures. Let's stick to this original version for now, though. The two species of electrons hybridize via

$$H_{\text{hyb}} = \sum_{\vec{k}, \sigma} \left(V_{\vec{k}} c_{\vec{k}\sigma}^\dagger d_{\sigma} + h.c. \right), \quad (3.8)$$

$$V_{\vec{k}} = \sum_i e^{i\vec{k}\vec{R}_i} \langle \phi^d | H | \phi_i^c \rangle, \quad (3.9)$$

where $\langle \phi^d |$ is the localized impurity state, H the Hamiltonian, and $|\phi_i^c\rangle$ the conduction-electron state at site i (centered at position \vec{R}_i). Alternatively, with Wannier functions, the hybridization prefactor is

$$V_{\vec{k}} = \sum_i e^{i\vec{k}\vec{R}_i} \iint_{\mathbb{R}^d \otimes \mathbb{R}^d} d^d r \, d^d r' \, \phi_d^*(\vec{r}) \langle \vec{r} | H | \vec{r}' \rangle \phi_c(\vec{R}_i, \vec{r}') \quad (3.10)$$

² I want to clarify here that, despite the Hubbard model being briefly discussed before the Anderson impurity model in this thesis, the latter was proposed in 1961 [32], whereas the Hubbard model came to life two years later, in 1963 [26].

The Hamiltonian can—in principle—contain terms of kinetic energy, impurity potential, Coulomb potential, spin-orbit interaction, and coupling to external fields.

Anderson argued that the overlap should be minimal—if not zero—on-site due to the orthogonality of orbital wave functions on the same atom. It turns out that the approximation $V_{\vec{k}} = V_0$ is often justified either due to high (almost spherical) symmetry or when one is interested in low-energy physics. As we will see later, the details of the conduction electrons and hybridization will not be important for the low-energy sector, which is typically the region of interest.

The full Hamiltonian is the sum of all three,

$$H_{\text{SIAM}} = H_c + H_d + H_{\text{hyb}} \quad (3.11)$$

$$= \sum_{\vec{k}, \sigma} \left(\varepsilon_{\vec{k}}^c - \mu \right) c_{\vec{k}\sigma}^\dagger c_{\vec{k}\sigma} + \sum_{\sigma} \left(\varepsilon^d - \mu \right) d_{\sigma}^\dagger d_{\sigma} + U n_{\uparrow}^d n_{\downarrow}^d + \sum_{\vec{k}, \sigma} \left(V_{\vec{k}} c_{\vec{k}\sigma}^\dagger d_{\sigma} + h.c. \right). \quad (3.12)$$

This is known as the single-impurity Anderson model (SIAM). In the most interesting regime (local moment regime, c.f. next section), the parameters are $\varepsilon^d < E_F$, $V < D/10$, $U > |\varepsilon^d|$, and $U \gtrsim D$, where E_F is the Fermi energy and D the half bandwidth of the conduction electrons. Single-particle energies are usually defined in reference to the Fermi energy, a convention I will adhere to in the following except where explicitly stated otherwise.

Although the following discussion was composed by myself, it is—of course—not unique. Many people have analyzed the SIAM and came to similar or identical conclusions. I want to highlight an, in my eyes, outstanding review of the topic by Antoine Georges [33].

3.3.1 Spectrum of the SIAM I

Analyzing the impurity part of Eq. (3.12) we can estimate the shape of the spectrum. First, the spectral function is the imaginary part of the advanced Green function. If we write this in the Lehmann-representation [34]

$$A_{\sigma}(\omega) = \frac{1}{Z} \sum_{n,m} \delta(\omega - (E_n - E_m)) \left(e^{-\beta E_m} + e^{-\beta E_n} \right) |\langle m | d_{\sigma} | n \rangle|^2 \quad (3.13)$$

we can identify the individual single-particle processes that will lead to peaks. The local impurity state has three different valence configurations: empty, singly occupied, and doubly occupied. The three states have respective energy 0, $\varepsilon^d - \mu$, and $2(\varepsilon^d - \mu) + U$. An illustration of this level scheme is plotted in Fig. 3.2 for three different cases.

We can now systematically go through those states, reducing the particle number by one.

- First, the transition from doubly- to singly occupied. The energy difference is $E_n - E_m = \varepsilon^d - \mu + U$. This will lead to a peak above the Fermi energy for cases (a) and (b) in Fig. 3.2.
- The transition from singly- to unoccupied. The energy difference is $E_n - E_m = \varepsilon^d - \mu$. This will lead to a peak below the Fermi energy for cases (a) and (b) in Fig. 3.2.

This spectrum is sketched in Fig. 3.3, where the peaks are just Lorentzians of a given width $\Gamma(\omega) = \pi |V|^2 \rho^c(\omega)$ at the appropriate positions. The broadening of peaks works in the same way as for the resonant-level model (c.f. Eq. (2.56)). In this context, $\Gamma(\omega)$ is often called the *hybridization function* and plays an essential role in the physics of impurity systems.

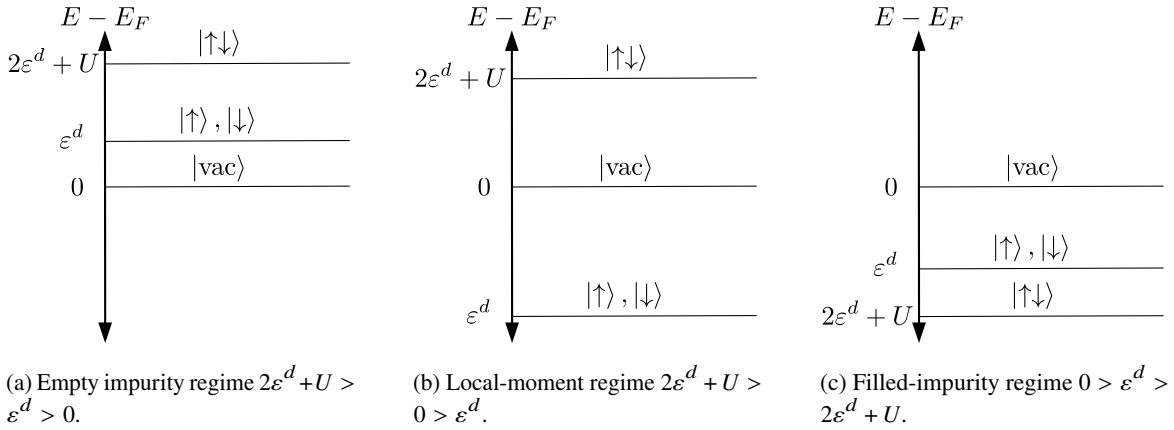


Figure 3.2: Illustration of the impurity level-scheme in the SIAM. The corresponding energies are the level-energies, *not* the single-particle excitations. Energies are given in reference to the Fermi energy.

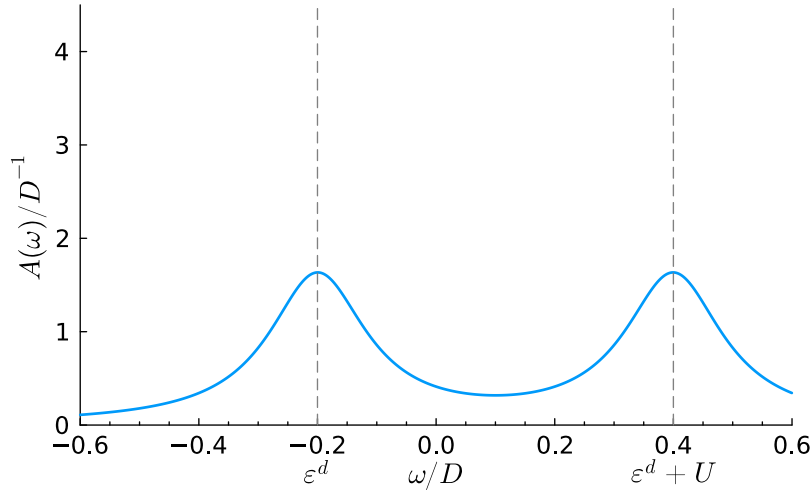


Figure 3.3: Sketch of the impurity spectral function in the single-impurity Anderson model with $\Gamma/D = 0.1$, $\varepsilon^d/D = -0.2$, and $U/D = 0.6$.

3.3.2 Parameter Regimes of the SIAM

A significant advantage of the model is the ability to describe impurity physics over a range of electronic valence. For this, let's assume Γ to be constant, which includes the $\Gamma = 0$ case of a decoupled impurity.

Let's restrict the discussion to the ordering $\varepsilon^d - \mu \leq \varepsilon^d - \mu + U$, with the empty state being pinned to the Fermi energy, i.e. $E = 0$. If the order is reversed, the discussion can be re-formulated in terms of electron holes; the assumption, therefore, does not restrict the generality of the results. The average occupation of the impurity in the context of the previous discussion and the above assumption of a

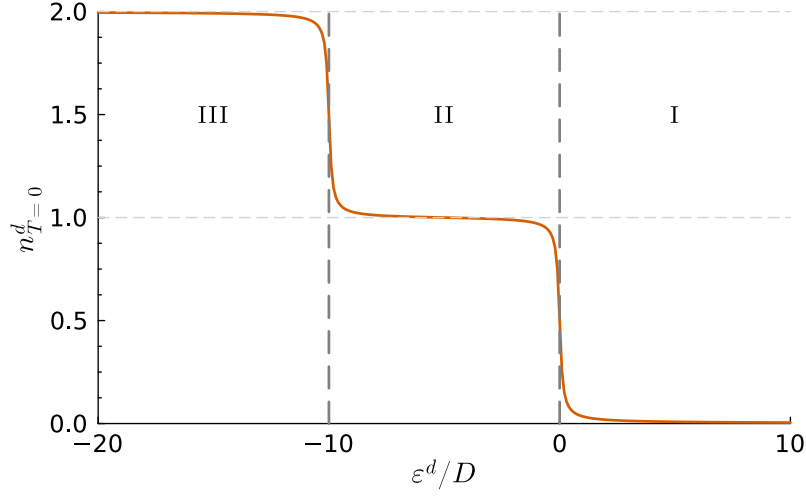


Figure 3.4: Exemplary $T = 0$ and $\Gamma/D = 1$ impurity occupation according to Eq. (3.14) with $U/D = 10$. Thick dashed lines represent the positions of the two Lorentzian peaks in the spectrum; thin dashed lines are a guide to the eye.

constant Γ is (c.f. Eq (2.57))

$$n^d = \int_{-\infty}^{\infty} d\omega n_F(\omega, T) \frac{\Gamma}{\pi} \left(\frac{1}{(\omega - \varepsilon^d)^2 + \Gamma^2} + \frac{1}{(\omega - (\varepsilon^d + U))^2 + \Gamma^2} \right), \quad (3.14)$$

where $n_F(\omega, T)$ is the Fermi-Dirac distribution function at temperature T . The parameter regimes can be classified by the average occupation of which an exemplary parameter scan is shown in Fig. 3.4.

- I. Empty impurity: If $\varepsilon^d - \mu > 0$ and $\varepsilon^d - \mu + U > 0$, since the empty state is pinned to the Fermi energy, the occupation will be close to zero. This corresponds to the third sector
- II. Local moment: The case $\varepsilon^d - \mu < 0$ and $\varepsilon^d - \mu + U > 0$ leads to an average occupation of approximately unity.
- III. Filled impurity: For $\varepsilon^d - \mu < 0$ and $\varepsilon^d - \mu + U < 0$ the impurity occupation will be close to two.
 - Mixed valence: The above occupations become exactly zero, one, and two for $T = 0$ and $\Gamma = 0$. In reality, either of the two parameters induces a finite crossover between the regimes in which the occupation is non-integer. Those regions are of *mixed valence*.

Notably, the local-moment case is also exactly realized for a particle-hole symmetric model of finite Γ . Another case is the $U = 0$ limit, in which the model reduces to the resonant-level model of Section 2.2. Despite looking deceptively similar, the major difference is the second term of the right-hand side of Eq. (3.14) now being identical to the first one, resulting in the collapse of the picture in Fig. 3.4 to the picture in Fig. 2.4 with the absence of the local-moment regime (apart from

the—unlikely—particle-hole symmetric case). This is ultimately why the Hubbard- U term is often needed to describe impure metals.

3.3.3 Spectrum of the SIAM II

The discussion was so far only concerned with simple single-particle effects, which turns out to be incomplete. The strong-coupling limit, which favors the local-moment regime, leads an enhanced exchange coupling, which is an effect already discussed in the context of the Hubbard model in Section 3.1. For low temperatures, the occupation of the impurity is pinned to unity, but is spin-degenerate. The local moment can, therefore, fluctuate.

Let's investigate the level scheme of the strong-coupling limit, illustrated in Fig. 3.2. An electron on the impurity with spin σ can only change its spin orientation via an intermediate state. Due to the large energy of the doubly occupied state, the best option is via the empty state. At finite temperatures, the corresponding first-order particle exchange is energetically allowed, and the intermediate state is thermally occupied. At zero temperature, the impurity spends no time in the empty state and must be occupied instantly. Due to spin degeneracy, the “new” electron can have an opposite spin, resulting in a spin-flip of the impurity. This is mediated via conduction electrons such that, due to the intermediate state being virtual, there is a simultaneous spin flip of conduction- and impurity electrons. In an idealized picture ($\Gamma \rightarrow 0$), this process has an excitation energy of $\omega \rightarrow 0$, so it will reside precisely at the Fermi edge. In reality, the excitation energy is not restricted to exactly zero due to the broadening of the single-particle peak, which is the peak of the spectrum corresponding to the single occupation.

If the resulting spin exchange is energetically attractive, i.e. an effective antiferromagnetic spin-coupling arises, the ground state will be a stable spin-singlet between conduction- and impurity electrons. We now need to remember that this purely arises from the local Coulomb interaction, as discussed in the previous section. It should, therefore, be reflected in the impurity self-energy $\Sigma(\omega)$ as a local minimum due to the stability of the singlet state. This minimum must be temperature-dependent due to the aforementioned temperature-dependent transition from a single-particle process to a

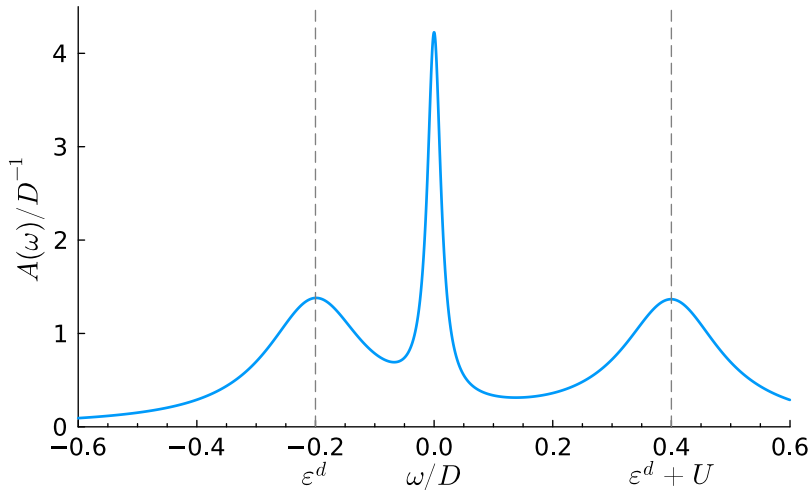


Figure 3.5: Sketch of the impurity spectral function in the single-impurity Anderson model with $\Gamma/D = 0.1$, $\epsilon^d/D = -0.2$, and $U/D = 0.6$ including the Kondo peak.

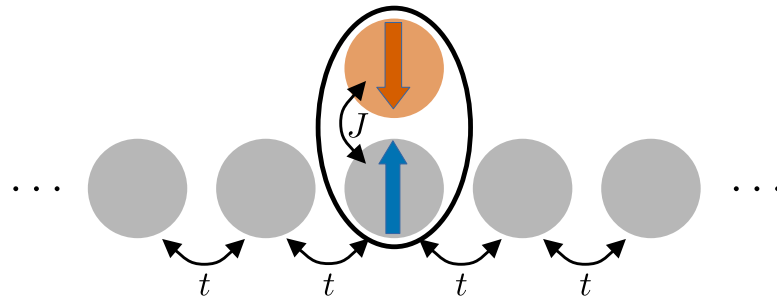


Figure 3.6: Sketch of one component of the localized spin singlet in the Kondo model. The conduction-electron hopping in this picture is assumed to be between nearest neighbors.

two-particle process. The development of an attractive singlet state leads to a peak in the spectrum, the so-called Abrikosov-Suhl resonance [35–37], or Kondo peak, due to its origin in the Kondo effect, which will be discussed in the next section. A sketch of the low-temperature spectrum is shown in Fig. 3.5.

A local Fermi-liquid description can also be made to explain the appearance of this feature in the spectrum [38, 39], which is the famous Nozières Fermi liquid. There, the hopping of conduction electrons is considered a perturbation to the local singlet state, c.f. Fig. 3.6.

Another important observation can be made in the absence of particle-hole symmetry. Then, one of the peaks will be closer to the Kondo resonance than the other, resulting in a level repulsion effect, where the Kondo peak is shifted either above or below the Fermi energy.

Finally, Schrieffer and Wolff in 1966 [40] were able to construct an effective low-energy model of the SIAM via a unitary transformation. This *Schrieffer-Wolff transformation* connected Anderson’s model from 1961 to the famous *s-d* model (or Kondo model), with which Kondo was able to explain the resistance minimum in impure metals [2] in 1964. Thus ending the debate about the sign of the spin-interaction (ferromagnetic or antiferromagnetic) in favor of antiferromagnetic coupling since the other case would not lead to the observed behavior of a resistance minimum.

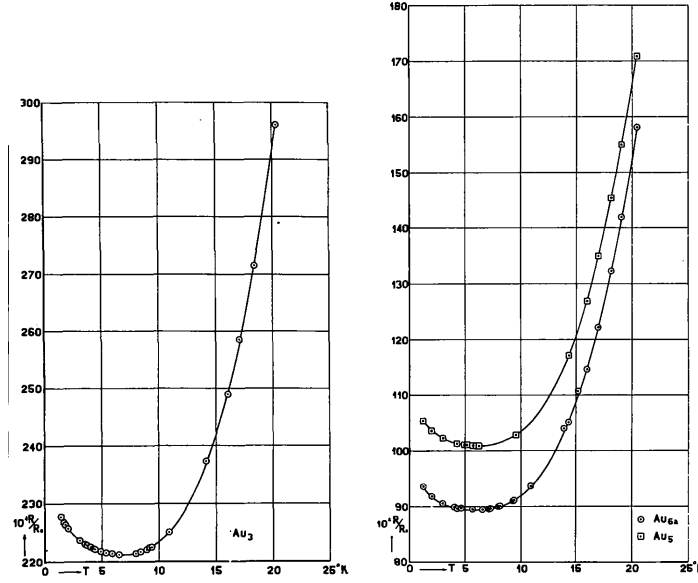


Figure 3.7: Measured resistance of various gold-wire samples by W.J. De Haas and G.H. Van Den Berg in 1936. Plots taken from [41].

3.4 The s - d Model and Kondo's Treatment

A particular interest in the physics of impure metals arose in the 1930s due to the unexpected measurements of resistance minima in metals at low temperatures, an example of which is shown in Fig. 3.7. Early explorations of possible explanations were focused on potential scattering, pioneered by Friedel [42]. Despite giving rise to the concept of virtual bound states, which would become vital in the understanding of involved physics, potential scattering ultimately did not explain the minimum. Only when the s - d -model was outlined by Zener [43] and refined by Kasuya [4] and Yosida [5] in the 1950s spin-interactions were brought into focus which lead to the explanation of the resistance minimum by Kondo [2] in 1964.

The most concise form of the s - d -model is the one that was put forward by Kasuya [4]³,

$$H_{s-d} = \sum_{\vec{k}, \sigma} \varepsilon_{\vec{k}} c_{\vec{k}\sigma}^\dagger c_{\vec{k}\sigma} + \sum_{\vec{q}} J(\vec{q}) \vec{S}_{\vec{q}} \cdot \vec{s}_{-\vec{q}}, \quad (3.15)$$

$$\vec{S}_{\vec{q}} = \sum_n e^{i\vec{q}\vec{R}_n} \vec{S}_n, \quad (3.16)$$

$$\vec{s}_{\vec{q}} = \sum_i e^{i\vec{q}\vec{r}_i} \vec{s}_i, \quad (3.17)$$

$$\vec{s}_i = \frac{1}{2} \sum_{\tau, \tau'} c_{i\tau}^\dagger \vec{\sigma}_{\tau\tau'} c_{i\tau'} = \sum_{\vec{k}, \vec{k}'} e^{i(\vec{k}' - \vec{k})\vec{r}_i} c_{\vec{k}\tau}^\dagger \vec{\sigma}_{\tau\tau'} c_{\vec{k}'\tau'}, \quad (3.18)$$

³ The sign convention of the spin interaction varies strongly between the different treatments. I will consistently use the sign so that a positive J leads to antiferromagnetic coupling.

where \vec{S}_n is the localized spin at the lattice vector \vec{R}_n and \vec{s}_i is the conduction-electron spin at position \vec{r}_i .

The model is, in principle, a lattice model but can also describe dilute impurity systems by considering a reduced localized-spin concentration. If the concentration is low enough such that impurities are far apart, the physics of this system should be dominated by local contributions, leading to a simpler model

$$H_{\text{Kondo}} = \sum_{\vec{k}, \sigma} \varepsilon_{\vec{k}}^c c_{\vec{k}\sigma}^\dagger c_{\vec{k}\sigma} + J \vec{S} \cdot \vec{s}, \quad (3.19)$$

with only a single impurity spin at position $\vec{R} = 0$. It is often useful to write the spin-scattering term in the original s - d -model formulation

$$J \vec{S} \cdot \vec{s} = + \sum_{\vec{k}, \vec{k}'} J \left(S^+ c_{\vec{k}\downarrow}^\dagger c_{\vec{k}'\uparrow} + S^- c_{\vec{k}\uparrow}^\dagger c_{\vec{k}'\downarrow} + S_z \left[c_{\vec{k}\uparrow}^\dagger c_{\vec{k}'\uparrow} - c_{\vec{k}\downarrow}^\dagger c_{\vec{k}'\downarrow} \right] \right), \quad (3.20)$$

where S^\pm are the impurity-spin ladder operators. The model can then be extended to the dilute case with a given impurity concentration, assuming a random orientation of the local moments such that each occurring sum over impurities can be replaced by a concentration-weighted single-impurity quantity, which is what Kondo used in his seminal paper. For completeness, this model is lacking the potential-scattering term [24]

$$H_{\text{pot.}} = \sum_{\vec{k}, \vec{k}', \sigma} \langle \vec{k} | V_{\text{imp}}^{\text{eff}} | \vec{k}' \rangle c_{\vec{k}\sigma}^\dagger c_{\vec{k}'\sigma}, \quad (3.21)$$

where $V_{\text{imp}}^{\text{eff}}$ is the effective impurity potential. In a system where an impurity atom substitutes a host-metal atom, this potential can be seen as the additional (usually Coulomb-) potential generated by the locally increased or reduced charge. In any case, it is a single-particle term and thus only renormalizes the free conduction-electron spectrum in a straightforward way (c.f. resonant-level model in Sec. 2.2).

For completeness, linking this section back to the previously discussed single-impurity Anderson model, the parameter J of Eq. (3.20) can be expressed in terms of the parameters of the SIAM (Eq. (3.12)) via the Schrieffer-Wolff transformation [40] as

$$J_{\vec{k}\vec{k}'} = -2V_{\vec{k}}^* V_{\vec{k}'} \left\{ \frac{1}{\varepsilon^d - \varepsilon_{\vec{k}}^c} - \frac{1}{\varepsilon^d - \varepsilon_{\vec{k}'}^c + U} \right\}, \quad (3.22)$$

$$\Rightarrow J_{\vec{k}_F \vec{k}_F} = -2 |V_{\vec{k}_F}|^2 \left\{ \frac{1}{\varepsilon^d} - \frac{1}{\varepsilon^d + U} \right\} = - |V_{\vec{k}_F}|^2 \frac{2U}{(\varepsilon^d + U)\varepsilon^d}. \quad (3.23)$$

The Fermi energy is zero here since both ε^d and ε^c are expressed with respect to the Fermi energy, making $\varepsilon_{\vec{k}_F}^c = 0$. It can also be seen that the sign of $J_{\vec{k}_F \vec{k}_F}$ in the local moment regime ($\varepsilon^d < 0$ and $\varepsilon + U > 0$) is positive, resulting in an antiferromagnetic coupling. Additionally, this connects the hybridization function $\Gamma(\omega) = \pi |V|^2 \rho^{(0)}(\omega)$ used in the context of the SIAM to the Kondo coupling J , emphasizing the importance of this quantity.

Although the Kondo model itself is not the central subject of this thesis, I will discuss the derivation of the resistance minimum for completeness, following [24] with minor modifications and simplifications.

3.4.1 Resistivity and Conductivity via Boltzmann's Equation

The Boltzmann equation describes the total time-derivative of an effective distribution function f_E of particles in an ensemble in terms of contributions from an external force, diffusion, and collisions. Closely following [44], I will lay out the derivation of the equation, following up with the relaxation-time approximation following [24]. Let's start from

$$\frac{df_E(\vec{r}, \vec{p}, t)}{dt} = \left(\frac{\partial f_E}{\partial t} \right)_{\text{force}} + \left(\frac{\partial f_E}{\partial t} \right)_{\text{diff}} + \left(\frac{\partial f_E}{\partial t} \right)_{\text{coll}}. \quad (3.24)$$

The function f_E depends on position \vec{r} , momentum \vec{p} and time t . Without collisions, the phase-space is incompressible. Particles within a given phase-space volume are therefore moving uniformly according to their momentum $\vec{r} \rightarrow \vec{r} + \vec{p}\Delta t/m$ and the acceleration due to the external field $\vec{p} \rightarrow \vec{p} + \vec{F}\Delta t$. In other words, the particle density in a given phase-space volume remains stationary. Due to their many-body nature, collisions modify the particle density in phase space. Comparing both statements results in the conclusion that the total time-derivative df_E/dt is equal to just the collision contribution $(\partial f_E/\partial t)_{\text{coll}}$. On the other hand, by expanding the total differential in the variation of its dependencies, one gets

$$df_E = \left(\vec{\nabla}_{\vec{r}} f_E \right) d\vec{r} + \left(\vec{\nabla}_{\vec{p}} f_E \right) d\vec{p} + \frac{\partial f_E}{\partial t} dt \quad (3.25)$$

$$= \left(\vec{\nabla}_{\vec{r}} f_E \right) \vec{v} dt + \left(\vec{\nabla}_{\vec{p}} f_E \right) \vec{F} dt + \frac{\partial f_E}{\partial t} dt \quad (3.26)$$

$$\Rightarrow \frac{df_E}{dt} = \left(\vec{\nabla}_{\vec{r}} f_E \right) \vec{v} + \left(\vec{\nabla}_{\vec{p}} f_E \right) \vec{F} + \frac{\partial f_E}{\partial t} \quad (3.27)$$

$$= \left(\vec{\nabla}_{\vec{r}} f_E \right) \frac{\vec{p}}{m} + \left(\vec{\nabla}_{\vec{p}} f_E \right) \vec{F} + \frac{\partial f_E}{\partial t} = \left(\frac{\partial f_E}{\partial t} \right)_{\text{coll}}. \quad (3.28)$$

Assuming a uniform equilibrium distribution, the Boltzmann equation reads

$$\frac{\partial f_E}{\partial t} = \left(\frac{\partial f_E}{\partial t} \right)_{\text{coll}} - \vec{\nabla}_{\vec{p}} f_E \vec{F}. \quad (3.29)$$

If the field is switched off, the distribution f_E will return to the equilibrium distribution f_0 by collisions. The characteristic time scale for this is the relaxation rate $\tau_1(\vec{k})$ by

$$\left(\frac{\partial f_E(\vec{k})}{\partial t} \right)_{\text{coll}} = -\frac{f_E(\vec{k}) - f_0(\vec{k})}{\tau_1(\vec{k})} = \left(\frac{df_E(\vec{k})}{dt} \right), \quad (3.30)$$

where time- and position arguments are suppressed. By demanding the partial derivative w.r.t. time

vanishing and identifying the Lorentz force $\vec{F} = -e\vec{E}$ (and realizing that $\vec{p} = \vec{k}$ for $\hbar = 1$) we get

$$-\frac{f_E(\vec{k}) - f_0(\vec{k})}{\tau_1(\vec{k})} = -q\vec{\nabla}_{\vec{k}} f_E(\vec{k})\vec{E}. \quad (3.31)$$

Finally, expanding f_E on the right in \vec{E} and keeping only terms that are overall linear in \vec{E} , i.e. f_E is replaced by f_0 , we arrive at

$$f_E(\vec{k}) = f_0(\vec{k}) + e\tau_1(\vec{k})\vec{E} \cdot \vec{\nabla}_{\vec{k}} f_0(\vec{k}) \quad (3.32)$$

$$= f_0(\vec{k}) + e\tau_1(\vec{k})\vec{E} \cdot \left(\vec{\nabla}_{\vec{k}} \varepsilon_{\vec{k}}^c\right) \frac{\partial f_0(\varepsilon_{\vec{k}}^c)}{\partial \varepsilon_{\vec{k}}^c}. \quad (3.33)$$

This is related to the current by using the average velocity $\vec{v}_{\vec{k}}$ via $\vec{j} = -e\vec{v}_{\vec{k}}$. It can be calculated from the distribution function replacing the velocity by momentum via $m\vec{v} = \vec{k}$ such that

$$\vec{j} = -2e \int_{\mathbb{R}^3} \frac{d^3k}{(2\pi)^3} f_E(\vec{k}) \frac{\vec{k}}{m}, \quad (3.34)$$

where the factor 2 is from the spin degeneracy of f_E . Inserting Eq. (3.32) and realizing that the equilibrium current at vanishing field is zero and assuming the electron dispersion to be the free, quadratic dispersion, the remainder is

$$\vec{j} = -2e \int_{\mathbb{R}^3} \frac{d^3k}{(2\pi)^3} \tau_1(\vec{k}) \frac{\vec{k}}{m} \frac{\vec{E} \cdot \vec{k}}{m} \frac{\partial f_0}{\partial \varepsilon_{\vec{k}}^c}. \quad (3.35)$$

Assuming isotropy, the Drude relation is simply $\vec{j} = \sigma(T)\vec{E}$ and the angular integrals in Eq. (3.35) can be performed explicitly. The conductivity

$$\sigma(T) = -\frac{2e^2}{3} \int_0^\infty \frac{d^3k}{(2\pi)^3} \frac{\tau_1(k)k^2}{m^2} \frac{\partial f_0}{\partial \varepsilon_k^c} \quad (3.36)$$

can be explicitly evaluated at $T = 0$ under the given assumptions, where the integral collapses to

$$\sigma(T = 0) = \frac{k_F^3}{3\pi^2} \frac{e^2 \tau_1(k_F)}{m} = \frac{n e^2 \tau_1(k_F)}{m} \quad (3.37)$$

where n is the number of conduction electrons per unit volume. This is identical to the transport theory predictions in the Drude model, with $\tau_1(k_F)$ being interpreted as the transport lifetime.

The last step is now calculating the relaxation time from the T -matrix of scattering theory. The scattering rate $W_{\vec{k}'\vec{k}}$ from \vec{k} to \vec{k}' can be extracted from the T -matrix via the analogous equation to Fermi's golden rule

$$W_{\vec{k}'\vec{k}} = 2\pi |T_{\vec{k}'\vec{k}}|^2 \delta(\varepsilon_{\vec{k}} - \varepsilon_{\vec{k}'}). \quad (3.38)$$

Details of the derivation of this equation can be found in [24]. To get the rate of change of $f_E(\vec{k})$

due to collisions, the scattering rate into the state \vec{k} , $W_{\vec{k}\vec{k}'}$, must be multiplied by the probability of \vec{k} being unoccupied and \vec{k}' being occupied and then averaged over all possible \vec{k}' . The reverse process contributes with a relative sign. If the T -matrix is calculated from a local approximation (dilute limit), the rate must be additionally multiplied by the impurity concentration.

$$\left(\frac{\partial f_E}{\partial t}\right)_{\text{coll}} = -2\pi c_{\text{imp}} \int_{\mathbb{R}^3} \frac{d^3 k}{(2\pi)^3} \delta(\varepsilon_{\vec{k}} - \varepsilon_{\vec{k}'}) \left[|T_{\vec{k}\vec{k}'}|^2 f_E(\vec{k})(1 - f_E(\vec{k}')) - |T_{\vec{k}'\vec{k}}|^2 f_E(\vec{k}')(1 - f_E(\vec{k})) \right] \quad (3.39)$$

$$= -2\pi c_{\text{imp}} \int_{\mathbb{R}^3} \frac{d^3 k}{(2\pi)^3} \delta(\varepsilon_{\vec{k}} - \varepsilon_{\vec{k}'}) |T_{\vec{k}\vec{k}'}|^2 \left[f_E(\vec{k}) - f_E(\vec{k}') \right] (1 - f_E(\vec{k}')) \quad (3.40)$$

$$= -e\vec{E} \cdot \vec{\nabla}_{\vec{k}} f_E(\vec{k}) \quad (3.41)$$

Here, the symmetric nature of the T -matrix was used in the second line, and an intermediate result derived above was used in the last line. Being an integro-differential equation, it is typically hard to solve. Using Eq. (3.32) though gives an equation for $\tau_1(\vec{k})$, assuming that the T -matrix only depends on the angle θ between \vec{k} and \vec{k}' :

$$\frac{1}{\tau_1(\vec{k})} = 2\pi c_{\text{imp}} \int \frac{d\vec{k}'}{(2\pi)^3} \delta(\varepsilon_{\vec{k}} - \varepsilon_{\vec{k}'}) |T_{\vec{k},\vec{k}'}|^2 (1 - \cos \theta') \quad (3.42)$$

$$\sigma = \frac{1}{R} = \frac{k_F^3}{3\pi^2} \frac{e^2 \tau_1(k_F)}{m} \quad (3.43)$$

$$\Leftrightarrow R = \frac{1}{\tau_1(k_F)} \frac{3\pi^2 m}{k_F^3 e^2} = \frac{1}{\tau_1(k_F)} \frac{m}{n e^2} \quad (3.44)$$

Here, $n = k_F^3/3\pi^2$ is the conduction-electron density of the metal. We can now proceed to calculate the T -matrix in the next section.

3.4.2 T -Matrix Perturbation Theory in J

The Kondo-Hamiltonian describes the spin-scattering of an impurity. As such, it is natural to use a perturbation theory in the spin-scattering, for which the T -matrix formalism is ideal since it contains an increasing number of scattering vertices V that are connected via free conduction electrons

$$T = V + VG_0V + VG_0VG_0V + \dots = T^{(1)} + T^{(2)} + T^{(3)} + \dots \quad (3.45)$$

Using Eq. (3.20), the matrix elements of T in terms of conduction-electron states, and to first order in J are

$$\langle \vec{k}', \uparrow | T^{(1)}(\varepsilon + i\eta) | \vec{k}, \uparrow \rangle = JS_z = -\langle \vec{k}', \downarrow | T^{(1)}(\varepsilon + i\eta) | \vec{k}, \downarrow \rangle, \quad (3.46)$$

$$\langle \vec{k}', \downarrow | T^{(1)}(\varepsilon + i\eta) | \vec{k}, \uparrow/\downarrow \rangle = JS^\pm. \quad (3.47)$$

Inserting this in Eq. (3.42) gives

$$\frac{1}{\tau_1(\vec{k})} = \frac{3\pi n c_{\text{imp}} J^2 S(S+1)}{2\varepsilon_F} \quad (3.48)$$

$$\Rightarrow R_{\text{imp}} = \frac{3\pi m c_{\text{imp}} J^2 S(S+1)}{2e^2 \varepsilon_F}, \quad (3.49)$$

where $S(S+1) = 2S_z^2 + S^+ S^- + S^- S^+$. It is constant in temperature and very similar to the contribution from potential scattering in the first Born approximation, where $J^2 S(S+1)$ would be V^2 . The next order thus has to be taken into account:

$$\langle \vec{k}', \sigma' | T^{(2)}(\varepsilon + i\eta) | \vec{k}, \sigma \rangle = \langle \vec{k}', \sigma' | H_{s-d} G_0^R(\varepsilon) H_{s-d} | \vec{k}, \sigma \rangle, \quad (3.50)$$

where G_0^R is the retarded, free Green function and H_{s-d} the term in equation (3.20). Exemplary, the $\sigma = \sigma' = \uparrow$ component of the second order term of the T-matrix expansion with intermediate spin flips is the sum of

$$\frac{J^2}{N_s^2} \sum_{\vec{k}_1, \vec{k}'_1, \vec{k}_2, \vec{k}'_2} \langle \vec{k}', \uparrow | S^- c_{\vec{k}_1 \uparrow}^\dagger c_{\vec{k}'_1 \downarrow} (\varepsilon + i\eta - H_c)^{-1} S^+ c_{\vec{k}_2 \downarrow}^\dagger c_{\vec{k}'_2 \uparrow} | \vec{k}, \uparrow \rangle \quad (3.51)$$

$$= \frac{J^2}{N_s^2} \sum_{\vec{k}_2} S^- S^+ \frac{1 - f(\varepsilon_{\vec{k}_2})}{\varepsilon + i\eta - \varepsilon_{\vec{k}_2}} \quad (3.52)$$

and

$$\frac{J^2}{N_s^2} \sum_{\vec{k}_1, \vec{k}'_1, \vec{k}_2, \vec{k}'_2} \langle \vec{k}', \uparrow | S^+ c_{\vec{k}_2 \downarrow}^\dagger c_{\vec{k}'_2 \uparrow} (\varepsilon + i\eta - H_0)^{-1} S^- c_{\vec{k}_1 \uparrow}^\dagger c_{\vec{k}'_1 \downarrow} | \vec{k}, \uparrow \rangle \quad (3.53)$$

$$= \frac{J^2}{N_s^2} \sum_{\vec{k}_2} S^+ S^- \frac{f(\varepsilon_{\vec{k}_2})}{\varepsilon + i\eta - \varepsilon_{\vec{k}_2}}, \quad (3.54)$$

where H_c is the free conduction-electron Hamiltonian, and the anticommutation relation of the fermionic particles was used to exchange positions of the creation and annihilation operators in the process of evaluating the expression. Using $[S^+, S^-] = 2S_z$ and $S^2 = S_z^2 + S_z + S^- S^+$, this term can be re-written and summed up with similarly derived terms for the processes without intermediate spin flips. The result is

$$\langle \vec{k}', \uparrow | T^{(2)}(\varepsilon + i\eta) | \vec{k}, \uparrow \rangle = S_z \frac{J}{N_s} (1 - 2Jg(\varepsilon)), \quad (3.55)$$

with

$$g(\varepsilon) = \frac{1}{N_s} \sum_{\vec{k}} \frac{f(\varepsilon_{\vec{k}})}{\varepsilon_{\vec{k}} - \varepsilon - i\eta}. \quad (3.56)$$

Summing up all the contributing terms up to order J^3 results in⁴

$$\frac{1}{\tau(\vec{k})} = \frac{3n c_{\text{imp}} J^2 S(S+1)}{2e^2 \varepsilon_F} \left(1 - 4J \operatorname{Re} g(\varepsilon_{\vec{k}})\right). \quad (3.57)$$

The real part of $g(\varepsilon)$ has to be calculated via a Cauchy principal value integral (details in [24]). It gives rise to a logarithmic contribution of $\rho(\varepsilon_F) \log\left(\frac{k_B T}{D}\right)$, with an energy cutoff parameter $D \gg \varepsilon_F$. From eq. (3.43), the contribution to the resistivity is given by

$$R_{\text{imp}}^{\text{spin}} = \frac{3\pi m c_{\text{imp}} J^2 S(S+1)}{2e^2 \varepsilon_F} \left(1 - 4J \rho(\varepsilon_F) \log\left(\frac{k_B T}{D}\right)\right), \quad (3.58)$$

which results in a total resistivity of

$$R(T) = c_{\text{imp}} R_0 - c_{\text{imp}} R_1 \log\left(\frac{k_B T}{D}\right) + R^{\text{phonon}}(T), \quad (3.59)$$

where R_0 and R_1 are constants and we are taking the contribution of phonons into account, which will vanish like T^5 at low temperatures. With this, Kondo was able to describe the logarithmic increase at low T and, therefore, the experimentally observed resistance minimum. The logarithmic divergence due to impurity scattering is the famous *Kondo effect*, and the associated temperature scale at which the perturbation becomes as large as the static contribution (c.f. Eq. (3.58)) is the *Kondo temperature*. Since $R_1 \sim J^3$, Kondo was also able to settle the debate on the sign of J by comparing his results to experiments. In Eq. (3.19), $J > 0$ describes the experiment and leads to an antiferromagnetic coupling.

3.4.3 The Kondo Temperature

Just a year after Kondo, Abrikosov approached the problem with field theory by describing the spin operators by fermionic fields, the so-called Abrikosov pseudofermions [37]. This makes the linear-response calculation for the magnetic susceptibility feasible and leads to

$$\chi_{\text{imp}} = \frac{(g\mu_B)^2 S(S+1)}{3k_B T} \left(1 - \frac{2J\rho_0}{1 + 2J\rho_0 \log(k_B T/D)} + c_2 (2J\rho_0)^2\right), \quad (3.60)$$

where ρ_0 is the conduction-electron DOS at the Fermi energy. The logarithmic divergence is now in the denominator due to a geometric series summation. The logarithmic term diverges at a temperature

$$1 = -2J\rho_0 \log(k_B T_K/D) \quad (3.61)$$

$$\Leftrightarrow k_B T_K = D e^{-\frac{1}{2J\rho_0}}, \quad (3.62)$$

which is, once again, the famous Kondo temperature. Notably, $\chi_{\text{imp}} \sim 1/T$ for $T \gg T_K$ and $\chi_{\text{imp}} \sim 1/\log(T)$ for $T - T_K \rightarrow 0^+$. The antiferromagnetic case ($J > 0$, c.f. Eq. (3.19)) results in an

⁴ The first correction was J^2 because the T-matrix T was first order in J , and it enters as $|T|^2$. When expanding T to $T = O(J) + O(J^2)$, the next order of $|T|^2$ in J is J^3 .

exponentially small Kondo temperature.

Another approach that allows for an extraction of this temperature is the perturbative renormalization group for the Kondo problem, Anderson’s “poor man’s scaling” [45]. There are multiple ways of defining the Kondo temperature, and since the Kondo effect is universal, it is the universal energy scale for this effect - independent of description. Albeit the universality, it can be defined with different numerical prefactors depending on the calculation. A good definition, especially when considering the dynamical mean-field theory for the Anderson model, is in terms of the half width at half maximum of the Kondo peak [38, 46–49].

3.4.4 Screening of Local Moments and the Kondo Cloud

The diverging antiferromagnetic coupling leads to a local singlet formation between conduction electrons and the impurity, which was already discussed in Section 3.3. We can now understand that forming a stable *Kondo singlet* leads to a screening of the impurity spin. Despite the spin scattering happening locally, the local singlet will have a finite spatial extent due to it not being a sharp bound state of the system (the resonance is broadened, c.f. the discussion in Section 3.3).

- The characteristic energy scale of this stable singlet is the Kondo temperature of Eq. (3.61), which is often around $10^{-4}D$ to $10^{-3}D$. The inverse of T_K gives the characteristic time scale for fluctuations of the singlet state.
- The formation of those singlets happens at the Fermi energy; conduction electrons participating in the singlet formation will thus move with the Fermi velocity.
- The characteristic length scale of the singlet formation is thus $\xi_K \sim v_F/T_K$ (with $\hbar = k_B = 1$).

This length scale defines the *Kondo cloud*, a region around the impurity that participates in the screening. The cloud size is surprisingly large with a typical size of $\xi_K \sim 1 \mu\text{m}$. This cloud has not yet been *directly* measured in experiments.

3.5 Impurity Lattice Models

For systems with large impurity concentrations, like alloys of atoms with strongly localized valence electrons (rare-earth elements, actinides, transition metals, partially filled *d*- or *f*-shell) with good metals (mostly *s*- and *p*-shell, weakly localized electrons) the physics can drastically change compared to the dilute case. Analogous to the discussion about the two-band hybridization model in Section 2.3, the admixture of periodically arranged localized states can lead to the development of a true gap (Kondo insulator) or the enhancement of the DOS at the Fermi energy (heavy Fermi liquid). Localized impurity states can become lattice-coherent via second-order hopping processes and potentially form long-range ordered states via the same mechanism. This long-range interaction is the famous Ruderman-Kittel-Kasuya-Yosida (RKKY) interaction [3–5]. This poses a challenging competition between the localized Kondo effect and the long-range magnetic order, both originating from the same spin interaction. Some heavy-fermion materials are unconventional superconductors with varying pairing mechanisms and critical temperatures [50].

The first heavy Fermi liquid metal was discovered by Andres, Graebner, and Ott in 1975 [51], marking the onset of a whole new field of physics that continues to fascinate and surprise still today. The first heavy-fermion superconductor was found by Steglich et al. in 1979 [52].

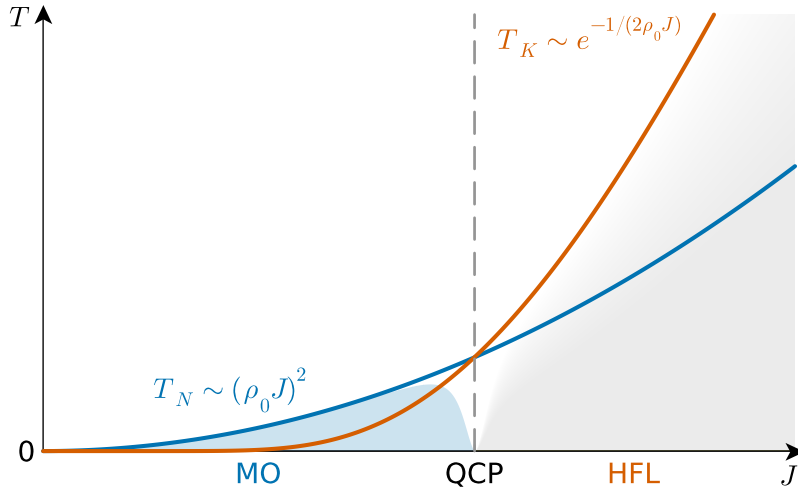


Figure 3.8: Modernized sketch of the Doniach phase diagram [6] inspired by its renditions in [49] and [53]. The blue curve is the critical temperature of magnetic ordering via RKKY-interaction; the blue region below it shows the magnetically ordered (MO) phase. The orange curve is the Kondo temperature for the crossover to the heavy Fermi liquid, which is the colored region below it. The regions are separated by a quantum-critical point (QCP), denoted by a dashed gray line.

On the theoretical side, Doniach pioneered the study of Kondo lattices in 1977 [6] and derived the famous Doniach phase diagram [54], sketched in a modernized version in Fig. 3.8, in which he compared antiferromagnetic order due to the RKKY interaction with the tendency to form a heavy Fermi liquid in terms of the respective low-energy scales⁵. This is an example of a quantum phase transition, i.e. a phase transition that is driven by quantum fluctuations instead of thermal fluctuations. heavy-fermion superconductivity was first understood in terms of spin-mediated pairing mechanisms [56, 57]. Unfortunately, heavy-fermion superconductivity is not within the scope of this thesis, and we shall, from now on, focus on the other aspect mentioned above.

3.5.1 The Kondo Lattice Model and the Large- N Limit

The Kondo model of Eq. (3.19) is straightforwardly generalized to the lattice case

$$H_{\text{Kondo}} = \sum_{\vec{k}, \sigma} \varepsilon_{\vec{k}}^c c_{\vec{k}\sigma}^\dagger c_{\vec{k}\sigma} - J \sum_i \vec{S}_i \cdot \vec{s}_i, \quad (3.63)$$

where the spins now are localized on each lattice site i . Disregarding RKKY, the ground-state is still a heavy Fermi liquid, as argued by Nozières, but not restricted locally due to the lattice translational symmetry. In 1983, Piers Coleman was able to perform a $1/N$ expansion, N being the degeneracy of the impurity spin, which is often large due to a large orbital degree of freedom⁶. His approach was based on Abrikosov's pseudofermion technique [37], which will be discussed later in this thesis. He

⁵ The idea itself was already formulated by Mott in 1974 [55], but it was only discussed in a heuristic manner.

⁶ There is an argument to be had that typically, since spin-orbit coupling and the crystal-field effect lead to distinct ground states with reduced degeneracy, the picture of a large N breaks down for low enough temperatures. This was pioneered by Nozières and Blandin in 1980 [58] and will also be discussed later in the thesis.

derived the local-model Kondo temperature (setting $k_B = 1$ and neglecting a factor e)

$$T_K^{\text{latt}} \approx D (NJ\rho_0)^{\frac{1}{N}} e^{-\frac{1}{NJ\rho_0}}, \quad (3.64)$$

where D is the conduction-electron half bandwidth and ρ_0 is the free conduction-electron density of states at the Fermi energy. He then further argued that the situation is not expected to change drastically in the lattice case, which is still an active and not fully resolved area of research today. Assuming this hypothesis holds, all the extension to a lattice does is introduce a second-order in J , long-range interaction between distant impurities via itinerant conduction electrons, the aforementioned RKKY interaction. Coleman derived the critical (Néel) temperature of magnetic ordering due to RKKY in the absence of a competition with the Kondo effect to be

$$T_N^{\text{RKKY}} \approx D(J\rho_0)^2. \quad (3.65)$$

Originally, he considered a re-scaled Kondo coupling $\tilde{J} = NJ$, which he kept fixed in the limit $N \rightarrow \infty$ such that the limit is defined in terms of his expansion. In this case, the RKKY term vanishes as $1/N^2$ in contrast to the Kondo temperature, which approaches the constant $D \exp(-1/\tilde{J}\rho_0)$. He, therefore, argued that the large- N Kondo lattice model would have a suppressed magnetic ordering in favor of a heavy Fermi liquid.

3.5.2 The Fate of the Fermi Surface

In the heavy Fermi state of a periodic Kondo model, a characteristic enhancement of the Fermi surface can be observed, with which the behavior of many observables can be easily understood. As laid out earlier, the local spin-singlets appear as composite quasiparticles that obtain a large effective mass due to their localized nature only being perturbed by the itinerant nature of the conduction electrons. This is genuinely a lattice effect; a single impurity always leads to a spatially confined singlet. In the lattice case, this picture is periodically repeated, and the quasiparticles can form a Bloch band. They, therefore, contribute to the Fermi surface, which is, according to Luttinger and Ward [59, 60], enhanced due to the additional fermions. This can also be understood by investigating the result of the two-band hybridization model, assuming the Kondo peak can be modeled by a resonant level slightly above the Fermi energy⁷, which is illustrated in Fig. 3.9. The original Fermi momentum $k_{F,0}$ (gray dashed line) gets enhanced to $k_{F,1}$ (green dashed line) due to the bending down of the band. This configuration is the *large Fermi-surface* case.

If the Kondo peak sits at precisely the Fermi energy, as is the case for particle-hole symmetric systems, the notion of a Fermi surface would break down due to the formation of a (pseudo-) gap. This configuration is the *Kondo-insulator* case. In reality, the finite width of the Kondo resonance relaxes the strict need for particle-hole symmetry. Only slightly, though, since the width of the Kondo peak is of the order T_K , which is small compared to the electronic bandwidth. Another condition for the formation of a Kondo insulator is an even number of conduction- and impurity electrons combined per unit cell, allowing for the exact filling of bands below the gap and the complete depletion of bands above the gap.

A different situation arises when the local moments order due to RKKY. Then, the Kondo effect is

⁷ The Kondo peak can—of course—not be faithfully modeled by a resonant level at the Fermi energy. The picture is still helpful in understanding the physics.

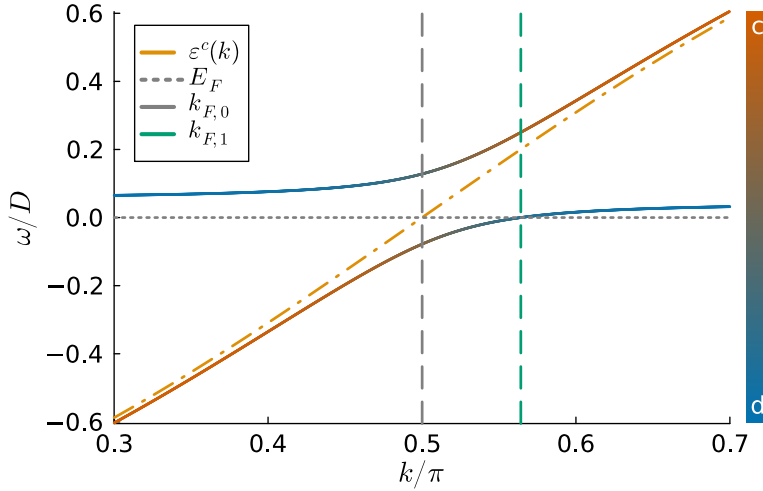


Figure 3.9: Two-band hybridization model from Section 2.3 with $(\varepsilon^d - E_F)/D = 0.05$ and $V/D = 0.1$. The free conduction-electron dispersion is shown as an orange dashed-dotted line, the dotted gray line is the Fermi energy, and the gray and green dashed lines correspond to the free and renormalized Fermi momenta.

suppressed, and the impurities remain fully localized due to the suppressed local coupling to itinerant conduction electrons. As such, they don't contribute to the conduction band and are missing from the Fermi surface. This configuration is the *small Fermi-surface* case. Notably, a transition from the ordered state to the heavy Fermi state was observed experimentally by Shishido et al. [61], in which a sudden increase of the Fermi surface of CeRhIn₅ was seen above a critical pressure at which the system undergoes a phase transition from magnetically ordered to heavy Fermi liquid.

3.5.3 The Periodic Anderson Impurity Model

As already established, the Kondo model is the low-energy effective model of Anderson's impurity model. The same relation can be expected between the Kondo lattice model and the Anderson (impurity⁸) model of a lattice of impurities⁹, often called the *periodic Anderson (impurity) model* (PAM) or the *Anderson (impurity) lattice model* (ALM).

$$H_{\text{PAM}} = \sum_{\vec{k}, \sigma} \left(\varepsilon_{\vec{k}}^c - \mu \right) c_{\vec{k}\sigma}^\dagger c_{\vec{k}\sigma} + \sum_{\vec{k}, \sigma} \left(\varepsilon_{\vec{k}}^d - \mu \right) d_{\vec{k}\sigma}^\dagger d_{\vec{k}\sigma} + U \sum_i n_{i\uparrow}^d n_{i\downarrow}^d + \sum_{\vec{k}, \vec{k}', \sigma} \left(V_{\vec{k}\vec{k}'} c_{\vec{k}\sigma}^\dagger d_{\vec{k}'\sigma} + h.c. \right). \quad (3.66)$$

As in the single-impurity case, this model can extend the discussion of Kondo lattices to a broader range of parameters and applications. It is especially useful for systems with a more complex intrinsic impurity structure, which will become clear in a later chapter. Typically, the impurities are so strongly localized that the spatial overlap of neighboring sites vanishes, in which case their dispersion $\varepsilon_{\vec{k}}^d = \varepsilon^d$

⁸ Anderson is also famous for his model of localization in disordered systems, the *Anderson model*. I have added parentheses to clarify which model is being discussed to avoid confusion. However, the context often makes it clear, and it will always be the impurity model in this thesis.

⁹ To the best of my knowledge, it was first discussed by Leder and Mühlischlegel in 1978 [62].

is exactly flat. Hence, a local description on the impurity site is justified

$$H_{\text{PAM}} \rightarrow \sum_{\vec{k}, \sigma} \left(\varepsilon_{\vec{k}}^c - \mu \right) c_{\vec{k}\sigma}^\dagger c_{\vec{k}\sigma} + \sum_{i, \sigma} \left(\varepsilon^d - \mu \right) d_{i\sigma}^\dagger d_{i\sigma} + U \sum_i n_{i,\uparrow}^d n_{i,\downarrow}^d + \sum_{\vec{k}, i, \sigma} \left(V_{\vec{k}i} c_{\vec{k}\sigma}^\dagger d_{i\sigma} + h.c. \right). \quad (3.67)$$

The parameter regimes are—at first glance—the same as for the single-impurity case. There are more phases to arise, though, as we have seen in the previous section. Essentially, a weakly hybridizing system will become magnetically ordered, whereas a strongly hybridizing system will tend towards a heavy Fermi liquid. The $U \rightarrow \infty$ limit of this model will be heavily utilized in this thesis and discussed throughout the following chapters.

Modeling Realistic Materials

The derivation of models discussed in the previous chapters relies on breaking down the physics to the bare minimum, respecting and utilizing symmetries of the systems at hand, and exploiting scale separation. The Kondo model (Sec. 3.4) relies on modeling a local impurity by just its spin. In the derivation of the regular single-impurity Anderson model (Sec. 3.3), the electronic d - or f -orbital states are reduced to a single, twofold degenerate state, such that the impurity Hamiltonian is of a simple spin- $1/2$ fermion form.

This seems odd at first, but it can be justified by a series of arguments that will successively reduce the degeneracy of the atomic orbital, often leading to a twofold, symmetry protected degeneracy of the ground state. Hence proving that the previously derived models are physically sound.

Being interested mostly in the physics of matter from around room temperature down to the lowest temperatures, or even the ground state, level splittings larger than $k_B \cdot 300 \text{ K} \approx 30 \text{ meV}$ can be considered infinite. Typically, in the d - or f -orbital impurity hosts, spin-orbit interaction induces a splitting of $O(100 \text{ meV})$ or larger and the crystal-field effect a further splitting of $O(10 \text{ meV} - 100 \text{ meV})$. Low energy physics is, therefore, well described by only considering the impurity ground state. Excited states can, however, sometimes be relevant for intermediate temperatures. This will be crucial in the discussion of $\text{PrV}_2\text{Al}_{20}$.

In order to fully understand and appreciate the unification of complexity and simplicity, the following discussions will highlight the group-theory aspect of angular momenta in general and atomic orbitals in particular. The case of spinful particles necessitates the coupling of angular momenta and a discussion of the expected spin-orbit coupled ground state via Hund's rules. Finally, the crystal-field effect and its implications are discussed.

4.1 Orbital Angular Momentum

In quantum mechanics, a (continuous) transformation of a state must be unitary due to the conservation of probability. A continuous transformation is an operator $\hat{U}(\alpha)$ whose action on a state is defined in terms of its expansion for an infinitesimal parameter δ such that $\hat{U}(\alpha) = [\hat{U}(\delta)]^{\alpha/\delta}$. For simplicity, let's assume α dimensionless. Since δ is infinitesimal, the expansion of \hat{U} contains only the terms of order zero and one

$$\hat{U}(\delta) = \mathbb{1} + i\delta\hat{G}, \quad (4.1)$$

where \hat{G} is a hermitian operator called the *generator* of the transformation \hat{U} . The prefactor of i is needed for unitarity. The next step would be taking the limit $\delta \rightarrow 0$ for a transformation of finite α . This is done best by defining a slicing of the parameter α into n parts such that $\hat{U}(\alpha) = [\hat{U}(\alpha/n)]^n$ and then sending $n \rightarrow \infty$. If n is large enough, we can use Eq. (4.1) to obtain

$$\hat{U}(\alpha) = \lim_{\delta \rightarrow 0} [\mathbb{1} + i\delta\hat{G}]^{\frac{\alpha}{\delta}} = \exp(i\alpha\hat{G}). \quad (4.2)$$

A particular, well-known continuous transformation is the time translation via the time-evolution operator. There, the generator is the Hamiltonian. Invariance under a continuous transformation can, therefore, be broken down to the commutator $[\hat{G}, \hat{H}] = 0$. This immediately defines \hat{G} as a symmetry of the system described by \hat{H} . Consequently, eigenstates of \hat{G} will continue to be eigenstates of the same eigenvalue under time evolution.

Among the large class of possible transformations, the class of rotational transformations is of particular interest. From Noether's theorem in classical (and quantum-) physics, we know that a continuous symmetry of a system results in a conserved quantity. If we think of angular momentum as the conserved quantity arising from rotational invariance, it is easy to see that the generator of the continuous rotation transformation must be the angular momentum operator.

The eigenstates of a fully rotationally invariant system can, therefore, be expressed in terms of angular momentum eigenstates, whose wavefunctions are the spherical harmonics. The angular momentum eigenvalues are classified by the quantum number l , which can, just from the solution of the eigenvalue equation, be half-integer or integer. Real-space rotations lead only to integer angular momenta l (including zero) due to the condition of full invariance under a full rotation. Such real-space arguments hold for electronic orbitals. Half-integer angular momenta describe the spin of fermionic particles. They obtain a phase under a full rotation. Bringing the two concepts together will be the topic of the next section.

4.2 Spin-Orbit Interaction and Hund's Rules

As established above, orbital angular momentum is of integer quantum number l , whereas spin can be of half-integer quantum number s . Spin is an intrinsic (relativistic) property of particles and must be added ad-hoc to nonrelativistic quantum mechanics. It has all the qualities of an angular momentum, and—as such—can be treated on equal footing as the orbital angular momentum. If we are interested in the angular momentum of a particle with both spin and orbital angular momentum, the two need to be added to a total spin $\hat{J} = \hat{L} + \hat{S}$ on the operator level to describe systems in which the Hamiltonian contains terms that connect \hat{L} and \hat{S} . The operator hats will be omitted from now on. The textbook

example for a Hamiltonian that requires this addition of angular momenta is spin-orbit coupling, which, in simple words, describes the dipole interaction of the intrinsic magnetic dipole and the induced dipole of a charged particle on a circular trajectory (plus corrections).

4.2.1 The Addition of Angular Momenta

Angular momentum operators L_i , where i labels a spatial axis, satisfy the algebra $[L_i, L_j] = i \sum_k \varepsilon_{ijk} L_k$, where $i, j, k \in \{x, y, z\}$ and ε is the Levi-Civita symbol¹. From this $[\vec{L}^2, L_i] = 0$ follows. Angular momentum eigenstates are therefore not only characterized by their quantum number l (via the eigenvalue $l(l+1)$ of \vec{L}^2) but also the eigenvalue m of one component L_i , which is usually chosen to be the z -axis. If the two added angular momenta are independent, their operators commute $[L_i, S_j] = 0$, and a common eigenbasis $\{l, m_l, s, m_s\}$ can be found. The total angular momentum also satisfies the angular momentum algebra, and its eigenstates can, therefore, be characterized by two quantum numbers $\{j, m_j\}$ and expressed in the aforementioned common eigenbasis of L and S . In order to derive the possible quantum numbers j in terms of l and s the square of \vec{J} has to be reformed into the form

$$\vec{J}^2 = \vec{L}^2 + \vec{S}^2 + L^+ S^- + L^- S^+ + 2L_z S_z, \quad (4.3)$$

where L^\pm and S^\pm are ladder operators of the respective angular momenta, changing the z -component by one. It is easily seen that the state with $m_l = l$ and $m_s = s$ is an eigenstate of \vec{J}^2 with quantum number $j_{\max} = l + s$. Simultaneously, the state is an eigenstate of J_z with $m_j = j$. All other m_j can then be constructed using the ladder operators for J , $J^\pm = L^\pm + S^\pm$.

When this is done, the next quantum number $j_{\max} - 1$ can be generated from knowing that $J_z = L_z + S_z$, so $m_j = m_l + m_s$ always. Therefore, knowing the $m_j = j_{\max} - 1$ state for $j = j_{\max}$ we can construct the $j = j_{\max} - 1$ and $m_j = j_{\max} - 1$ state by summing up all states with the correct m quantum numbers demanding the resulting state to be orthogonal

$$\langle j, m | j - 1, m \rangle = 0. \quad (4.4)$$

Once this is done, we can again use ladder operators to generate all m_j and finally repeat the whole process until we reach the minimal $m_{j, \min} = -(l + s)$. The coefficients appearing in the construction of $\{j, m_j\}$ states from $\{l, m_l, s, m_s\}$ states are the matrix elements of the basis transformation and known by the name *Clebsch-Gordan coefficients*.

Notably, the minimal j can be found by finding the combination with the smallest number of m_j states. Since $|m_j| \leq j$ and the smallest modulus $|m_j|$ is $|l - s|$ the minimal j is $j_{\min} = |l - s|$. So $|l - s| \leq j \leq l + s$.

This scheme can also be used to add angular momenta of multiple particles via successive coupling in pairs. First, the LS -coupled J for each particle is determined. Then the resulting J^i angular momenta, where i labels the particles, are added either successively pairwise or all at once. The order can be reversed, leading to the same result. Depending on the circumstances, one or the other method might be beneficial.

¹ The Levi-Civita symbol ε_{ijk} gives a minus sign if the permutation ijk is odd and unity if even. It vanishes if any index appears doubly.

4.2.2 Hund's Rules

Determining the ground state of a spin-orbit coupled system involving multiple particles is a tremendously challenging task. Friedrich Hund, working on molecular spectra in the 1920s, proposed a set of rules based on quantum-mechanical (partially heuristic) considerations to address this challenge for atoms with exactly one partially filled atomic shell. Hund's rules systematically find the ground state by first determining the energetically optimal total spin (S), then the total orbital angular momentum (L), and finally the total angular momentum (J) through the energetically optimized coupling of S and L .

Hund's rules can be understood through arguments based on Pauli's exclusion principle, electronic exchange interaction, and phase space volume. They allow for the prediction of the correct ground state in an overwhelming majority of cases, extending the knowledge about the electronic structure of atoms beyond the Aufbau principle. This section will discuss the three rules in a concise form without proof² and give three examples.

1. The simple case of a Ce^{3+} atom with only a single electron in the f -shell to illustrate the procedure.
2. The case of an Yb^{3+} atom, which is the hole-analogue to the first case and involves many more terms.
3. The slightly harder case of Pr^{3+} with two electrons in the f -shell as a pedagogical next step but also in anticipation of the discussion of $\text{PrV}_2\text{Al}_{20}$.

The first step in determining the ground state is analyzing the electron configuration of the atom at hand. Typically, in a solid, electrons are "lost" from individual atomic shells to bonding mechanisms between the atoms. This is called *oxidization*, and expected oxidization configurations are often listed in periodic tables of elements or the accompanying texts. The electron configuration in the oxidized state can be estimated in terms of localization of different orbitals. Less localized electrons are more likely to contribute to bonding between atoms than those that are more localized on the atom. The unfilled shells of the oxidized ion determine their electrical valence states, i.e. the occupation number of the unfilled shell. For a single *unfilled* shell of any number of electrons, Hund's rules are as follows.

1. Hund's first rule is to maximize the multiplicity of the spin S , which means aligning all available spins in the orbital until the shell is filled. Each additional spin must be of opposite orientation, reducing the possible S_{tot} . Effectively, this rule states that it is energetically attractive to fill any given m_l orbital only once, if possible.
2. The second rule is to maximize the orbital angular momentum L via a selection of m_l such that L_{tot} is maximized. The first rule filled the shells with a single electron, if possible, but did not specify the m_l quantum number. The second rule, therefore, fills the m_l quantum number from large to small modulus. Notably, although it does not matter if one starts from $m_l = -l$ or $m_l = l$, the filling has to be in order, and one should not fill only by modulus since this will *reduce* the multiplicity of the resulting possible L_{tot} . The rule can be understood as minimizing the Coulomb repulsion between the electrons.

² There is no general proof for Hund's rules as of now. They might be "unprovable" due to their heuristic nature.

3. Lastly, the third rule is to minimize the coupled angular momentum J (remembering $|L - S| \leq J \leq |L + S|$ from above) for the two previously determined S_{tot} and L_{tot} in the case of a shell that is half-filled or less. If it is more than half filled, the largest possible value of J will be the lowest in energy. The origin of this rule can be traced back to the expected splitting induced by spin-orbit coupling.

Example 1: Ce³⁺

Let's first consider a simple example, Ce³⁺, a prototypical $4f$ -shell ion. The electron configuration of charge-neutral Cerium is $[\text{Xe}] 4f^1 5d^1 6s^2$, which means it has the filled-shell configuration of the noble-gas Xenon and four electrons in partially filled shells. A common oxidization state of Cerium is Ce³⁺, whose electron configuration is $[\text{Xe}] 4f^1$ from losing its less localized electrons to bonds between atoms. Hund's rules are then applied straightforwardly:

1. $S = 1/2$
2. $L = 3$
3. $J_{\text{min}} = 5/2$

The ground state is, therefore, $2J + 1 = 6$ -fold degenerate and of half-integer spin.

Example 2: Yb³⁺

The next example is the electronic hole analogue of the previous case. The electron configuration of charge-neutral Ytterbium is $[\text{Xe}] 4f^{14} 6s^2$, leading to the configuration $[\text{Xe}] 4f^{13}$ in Yb³⁺. The ion, therefore, has an f -shell with only a single vacancy. Hund's rules now need some more consideration but are still straightforward:

1. The f -shell has $2L + 1 = 7$ orbitals, and we have 13 electrons, so the spins align in a way that fixes $S = 7 \cdot 1/2 - 6 \cdot 1/2 = 1/2$.
2. Since we now filled all orbitals, except for one, with two electrons, the total angular momentum is $L = 2 \cdot (3 + 2 + 1 + 0 - 1 - 2) - 3 = 3$.
3. $J_{\text{max}} = 7/2$

The ground state is, therefore, $2J + 1 = 8$ -fold degenerate and of half-integer spin. This looks surprisingly similar to the Ce³⁺ case, which is due to the particle-hole analogy between the two. We could have made the derivation in terms of electron holes, where Yb³⁺ would have a single f -shell hole. Hund's rules almost work in the same way there, just the spin-orbit coupling part of the third rule has a reversed argument now due to the sign-change of the coupling under a particle-hole transformation.

Example 3: Pr³⁺

The final example is the next larger f -shell occupation $4f^2$, which is realized in Pr³⁺. Charge-neutral Praseodymium has [Xe] $4f^3 6s^2$ and Pr³⁺ has [Xe] $4f^2$. For this case, Hund's rules are:

1. $S = 1/2 + 1/2 = 1$
2. $L = 3 + 2 = 5$
3. $J_{\min} = 4$

The ground state is, therefore, $2J + 1 = 9$ -fold degenerate and of integer spin. This illustrates nicely how the ground state of an even-number occupation will typically lead to a bosonic state.

4.3 Crystal Fields and Group Theory

So far, the discussion of angular momenta was only concerned with fully spherically symmetric systems and the coupling of internal angular momentum (spin S) to orbital angular momentum (L). Crystalline solids lack this full rotational invariance due to the arrangement of atoms on periodically repeating lattice sites. The Coulomb-potential at any given site is, therefore, the sum of the regular ionic potential $V_0(\vec{r})$ and the sum of potentials from other sites in the lattice $V_{\text{CF}}(\vec{r})$ often called *crystal-(electric-)field (CF/CEF) potential*³. Here, $V_0(\vec{r})$ has full rotational invariance, $V_{\text{CF}}(\vec{r})$ however is only invariant under discrete rotations that map lattice-sites onto lattice-sites. This discrete rotational symmetry leads to a reduced symmetry of the local energy-eigenfunctions and, in the same way as spin-orbit coupling lifts the individual $L - S$ degeneracy in terms of the coupled J , crystal fields further lift the J degeneracy by inducing a splitting in energy, the so-called *crystal-field splitting*. It is at this point that group theory becomes a most useful tool. Continuous rotational transformations form a continuous (i.e. Lie-) group. Discrete rotations form discrete groups that map points in real space onto each other, hence they are called point-groups.

Since we are going from a full, continuous symmetry to a discrete symmetry, the change of the basis will be more drastic the lower the final symmetry is. Consequently, the CEF splitting is also expected to become larger in this case. Additionally, the splitting originally stems from the Coulomb interaction with remote ions, so farther away contributions will give smaller contributions. Combining these two arguments, looking at the closest neighbors of any given local atom is usually enough to determine the dominant point-group symmetry and the splitting.

Assuming we know the point group of the crystal-field symmetry, what can we do with it? Knowing the spin-orbit-coupled ground state, we have to break down the degenerate eigenstates of the given J into the eigenbasis of the reduced symmetry. The methods and prerequisites for this will be discussed in the following section. For most parts, I will closely follow [63].

³ Historically, many texts talk about *ligand fields*, which is the combination of crystal fields and molecular theory of bonds. Often, also throughout this thesis, the term *crystal electric field (CEF)* is used interchangeably with *crystal field (CF)*.

4.3.1 Representations of Groups and their Character

A group is a non-empty set G which is closed under a binary operation (\cdot, \cdot) , i.e. $a \cdot b \in G, \forall a, b \in G$, for which the following axioms hold:

1. Associativity: $(a \cdot b) \cdot c = a \cdot (b \cdot c) \forall a, b, c \in G$.
2. Identity: $\exists \mathbb{1} \in G : \mathbb{1} \cdot a = a \cdot \mathbb{1} = a, \forall a \in G$.
3. Inverse: $\forall a \in G \exists b \in G : b \cdot a = a \cdot b = \mathbb{1}; b = a^{-1}$.

Two elements $a, b \in G$ are *conjugate* if $\exists g \in G : gbg^{-1} = b$. Closed sets of a, b form the *conjugacy classes* C_k of a group. A closed set \tilde{G} within a group G that itself forms a group is called *subgroup* of G .

A prominent example of a group is the special orthogonal group in three dimensions $SO(3)$, which describes rotations in three-dimensional Euclidean space via orthogonal 3×3 matrices of unit determinant. The group operation, in this case, is simply the matrix multiplication. The $SO(3)$ is a *Lie-group*, which is a group that is also a differentiable manifold. Therefore, one can consider it a *continuous* group. This makes sense in the context of rotations; there are three Euler angles, which are parameters in \mathbb{R} and, as such, are taken from a continuum. Elements of the $SO(3)$ can be generated via its *Lie-algebra* $\mathfrak{so}(3)$, which is the group of all exponents in the mapping $\mathfrak{g} \rightarrow \exp(ig) \in SO(3)$, where $\mathfrak{g} \in \mathfrak{so}(3)$, c.f. Sec. 4.1.

This group is most useful in situations where there is full rotational symmetry. In regular lattices, the spatial symmetry of ionic potentials in any given fixed ion's environment is discrete. In such cases, one must determine the symmetry's *point group*. Point groups contain only symmetry operations with a fixed point in common, the origin of a suitable coordinate system. An example would be the cyclic groups $C_n, n \in \mathbb{N}$, which contains n -fold rotations around a single rotation axis. As an example, C_3 contains the rotations by $2\pi/3, 4\pi/3$, and $6\pi/3 = 2\pi$ around a given axis. It is a subgroup of $SO(3)$.

As explained above, reducing the full rotational symmetry to a discrete one will (partially) lift the degeneracy of full-rotation eigenstates. For this, we need the concept of *representation* and *character* of a group.

Representations of a Group

It is often desirable to link the (abstract) symmetry to the (quantum-) states of the system. For this, a (*matrix-*) *representation* Γ has to be constructed. Such a representation must preserve the group axioms, it must not only form a group itself but the representation itself must be a mapping D_Γ from G to Γ such that all properties of G transfer directly to Γ . This is achieved if the representation respects

$$D_\Gamma(a \cdot b) = D_\Gamma(a) \cdot D_\Gamma(b). \quad (4.5)$$

Since group elements of Γ are matrices, the group operation is the matrix multiplication. In technical terms, representations are group homomorphisms from a group G to the general linear group GL .

A given group has infinitely many representations, but only a limited number⁴ of *irreducible representations* (irreps). A representation is reducible if we can bring all of its elements (i.e. all

⁴ The number of irreps is identical to the number of conjugacy classes of the group, which is not proven here, but a proof can be found in any standard textbook, e.g. [63].

matrices of the representation) into an upper-triangular block form via the *same* transformation T . If the transformation brings all elements into a block-*diagonal* form, the representation is *decomposable* into smaller representations. The smallest possible representations generated by this method, i.e. representations that can *not* be brought into an upper-triangular block form via transformation with the same T , are the irreducible representations. Since there is a limited number of irreps, they are labeled by an integer index i as Γ_i .

An example for representations are the spherical harmonics Y_{lm} , which are irreps of $SO(3)$. For any given angular-momentum quantum number l , a set of spherical harmonics labeled by m can be defined which are closed under rotations, i.e. any rotation of a given spherical harmonic Y_{lm} will result in a linear combination of spherical harmonics with the *same* l but potentially different m .

An irrep of a group describing a symmetry of a given system will commute with the Hamiltonian. State within this irrep are therefore energetically degenerate. Knowing the eigenstates of the ion under full rotational symmetry, it is therefore highly desirable to decompose those states into the eigenstates of the discrete rotational symmetry, which are simultaneous eigenstates of the Hamiltonian. Due to point groups being subgroups of $SO(3)$, irreps of $SO(3)$ can be decomposed into irreps of the subgroup G . For this, the concept of *character* can be used.

Character of a Representation

As seen above, irreducible representations are the essential components of interest when investigating the lifting of degeneracy due to a reduction in symmetry. Since there is a set of different irreps, a way of distinguishing clearly between them is necessary. For this, the concept of *character* is used. The character $\chi^{(\Gamma_i)}(a)$ of an element $a \in \Gamma_i$ is the trace of the corresponding matrix

$$\chi^{(\Gamma_i)}(a) = \text{Tr} \left(D_{(\Gamma_i)}(a) \right). \quad (4.6)$$

Since conjugacy (see definition above) becomes a similarity transform under the representation mapping, and due to the invariance of the trace under similarity transformations, the character of each element within a conjugacy class is identical. Also, since the identity trivially forms a conjugacy class of only one element, its character is the (matrix-)dimension of the irrep. Furthermore, there is always the trivial irrep, which maps every group element onto the same scalar. This irrep has character 1 in every conjugacy class.

There are two orthogonality theorems related to the character of irreps:

$$\sum_k \chi^{(\Gamma_i)}(C_k) \left[\chi^{(\Gamma_j)}(C_k) \right]^* N_k = h \delta_{\Gamma_i, \Gamma_j} \quad (4.7)$$

$$N_k \sum_i \chi^{(\Gamma_i)}(C_k) \left[\chi^{(\Gamma_i)}(C_{k'}) \right]^* = h \delta_{k, k'} \quad (4.8)$$

Here, h is the order of the group (the number of elements), and N_k is the number of elements in conjugacy class C_k .

With this combined, the irreducible representations of a given group can be presented appropriately

via a table, the *character table*⁵. An example for the group C_4 is given in Tab. 4.1. The first orthogonality

C_4	E	C_4	C_2	$(C_4)^3$
Γ_1	+1	+1	+1	+1
Γ_2	+1	-1	+1	-1
Γ_3	+1	+i	-1	-i
Γ_4	+1	-i	-1	+i

Table 4.1: Character table of the point group C_4 . Top left is the group designation, the rest of the first row are the conjugacy classes, and the rest of the first column are the irreducible representations.

relation can be interpreted as orthogonality between rows, the second one as orthogonality between columns. With this, a simple way of decomposing reducible representations into irreducible representations is possible. A good example is the tensor product of two irreps. A given product of irreps can be decomposed into the direct sum of individual irreps. The product is *simply reducible*. Another application is the aforementioned reduction of symmetry. The fact that the reduced-symmetry group \tilde{G} is a subgroup of the full-symmetry group G makes it possible to compare character between the two. Any conjugacy class of \tilde{G} must be a conjugacy (sub-)class of G , and as such, the character of any given irrep of G in \tilde{G} can be calculated. Equation (4.7) can then be used to decompose the irrep of G into a direct sum of irreps of \tilde{G} , which works in a very analogous way to decomposing vectors of a given basis into a new basis.

Character of $SO(3)$ Irreducible Representations

In order to determine the character of the irreps of $SO(3)$, one can resort to the definition of spherical harmonics Y_{lm} . The transformations that will be of interest in this context can be decomposed into inversions \hat{I} and rotations by an angle α around the z -axis C_α . Both can be handled in an elegant way when considering spherical harmonics, which depend only on the two angles Θ and φ , where Θ is the angle to the z -axis and φ is the angle of rotation around the z -axis.

First, for inversions, one gets

$$\hat{I}Y_{ll}(\Theta, \varphi) = Y_{ll}(\pi - \Theta, \varphi + \pi) = c \cdot e^{il(\varphi + \pi)} \sin^l(\pi - \Theta) = (-1)^l Y_{ll}(\Theta, \varphi), \quad (4.9)$$

where c is a complex constant that depends on the definition of Y_{lm} . Since $[\hat{L}, \hat{I}] = 0$, also $[\hat{L}_-, \hat{I}] = 0$ and, since the coefficient $c(m)$ in $\hat{L}_- |l, m\rangle = c(m) |l, m-1\rangle$ does not depend on l , the symmetry of all m states is the same. Hence

$$\chi^{(\Gamma_l)}(I) = (-1)^l \sum_{m=-l}^l 1 = (-1)^l (2l + 1). \quad (4.10)$$

Next, rotations by an angle α around the z -axis are just given by the transformation $\varphi \rightarrow \varphi + \alpha$ and,

⁵ A good source for character tables and much more is the Bilbao crystallographic server [64]. A standard textbook tabulating everything about point groups is from 1969 by Koster [65]. The book is known to have a non-negligible number of typos, though.

since spherical harmonics depend on φ only by an exponential,

$$Y_{lm}(\Theta, \varphi + \alpha) = e^{-im\alpha} Y_{lm}(\Theta, \varphi), \quad (4.11)$$

$$\Rightarrow \chi^{(\Gamma_l)}(C_\alpha) = \sum_{m=-l}^l e^{-im\alpha} = \sum_{m'=0}^{2l} e^{-i(m'-l)\alpha} = e^{il\alpha} \sum_{m'=0}^{2l} e^{-im'\alpha} \quad (4.12)$$

$$= e^{il\alpha} \frac{e^{-i(2l+1)\alpha} - 1}{e^{-i\alpha} - 1} = \frac{e^{-i(l+\frac{1}{2})\alpha} - e^{i(l+\frac{1}{2})\alpha}}{e^{-i\frac{\alpha}{2}} - e^{i\frac{\alpha}{2}}} \quad (4.13)$$

$$= \frac{\sin\left[\left(l + \frac{1}{2}\right)\alpha\right]}{\sin\left[\frac{\alpha}{2}\right]}, \quad (4.14)$$

where the sum was evaluated using the formula for an incomplete geometric series. The character for discrete rotations C_n can be read-off via $\alpha = 2\pi/n$.

Half-Integer J : Double Groups

In order to describe particles with half-integer spin or total angular momentum J , an extension to the point groups is needed. A rotation by 2π is not the identity in this case, which can be seen from Eq. (4.14) for half-integer j . In this case, the point groups have to be extended via an additional operation \mathcal{R} , rotation by 2π , which acts as the identity on integer J but is sign-changing for half-integer J . By comparing any point group G with its double group G' , a series of rules apply [63]:

1. A set of operations $\{g_K\}$ that forms a conjugacy class in G also forms a conjugacy class in G' and the set $\{\mathcal{R}g_K\}$ forms a different class in G' , except in the case discussed in 2. below.
2. For classes C_2 of rotation by π around an axis, if there exists another axis of twofold rotations that is *orthogonal* to the aforementioned one, then C_2 and $\mathcal{R}C_2$ are in the same class.
3. Any irreducible representation of G is also an irreducible representation of G' with the same set of characters $\chi^{(\Gamma_i)}(\mathcal{R}C_k) = \chi^{(\Gamma_i)}(C_k)$.
4. In addition to the irreducible representations of G , there must be additional ones to match the number of classes. The characters of these classes are $\chi^{\Gamma'}(\mathcal{R}C_k) = -\chi^{\Gamma'}(C_k)$. If the condition in 2. applies, the character must vanish for a group containing C_k and $\mathcal{R}C_k$.

Often, the application of \mathcal{R} is denoted by a bar, e.g. $\mathcal{R}C_k = \overline{C_k}$.

4.3.2 Examples for the Reduction of Symmetry

An example that will be useful later in the thesis is the case of the splitting of $J = 5/2, 4, 9/2$ states into irreps of the double-group T'_d . For this, we need the character table of T'_d , which is given in Tab. 4.2.

The character of the J irreps can be calculated using Eq. (4.10) and Eq. (4.14). Additionally, $S_n = C_n \otimes \sigma_h$, where σ_h represents reflection in a horizontal plane, i.e. a plane that is perpendicular to the axis of highest symmetry, and $\sigma_d = C_2 \otimes I$. Since character is multiplicative, the character can be immediately read off. Results for this are listed in Tab. 4.3. Using the orthogonality relation in

\mathbf{T}'_d	E	\bar{E}	$8C_3$	$8\bar{C}_3$	$\frac{3C_2}{3\bar{C}_2}$	$6S_4$	$6\bar{S}_4$	$\frac{6\sigma_d}{6\bar{\sigma}_d}$
Γ_1	1	1	1	1	1	1	1	1
Γ_2	1	1	1	1	1	-1	-1	-1
Γ_3	2	2	-1	-1	2	0	0	0
Γ_4	3	3	0	0	-1	1	1	-1
Γ_5	3	3	0	0	-1	-1	-1	1
Γ_6	2	-2	1	-1	0	$\sqrt{2}$	$-\sqrt{2}$	0
Γ_7	2	-2	1	-1	0	$-\sqrt{2}$	$\sqrt{2}$	0
Γ_8	4	-4	-1	1	0	0	0	0

Table 4.2: Character table for the T'_d double group. Integers in front of classes label the number of members in a class. The last three classes are additions to the point group T_d . The classes of T_d are: the identity E , threefold rotations C_3 , twofold rotations C_2 , improper fourfold rotations S_4 (rotation followed by a reflection in a perpendicular plane), and the reflection in a diagonal plane σ_d (the plane parallel to the symmetry axis but arranged in a specific way, which is not relevant to us here).

	E	\bar{E}	$8C_3$	$8\bar{C}_3$	$\frac{3C_2}{3\bar{C}_2}$	$6S_4$	$6\bar{S}_4$	$6\sigma_d$	$6\bar{\sigma}_d$
$\Gamma_{J=5/2}$	6	-6	0	0	0	$-\sqrt{2}$	$\sqrt{2}$	1	-1
$\Gamma_{J=4}$	9	9	0	0	1	1	1	1	1
$\Gamma_{J=9/2}$	10	10	-1	1	0	$\sqrt{2}$	$-\sqrt{2}$	1	-1

Table 4.3: Character of irreducible representations of $SO(3)$ under the classes of T'_d . Although σ_d and $\bar{\sigma}_d$ are conjugate in T'_d , they lead to different character for some irreps of $SO(3)$, so they have to be split up for the orthogonality.

Eq. (4.7) pairwise, the reduction of the given $SO(3)$ irreps in terms of T'_d irreps is

$$\Gamma_{J=5/2} = \Gamma_7 \oplus \Gamma_8 \quad (4.15)$$

$$\Gamma_{J=4} = \Gamma_1 \oplus \Gamma_3 \oplus \Gamma_4 \oplus \Gamma_5 \quad (4.16)$$

$$\Gamma_{J=9/2} = \Gamma_6 \oplus 2\Gamma_8. \quad (4.17)$$

Also, products of irreps can then be easily calculated⁶. For example, the products of some of the T'_d irreps are

$$\Gamma_6 \otimes \Gamma_3 = \Gamma_8 \quad (4.18)$$

$$\Gamma_6 \otimes \Gamma_5 = \Gamma_8 \oplus \Gamma_7. \quad (4.19)$$

⁶ They are, of course, also tabulated in [65].

4.3.3 Clebsch-Gordan Coefficients for Point Groups

Once the product of two irreps has been taken, we would like to construct a product basis in the new representations, e.g. we have the basis Γ_6 and Γ_5 of T'_d and want to compute the corresponding product-basis of Γ_8 (or Γ_7). In some cases, the products can be traced back to Clebsch-Gordan (CG) coefficients of known angular momenta, c.f. Sec. 4.2.1. A more general rule is necessary, though, which can be derived using the representation of classes [66].

Given the basis $|\Gamma_a, \alpha\rangle$ of a representation Γ_a and $|\Gamma_b, \beta\rangle$, where α and β are indices for the basis elements, we want to get the Clebsch-Gordan coefficients (matrix elements of unitary transformation) for the transformation from the product basis to a third basis $|\Gamma_c, \gamma\rangle$, for which $\Gamma_c \in \Gamma_a \otimes \Gamma_b$. This transformation block-diagonalizes the product basis. The coefficients are orthogonal and complete:

$$\sum_{\alpha, \beta} C^*(\Gamma_a \alpha, \Gamma_b \beta; \Gamma_c \gamma) C(\Gamma_a \alpha, \Gamma_b \beta; \Gamma_c \gamma') = \delta_{c, c'} \delta_{\gamma, \gamma'} \quad (4.20)$$

$$\sum_{c, \gamma} C^*(\Gamma_a \alpha, \Gamma_b \beta; \Gamma_c \gamma) C(\Gamma_a \alpha', \Gamma_b \beta'; \Gamma_c \gamma) = \delta_{\alpha, \alpha'} \delta_{\beta, \beta'} \quad (4.21)$$

Having the block-diagonal form M of the direct product of all irreps Γ_c contained in $\Gamma_a \otimes \Gamma_b$, the transformation U produces the tensor-product basis of $\Gamma_a \otimes \Gamma_b$ via $U M U^\dagger$. This translates to

$$D_{\Gamma_a}(g)_{\alpha\alpha'} D_{\Gamma_b}(g)_{\beta\beta'} = \sum_{c, \gamma, \gamma'} C(\Gamma_a \alpha, \Gamma_b \beta; \Gamma_c \gamma) D_{\Gamma_c}(g)_{\gamma\gamma'} C^*(\Gamma_a \alpha', \Gamma_b \beta'; \Gamma_c \gamma') . \quad (4.22)$$

We also need the orthogonality theorems for irreducible representations

$$\sum_i^h D_{\Gamma_a}(g_i)_{\alpha\alpha'}^* D_{\Gamma_b}(g_i)_{\beta\beta'} = \delta_{\alpha, \alpha'} \delta_{\beta, \beta'} \quad (4.23)$$

$$\frac{n_a}{h} \sum_i^h D_{\Gamma_a}(g_i)_{\alpha\alpha'}^* D_{\Gamma_a}(g_i)_{\tilde{\alpha}\tilde{\alpha}'} = \delta_{\alpha, \tilde{\alpha}} \delta_{\alpha', \tilde{\alpha}'} \quad (4.24)$$

where n_a is the dimensionality of Γ_a , i.e. the identity character of the irrep, and h is the order of the group, i.e. the number of elements. Using Eq. (4.22) and this, the triple product of irreps can be written as

$$\begin{aligned} & \frac{n_c}{h} \sum_i^h D_{\Gamma_a}(g_i)_{\alpha\alpha'} D_{\Gamma_b}(g_i)_{\beta\beta'} D_{\Gamma_c}^*(g_i)_{\gamma\gamma'} \\ &= \sum_{\tilde{c}, \tilde{\gamma}, \tilde{\gamma}'} C(\Gamma_a \alpha, \Gamma_b \beta; \Gamma_{\tilde{c}} \tilde{\gamma}) C^*(\Gamma_a \alpha', \Gamma_b \beta'; \Gamma_{\tilde{c}} \tilde{\gamma}') \frac{n_c}{h} \sum_i^h D_{\Gamma_c}^*(g_i)_{\gamma\gamma'} D_{\Gamma_{\tilde{c}}}(g_i)_{\tilde{\gamma}\tilde{\gamma}'} \quad (4.25) \end{aligned}$$

$$= \sum_{\tilde{c}, \tilde{\gamma}, \tilde{\gamma}'} C(\Gamma_a \alpha, \Gamma_b \beta; \Gamma_{\tilde{c}} \tilde{\gamma}) C^*(\Gamma_a \alpha', \Gamma_b \beta'; \Gamma_{\tilde{c}} \tilde{\gamma}') \frac{n_c}{h} \delta_{c, \tilde{c}} \delta_{\gamma\tilde{\gamma}} \delta_{\gamma'\tilde{\gamma}'} \quad (4.26)$$

$$= C(\Gamma_a \alpha, \Gamma_b \beta; \Gamma_c \gamma) C^*(\Gamma_a \alpha', \Gamma_b \beta'; \Gamma_c \gamma') . \quad (4.27)$$

Choosing $\alpha = \alpha' = \alpha_0$, $\beta = \beta' = \beta_0$, and $\gamma = \gamma' = \gamma_0$ gives

$$C(\Gamma_a \alpha_0, \Gamma_b \beta_0; \Gamma_c \gamma_0) = e^{i\phi} \sqrt{\frac{n_c}{h} \sum_i^h D_{\Gamma_a}(g_i)_{\alpha_0 \alpha_0} D_{\Gamma_b}(g_i)_{\beta_0 \beta_0} D_{\Gamma_c}^*(g_i)_{\gamma_0 \gamma_0}}, \quad (4.28)$$

where $e^{i\phi}$ is undetermined due to the modulus of C appearing in the derivation. It is often chosen such that $C(\Gamma_a \alpha_0, \Gamma_b \beta_0; \Gamma_c \gamma_0) > 0$. From this, one can then generate all other CG coefficients via

$$C(\Gamma_a \alpha, \Gamma_b \beta; \Gamma_c \gamma) = \frac{\frac{n_c}{h} \sum_i^h D_{\Gamma_a}(g_i)_{\alpha \alpha_0} D_{\Gamma_b}(g_i)_{\beta \beta_0} D_{\Gamma_c}^*(g_i)_{\gamma \gamma_0}}{C(\Gamma_a \alpha_0, \Gamma_b \beta_0; \Gamma_c \gamma_0)}. \quad (4.29)$$

When a product basis contains an irrep more than once, additional steps have to be taken, which is omitted here but can be found in [66]. The matrix representations are tabulated in [64].

4.3.4 Crystal-Field States in Quantum Field Theory

Once the relevant CEF states have been identified, they can be incorporated into our models. This is not necessarily straightforward, though, and depends on details. Let's assume we want to write down a Hamiltonian describing the dominant physics of the f -orbital on Ce^{3+} . Without any more information, we can assume $4f^1$ to be the ground state configuration. The two closest-in-energy states will be the $4f^0$ and $4f^2$. A simple case would be just $H = \sum_{\sigma} \varepsilon d_{\sigma}^{\dagger} d_{\sigma}$. The operator d_{σ}^{\dagger} creates a particle and, by that, describes the transition from a state of n particles to a state of $n + 1$ particles, i.e. a transition between electronic valence configurations. We can associate a negative energy ε to adding a particle because we know that $4f^1$ should be the ground state. If we now add a second particle, the same (negative) energy is added to the system; the energy difference between valence configurations is therefore assumed to be equidistant. This can be addressed by attaching an additional energy to the operator of double occupation. This must necessarily be a product of two single-particle operators, and we immediately arrive at the construction of the Hubbard model. The creation operator in our lowest-order approximation would take care of the transition from the $4f^0$ CEF ground state to the $4f^1$ ground state and, on repeated application, from $4f^1$ to the $4f^2$ CEF ground state.

A problem arises when we want to add $4f^3$ now, to which a solution was already presented in Section 3.2 in Hubbard operators. One essentially goes back from using field operators to projectors onto individual states. Similarly, if we have the situation of a small crystal-field splitting (usually of the order of the temperature we want to investigate), it can be beneficial to also take the first excited CEF state of the $4f^1$ configuration into account. This will be the dominant correction beyond taking only CEF ground states into account. The electronic ground state $4f^1$ will be fully thermally occupied, and the excited states $4f^0$ and $4f^2$ depleted at temperatures where the splitting between the $4f^1$ CEF states is not yet thermally resolved (c.f. scale comparison in this chapter's introduction). Adding additional CEF states also necessitates the use of Hubbard operators. Finally, the same can be said if states are removed from the discussion, as would be the case for a $U \rightarrow \infty$ Hubbard- or Anderson impurity model.

Hubbard operators have non-canonical commutation relations, and treating them in quantum field theory is, therefore, especially tedious due to the inapplicability of Wick's theorem. This will be resolved by introducing auxiliary particles in the next chapter.

Methods and Approximations

In the previous chapters, interacting models for the description of heavy fermion physics have been discussed. Generally, large interactions are problematic for the naturally perturbative approach of quantum field theory. Hubbard operators were already presented as a first step towards treating strongly interacting systems. They came at the cost of losing the applicability of Wick's theorem, seriously hindering their usefulness. In this chapter, a method of addressing this problem via the introduction of auxiliary particles [67, 68] is presented. There, each Hubbard operator is represented by a combination of artificial auxiliary fields. This enhances the Hilbert space and a projection down to the physical sector is needed.

Once the model of interest is re-written in terms of auxiliary particles, it can be solved via mean-field theory or more intricate methods. One of those methods is the non-crossing approximation (NCA), summing up an infinite number of self-energy diagrams without crossing lines [69–71]. This approximation is able to capture many aspects of the Anderson impurity model and proves to be extremely versatile and controlled.

The extension to the lattice case is then presented in dynamical mean-field theory (DMFT). There, the impurity interaction is assumed to be local, which becomes exact in infinite dimensions. For finite dimensions, it is often a surprisingly good approximation. From the derivation it will become clear that DMFT and NCA go well together in that both are diagrammatic methods concerned with local quantities.

5.1 Auxiliary Particles

The discussion in Chapter 4 revealed the necessity for Hubbard operators beyond their original designation. While greatly enhancing our ability to construct more realistic and/or tunable models, they hinder our ability to solve them via efficient quantum field theory methods. Their non-canonical commutation relations disallow the application of Wick’s theorem, which is the backbone for perturbation expansions in small parameters, allowing us to break complex expectation values down to products of much simpler, quadratic expectation values. The following paragraphs will give a historical overview. Each approach had its strengths and weaknesses, which were later remedied by improved approaches. The—to date—correct approach will be presented in the following Section 5.1.1.

Ideally, we would want to replace the non-canonically commuting objects with canonically commuting ones, a bold ask at first glance. There is, however, a way of achieving this. A similar problem was faced by Abrikosov [37] when he tried to apply field-theoretical methods to the Kondo model. Spin operators obey the spin-algebra, which is incompatible with the canonical commutation relations of field operators. The conduction-electron spin can readily be substituted by conduction-electron fields of appropriate combinations (c.f. Eq 3.18), but the same can not be done easily for the impurity spin. In essence, if no conduction electron exists at any given site, the conduction-electron spin also vanishes. The impurity spin, on the other hand, is pinned to a specific site and must always exist; it can only change orientation. Abrikosov proposed an elegant solution to the problem, introducing local auxiliary particles, or “virtual fields”, a_σ that describe the impurity spin in the same way as the conduction-electron fields describe their respective spin operator. Realizing that this extends the Hilbert space by adding unphysical states, he proposed a method of fixing the expectation values via the addition of an artificial fugacity $e^{\beta\lambda}$ to states of occupation two, sending $\lambda \rightarrow \infty$. Double occupation would be shifted to infinite energy and single-occupation, which is the physically correct state, would be untouched. The sector of no auxiliary particle were disregarded because expectation values of interest tend to annihilate this sector. Abrikosov partially addressed that summation over fields would give a wrong normalization, which would have to be fixed by an additional prefactor.

More than two decades later, Barnes [67, 68] picked up Abrikosov’s idea and applied it to a more general case, the single-impurity Anderson model (c.f. Sec. 3.3). Here, the impurity is modeled via a full local fermion with a quadratic term and a Hubbard- U term. The reason for introducing auxiliary particles here was not due to commutation relations—they are canonical for the impurity field—but rather due to problems in the large- U case, where perturbation theory in U is non-converging. The original Hamiltonian can be re-written in terms of Hubbard operators for the impurity states

$$\begin{aligned}
 H_{\text{SIAM}} = & \sum_{\vec{k}, \sigma} \left(\varepsilon_{\vec{k}}^c - \mu \right) c_{\vec{k}\sigma}^\dagger c_{\vec{k}\sigma} + \sum_{\sigma} \left(\varepsilon^d - \mu \right) |d; \sigma\rangle \langle d; \sigma| + U |d; 2\rangle \langle d; 2| \\
 & + \sum_{\vec{k}, \sigma} \left(V_{\vec{k}} c_{\vec{k}\sigma}^\dagger (|d; 0\rangle \langle d; \sigma| + |d; \bar{\sigma}\rangle \langle d; 2|) + h.c. \right), \quad (5.1)
 \end{aligned}$$

where $\bar{\sigma}$ is the conjugate spin, i.e. $-\sigma$ for spin- $1/2$. Barnes introduced four auxiliary particles, one for each involved state. Two fermions $a_\sigma^\dagger |\text{vac}\rangle = |d; \sigma\rangle$ and two bosons $b_0^\dagger |\text{vac}\rangle = |d; 0\rangle$ and $b_{\uparrow\downarrow}^\dagger |\text{vac}\rangle = |d; 2\rangle$. He specifically chose bosons for the latter two cases such that vertices of hybridization would conserve the fermion number. He also interpreted the condition of total auxiliary particle occupation being equal to unity as a projection onto the physical Hilbert space. Implementing

this using a chemical potential λ as $\lambda (\langle \hat{n}^a \rangle - 1)$ and $\lambda \rightarrow \infty$ in the spirit of Abrikosov's approach gave a clear physical interpretation to the previously used projection.

5.1.1 Constructing Auxiliary-Particle Representations

So, how does one go about constructing an auxiliary particle representation? First, all many-body states of a given system need to be collected. For example, this could be the s -shell of an atom, which has three different valence states. Each of those states should be representable by a combination of single-particle operators acting on the vacuum. Enumerating all the states can be quite tedious due to the increasing number of possible combinations. The states are

$$\begin{aligned} |0\rangle &= |\text{vac}\rangle_{\text{phys}} , & |s^1; \uparrow\rangle &= c_{\uparrow}^{\dagger} |0\rangle , \\ |s^2\rangle &= c_{\uparrow}^{\dagger} c_{\downarrow}^{\dagger} |0\rangle , & |s^1; \downarrow\rangle &= c_{\downarrow}^{\dagger} |0\rangle , \end{aligned}$$

where the order of operators constructing $|f^2\rangle$ is arbitrarily chosen. The vacuum has a subscript to denote that this is the physical, *real* vacuum. The doubly occupied state is automatically the singlet state due to Pauli's exclusion principle and the canonical commutation relation of the c operators¹.

The next step is to define the auxiliary particles that create each individual state

$$\begin{aligned} |0\rangle &= b^{\dagger} |\text{vac}\rangle , & |s^1; \uparrow\rangle &= f^{\dagger} |\text{vac}\rangle , \\ |s^2\rangle &= a^{\dagger} |\text{vac}\rangle , & |s^1; \downarrow\rangle &= g^{\dagger} |\text{vac}\rangle , \end{aligned}$$

with a *new* vacuum $|\text{vac}\rangle$. At this point, we can leave the statistics of the auxiliary particles open. The enlarged Hilbert space can be quantified by the auxiliary particle occupation number

$$\hat{Q} = b^{\dagger} b + f^{\dagger} f + g^{\dagger} g + a^{\dagger} a \quad (5.2)$$

Its eigenvalues are positive integers, of which the case $\langle \hat{Q} \rangle = Q = 1$ is the physical. The Hamiltonian, which we want to express in terms of auxiliary particles, must commute with \hat{Q} , conserving Q . This allows the implementation of a constraint $Q = 1$ on the operator level ($\hat{Q} = \mathbb{1}$) via a chemical potential, which is sent to infinity. This method will be discussed in detail in Section 5.1.2. For now, let's assume that $\hat{Q} = \mathbb{1}$ is fixed.

Statistics of Auxiliary Particles

In order to have a faithful representation of the states, the superalgebra of Hubbard operators $X_{\alpha\beta} = |\alpha\rangle \langle\beta|$ constructed from those states must be respected. If the particle number difference $|n_{\alpha} - n_{\beta}|$ is odd, the operator is of fermionic type. If it is even, it is of bosonic type. Their superalgebra is

$$[X_{\alpha,\beta}, X_{\gamma,\delta}]_{\pm} = X_{\alpha,\delta} \delta_{\beta,\gamma} \pm X_{\gamma,\beta} \delta_{\delta,\alpha} , \quad (5.3)$$

¹ In an s -shell, one can not construct a triplet state without additional quantum numbers to distinguish the particles.

where the sign is positive if both Hubbard operators are of a fermionic type. Replacing the Hubbard operators by auxiliary fields in a most general way

$$X_{\alpha\beta} = |\alpha\rangle\langle\beta| = \alpha^\dagger |\text{vac}\rangle\langle\text{vac}| \beta \stackrel{\hat{Q}=1}{=} \alpha^\dagger \beta. \quad (5.4)$$

The condition $\hat{Q} = 1$ ensures that the in-between state is always the vacuum, so the projector onto it can be dropped. If $X_{\alpha\beta}$ is fermionic, the two auxiliary particles must have different statistics, i.e. one must be fermionic, the other one bosonic. From this, we can see that if the particle numbers of two states differ by an odd number, the auxiliary particles of those states must be of different statistics. Consequently, if the particle number differs by an even number, the particles must be of the same statistics.

The situation is more delicate if $X_{\alpha\beta}$ is bosonic. Trivially, if $\alpha = \beta$, the operator is just a number operator, which is known to be bosonic. The case $\alpha \neq \beta$ demands a quick calculation.

$$[X_{0,2}, X_{2,0}]_- = X_{0,0}\delta_{2,2} - X_{2,2}\delta_{0,0} = X_{0,0} - X_{2,2} \quad (5.5)$$

$$= [b^\dagger a, a^\dagger b] = b^\dagger a a^\dagger b - a^\dagger b b^\dagger a \quad (5.6)$$

$$= b^\dagger b (1 \pm a^\dagger a) - (1 \pm b^\dagger b) a^\dagger a = b^\dagger b - a^\dagger a = X_{0,0} - X_{2,2}, \quad (5.7)$$

where plus is for both particles being bosons and minus for both being fermions. This equation holds true as long as both particles are of the same statistic. The argument directly translates to arbitrary bosonic Hubbard operators.

This proves that there is a freedom of choice in auxiliary particle statistics. Typically, the physical vacuum state is defined as a boson, resulting in even-number occupations being described by bosonic operators and odd-number occupations being described by fermions. This is the most natural definition since it assures fermion number conservation in the auxiliary particle Hamiltonian works as expected. Under this choice, the two particles f and g can be assigned the same letter but with a subscript of spin, i.e. $f \rightarrow f_\uparrow$ and $g \rightarrow f_\downarrow$. This notation was avoided above as the statistics were not fixed, and it might appear wrong to see a spin- $1/2$ attached to a boson. In the context of auxiliary particles, this concept is, however, not problematic.

Historically, the fermionic auxiliary particles are called *pseudofermions*, whereas the bosonic ones are called *slave-bosons*.

Constructing (Effective) Physical Particle-Operators from Auxiliary Particles

In the s -shell case presented above, creation- and annihilation operators of the physical electrons can be expressed fully through a linear combination of auxiliary particles by analyzing the action of c on the individual states.

$$c_\sigma |s^0\rangle = 0 \quad (5.8)$$

$$c_\sigma |s^1; \sigma'\rangle = \delta_{\sigma\sigma'} |0\rangle \quad (5.9)$$

$$c_\uparrow |s^2\rangle = c_\uparrow c_\uparrow^\dagger c_\downarrow^\dagger |0\rangle = c_\downarrow^\dagger c_\uparrow c_\uparrow^\dagger |0\rangle = |s^1; \downarrow\rangle \quad (5.10)$$

$$c_\downarrow |s^2\rangle = c_\downarrow c_\uparrow^\dagger c_\downarrow^\dagger |0\rangle = -c_\uparrow^\dagger c_\downarrow c_\downarrow^\dagger |0\rangle = -|s^1; \uparrow\rangle \quad (5.11)$$

When acting on the doubly occupied state, c_{\downarrow} produces a negative sign due to the fixed (but arbitrarily chosen) order of creation operators in the definition of $|2\rangle$. We can, therefore, conclude

$$c_{\sigma} = b^{\dagger} f_{\sigma} + \text{sgn}(\sigma) \cdot f_{\tilde{\sigma}}^{\dagger} a, \quad (5.12)$$

where $\tilde{\sigma}$ is the conjugate spin, i.e. $-\sigma$ in this case. It can also be derived by demanding the linear superposition of auxiliary particles respect the canonical commutation relations of c . The diagonal elements directly lead to $\hat{Q} = \mathbb{1}$, whereas the off-diagonal elements fix the sign of the double-occupancy term.

Let's investigate the slightly more complex case of p -shell states with occupancy p^1 , p^2 and p^3 . In anticipation of structures used later in the thesis, let's assume we have identified the lowest-lying states of each configuration and determined those to be a Kramers doublet² for p^1 and p^3 each and a spin-singlet with twofold orbital degree of freedom for p^2 . Let's assume that those states in terms of c_{σ, m_l} are given by

$$|p^1; \sigma\rangle = c_{\sigma, 0}^{\dagger} |0\rangle, \quad (5.13)$$

$$|p^2; \alpha\rangle = c_{\uparrow, \alpha}^{\dagger} c_{\downarrow, \alpha}^{\dagger} |0\rangle, \quad (5.14)$$

$$|p^3; \sigma\rangle = c_{\sigma, 0}^{\dagger} \frac{1}{\sqrt{2}} \left(c_{\uparrow, 1}^{\dagger} c_{\downarrow, 1}^{\dagger} - c_{\uparrow, -1}^{\dagger} c_{\downarrow, -1}^{\dagger} \right) |0\rangle, \quad (5.15)$$

where $\alpha = \pm 1$. We can construct an effective fermionic operator for this set of states. Due to Pauli's principle, only sets of states that have $n_{\max} - n_{\min} = 2$ can be represented by a fermionic operator³. Let's define auxiliary particles, this time representing odd occupations with bosons⁴

$$|p^1; \sigma\rangle = b_{\sigma}^{\dagger} |\text{vac}\rangle, \quad (5.16)$$

$$|p^2; \alpha\rangle = f_{\alpha}^{\dagger} |\text{vac}\rangle, \quad (5.17)$$

$$|p^3; \sigma\rangle = a_{\sigma}^{\dagger} |\text{vac}\rangle. \quad (5.18)$$

A fermionic operator describing the set of states must generally be of the form

$$d_{\sigma, \alpha} = \beta_{\sigma, \alpha} b_{\sigma}^{\dagger} f_{\alpha} + \gamma_{\sigma, \alpha} f_{\tilde{\alpha}}^{\dagger} a_{\sigma}. \quad (5.19)$$

This is a unique form since it incorporates two quantum numbers that each individually appear in initial and final states. Unfortunately, we can not use the same simple construction as above. The states d is describing are constructed in a non-trivial way from c operators. Hence, the anti-commutation relation must be used.

$$[d_{\sigma, \alpha}, d_{\sigma', \alpha'}^{\dagger}]_{+} \stackrel{!}{=} \delta_{\sigma, \sigma'} \delta_{\alpha, \alpha'}. \quad (5.20)$$

² A Kramers doublet's degeneracy is time-reversal symmetry protected [72, 73].

³ An interesting case will be presented later, where due to sending one state to infinite energies, the physical fermionic operator is faithfully represented by only two different adjacent particle numbers, leading to a couple of interesting, seemingly non-physical properties.

⁴ Again, this has no real consequence and is just done for convenience to connect it to the aforementioned case relevant later in the thesis.

This results in a set of non-trivial constraints, which is why constructing an *effective, fermionic operator* for such a set of states should be avoided, if possible.

5.1.2 Fixing the Operator Constraint $\hat{Q} = 1$

In order to control the operator constraint $\hat{Q} = 1$, a chemical potential $-\lambda$ is implemented via adding $\lambda(\hat{Q} - \mathbb{1})$ to the Hamiltonian. As mentioned above, this trick was originally introduced by Abrikosov and later refined by Barnes [37, 67, 68]. The associated grand-canonical (w.r.t. λ) density matrix is

$$\hat{\rho}_G = \frac{1}{Z_G} e^{-\beta(\hat{H} + \lambda(\hat{Q} - \mathbb{1}))}. \quad (5.21)$$

Expectation values are thus given by the usual trace over the operator of interest and $\hat{\rho}_G$, where the trace can be subdivided into the different sectors of positive-integer \hat{Q} eigenvalues

$$\langle \hat{A} \rangle = \frac{1}{Z_G} \text{Tr} \left(\hat{A} e^{-\beta(\hat{H} + \lambda(\hat{Q} - \mathbb{1}))} \right) \quad (5.22)$$

$$= \frac{1}{Z_G} \left[e^{\beta\lambda} \text{Tr} \left(\hat{A} e^{-\beta\hat{H}} \right)_{Q=0} + e^0 \text{Tr} \left(\hat{A} e^{-\beta\hat{H}} \right)_{Q=1} + e^{-\beta\lambda} \text{Tr} \left(\hat{A} e^{-\beta\hat{H}} \right)_{Q=2} + \dots \right]. \quad (5.23)$$

All observables of interest annihilate the $Q = 0$ sub-space (non-existence of an impurity), so the first term vanishes. By sending λ to infinity, all $Q > 2$ are exponentially suppressed, and one ends up with the expectation value in the $Q = 1$ sub-space. The only problem left is the grand-canonical partition function, which still takes the $Q = 0$ sub-space into account. To avoid this, expectation values must be divided by $\langle \hat{Q} \rangle_G$.

$$\begin{aligned} \lim_{\lambda \rightarrow \infty} \frac{\langle \hat{A} \rangle_G}{\langle \hat{Q} \rangle_G} &= \lim_{\lambda \rightarrow \infty} \frac{\frac{1}{Z_G} \left[e^{\beta\lambda} \text{Tr} \left(\hat{A} e^{-\beta\hat{H}} \right)_{Q=0} + e^0 \text{Tr} \left(\hat{A} e^{-\beta\hat{H}} \right)_{Q=1} + e^{-\beta\lambda} \text{Tr} \left(\hat{A} e^{-\beta\hat{H}} \right)_{Q=2} + \dots \right]}{\frac{1}{Z_G} \left[e^{\beta\lambda} \text{Tr} \left(\hat{Q} e^{-\beta\hat{H}} \right)_{Q=0} + e^0 \text{Tr} \left(\hat{Q} e^{-\beta\hat{H}} \right)_{Q=1} + e^{-\beta\lambda} \text{Tr} \left(\hat{Q} e^{-\beta\hat{H}} \right)_{Q=2} + \dots \right]} \\ &= \frac{\text{Tr} \left(\hat{A} e^{-\beta\hat{H}} \right)_{Q=1}}{\text{Tr} \left(\hat{Q} e^{-\beta\hat{H}} \right)_{Q=1}} = \frac{\text{Tr} \left(\hat{A} e^{-\beta\hat{H}} \right)_{Q=1}}{\text{Tr} \left(e^{-\beta\hat{H}} \right)_{Q=1}} = \frac{\text{Tr} \left(\hat{A} e^{-\beta\hat{H}} \right)_{Q=1}}{Z_{C,Q=1}} = \langle \hat{A} \rangle_{C,Q=1} \end{aligned} \quad (5.24)$$

Utilizing the fact that the trace over all $Q = 1$ states is in an eigenbasis of \hat{Q} , the operator is replaced by the eigenvalue in the second step of the last line. The trace in the denominator is nothing else than the canonical partition function in the $Q = 1$ sub-space so that the whole expression is identical to the canonical expectation value in this sub-space, which is the physical expectation value.

Fixing the Constraint for Path Integrals

The same can be elegantly achieved for path integrals. Using the Fourier representation of the Dirac delta-distribution

$$\delta(Q - 1) = \int_{-\infty}^{\infty} d\lambda e^{i(Q-1)\lambda} \quad (5.25)$$

any given path-integral with physical field ψ, \dots and auxiliary fields b, \dots can be extended by this condition via

$$\int \mathcal{D}[\psi, \bar{\psi}, b, \bar{b}, \dots] e^{-S[\psi, \bar{\psi}, b, \bar{b}, \dots]} \rightarrow \int \mathcal{D}[\psi, \bar{\psi}, \lambda, \dots] e^{-S[\psi, \bar{\psi}, b, \bar{b}, \dots] - S_{Q-1}[b, \bar{b}, \lambda, \dots]}, \quad (5.26)$$

$$S_{Q-1}[b, \bar{b}, \lambda, \dots] = \int_0^\beta d\tau \lambda \cdot (Q[b, \bar{b}, \dots] - 1). \quad (5.27)$$

5.1.3 The Single-Impurity Anderson Model with Auxiliary Particles

We can now construct an auxiliary-particle representation for the single-impurity Anderson model with Hubbard operators (Eq. (5.1)) via

$$|d^0\rangle = b^\dagger |\text{vac}\rangle, \quad (5.28)$$

$$|d^1; \sigma\rangle = f_\sigma^\dagger |\text{vac}\rangle, \quad (5.29)$$

$$|d^2\rangle = a^\dagger |\text{vac}\rangle, \quad (5.30)$$

and with $d_\sigma = b^\dagger f_\sigma + \text{sgn}(\sigma) \cdot f_\sigma^\dagger a$ (c.f. Eq. (5.12)). The Hamiltonian, in terms of auxiliary particles, is

$$\begin{aligned} H_{\text{SIAM}} = & \sum_{\vec{k}, \sigma} \left(\varepsilon_{\vec{k}}^c - \mu \right) c_{\vec{k}\sigma}^\dagger c_{\vec{k}\sigma} + \sum_{\sigma} \left(\varepsilon^d - \mu + \lambda \right) f_\sigma^\dagger f_\sigma + \lambda b^\dagger b + \left(\varepsilon^a - 2\mu + \lambda \right) a^\dagger a \\ & + \sum_{\vec{k}, \sigma} \left(V_{\vec{k}} c_{\vec{k}\sigma}^\dagger b^\dagger f_\sigma + V_{\vec{k}} \text{sgn}(\sigma) c_{\vec{k}\sigma}^\dagger f_\sigma^\dagger a + h.c. \right) - \lambda, \end{aligned} \quad (5.31)$$

with $\varepsilon^a = U + 2\varepsilon^d$. The interacting (quartic) part of the Hamiltonian is transformed into a quadratic part at the cost of adding two bosons, which can be treated with field-theoretical methods. In contrast to expansion in U , this model is suitable for an expansion in V , allowing for a simultaneously faithful description of the strongly interacting and the weakly interacting regime.

Remarkably, the $U \rightarrow \infty$ limit can now also be taken in a controlled way, effectively removing the double-occupation boson a from the Hamiltonian. This would have posed a great complication in the original Hamiltonian, where a large U leads to problems in perturbation theory. A description in terms of Hubbard operators would have been necessary, which is problematic due to the non-canonical commutation relations. The auxiliary-particle representation⁵ is a clever way of dealing with exactly this situation. A method of solving this model is presented in the next section.

5.2 The Luttinger-Ward Functional

Field theoretical approximations often expand self-energies in contributions from free Green functions alone. While being beneficial in only using the free Green function, which is typically exactly known, incomplete expansions can lead to broken conservation laws. Alternatively, a conserving approximation can be pursued with infinite summations of specific classes of diagrams. Such

⁵ The representation used by Barnes is especially tailored to the SIAM and works best in the strongly interacting limit.

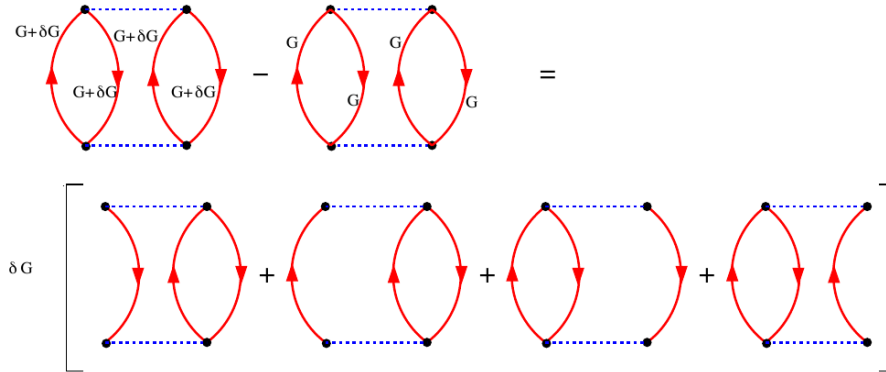


Figure 5.1: Illustration of the variation of a Green function in terms of Feynman diagrams, taken from [74]. The missing line comes from the factoring out of the variation δG .

approximations can be efficiently generated from the Luttinger-Ward functional (LW) [59]. Deriving this function exactly is a tedious procedure and not essential in the context of this thesis. I will, therefore, present a heuristic derivation without proofs⁶, closely following [74].

The Luttinger-Ward functional $\Phi[\mathbf{G}]$ can be understood as an object assigning a number to a Green function via a summation over all closed, connected, two-particle irreducible (2PI) skeleton diagrams of the full Green functions. In other words, the diagrams have no external lines, they don't factorize, they don't fall apart by cutting two lines, no Green function contains self-energy insertions, only bare vertices are considered, and all appearing lines are full Green functions, i.e. they are renormalized by their full self-energy. Each diagram in the sum is multiplied by a factor $-1/S$, where S is the symmetry of the individual diagrams. It is a combinatorial factor counting the ways how a diagram can be constructed by permitting and relabeling vertices and propagators. This removes double counting from the construction.

Self-energies, on the other hand, are generated by connected single-particle irreducible (1PI) skeleton diagrams with a single entry- and a single exit point. Hence, just by comparing the definitions, the structure of a self-energy diagram can be obtained from the Luttinger-Ward functional by cutting a single line and using the resulting stumps as entry- and exit points. Due to the LW being a functional of Green functions, derivatives with respect to the same are well defined. Diagrammatically, this can be understood as cutting a Green function line, as illustrated in Fig. 5.1. The figure shows how the differentiation works in terms of diagrams by taking the difference between a diagram of $\mathbf{G} + \delta\mathbf{G}$ and the same diagram of \mathbf{G} . Due to such a diagram representing the product of Green functions, the lowest order in $\delta\mathbf{G}$ can be represented as removing a line from the diagram, summing up all possible choices.

Variation with respect to a function replaces the respective function in the functional by delta functions of each quantum number, e.g. $\delta\Phi/\delta\mathbf{G}_{a,b}(i\omega_n) = \Sigma_{b,a}(i\omega_n)$. The indices need to be switched under differentiation, which can be easily understood from the directionality of Green function lines; $\mathbf{G}_{a,b}$ links b to a , hence b is the exit of a vertex and a the entry point, necessitating the structure $\Sigma_{b,a}$. Within the Matsubara Green function technique, each sum over a Matsubara frequency is accompanied by a factor $1/\beta$. The differentiation fixes the Matsubara frequency, resolving the sum but leaving the prefactor behind. Lastly, the factor $-1/S$ cancels the degeneracy in which line to cut

⁶ For a nice discussion of the two-particle irreducible effective action from which this can be derived, see [75].

under differentiation and the minus sign accounts for the reduced number of Fermion loops when cutting a Fermion line. This results in the relation

$$\frac{\delta\Phi[\mathbf{G}]}{\delta G_{a,b}(i\omega_n)} = \pm \frac{1}{\beta} \Sigma_{b,a}(i\omega_n), \quad (5.32)$$

where the plus sign is for fermions⁷.

⁷ This is not contradictory to what was argued before due to an overall minus sign in the definition of the functional.

5.3 The Non-Crossing Approximation

Now that the Hamiltonian (Eq. (5.31)) is set up, a diagrammatic expansion of the field theory can be constructed [69–71]. It contains four different particle species, connected via two types of three-point hybridization vertices (c.f. Fig. 5.2). Each vertex preserves momentum, spin and Matsubara frequency, each line represents a (full) Green function. Following [76], a perturbation series in terms of $V/D \ll 1$ is calculated to lowest order, with D being the bandwidth of the conduction-electron band. Logarithmic divergences in the perturbation series are circumvented by selection and summation of the most relevant terms. This is done in the framework of a conserving approximation from a Luttinger-Ward functional Φ [77], represented as the diagram in Fig. 5.3. Auxiliary-particle self-energies $\Sigma_{b/f/a}$ are then given by functional derivatives of Φ w.r.t. the respective propagators, where Φ evaluates to

$$\Phi = -\frac{1}{\beta^2} \sum_{i\nu_n} \sum_{\sigma, \sigma'} \sum_{\vec{k}, \vec{k}'} V_{\vec{k}} V_{\vec{k}'}^* G_{\sigma' \sigma}^c(i\nu_n; \vec{k}', \vec{k}) \left[G_{\sigma \sigma'}^f(i\mu_m + i\nu_n) G^b(i\mu_m) - G_{-\sigma', -\sigma}^f(i\mu_m - i\nu_n) G^a(i\mu_m) \right]. \quad (5.33)$$

The relative minus sign comes from the lack of fermion loops in the second diagram. Here and henceforth, fermionic Matsubara frequencies have a subscript n and bosonic ones a subscript m . In a diagrammatic representation, taking derivatives is represented by cutting the respective propagator line. All diagrams that appear show no crossing lines, hence the name "non-crossing approximation" (NCA).

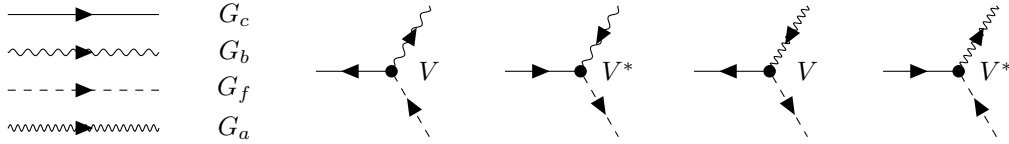


Figure 5.2: Simplified Feynman rules for the single-impurity Anderson model with auxiliary particles, c.f. Eq. (5.31).

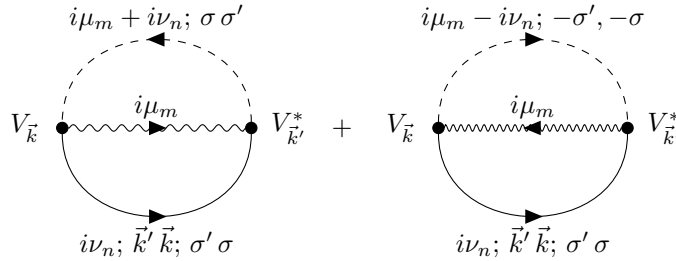


Figure 5.3: Diagrammatic representation of the Luttinger-Ward functional for the SIAM in terms of auxiliary particles with the convention of quantum numbers associated with the creation operator appearing first, those associated with the annihilation operator second.

5.3.1 Conduction-Electron Self-Energy

The conduction electron self-energy in Fig. 5.4 is to be calculated first since it will give rise to a great simplification of the following calculations. In order to evaluate the Matsubara sum, a contour integral in complex frequency space over the Green functions times the Bose distribution function n_b is used [49].

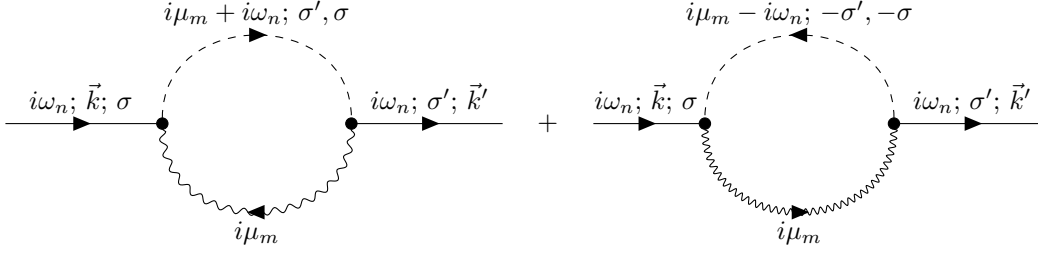


Figure 5.4: Diagrammatic representation of the conduction electron self-energy. The incoming and outgoing lines are just shown for bookmarking of the conserved quantities.

Utilizing a matrix notation in spin-space (bold objects are matrices), the first diagram evaluates to

$$\Sigma_{1; \vec{k}' \vec{k}}^c(i\omega_n) = -V_{\vec{k}} V_{\vec{k}'}^* \frac{1}{\beta} \sum_{i\mu_m} \mathbf{G}^f(i\mu_m + i\omega_n) G^b(i\mu_m) \quad (5.34)$$

$$= -V_{\vec{k}} V_{\vec{k}'}^* \oint \frac{dz}{2\pi i} n_B(z) \mathbf{G}^f(z + i\omega_n) G^b(z) \quad (5.35)$$

$$= -V_{\vec{k}} V_{\vec{k}'}^* \int_{-\infty}^{\infty} \frac{d\varepsilon}{2\pi i} \left\{ n_B(\varepsilon) \mathbf{G}^f(\varepsilon + i\omega_n) \left[G^b(\varepsilon + i\eta) - G^b(\varepsilon - i\eta) \right] \right. \\ \left. + n_B(\varepsilon - i\omega_n) \left[\mathbf{G}^f(\varepsilon + i\eta) - \mathbf{G}^f(\varepsilon - i\eta) \right] G^b(\varepsilon - i\omega_n) \right\}, \quad (5.36)$$

where $\eta > 0$ is an infinitesimal number. The contour for evaluating the Matsubara sum is shown in Fig. 5.5. The shifted Bose function $n_B(\varepsilon - i\omega_n)$ is just the negative Fermi function, which can be shown via $e^{i\omega_n} = -1$ (fermionic Matsubara frequency):

$$n_{F/B}(\varepsilon - i\omega_n) = \left(e^{\beta(\varepsilon - i\omega_n)} \pm 1 \right)^{-1} = \left(e^{\beta\varepsilon} e^{-i\omega_n\beta} \pm 1 \right)^{-1} \quad (5.37)$$

$$= \left(-e^{\beta\varepsilon} \pm 1 \right)^{-1} = -n_{B/F}(\varepsilon). \quad (5.38)$$

By identifying $G(\varepsilon \pm i\eta) = G^{R/A}(\varepsilon)$, the advanced and retarded Green functions, the Spectral function can be substituted via

$$G^R(\varepsilon) - G^A(\varepsilon) = 2i \text{Im} G^R(\varepsilon) = -2\pi i A(\varepsilon). \quad (5.39)$$

Carrying out the substitution, the diagram evaluates to

$$\Sigma_1^c(i\omega_n) = V_{\vec{k}} V_{\vec{k}'}^* \int_{-\infty}^{\infty} d\varepsilon \left\{ n_B(\varepsilon) \mathbf{G}^f(\varepsilon + i\omega_n) A^b(\varepsilon) - n_F(\varepsilon) \mathbf{A}^f(\varepsilon) G^b(\varepsilon - i\omega_n) \right\}. \quad (5.40)$$

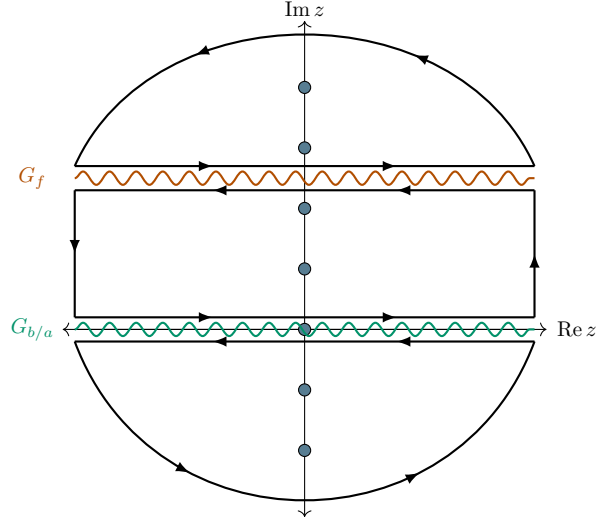


Figure 5.5: Contour for evaluating the Matsubara-sum in the conduction-electron self-energy. Curly lines visualize the branch cuts of the respective Green functions. Bosonic Matsubara frequencies are shown as blue dots.

In order to take the limit $\lambda \rightarrow \infty$, all explicit λ -dependencies should be treated. Since λ is a chemical potential for the auxiliary particles, it appears only as an energy shift, which can be removed explicitly via $\omega \rightarrow \omega' = \omega - \lambda$ such that

$$G^f(\omega) = \frac{1}{\omega - \lambda - (\varepsilon^d - \mu) - \Sigma^f(\sigma, \omega)} \Rightarrow G^f(\omega') = \frac{1}{\omega' - (\varepsilon^d - \mu) - \Sigma^f(\sigma, \omega' + \lambda)}, \quad (5.41)$$

$$G^a(\omega) = \frac{1}{\omega - \lambda - (\varepsilon^a - 2\mu) - \Sigma^a(\omega)} \Rightarrow G^a(\omega') = \frac{1}{\omega' - (\varepsilon^a - 2\mu) - \Sigma^a(\omega' + \lambda)}, \quad (5.42)$$

$$G^b(\omega) = \frac{1}{\omega - \lambda - \Sigma^b(\omega)} \Rightarrow G^b(\omega') = \frac{1}{\omega' - \Sigma^b(\omega' + \lambda)}, \quad (5.43)$$

with $\varepsilon^a = U + 2\varepsilon^d$ as defined in the Hamiltonian (Eq. (5.31)). The quantum numbers have been intentionally omitted, and fractions have to be understood as matrix-inversion in the most general case. This construction redefines the energy argument to be in the reference frame with respect to λ . The dependency in the conduction-electron self-energy can thus be removed by applying $\varepsilon \rightarrow \varepsilon' = \varepsilon - \lambda$ in the integrals:

$$\Sigma_1^c(i\omega_n) = V_{\vec{k}} V_{\vec{k}'}^* \int_{-\infty}^{\infty} d\varepsilon' \left\{ n_B(\varepsilon' + \lambda) \mathbf{G}^f(\varepsilon' + \lambda + i\omega_n) \mathbf{A}^b(\varepsilon' + \lambda) - n_F(\varepsilon' + \lambda) \mathbf{A}^f(\varepsilon' + \lambda) \mathbf{G}^b(\varepsilon' + \lambda - i\omega_n) \right\}. \quad (5.44)$$

The only remaining λ -dependence is in the distribution functions. Upon taking the infinity limit, both

vanish exponentially:

$$n_{F/B}(\varepsilon' + \lambda) = \left(e^{\beta\varepsilon'} e^{\beta\lambda} \pm 1 \right)^{-1} \quad (5.45)$$

$$= e^{-\beta\lambda} \left(e^{\beta\varepsilon'} \pm e^{-\beta\lambda} \right)^{-1} \xrightarrow{\lambda \gg 1} e^{-\beta\lambda} e^{-\beta\varepsilon'} \xrightarrow{\lambda \rightarrow \infty} 0. \quad (5.46)$$

For the second diagram, in order to use the same matrix notation, we need to define a spin-flipped matrix-Green-function

$$\left(\bar{\mathbf{G}} \right)_{\sigma'\sigma} = \left(\mathbf{G} \right)_{-\sigma', -\sigma}. \quad (5.47)$$

The second diagram can then be evaluated to

$$\Sigma_2^c(i\omega_n) = V_{\vec{k}} V_{\vec{k}'}^* \frac{1}{\beta} \sum_{i\mu_m} \bar{\mathbf{G}}^f(i\mu_m - i\omega_n) G^a(i\mu_m) \quad (5.48)$$

$$= V_{\vec{k}} V_{\vec{k}'}^* \oint \frac{dz}{2\pi i} n_B(z) \bar{\mathbf{G}}^f(z - i\omega_n) G^a(z) \quad (5.49)$$

$$= V_{\vec{k}} V_{\vec{k}'}^* \int_{-\infty}^{\infty} \frac{d\varepsilon}{2\pi i} \left\{ n_B(\varepsilon) \bar{\mathbf{G}}^f(\varepsilon - i\omega_n) [G^a(\varepsilon + i\eta) - G^a(\varepsilon - i\eta)] \right. \\ \left. + n_B(\varepsilon + i\omega_n) [\bar{\mathbf{G}}^f(\varepsilon + i\eta) - \bar{\mathbf{G}}^f(\varepsilon - i\eta)] G^a(\varepsilon + i\omega_n) \right\}. \quad (5.50)$$

Following the same steps as before, one gets

$$\Sigma_{2; \vec{k}, \vec{k}'}^c(i\omega_n) = -V_{\vec{k}} V_{\vec{k}'}^* \int_{-\infty}^{\infty} d\varepsilon' \left\{ n_B(\varepsilon' + \lambda) \bar{\mathbf{G}}^f(\varepsilon' + \lambda - i\omega_n) A^a(\varepsilon' + \lambda) \right. \\ \left. - n_F(\varepsilon' + \lambda) \bar{\mathbf{A}}^f(\varepsilon' + \lambda) G^a(\varepsilon' + \lambda + i\omega_n) \right\}. \quad (5.51)$$

This vanishes under $\lambda \rightarrow \infty$ for the same reasons as Σ_1^c .

In any grand-canonical calculation (w.r.t. λ), conduction electron Green functions can, therefore, be replaced by free conduction-electron Green functions, greatly simplifying the complexity of the following calculations.

5.3.2 Impurity Green Function

Although vanishing in the limit $\lambda \rightarrow \infty$, the previous calculations can be recycled for the conduction-electron T -matrix. Already defined in the context of previously discussed models (c.f. Eq (2.102)), the T -matrix for the conduction electrons is the *full* impurity Green function with hybridization-vertices attached on both sides

$$\mathbf{G}_{\vec{k}'\vec{k}}^c(\omega) = \delta_{\vec{k}',\vec{k}} \mathbf{G}_{\vec{k}}^c(0)(\omega) + \mathbf{G}_{\vec{k}'}^c(0)(\omega) V_{\vec{k}'} \mathbf{G}^d(\omega) V_{\vec{k}} \mathbf{G}_{\vec{k}}^c(0)(\omega) \quad (5.52)$$

$$= \delta_{\vec{k}',\vec{k}} \mathbf{G}_{\vec{k}}^c(0)(\omega) + \mathbf{G}_{\vec{k}'}^c(0)(\omega) \mathbf{T}_{\vec{k}'\vec{k}}^d(\omega) \mathbf{G}_{\vec{k}}^c(0)(\omega). \quad (5.53)$$

The diagram describing the T -matrix is exactly the same as for the conduction-electron self-energy from before (Fig. 5.4) with the difference that it should be evaluated in the canonical ensemble, as discussed in Sec. 5.1.2. It therefore must be divided by $\langle Q \rangle_G$, which is

$$\langle \hat{Q} \rangle_G = \int_{-\infty}^{\infty} d\varepsilon \left[n_B(\varepsilon) \left(A^b(\varepsilon) + A^a(\varepsilon) \right) + n_F(\varepsilon) \sum_{\sigma} A_{\sigma\sigma}^f(\varepsilon) \right] \quad (5.54)$$

$$= \int_{-\infty}^{\infty} d\varepsilon' \left[n_B(\varepsilon' + \lambda) \left(A^b(\varepsilon' + \lambda) + A^a(\varepsilon' + \lambda) \right) + n_F(\varepsilon' + \lambda) \sum_{\sigma} A_{\sigma\sigma}^f(\varepsilon' + \lambda) \right] \quad (5.55)$$

$$= e^{-\beta\lambda} \int_{-\infty}^{\infty} d\varepsilon' \left[\frac{A^b(\varepsilon' + \lambda) + A^a(\varepsilon' + \lambda)}{e^{\beta\varepsilon'} - e^{-\beta\lambda}} + \frac{\sum_{\sigma} A_{\sigma\sigma}^f(\varepsilon' + \lambda)}{e^{\beta\varepsilon'} + e^{-\beta\lambda}} \right]. \quad (5.56)$$

The reduction of all distribution functions to the Boltzmann factor highlights the irrelevancy of the choice of auxiliary-particle statistics. The prefactor $e^{-\beta\lambda}$ exactly cancels the corresponding term that appears in the previously derived equations, resulting in a non-vanishing expression for the T -matrix

$$\mathbf{G}_1^d(i\omega_n) = \lim_{\lambda \rightarrow \infty} \frac{e^{-\beta\lambda} \int_{-\infty}^{\infty} d\varepsilon' \left\{ \frac{\mathbf{G}^f(\varepsilon' + i\omega_n + \lambda) A^b(\varepsilon' + \lambda)}{e^{\beta\varepsilon'} - e^{-\beta\lambda}} - \frac{\mathbf{A}^f(\varepsilon' + \lambda) \mathbf{G}^b(\varepsilon' - i\omega_n + \lambda)}{e^{\beta\varepsilon'} + e^{-\beta\lambda}} \right\}}{e^{-\beta\lambda} \int_{-\infty}^{\infty} d\varepsilon' \left[\frac{A^b(\varepsilon' + \lambda) + A^a(\varepsilon' + \lambda)}{e^{\beta\varepsilon'} - e^{-\beta\lambda}} + \frac{\sum_{\sigma} A_{\sigma\sigma}^f(\varepsilon' + \lambda)}{e^{\beta\varepsilon'} + e^{-\beta\lambda}} \right]} \quad (5.57)$$

$$= \frac{\int_{-\infty}^{\infty} d\varepsilon' e^{-\beta\varepsilon'} \left\{ \mathbf{G}^f(\varepsilon' + i\omega_n) A^b(\varepsilon') - \mathbf{A}_{\sigma\sigma}^f(\varepsilon') \mathbf{G}^b(\varepsilon' - i\omega_n) \right\}}{\int_{-\infty}^{\infty} d\varepsilon' e^{-\beta\varepsilon'} \left[A^b(\varepsilon') + A^a(\varepsilon') + \sum_{\sigma} A_{\sigma\sigma}^f(\varepsilon') \right]}, \quad (5.58)$$

where the Green functions and spectral functions in the last step have been replaced by the reference-energy λ ones from above. In order to calculate the (advanced) Green function⁸ in physical frequency space, $i\omega_n$ is replaced by $\omega - i\eta$ and the imaginary part is taken

$$\text{Im } \mathbf{G}_1^{dA}(\omega) = \pi \frac{\int_{-\infty}^{\infty} d\varepsilon e^{-\beta\varepsilon} \left\{ \mathbf{A}^f(\varepsilon + \omega) A^b(\varepsilon) + \mathbf{A}^f(\varepsilon) A^b(\varepsilon - \omega) \right\}}{\int_{-\infty}^{\infty} d\varepsilon e^{-\beta\varepsilon} \left[A^b(\varepsilon) + A^a(\varepsilon) + \sum_{\sigma} A_{\sigma\sigma}^f(\varepsilon) \right]}. \quad (5.59)$$

⁸ The reason for taking the advanced one is that imaginary parts are often strictly positive. The choice is just for convenience; we could have taken the retarded ones equally well.

Note that the sign change in the second term arises from the fact that in the slave-boson Green function, the external frequency $i\omega_n$ enters with a negative sign. Thus, G^b is the retarded function if G^d is chosen to be advanced since the sign of the infinitesimal imaginary offset is reversed. A substitution of $\varepsilon' = \varepsilon - \omega$ in the second term and relabeling $\varepsilon' \rightarrow \varepsilon$ gives

$$\text{Im } \mathbf{G}_1^{dA}(\omega) = \pi \frac{\int_{-\infty}^{\infty} d\varepsilon e^{-\beta\varepsilon} (1 + e^{-\beta\omega}) \mathbf{A}^f(\varepsilon + \omega) A^b(\varepsilon)}{\int_{-\infty}^{\infty} d\varepsilon e^{-\beta\varepsilon} [A^b(\varepsilon) + A^a(\varepsilon) + \sum_{\sigma} A_{\sigma\sigma}^f(\varepsilon)]}. \quad (5.60)$$

Equivalently, the second term is

$$\text{Im } \mathbf{G}_2^{dA}(\omega) = \pi \frac{\int_{-\infty}^{\infty} d\varepsilon e^{-\beta\varepsilon} \left\{ \bar{\mathbf{A}}^f(\varepsilon - \omega) A^a(\varepsilon) + \bar{\mathbf{A}}^f(\varepsilon) A^a(\varepsilon + \omega) \right\}}{\int_{-\infty}^{\infty} d\varepsilon e^{-\beta\varepsilon} [A^b(\varepsilon) + A^a(\varepsilon) + \sum_{\sigma} A_{\sigma\sigma}^f(\varepsilon)]} \quad (5.61)$$

$$= \pi \frac{\int_{-\infty}^{\infty} d\varepsilon e^{-\beta\varepsilon} (1 + e^{\beta\omega}) \bar{\mathbf{A}}^f(\varepsilon - \omega) A^a(\varepsilon)}{\int_{-\infty}^{\infty} d\varepsilon e^{-\beta\varepsilon} [A^b(\varepsilon) + A^a(\varepsilon) + \sum_{\sigma} A_{\sigma\sigma}^f(\varepsilon)]}. \quad (5.62)$$

The real part can then be obtained from the Kramers-Kronig relation [78, 79] and the full Green function is the sum $\mathbf{G}^d = \mathbf{G}_1 + \mathbf{G}_2$.

5.3.3 Auxiliary-Particle Self-Energies

The auxiliary-particle self-energies need to be evaluated in the grand-canonical ensemble but under $\lambda \rightarrow \infty$. It was already shown above that, in this case, the conduction-electron Green function reduces to the free one. Due to Matsubara sums of two Green functions with one being shifted by an external, fixed Matsubara frequency, two terms always appear. This was already the case for the calculations above. The projection will suppress one of two terms in the self-energy diagrams to zero, reducing the complexity further.

The full self-energies of the auxiliary particles, therefore, depend on the free conduction-electron Green function and full Green functions of different auxiliary-particle flavor. The final result will consequently be a self-consistent set of equations of only auxiliary particles. Each self-energy is derived in detail below.

Pseudofermion f Self-Energy

The Feynman diagrams representing the pseudofermion self-energy are shown in Fig. 5.6.

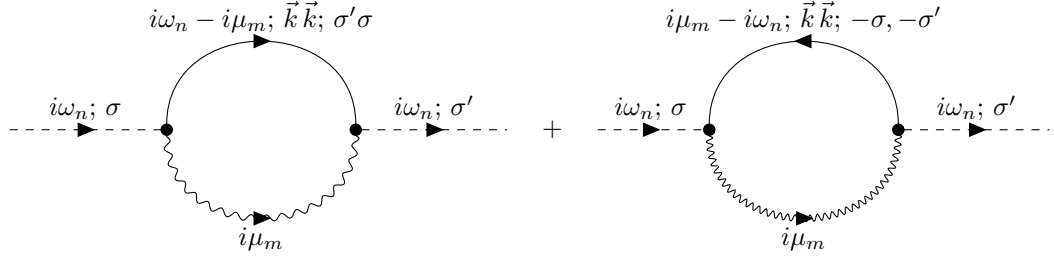


Figure 5.6: Diagrammatic representation of the pseudofermion self-energy.

Following the same steps as before, the first diagram evaluates to

$$\Sigma_1^f(i\omega_n) = -\frac{1}{\beta} \sum_{i\mu_m} \sum_{\vec{k}} |V_{\vec{k}}|^2 \mathbf{G}_{\vec{k}\vec{k}}^c(i\omega_n - i\mu_m) G^b(i\mu_m) \quad (5.63)$$

$$= -\oint \frac{dz}{2\pi i} n_B(z) \sum_{\vec{k}} |V_{\vec{k}}|^2 \mathbf{G}_{\vec{k}\vec{k}}^c(i\omega_n - z) G^b(z) \quad (5.64)$$

$$= -\int_{-\infty}^{\infty} \frac{d\varepsilon}{2\pi i} \sum_{\vec{k}} |V_{\vec{k}}|^2 \left\{ n_B(\varepsilon) \mathbf{G}_{\vec{k}\vec{k}}^c(i\omega_n - \varepsilon) \left[G^b(\varepsilon + i\eta) - G^b(\varepsilon - i\eta) \right] \right. \\ \left. - n_B(i\omega_n - \varepsilon) \left[\mathbf{G}_{\vec{k}\vec{k}}^c(\varepsilon + i\eta) - \mathbf{G}_{\vec{k}\vec{k}}^c(\varepsilon - i\eta) \right] G^b(i\omega_n - \varepsilon) \right\} \quad (5.65)$$

$$= \int_{-\infty}^{\infty} d\varepsilon \sum_{\vec{k}} |V_{\vec{k}}|^2 \left\{ n_B(\varepsilon) \mathbf{G}_{\vec{k}\vec{k}}^c(i\omega_n - \varepsilon) A^b(\varepsilon) + n_F(-\varepsilon) \mathbf{A}_{\vec{k}\vec{k}}^c(\varepsilon) G^b(i\omega_n - \varepsilon) \right\}. \quad (5.66)$$

The negative sign in the second term stems from the integration over $\varepsilon = i\omega_n - z \Leftrightarrow z = i\omega_n - \varepsilon$, which introduces a jacobian of -1 to the integral⁹. The integration contour used in the second line is shown in Fig. 5.7. In order to extract the λ -dependence, the external frequency needs to be shifted

⁹ This can also be understood as the contour being traversed in opposite direction in this case.

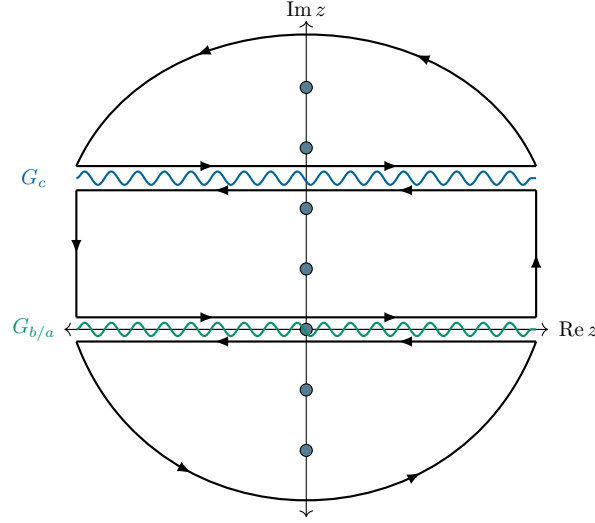


Figure 5.7: Contour for evaluating the Matsubara-sum in the pseudofermion self-energy. Curly lines visualize branch cuts of the respective Green functions. Bosonic Matsubara frequencies are shown as blue dots.

$i\omega_n \rightarrow i\omega'_n = i\omega_n - \lambda$ such that

$$\begin{aligned} \Sigma_1^f(i\omega'_n + \lambda) = \int_{-\infty}^{\infty} d\varepsilon \sum_{\vec{k}} |V_{\vec{k}}|^2 \left\{ n_B(\varepsilon) \mathbf{G}_{\vec{k}\vec{k}}^c(i\omega'_n + \lambda - \varepsilon) A^b(\varepsilon) \right. \\ \left. + n_F(-\varepsilon) \mathbf{A}_{\vec{k}\vec{k}}^c(\varepsilon) G^b(i\omega'_n + \lambda - \varepsilon) \right\}. \end{aligned} \quad (5.67)$$

Note that the external frequency now exactly matches the one in equation (5.41) and the argument of G^b in the second line is compatible with Eq. (5.43). Before we can take the limit, though, the first term needs to be modified to shift λ from the conduction electron to the slave-bosons. This is achieved by shifting the internal energy ε via $\varepsilon \rightarrow \varepsilon' = \varepsilon - \lambda$ such that

$$\begin{aligned} \Sigma_1^f(i\omega'_n + \lambda) = \sum_{\vec{k}} |V_{\vec{k}}|^2 \left\{ \int_{-\infty}^{\infty} d\varepsilon' n_B(\varepsilon' + \lambda) A^b(\varepsilon' + \lambda) \mathbf{G}_{\vec{k}\vec{k}}^c(i\omega'_n - \varepsilon') \right. \\ \left. + \int_{-\infty}^{\infty} d\varepsilon n_F(-\varepsilon) G^b(i\omega'_n + \lambda - \varepsilon) \mathbf{A}_{\vec{k}\vec{k}}^c(\varepsilon) \right\}. \end{aligned} \quad (5.68)$$

Using

$$n_F(-\varepsilon) = \frac{1}{e^{-\beta\varepsilon} + 1} = \frac{e^{\beta\varepsilon}}{1 + e^{\beta\varepsilon}} \quad (5.69)$$

$$= \frac{e^{\beta\varepsilon} + 1 - 1}{e^{\beta\varepsilon} + 1} = 1 - \frac{1}{e^{\beta\varepsilon} + 1} = 1 - n_F(\varepsilon), \quad (5.70)$$

the expression can be re-written as

$$\begin{aligned} \Sigma_1^f(i\omega'_n + \lambda) = \sum_{\vec{k}} |V_{\vec{k}}|^2 \left\{ \int_{-\infty}^{\infty} d\varepsilon' n_B(\varepsilon' + \lambda) A^b(\varepsilon' + \lambda) \mathbf{G}_{\vec{k}\vec{k}}^c(i\omega'_n - \varepsilon') \right. \\ \left. + \int_{-\infty}^{\infty} d\varepsilon (1 - n_F(\varepsilon)) G^b(i\omega'_n + \lambda - \varepsilon) \mathbf{A}_{\vec{k}\vec{k}}^c(\varepsilon) \right\}. \end{aligned} \quad (5.71)$$

Upon taking the limit $\lambda \rightarrow \infty$, $n_B(\varepsilon' + \lambda) \rightarrow 0$ exponentially, as shown before. Furthermore, the conduction-electron density of states reduces to the free one. The final expression reads

$$\Sigma_1^f(i\omega'_n + \lambda) = \int_{-\infty}^{\infty} d\varepsilon (1 - n_F(\varepsilon)) G^b(i\omega_n - \varepsilon) \sum_{\vec{k}} |V_{\vec{k}}|^2 \mathbf{A}_{\vec{k}\vec{k}}^c(0)(\varepsilon), \quad (5.72)$$

where the slave-boson Green function and the self-energy have been replaced by the reference-frame λ ones, allowing for dropping the explicit λ in the arguments, as well as the prime in $i\omega'_n$. Taking the imaginary part of the advanced self-energy yields

$$\text{Im} \Sigma_1^{fA}(\omega) = \pi \int_{-\infty}^{\infty} d\varepsilon (1 - n_F(\varepsilon)) A^b(\omega - \varepsilon) \sum_{\vec{k}} |V_{\vec{k}}|^2 \mathbf{A}_{\vec{k}\vec{k}}^c(0)(\varepsilon) \quad (5.73)$$

The same must now also be done for the second diagram

$$\Sigma_2^f(i\omega_n) = \frac{1}{\beta} \sum_{i\mu_m} \sum_{\vec{k}} |V_{\vec{k}}|^2 \bar{\mathbf{G}}_{\vec{k}\vec{k}}^c(i\mu_m - i\omega_n) G^a(i\mu_m) \quad (5.74)$$

$$= \oint \frac{dz}{2\pi i} n_B(z) \sum_{\vec{k}} |V_{\vec{k}}|^2 \bar{\mathbf{G}}_{\vec{k}\vec{k}}^c(z - i\omega_n) G^a(z) \quad (5.75)$$

$$\begin{aligned} = \int_{-\infty}^{\infty} \frac{d\varepsilon}{2\pi i} \sum_{\vec{k}} |V_{\vec{k}}|^2 \left\{ n_B(\varepsilon) \bar{\mathbf{G}}_{\vec{k}\vec{k}}^c(\varepsilon - i\omega_n) [G^a(\varepsilon + i\eta) - G^a(\varepsilon - i\eta)] \right. \\ \left. + n_B(\varepsilon + i\omega_n) \left[\bar{\mathbf{G}}_{\vec{k}\vec{k}}^c(\varepsilon + i\eta) - \bar{\mathbf{G}}_{\vec{k}\vec{k}}^c(\varepsilon - i\eta) \right] G^a(\varepsilon + i\omega_n) \right\} \end{aligned} \quad (5.76)$$

$$= \int_{-\infty}^{\infty} d\varepsilon \sum_{\vec{k}} |V_{\vec{k}}|^2 \left\{ -n_B(\varepsilon) \bar{\mathbf{G}}_{\vec{k}\vec{k}}^c(\varepsilon - i\omega_n) A^a(\varepsilon) + n_F(\varepsilon) \bar{\mathbf{A}}_{\vec{k}\vec{k}}^c(\varepsilon) G^a(\varepsilon + i\omega_n) \right\}. \quad (5.77)$$

Taking the same steps as above, i.e. $i\omega_n = \omega + i\eta + \lambda$, substituting $\varepsilon' = \varepsilon - \lambda$ in the first term, sending $\lambda \rightarrow \infty$ and finally relabeling for convenience results in

$$\text{Im} \Sigma_2^{fA}(\omega) = \pi \int_{-\infty}^{\infty} d\varepsilon n_F(\varepsilon) A^a(\varepsilon + \omega) \sum_{\vec{k}} |V_{\vec{k}}|^2 \bar{\mathbf{A}}_{\vec{k}\vec{k}}^c(0)(\varepsilon). \quad (5.78)$$

Slave-Boson b Self-Energy

The Feynman diagram representing the self-energy of the slave-boson b is shown in Fig. 5.8.

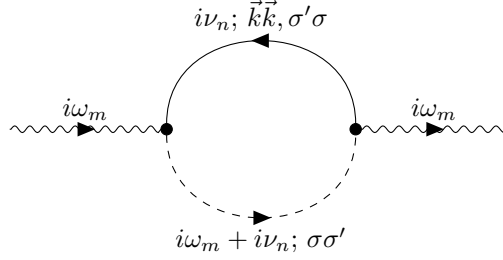


Figure 5.8: Diagrammatic representation of the slave-boson b self-energy.

Again, following the same steps as for the other diagrams:

$$\Sigma^b(i\omega_m) = +\frac{1}{\beta} \sum_{i\nu_n} \sum_{\vec{k}} |V_{\vec{k}}|^2 \text{Tr} \left\{ \mathbf{G}_{\vec{k}\vec{k}}^c(i\nu_n) \mathbf{G}^f(i\omega_m + i\nu_n) \right\} \quad (5.79)$$

$$= -\oint \frac{dz}{2\pi i} n_F(z) \sum_{\vec{k}} |V_{\vec{k}}|^2 \text{Tr} \left\{ \mathbf{G}_{\vec{k}\vec{k}}^c(z) \mathbf{G}^f(i\omega_m + z) \right\} \quad (5.80)$$

$$= -\int_{-\infty}^{\infty} \frac{d\varepsilon}{2\pi i} \sum_{\vec{k}} |V_{\vec{k}}|^2 \text{Tr} \left\{ n_F(\varepsilon) \left[\mathbf{G}_{\vec{k}\vec{k}}^c(\varepsilon + i\eta) - \mathbf{G}_{\vec{k}\vec{k}}^c(\varepsilon - i\eta) \right] \mathbf{G}^f(\varepsilon + i\omega_m) \right. \\ \left. + n_F(\varepsilon - i\omega_m) \mathbf{G}_{\vec{k}\vec{k}}^c(\varepsilon - i\omega_m) \left[\mathbf{G}^f(\varepsilon + i\eta) - \mathbf{G}^f(\varepsilon - i\eta) \right] \right\} \quad (5.81)$$

$$= \int_{-\infty}^{\infty} d\varepsilon \sum_{\vec{k}} |V_{\vec{k}}|^2 \text{Tr} \left\{ n_F(\varepsilon) \mathbf{A}_{\vec{k}\vec{k}}^c(\varepsilon) \mathbf{G}^f(\varepsilon + i\omega_m) + n_F(\varepsilon) \mathbf{G}_{\vec{k}\vec{k}}^c(\varepsilon - i\omega_m) \mathbf{A}^f(\varepsilon) \right\}, \quad (5.82)$$

where the major difference is a missing minus sign in the first line from the definition through the Luttinger-Ward functional (i.e. missing fermion loop) and the appearance of a minus sign in the second line due to the replacement of fermionic Matsubara frequencies by a contour integral. There is no relative sign between the two expressions since $e^{i\omega_m} = 1$ for bosonic Matsubara frequencies. The integration contour for evaluating the Matsubara sum is shown in Fig. 5.9. As before, the first step is shifting the external frequency $i\omega_m \rightarrow i\omega'_m = i\omega_m - \lambda$, c.f. Eq (5.43) and Eq (5.41).

$$\Sigma^b(i\omega'_m + \lambda) = \int_{-\infty}^{\infty} d\varepsilon \sum_{\vec{k}} |V_{\vec{k}}|^2 \text{Tr} \left\{ n_F(\varepsilon) \mathbf{A}_{\vec{k}\vec{k}}^c(\varepsilon) \mathbf{G}^f(\varepsilon + i\omega'_m + \lambda) \right. \\ \left. + n_F(\varepsilon) \mathbf{G}^c(\varepsilon - i\omega'_m - \lambda) \mathbf{A}^f(\varepsilon) \right\} \quad (5.83)$$

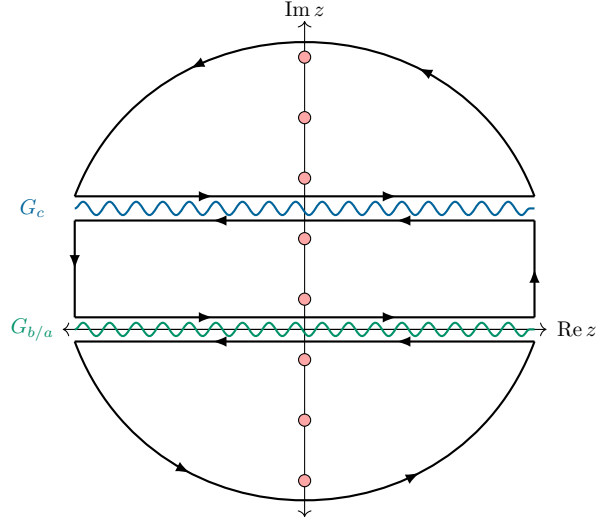


Figure 5.9: Contour for evaluating the Matsubara sum in the slave-boson self-energy. Curly lines visualize branch cuts of the respective Green functions. Fermionic Matsubara frequencies are shown as red dots.

The internal energy ε has to be shifted in the second term via $\varepsilon \rightarrow \varepsilon' = \varepsilon - \lambda$.

$$\begin{aligned} \Sigma^b(i\omega'_m + \lambda) = \sum_{\vec{k}} |V_{\vec{k}}|^2 \text{Tr} \left\{ \int_{-\infty}^{\infty} d\varepsilon n_F(\varepsilon) \mathbf{A}_{\vec{k}\vec{k}}^c(\varepsilon) \mathbf{G}^f(\varepsilon + i\omega'_m + \lambda) \right. \\ \left. + \int_{-\infty}^{\infty} d\varepsilon' n_F(\varepsilon' + \lambda) \mathbf{G}_{\vec{k}\vec{k}}^c(\varepsilon' - i\omega'_m) \mathbf{A}^f(\varepsilon' + \lambda) \right\} \end{aligned} \quad (5.84)$$

After relabeling ε' to ε , the expression reads

$$\begin{aligned} \Sigma^b(i\omega'_m + \lambda) = \int_{-\infty}^{\infty} d\varepsilon \sum_{\vec{k}} |V_{\vec{k}}|^2 \text{Tr} \left\{ n_F(\varepsilon) \mathbf{A}_{\vec{k}\vec{k}}^c(\varepsilon) \mathbf{G}^f(\varepsilon + i\omega'_m + \lambda) \right. \\ \left. + n_F(\varepsilon + \lambda) \mathbf{G}_{\vec{k}\vec{k}}^c(\varepsilon - i\omega'_m) \mathbf{A}^f(\varepsilon + \lambda) \right\} \end{aligned} \quad (5.85)$$

Taking the limit $\lambda \rightarrow \infty$ will suppress the second term exponentially, just as for the pseudofermion self-energy. The final expression with G^f and Σ^b being replaced by the expressions in the reference frame of λ reads

$$\Sigma^b(i\omega_m) = \int_{-\infty}^{\infty} d\varepsilon n_F(\varepsilon) \sum_{\vec{k}} |V_{\vec{k}}|^2 \text{Tr} \left\{ \mathbf{A}_{\vec{k}\vec{k}}^{c(0)}(\varepsilon) \mathbf{G}^f(\varepsilon + i\omega_m) \right\}. \quad (5.86)$$

The imaginary part of the advanced self-energy is then

$$\text{Im} \Sigma^b A(\omega) = \pi \int_{-\infty}^{\infty} d\varepsilon n_F(\varepsilon) \sum_{\vec{k}} |V_{\vec{k}}|^2 \text{Tr} \left\{ \mathbf{A}_{\vec{k}\vec{k}}^{c(0)}(\varepsilon) \mathbf{A}^f(\varepsilon + \omega) \right\}. \quad (5.87)$$

In the spin-diagonal and degenerate case, the trace gives a factor N of the associated $SU(N)$ symmetry.

Slave-Boson a Self-Energy

The Feynman diagram representing the self-energy of the slave-boson a is shown in Fig. 5.10. Utilizing

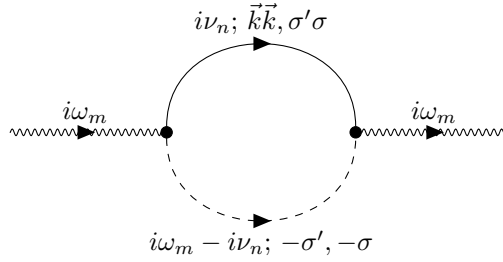


Figure 5.10: Diagrammatic representation of the slave-boson a self-energy.

the transposed spin-flipped matrix-Green-function $\tilde{\mathbf{G}}_{\sigma\sigma'}^T = G_{-\sigma', -\sigma}$, the diagram evaluates to

$$\Sigma^a(i\omega_m) = -\frac{1}{\beta} \sum_{i\nu_n} \sum_{\vec{k}} |V_{\vec{k}}|^2 \text{Tr} \left\{ \mathbf{G}_{\vec{k}\vec{k}}^c(i\nu_n) \tilde{\mathbf{G}}^{fT}(i\omega_m - i\nu_n) \right\} \quad (5.88)$$

$$= + \oint \frac{dz}{2\pi i} n_F(z) \sum_{\vec{k}} |V_{\vec{k}}|^2 \text{Tr} \left\{ \mathbf{G}_{\vec{k}\vec{k}}^c(z) \tilde{\mathbf{G}}^{fT}(i\omega_m - z) \right\} \quad (5.89)$$

$$= \int_{-\infty}^{\infty} \frac{d\varepsilon}{2\pi i} \sum_{\vec{k}} |V_{\vec{k}}|^2 \text{Tr} \left\{ n_F(\varepsilon) \left[\mathbf{G}_{\vec{k}\vec{k}}^c(\varepsilon + i\eta) - \mathbf{G}_{\vec{k}\vec{k}}^c(\varepsilon - i\eta) \right] \tilde{\mathbf{G}}^{fT}(i\omega_m - \varepsilon) \right. \\ \left. - n_F(i\omega_m - \varepsilon) \mathbf{G}_{\vec{k}\vec{k}}^c(i\omega_m - \varepsilon) \left[\tilde{\mathbf{G}}^{fT}(\varepsilon + i\eta) - \tilde{\mathbf{G}}^{fT}(\varepsilon - i\eta) \right] \right\} \quad (5.90)$$

$$= \int_{-\infty}^{\infty} d\varepsilon \sum_{\vec{k}} |V_{\vec{k}}|^2 \text{Tr} \left\{ -n_F(\varepsilon) \mathbf{A}_{\vec{k}\vec{k}}^c(\varepsilon) \tilde{\mathbf{G}}^{fT}(i\omega_m - \varepsilon) \right. \\ \left. + n_F(-\varepsilon) \mathbf{G}_{\vec{k}\vec{k}}^c(i\omega_m - \varepsilon) \mathbf{A}^{fT}(\varepsilon) \right\}. \quad (5.91)$$

where the contour as in the b -case (c.f. Fig. 5.9) can be used. Note that there is an overall sign from the lack of a fermion loop compared to the b -case and the relative sign due to the Jacobian from $\varepsilon = i\omega_m - z$, as explained before. We can now replace $i\omega'_n = i\omega_n - \lambda$ to get

$$\Sigma^a(i\omega'_m + \lambda) = \int_{-\infty}^{\infty} d\varepsilon \sum_{\vec{k}} |V_{\vec{k}}|^2 \text{Tr} \left\{ -n_F(\varepsilon) \mathbf{A}_{\vec{k}\vec{k}}^c(\varepsilon) \tilde{\mathbf{G}}^{fT}(i\omega'_m + \lambda - \varepsilon) \right. \\ \left. + n_F(-\varepsilon) \mathbf{G}_{\vec{k}\vec{k}}^c(i\omega'_m + \lambda - \varepsilon) \mathbf{A}^{fT}(\varepsilon) \right\}. \quad (5.92)$$

In the second term, shifting $\varepsilon' = \varepsilon - \lambda$ and relabeling $\varepsilon' \rightarrow \varepsilon$ gives

$$\begin{aligned} \Sigma^a(i\omega'_m + \lambda) = \int_{-\infty}^{\infty} d\varepsilon \sum_{\vec{k}} |V_{\vec{k}}|^2 \text{Tr} \left\{ -n_F(\varepsilon) \mathbf{A}_{\vec{k}\vec{k}}^c(\varepsilon) \bar{\mathbf{G}}^{fT}(i\omega'_m + \lambda - \varepsilon) \right. \\ \left. + n_F(-(\varepsilon + \lambda)) \mathbf{G}_{\vec{k}\vec{k}}^c(i\omega'_m - \varepsilon) \mathbf{A}^{fT}(\varepsilon + \lambda) \right\}. \end{aligned} \quad (5.93)$$

The Fermi function now needs to be replaced by $n_F(-(\varepsilon + \lambda)) = 1 - n_F(\varepsilon + \lambda)$ in order to take the limit. Relabeling in the same way as for b , the result is

$$\begin{aligned} \Sigma^a(i\omega_m) = \int_{-\infty}^{\infty} d\varepsilon \sum_{\vec{k}} |V_{\vec{k}}|^2 \text{Tr} \left\{ -n_F(\varepsilon) \mathbf{A}_{\vec{k}\vec{k}}^{c(0)}(\varepsilon) \bar{\mathbf{G}}^{fT}(i\omega_m - \varepsilon) \right. \\ \left. + \mathbf{G}_{\vec{k}\vec{k}}^{c(0)}(i\omega_m - \varepsilon) \mathbf{A}^{fT}(\varepsilon) \right\}. \end{aligned} \quad (5.94)$$

We can now take the imaginary part of the advanced self-energy to get

$$\begin{aligned} \text{Im} \Sigma^{aA}(\omega) = \int_{-\infty}^{\infty} d\varepsilon \sum_{\vec{k}} |V_{\vec{k}}|^2 \text{Tr} \left\{ -n_F(\varepsilon) \mathbf{A}_{\vec{k}\vec{k}}^{c(0)}(\varepsilon) \bar{\mathbf{A}}^{fT}(\omega - \varepsilon) \right. \\ \left. + \mathbf{A}_{\vec{k}\vec{k}}^{c(0)}(\omega - \varepsilon) \mathbf{A}^{fT}(\varepsilon) \right\}. \end{aligned} \quad (5.95)$$

The last step is to substitute $\varepsilon' = \omega - \varepsilon$ in the second term and then relabeling $\varepsilon' \rightarrow \varepsilon$ to combine the two into

$$\text{Im} \Sigma^{aA}(\omega) = \int_{-\infty}^{\infty} d\varepsilon \sum_{\vec{k}} |V_{\vec{k}}|^2 \text{Tr} \left\{ (1 - n_F(\varepsilon)) \mathbf{A}_{\vec{k}\vec{k}}^{c(0)}(\varepsilon) \bar{\mathbf{A}}^{fT}(\omega - \varepsilon) \right\} \quad (5.96)$$

$$= \int_{-\infty}^{\infty} d\varepsilon n_F(-\varepsilon) \sum_{\vec{k}} |V_{\vec{k}}|^2 \text{Tr} \left\{ \mathbf{A}_{\vec{k}\vec{k}}^{c(0)}(\varepsilon) \bar{\mathbf{A}}^{fT}(\omega - \varepsilon) \right\}. \quad (5.97)$$

Similar to the previous case, the trace gives a factor N of the associated $SU(N)$ symmetry in the spin-diagonal and degenerate case.

5.3.4 Fixing the Auxiliary-Particle Energy Scale

Introducing auxiliary particles in the Hamiltonian leads to an additional, artificial $U(1)$ symmetry due to auxiliary particles always appearing in pairs of creation- and annihilation operators. This gauge degree of freedom is addressed by λ but not fixed by sending it to infinity, as will become clear later. Let's first explicitly prove the invariance of G^d w.r.t. shifts in auxiliary-particle energy by λ' .

$$\text{Im } \mathbf{G}_1^{dA}(\omega) \xrightarrow{\text{shift}} \pi \frac{\int_{-\infty}^{\infty} d\varepsilon e^{-\beta\varepsilon} \left\{ \mathbf{A}^f(\varepsilon + \omega + \lambda') A^b(\varepsilon + \lambda') + \mathbf{A}^f(\varepsilon + \lambda') A^b(\varepsilon - \omega + \lambda') \right\}}{\int_{-\infty}^{\infty} d\varepsilon e^{-\beta\varepsilon} \left[A^b(\varepsilon + \lambda') + A^a(\varepsilon + \lambda') + \sum_{\sigma} A_{\sigma\sigma}^f(\varepsilon + \lambda') \right]} \quad (5.98)$$

$$\stackrel{\varepsilon' = \varepsilon + \lambda'}{=} \pi \frac{\int_{-\infty}^{\infty} d\varepsilon' e^{-\beta(\varepsilon' - \lambda)} \left\{ \mathbf{A}^f(\varepsilon' + \omega) A^b(\varepsilon') + \mathbf{A}^f(\varepsilon') A^b(\varepsilon' - \omega) \right\}}{\int_{-\infty}^{\infty} d\varepsilon' e^{-\beta(\varepsilon' - \lambda)} \left[A^b(\varepsilon') + A^a(\varepsilon') + \sum_{\sigma} A_{\sigma\sigma}^f(\varepsilon') \right]} \quad (5.99)$$

$$= \pi \frac{e^{\beta\lambda'} \int_{-\infty}^{\infty} d\varepsilon' e^{-\beta\varepsilon'} \left\{ \mathbf{A}^f(\varepsilon' + \omega) A^b(\varepsilon') + \mathbf{A}^f(\varepsilon') A^b(\varepsilon' - \omega) \right\}}{e^{\beta\lambda'} \int_{-\infty}^{\infty} d\varepsilon' e^{-\beta\varepsilon'} \left[A^b(\varepsilon') + A^a(\varepsilon') + \sum_{\sigma} A_{\sigma\sigma}^f(\varepsilon') \right]} \quad (5.100)$$

$$= \text{Im } \mathbf{G}_1^{dA}(\omega) \frac{e^{\beta\lambda'}}{e^{\beta\lambda'}} = \text{Im } \mathbf{G}_1^{dA}(\omega) \quad (5.101)$$

The second term $\text{Im } \mathbf{G}_2^{dA}$ has the same structure, and its invariance can be shown using the same procedure.

All auxiliary-particle functions are in the reference frame of λ such that taking the limit $\lambda \rightarrow \infty$ is well-defined. This does not fix the gauge in the co-moving frame. We therefore have to split $\lambda = \lambda_0 + \lambda_1$, send $\lambda_1 \rightarrow \infty$, and use λ_0 to fix the gauge in this reference frame. A natural choice is adjusting λ_0 such that $\langle Q \rangle = 1$. It seems to be an odd choice since the projection is supposed to already enforce this. In reality, the auxiliary-particle equations derived above are still in the grand-canonical ensemble, we have just removed diagrams that would not contribute under the projection to the canonical ensemble, i.e. enforcing the operator constraint $\hat{Q} = \mathbb{1}$. In the co-moving frame, the *expectation value* $\langle Q \rangle$ is not fixed and, due to the grand-canonical nature of the theory, the associated chemical potential λ_0 must be adjusted dynamically to enforce constraints on expectation values. This can be done in many ways and typically improves the stability of NCA significantly.

Enforcing $\langle Q \rangle = 1$ is indeed not crucial in solving the theory, as physical observables become independent of $\langle Q \rangle$ by construction (c.f. Eq (5.24)). Another possibility for fixing the gauge is to adjust the peak positions of auxiliary-particle spectra during calculations. In fact, the numerical stability can be greatly increased by this method. In order to calculate the appropriate λ_0 for this method, one has to look at the definition of a full Green function in the co-moving frame (c.f. Eq. (5.41)-(5.42))

$$G(\omega) = (\omega - \varepsilon - \lambda_0 - \text{Re } \Sigma(\omega) - i \text{Im } \Sigma(\omega))^{-1} . \quad (5.102)$$

Disregarding $\text{Im } \Sigma$, the poles of such a Green function will be at $\omega - \varepsilon - \lambda_0 - \text{Re } \Sigma(\omega) = 0$. We can now shift the pole to $\omega = 0$ via

$$\lambda_0 = \min [\varepsilon - \text{Re } \Sigma(0)] , \quad (5.103)$$

where the minimum is with respect to the auxiliary-particle flavor, ensuring that the leftmost pole over all auxiliary-particle Green functions will be fixed to zero. In reality, this does not fully work due to the frequency structure of $\text{Im } \Sigma$; it is, however, stable, precisely defined, numerically fast, and, in fact, leads to better convergence of the dynamical mean-field theory, which will be discussed later.

5.3.5 Addressing the Diverging Boltzmann Factor via Tilde Functions

For low temperatures, auxiliary-particle spectral functions develop a sharp asymmetry around their main peak. Furthermore, the Boltzmann factor in the equation for G^d poses numerical challenges due to its strongly increasing values for $\omega < 0$ combined with the strongly decreasing values in auxiliary-particle spectra, counteracting the divergent behavior of $e^{-\beta\omega}$ to guarantee a finite result in Eq. (5.60) and (5.62).

In order to address this, a simple transformation can be utilized to reduce the asymmetry and remove the Boltzmann factor at the same time [76]

$$f(\omega) = n_F(-\omega)\tilde{f}(\omega) = [1 - n_F(\omega)]\tilde{f}(\omega). \quad (5.104)$$

The functions \tilde{f} are colloquially called *tilde functions*. The identification above is numerically non-invertible due to the same problems as discussed above when the Fermi function approaches zero. We can, however, replace all auxiliary-particle spectral functions and self-energies with their tilde version and form a closed set of equations for tilde functions. For this, a series of identities prove useful. First, the Fermi function can be expressed via a hyperbolic tangent

$$\begin{aligned} n_F(\varepsilon) &= \frac{1}{e^{\beta\varepsilon} + 1} = \frac{1}{2} \left(\frac{e^{\beta\varepsilon} + 1 - e^{\beta\varepsilon} - 1}{e^{\beta\varepsilon} + 1} \right) = \frac{1}{2} \left(1 - \frac{e^{\beta\varepsilon} - 1}{e^{\beta\varepsilon} + 1} \right) \\ &= \frac{1}{2} \left(1 - \frac{e^{\beta\varepsilon/2} - e^{-\beta\varepsilon/2}}{e^{\beta\varepsilon/2} + e^{-\beta\varepsilon/2}} \right) = \frac{1}{2} \left(1 - \tanh \frac{\beta\varepsilon}{2} \right). \end{aligned} \quad (5.105)$$

Products of Fermi distribution functions appear in the expressions for tilde functions, which can be efficiently recast using the above equation. They are

$$\begin{aligned} \frac{n_F(\varepsilon)n_F(-\varepsilon - \omega)}{n_F(-\omega)} &= n_F(\varepsilon) \frac{e^{-\beta\omega} + 1}{e^{-\beta(\omega+\varepsilon)} + 1} = n_F(\varepsilon) \frac{e^{\beta\varepsilon} + e^{\beta(\omega+\varepsilon)}}{e^{\beta(\omega+\varepsilon)} + 1} = n_F(\varepsilon) \frac{e^{\beta\varepsilon} + e^{\beta(\omega+\varepsilon)} + 1 - 1}{e^{\beta(\omega+\varepsilon)} + 1} \\ &= n_F(\varepsilon) + n_F(\omega + \varepsilon) \frac{e^{\beta\varepsilon} - 1}{e^{\beta\varepsilon} + 1} = n_F(\varepsilon) + n_F(\omega + \varepsilon) \tanh \frac{\beta\varepsilon}{2} \\ &= \frac{1}{2} \left(1 - \tanh \frac{\beta\varepsilon}{2} \right) + n_F(\omega + \varepsilon) \tanh \frac{\beta\varepsilon}{2} = \frac{1}{2} + \tanh \frac{\beta\varepsilon}{2} \left(n_F(\omega + \varepsilon) - \frac{1}{2} \right) \\ &= \frac{1}{2} \left(1 - \tanh \frac{\beta\varepsilon}{2} \tanh \frac{\beta(\omega + \varepsilon)}{2} \right), \end{aligned} \quad (5.106)$$

and similarly

$$\frac{n_F(-\varepsilon)n_F(-\omega + \varepsilon)}{n_F(-\omega)} = \frac{1}{2} \left(1 + \tanh \frac{\beta\varepsilon}{2} \tanh \frac{\beta(\omega - \varepsilon)}{2} \right). \quad (5.107)$$

First, let's express the self-energies in terms of tilde functions, leaving the conduction-electron Green function unaltered.

$$\text{Im } \Sigma_1^{fA}(\omega) = n_F(-\omega) \text{Im } \tilde{\Sigma}_1^{fA}(\omega) \quad (5.108)$$

$$= \pi \int_{-\infty}^{\infty} d\varepsilon (1 - n_F(\varepsilon)) n_F(-\omega + \varepsilon) \tilde{A}^b(\omega - \varepsilon) \sum_{\vec{k}} |V_{\vec{k}}|^2 \tilde{\mathbf{A}}_{\vec{k}\vec{k}}^c(0)(\varepsilon) \quad (5.109)$$

$$\Leftrightarrow \text{Im } \tilde{\Sigma}_1^{fA}(\omega) = \pi \int_{-\infty}^{\infty} d\varepsilon \frac{n_F(-\varepsilon)n_F(-\omega + \varepsilon)}{n_F(-\omega)} \tilde{A}^b(\omega - \varepsilon) \sum_{\vec{k}} |V_{\vec{k}}|^2 \tilde{\mathbf{A}}_{\vec{k}\vec{k}}^c(0)(\varepsilon) \quad (5.110)$$

$$= \pi \int_{-\infty}^{\infty} d\varepsilon \frac{1}{2} \left(1 + \tanh \frac{\beta\varepsilon}{2} \tanh \frac{\beta(\omega - \varepsilon)}{2} \right) \tilde{A}^b(\omega - \varepsilon) \sum_{\vec{k}} |V_{\vec{k}}|^2 \tilde{\mathbf{A}}_{\vec{k}\vec{k}}^c(0)(\varepsilon) \quad (5.111)$$

$$\text{Im } \Sigma_2^{fA}(\omega) = n_F(-\omega) \text{Im } \tilde{\Sigma}_2^{fA}(\omega) \quad (5.112)$$

$$= \pi \int_{-\infty}^{\infty} d\varepsilon n_F(\varepsilon) n_F(-\varepsilon - \omega) \tilde{A}^a(\varepsilon + \omega) \sum_{\vec{k}} |V_{\vec{k}}|^2 \tilde{\mathbf{A}}_{\vec{k}\vec{k}}^c(\varepsilon) \quad (5.113)$$

$$\Leftrightarrow \text{Im } \tilde{\Sigma}_2^{fA}(\omega) = \pi \int_{-\infty}^{\infty} d\varepsilon \frac{1}{2} \left(1 - \tanh \frac{\beta\varepsilon}{2} \tanh \frac{\beta(\omega + \varepsilon)}{2} \right) \tilde{A}^a(\varepsilon + \omega) \sum_{\vec{k}} |V_{\vec{k}}|^2 \tilde{\mathbf{A}}_{\vec{k}\vec{k}}^c(\varepsilon) \quad (5.114)$$

$$\text{Im } \Sigma^{bA}(\omega) = n_F(-\omega) \text{Im } \tilde{\Sigma}^{bA}(\omega) \quad (5.115)$$

$$= \pi \int_{-\infty}^{\infty} d\varepsilon n_F(\varepsilon) n_F(-\varepsilon - \omega) \sum_{\vec{k}} |V_{\vec{k}}|^2 \text{Tr} \left\{ \tilde{\mathbf{A}}^f(\varepsilon + \omega) \mathbf{A}^c(0)(\varepsilon) \right\} \quad (5.116)$$

$$\Leftrightarrow \text{Im } \tilde{\Sigma}^{bA}(\omega) = \pi \int_{-\infty}^{\infty} d\varepsilon \frac{1}{2} \left(1 - \tanh \frac{\beta\varepsilon}{2} \tanh \frac{\beta(\omega + \varepsilon)}{2} \right) \sum_{\vec{k}} |V_{\vec{k}}|^2 \text{Tr} \left\{ \tilde{\mathbf{A}}^f(\varepsilon + \omega) \mathbf{A}^c(0)(\varepsilon) \right\} \quad (5.117)$$

$$\text{Im } \Sigma^{aA}(\omega) = n_F(-\omega) \text{Im } \tilde{\Sigma}^{aA}(\omega) \quad (5.118)$$

$$= \int_{-\infty}^{\infty} d\varepsilon n_F(-\varepsilon) n_F(-\omega + \varepsilon) \sum_{\vec{k}} |V_{\vec{k}}|^2 \text{Tr} \left\{ \mathbf{A}_{\vec{k}\vec{k}}^c(-\varepsilon) \tilde{\mathbf{A}}^{fT}(\omega - \varepsilon) \right\} \quad (5.119)$$

$$\Leftrightarrow \text{Im } \tilde{\Sigma}^{aA}(\omega) = \int_{-\infty}^{\infty} d\varepsilon \frac{1}{2} \left(1 + \tanh \frac{\beta\varepsilon}{2} \tanh \frac{\beta(\omega - \varepsilon)}{2} \right) \sum_{\vec{k}} |V_{\vec{k}}|^2 \text{Tr} \left\{ \mathbf{A}_{\vec{k}\vec{k}}^c(-\varepsilon) \tilde{\mathbf{A}}^{fT}(\omega - \varepsilon) \right\} \quad (5.120)$$

Next, we can express $\langle Q \rangle$ in terms of tilde functions.

$$\langle Q \rangle = \int_{-\infty}^{\infty} d\varepsilon e^{-\beta\varepsilon} \left[A^b(\varepsilon) + A^a(\varepsilon) + \text{Tr } \mathbf{A}^f(\varepsilon) \right] \quad (5.121)$$

$$= \int_{-\infty}^{\infty} d\varepsilon e^{-\beta\varepsilon} n_F(-\varepsilon) \left[\tilde{A}^b(\varepsilon) + \tilde{A}^a(\varepsilon) + \text{Tr } \tilde{\mathbf{A}}^f(\varepsilon) \right] \quad (5.122)$$

$$= \int_{-\infty}^{\infty} d\varepsilon n_F(\varepsilon) \left[\tilde{A}^b(\varepsilon) + \tilde{A}^a(\varepsilon) + \text{Tr } \tilde{\mathbf{A}}^f(\varepsilon) \right] \quad (5.123)$$

This also holds for each individual expectation value, i.e.

$$\langle \hat{n}_\alpha \rangle = \int_{-\infty}^{\infty} d\varepsilon n_F(\varepsilon) \tilde{A}^\alpha(\varepsilon) \quad (5.124)$$

for each auxiliary particle α .

Lastly, G^d can be expressed using only tilde functions as

$$\text{Im } \mathbf{G}_1^{dA}(\omega) = \pi \frac{\int_{-\infty}^{\infty} d\varepsilon e^{-\beta\varepsilon} (1 + e^{-\beta\omega}) n_F(-(\varepsilon + \omega)) n_F(-\varepsilon) \tilde{A}^f(\varepsilon + \omega) \tilde{A}^b(\varepsilon)}{\int_{-\infty}^{\infty} d\varepsilon n_F(\varepsilon) [\tilde{A}^b(\varepsilon) + \tilde{A}^a(\varepsilon) + \text{Tr } \tilde{A}^f(\varepsilon)]} \quad (5.125)$$

$$= \pi \frac{\int_{-\infty}^{\infty} d\varepsilon \frac{n_F(-\omega - \varepsilon) n_F(\varepsilon)}{n_F(-\omega)} \tilde{A}^f(\varepsilon + \omega) \tilde{A}^b(\varepsilon)}{\int_{-\infty}^{\infty} d\varepsilon n_F(\varepsilon) [\tilde{A}^b(\varepsilon) + \tilde{A}^a(\varepsilon) + \text{Tr } \tilde{A}^f(\varepsilon)]} \quad (5.126)$$

$$= \pi \frac{\int_{-\infty}^{\infty} d\varepsilon \frac{1}{2} \left(1 - \tanh \frac{\beta\varepsilon}{2} \tanh \frac{\beta(\omega + \varepsilon)}{2} \right) \tilde{A}^f(\varepsilon + \omega) \tilde{A}^b(\varepsilon)}{\int_{-\infty}^{\infty} d\varepsilon n_F(\varepsilon) [\tilde{A}^b(\varepsilon) + \tilde{A}^a(\varepsilon) + \text{Tr } \tilde{A}^f(\varepsilon)]}, \quad (5.127)$$

and

$$\text{Im } \mathbf{G}_2^{dA}(\omega) = \pi \frac{\int_{-\infty}^{\infty} d\varepsilon e^{-\beta\varepsilon} (1 + e^{\beta\omega}) n_F(-\varepsilon + \omega) n_F(-\varepsilon) \tilde{A}^f(\varepsilon - \omega) \tilde{A}^a(\varepsilon)}{\int_{-\infty}^{\infty} d\varepsilon e^{-\beta\varepsilon} [A^b(\varepsilon) + A^a(\varepsilon) + \text{Tr } \tilde{A}^f(\varepsilon)]} \quad (5.128)$$

$$= \pi \frac{\int_{-\infty}^{\infty} d\varepsilon \frac{n_F(\varepsilon) n_F(-\varepsilon + \omega)}{n_F(\omega)} \tilde{A}^f(\varepsilon - \omega) \tilde{A}^a(\varepsilon)}{\int_{-\infty}^{\infty} d\varepsilon e^{-\beta\varepsilon} [A^b(\varepsilon) + A^a(\varepsilon) + \text{Tr } \tilde{A}^f(\varepsilon)]} \quad (5.129)$$

$$= \pi \frac{\int_{-\infty}^{\infty} d\varepsilon \frac{1}{2} \left(1 + \tanh \frac{\beta\varepsilon}{2} \tanh \frac{\beta(\omega - \varepsilon)}{2} \right) \tilde{A}^f(\varepsilon - \omega) \tilde{A}^a(\varepsilon)}{\int_{-\infty}^{\infty} d\varepsilon e^{-\beta\varepsilon} [A^b(\varepsilon) + A^a(\varepsilon) + \text{Tr } \tilde{A}^f(\varepsilon)]}. \quad (5.130)$$

Evaluating the self-energies has thus become harder, but extracting G^d has become simpler. In any way, there are no numerical problems due to diverging functions anymore.

There are some more caveats when working with tilde functions. Advanced (retarded) Green functions are analytic in the lower (upper) complex half-plane. Due to the periodic pole-structure of the Fermi function, analyticity is broken, and Kramers-Kronig does not apply to tilde functions. Furthermore, since dividing by a Fermi function is numerically unstable, we can not transform regular functions into tilde functions; we can only do it the other way round. This implies a slightly more

complex structure for extracting a spectral function using self-energies:

$$n_F(-\omega) \tilde{A}(\omega) = \text{Im} \frac{1}{\omega - \varepsilon - \Sigma(\omega)} = \text{Im} \frac{\omega - \varepsilon - \Sigma^*(\omega)}{|\omega - \varepsilon - \Sigma(\omega)|^2} \quad (5.131)$$

$$= \frac{\text{Im} \Sigma(\omega)}{(\omega - \varepsilon - \text{Re} \Sigma(\omega))^2 + (\text{Im} \Sigma(\omega))^2} = \frac{n_F(-\omega) \text{Im} \tilde{\Sigma}(\omega)}{(\omega - \varepsilon - \text{Re} \Sigma(\omega))^2 + (\text{Im} \Sigma(\omega))^2} \quad (5.132)$$

$$\Leftrightarrow \tilde{A}(\omega) = \frac{n_F(-\omega) \text{Im} \tilde{\Sigma}(\omega)}{(\omega - \varepsilon - \text{Re} \Sigma(\omega))^2 + (\text{Im} \Sigma(\omega))^2}. \quad (5.133)$$

This is only straightforward for scalars. For matrices, one has to keep track of the Fermi functions while inverting matrices. An algorithm for this can be found in Appendix C.2.

5.3.6 The NCA Loop

Having collected all the ingredients, we can solve the NCA. Since self-energies depend on full auxiliary-particle Green functions and those depend on the self-energies again, one gets a self-consistent loop. One can, therefore, either solve for Green functions or for self-energies. Since auxiliary-particle spectra can become very sharp, indeed diverge for $T = 0$ [80], solving for self-energies is often a good idea. They tend to be finite and controlled. This also has the benefit of maintaining normalization and analyticity. We can also use the NCA equations exclusively for imaginary parts, which have a much better scaling for large $|\omega|$ ($1/\omega^2$ in contrast to $1/\omega$). The loop for this case is as follows:

- (0.) Initial guess for auxiliary-particle $\text{Im} \tilde{\Sigma}$.
 1. Generate $\text{Re} \Sigma$ via Kramers-Kronig on $\text{Im} \Sigma$, which is generated from the tilde-function definition.
 2. Determine λ_0 via $\text{Re} \Sigma$.
 3. Generate spectral functions using $\text{Im} \tilde{\Sigma}$, $\text{Im} \Sigma$ and $\text{Re} \Sigma$.
 4. Generate $\text{Im} \tilde{\Sigma}$ from the spectral functions of step 3 and the *free* conduction-electron spectrum.
- (5.) Go back to step 1 and repeat until converged.

In reality, just looping the equations is very unstable. The output of step 4 is mixed to a small percentage with the previous guess to change the values slowly. This helps avoid overshooting minima in configuration space, i.e. staying in valleys of attraction that lead to solutions. A more sophisticated yet still stable method utilizing longer histories can be used to accelerate and stabilize this process. The method used for all results presented in this thesis is the *Anderson mixing*¹⁰ [81].

¹⁰ The last name being identical to Phil W. Anderson's is a coincidence. The numerical method goes back to Donald G. Anderson.

5.3.7 Two Limits: Infinite U and Infinite ε^d

Having fully discussed the simple yet powerful method that is NCA, we can now utilize it to solve problems that are typically hard—if not impossible—to solve with regular quantum-field theory of the original model (c.f. Sec. 5.1.3).

The first that comes to mind is the large- U limit, which is a useful approximation for many f -electron systems, where the local Coulomb interaction can be much larger than the single-particle energy (c.f. Sec. 3.3.2). In this case, the impurity-occupation is strictly $n_d \leq 1$. Taking the limit $U \rightarrow \infty$ effectively removes the slave-boson a from the dynamics of the system. In Eq. (5.42), taking the limit as mentioned above is achieved by $\varepsilon^a \rightarrow \infty$, which shifts the peak of the spectrum to infinite positive energy. The self-energy vanishes under this limit (c.f. Eq. (5.96) for $\omega \rightarrow \infty$) resulting in $A^a(\omega)$ approaching $\delta(\omega - \varepsilon^a)$. Consequently, the contribution to G^d in Eq. (5.62) will vanish, except for a region around $\omega = \varepsilon^a$. This can be seen from the numerator G^d

$$\text{Im } \mathbf{G}_2^{dA}(\omega) \cdot \frac{\langle Q \rangle_{\lambda \rightarrow \infty}}{\pi} = \int_{-\infty}^{\infty} d\varepsilon e^{-\beta\varepsilon} (1 + e^{\beta\omega}) \bar{\mathbf{A}}^f(\varepsilon - \omega) A^a(\varepsilon) \quad (5.134)$$

$$= \int_{-\infty}^{\infty} d\varepsilon \left(e^{-\beta\varepsilon} + e^{\beta(\omega - \varepsilon)} \right) \bar{\mathbf{A}}^f(\varepsilon - \omega) \delta(\varepsilon - \varepsilon^a) \quad (5.135)$$

$$= \left(e^{-\beta\varepsilon^a} + e^{\beta(\omega - \varepsilon^a)} \right) \bar{\mathbf{A}}^f(\varepsilon^a - \omega) \quad (5.136)$$

$$\stackrel{\omega = \varepsilon^a + \delta}{=} \left(e^{-\beta\varepsilon^a} + e^{\beta(\delta)} \right) \bar{\mathbf{A}}^f(-\delta) \quad (5.137)$$

$$\stackrel{\varepsilon^a \rightarrow \infty}{\rightarrow} e^{\beta\delta} \bar{\mathbf{A}}^f(-\delta) \quad (5.138)$$

$$= e^{\beta(\delta)} n_F(\delta) \tilde{\bar{\mathbf{A}}}^f(-\delta) = n_F(-\delta) \tilde{\bar{\mathbf{A}}}^f(-\delta). \quad (5.139)$$

Using Eq. (5.124), the integral of this can be identified as the occupation number of the spin-flipped pseudofermions. If the a bosons are omitted, because they only contribute at $\varepsilon^a \rightarrow \infty$ energies, the impurity spectrum of spin σ will be normalized to $1 - \langle n_{-\sigma}^f \rangle$. This is not problematic due to the clear separation of energy scales. It just needs to be respected when testing the norm of spectral functions in the infinite- U case.

In this case, a positive side-effect is the improvement of the NCA Kondo temperature. The finite- U NCA drastically underestimates the Kondo temperature by generating a Kondo coupling of $J/2$ instead of J such that the Kondo temperature is the square of the correct value [82]. This stems from an asymmetry in treating the two virtual fluctuations via the unoccupied and doubly occupied state, which is not the case for $U \rightarrow \infty$ since only one of those terms remains.

The second case is the reverse of the above, namely fixing ε^a and sending $\varepsilon^d \rightarrow -\infty$. This limits the occupation to $2 \geq n_d \geq 1$, which can be relevant for hole-like f -orbital systems, e.g. Yb^{3+} with a single hole in the f -shell. In order to take this limit faithfully, we first need to use the $U(1)$ symmetry

to shift energies via $\lambda \rightarrow \lambda + 2\mu - \varepsilon^a$ such that a is of energy λ

$$H_{\text{SIAM}} = \sum_{\vec{k}, \sigma} \left(\varepsilon_{\vec{k}}^c - \mu \right) c_{\vec{k}\sigma}^\dagger c_{\vec{k}\sigma} + \sum_{\sigma} \left(\varepsilon^d + \mu - \varepsilon^a + \lambda \right) f_{\sigma}^\dagger f_{\sigma} + (\lambda + 2\mu - \varepsilon^a) b^\dagger b + (\lambda) a^\dagger a \quad (5.140)$$

$$+ \sum_{\vec{k}, \sigma} \left(V_{\vec{k}} c_{\vec{k}\sigma}^\dagger b^\dagger f_{\sigma} + V_{\vec{k}} \text{sgn}(\sigma) c_{\vec{k}\sigma}^\dagger f_{\sigma}^\dagger a + h.c. \right) - \lambda. \quad (5.141)$$

Re-defining $\varepsilon^d - \varepsilon^a = \tilde{\varepsilon}^a$, the energy associated with b is proportional to $\tilde{\varepsilon}^a - \varepsilon^d =: \varepsilon^b$, which goes to infinity under $\varepsilon^d \rightarrow -\infty$ while keeping $\tilde{\varepsilon}^a$ constant. Similar to the previous case, we can, therefore, remove b from the theory because it will not contribute to the dynamics. Doing so will send the numerator of the first term of G^d from Eq. (5.60) under $\omega = \delta + \varepsilon^d$ to

$$\text{Im } \mathbf{G}_1^{dA}(\omega) \cdot \frac{\langle Q \rangle_{\lambda \rightarrow \infty}}{\pi} = \int_{-\infty}^{\infty} d\varepsilon e^{-\beta\varepsilon} \left(1 + e^{-\beta\omega} \right) \mathbf{A}^f(\varepsilon + \omega) A^b(\varepsilon) \quad (5.142)$$

$$\xrightarrow{\varepsilon^d \rightarrow -\infty} e^{-\beta\delta} \mathbf{A}^f(\delta) = n_F(\delta) \tilde{\mathbf{A}}^f(\delta). \quad (5.143)$$

In this case, upon removing b , the spectrum is given by the contribution from the spin-flipped part in \mathbf{G}_2^{dA} and is normalized to $1 - \langle n_{\sigma}^f \rangle$.

How the NCA equations of this case can be mapped onto the $U \rightarrow \infty$ case is discussed in detail in Appendix D.

5.4 Dynamical Mean-Field Theory

One of the more recent advances in the theory of correlated systems is the dynamical mean-field theory [83] developed by Antoine Georges and Gabriel Kotliar in 1992. Motivated by the work of Walter Metzner and Dieter Vollhardt in 1989 [84], where they showed that self-energies tend to become local in infinite dimensions, Georges and Kotliar mapped an interacting lattice model onto a local single-impurity Anderson model in an effective bath of electrons. With this, the local impurity self-energy could be identified as the local self-energy in the lattice model, reducing the complexity of solving lattice models enormously. Since this construction is a local mapping, which is in the spirit of the Weiss mean-field theory [85] but constructing a local model that captures the full local dynamics (it is still the full, interacting local model), they named this mapping “dynamical mean-field theory” (DMFT). I will lay out the ideas involved in deriving DMFT in infinite dimensions closely following [86] and [87].

5.4.1 Electrons in Infinite Dimensions / Suppression of Non-Local Self-Energies

Interacting electrons in high dimensions tend to have local self-energies, which can be qualitatively understood from the fact that by averaging over neighboring sites, each individual contribution will become less and less important until averaging over neighbors results in an entirely local description. For simplicity, we shall investigate this behavior in the Fermi-Hubbard model on a hypercubic lattice of dimension d with nearest-neighbor hopping.

$$H = \sum_{i,j,\sigma} t_{ij} c_{i\sigma}^\dagger c_{j\sigma} + U \sum_i n_{i,\uparrow} n_{i,\downarrow} \quad \text{where } t_{ij} = \begin{cases} -t & \vec{R}_i - \vec{R}_j = \pm \vec{e}_n \\ 0 & \text{else} \end{cases}, \quad (5.144)$$

and the unit-cell basis vectors \vec{e}_n . This gives rise to the dispersion $\epsilon_{\vec{k}} = -2t \sum_i \cos k_i$. The kinetic energy per site poses a problem under the limit $d \rightarrow \infty$ in that it diverges, which can be seen from

$$E_{\text{kin},i}^0 = -t \sum_{\sigma} \underbrace{\sum_{j \text{ NN of } i} \langle c_{i,\sigma}^\dagger c_{j,\sigma} \rangle_0}_{\sim 1/\sqrt{2d}}. \quad (5.145)$$

The expectation value under the sum is the hopping amplitude, which is the square root of the hopping probability. Assuming isotropy, this is just one over the number of nearest neighbors $2d$. The sum over nearest neighbors then just gives $2d$, resulting in an overall scaling of $E_{\text{kin},i}^0 \sim \sqrt{2d}$. This can be fixed via re-scaling $t = t_*/\sqrt{2d}$ keeping t_* fixed under the limit. This directly gives rise to a Gaussian as the density of states of a hypercubic lattice in infinite dimensions, which is derived in App. C.3. The re-scaling has an implication on self-energy diagrams.

As discussed in Section 5.2, self-energy diagrams are IPI skeleton diagrams with an entry point i and an exit point j , e.g. in real space. All Green functions in a given diagram contribute $1/\sqrt{2d}$, and sums over intermediate positions give $2d$ due to the nearest-neighbor nature of the model. Analyzing the possible paths connecting two points illustrated in Fig. 5.11 gives additional insight into the scaling of self-energy diagrams. Since any meaningful (interaction) vertex must be at least a three-vertex, this will serve as the minimal example. First, if only one line connects the two points, the diagram would be 1-particle *reducible* by definition (first diagram in the figure). For two lines, all remaining lines

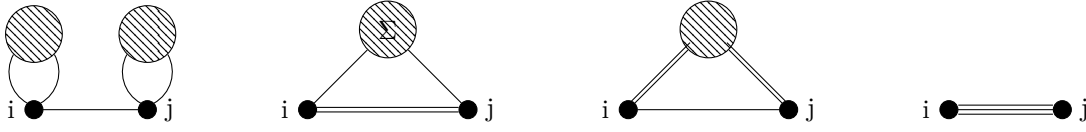


Figure 5.11: Different schematic Feynman diagrams for the non-local self-energy discussion. Diagrams no. 3 and 4 are valid self-energy diagrams, whereas 1 and 2 are not. Lines represent full Green functions; blobs represent diagram insertions.

(if any) must be of a self-energy type and, hence, lead to a prohibited self-energy insertion (second diagram). If only a single line directly connects the two points but the other lines connect indirectly, the resulting diagram is a valid self-energy diagram (third diagram). The same is true if all three lines directly connect both points (fourth diagram). Combining this with the aforementioned scaling of Green functions and sums, all non-local self-energy diagrams must vanish at least as $1/\sqrt{2d}$ for $d \rightarrow \infty$:

$$\Sigma_{ij\sigma}(\omega) = \delta_{i,j} \Sigma_{ij\sigma}(\omega) + \mathcal{O}\left(\frac{1}{\sqrt{2d}}\right) \Rightarrow \Sigma_{\vec{k}\sigma}(\omega) = \Sigma_{\sigma}(\omega). \quad (5.146)$$

The local lattice-Green-function is therefore

$$G_{\sigma}(\omega) = \int \frac{d^d k}{(2\pi)^d} \frac{1}{\omega + \mu - \epsilon_{\vec{k}} - \Sigma_{\sigma}(\omega)} = \int_{-\infty}^{\infty} d\epsilon \frac{\rho(\epsilon)}{\omega + \mu - \epsilon - \Sigma_{\sigma}(\omega)}. \quad (5.147)$$

This can be used to find an exact mapping of an infinite-dimensional lattice system onto a local system with a renormalized background via dynamical mean-field theory, which will be discussed in the next section.

5.4.2 Dynamical Mean-Field Theory for the Periodic Anderson Model

Assuming a local self-energy, a mapping can be found from the lattice model to the local model [88]. Although being only exact in infinite dimensions, DMFT was successfully used in the past¹¹. Although historically derived for the Hubbard model, a derivation for the periodic Anderson model is not only possible but, in fact, simpler and seemingly close to reality for low-dimensional lattices, i.e. real-world materials.

When extending the single-impurity Anderson model to a lattice case, an NCA would generate an infinite number of coupled self-consistent integral equations. A way of dealing with this extension is applying a slave-boson mean-field theory [92]. Typically, this results in a reduction to a local problem, where all non-local effects are absorbed in the mean field. In order to capture dynamical effects, the mean-field theory has to include self-energies or T-matrices, such that finite lifetime effects of quasi-particles are generated in the calculations. To set up the discussion, let's remember the

¹¹ For an overview, see [89–91].

Hamiltonian of the periodic Anderson model in Eq. (3.67)

$$H_{\text{PAM}} \rightarrow \sum_{\vec{k}, \sigma} (\varepsilon_{\vec{k}}^c - \mu) c_{\vec{k}\sigma}^\dagger c_{\vec{k}\sigma} + \sum_{i, \sigma} (\varepsilon^d - \mu) d_{i\sigma}^\dagger d_{i\sigma} + U \sum_i n_{i,\uparrow}^d n_{i,\downarrow}^d + \sum_{\vec{k}, i, \sigma} (V_{\vec{k}, i} c_{\vec{k}\sigma}^\dagger d_{i\sigma} + h.c.).$$

Reducing the lattice problem to a local problem can be done via the *cavity construction*, which singles out a specific lattice site, canonically chosen as $i = 0$. Historically, DMFT was derived using the path-integral formalism. We will follow a different path here, working with the equation of motion definition of the Green function, c.f. Sec. 2.2.1. For this, we shall separate the hybridization with the local impurity $H_{\text{loc}}^{cd} = \sum_{\vec{k}, \sigma} V_{\vec{k}, 0} c_{\vec{k}\sigma}^\dagger d_{0\sigma} + h.c.$ from the rest of the Hamiltonian H_{rest} . In the course of deriving the DMFT equations, we will use \mathcal{G} for full Green functions and \mathbf{G}^\emptyset for Green functions with the local hybridization removed. When indices are not given, the objects should be understood as matrices. The full Green function is defined via

$$\mathbb{1} = [i\omega_n \mathbb{1} - \mathbf{H}] \mathcal{G} \quad (5.148)$$

$$\Leftrightarrow \mathbb{1} = [i\omega_n \mathbb{1} - H_{\text{rest}} - H_{\text{loc}}^{cd}] \mathcal{G} \quad (5.149)$$

$$\Leftrightarrow [i\omega_n \mathbb{1} - H_{\text{rest}}] \mathcal{G} = \mathbb{1} + H_{\text{loc}}^{cd} \mathcal{G} \quad (5.150)$$

$$\Leftrightarrow \underbrace{\left(\frac{1}{i\omega_n \mathbb{1} - H_{\text{rest}}} \right)}_{=: \mathbf{G}^\emptyset} [i\omega_n \mathbb{1} - H_{\text{rest}}] \mathcal{G} = \left(\frac{1}{i\omega_n \mathbb{1} - H_{\text{rest}}} \right) [\mathbb{1} + H_{\text{loc}}^{cd} \mathcal{G}] \quad (5.151)$$

$$\Leftrightarrow \mathcal{G} = \mathbf{G}^\emptyset + \mathbf{G}^\emptyset H_{\text{loc}}^{cd} \mathcal{G}. \quad (5.152)$$

Fixing the position to be at the cavity site $i = j = 0$ we get for $\mathcal{G}_{i=0, j=0} = \mathcal{G}_{\text{loc}}$, in flavor-space (c.f. Sec. 2.2.1)

$$\begin{pmatrix} \mathcal{G}^c & \mathcal{G}^{cd} \\ \mathcal{G}^{dc} & \mathcal{G}^d \end{pmatrix}_{\text{loc}} = \begin{pmatrix} \mathbf{G}^{c\emptyset} & 0 \\ 0 & \mathbf{G}^{d\emptyset} \end{pmatrix}_{\text{loc}} + \left[\begin{pmatrix} \mathbf{G}^{c\emptyset} & 0 \\ 0 & \mathbf{G}^{d\emptyset} \end{pmatrix} \begin{pmatrix} 0 & \mathbf{V} \\ \mathbf{V}^\dagger & 0 \end{pmatrix} \begin{pmatrix} \mathcal{G}^c & \mathcal{G}^{cd} \\ \mathcal{G}^{cd} & \mathcal{G}^c \end{pmatrix} \right]_{\text{loc}}, \quad (5.153)$$

Each Green function is still to be understood as a matrix in other quantum numbers, e.g. spin. The local cavity Green function $\mathbf{G}_{\text{loc}}^\emptyset$ is flavor-diagonal due to the local hybridization being exactly factored out from the definition. Iterating this Dyson equation once decouples the diagonal and off-diagonal Green functions.

$$\begin{pmatrix} \mathcal{G}^c & \mathcal{G}^{cd} \\ \mathcal{G}^{cd} & \mathcal{G}^d \end{pmatrix}_{\text{loc}} = \begin{pmatrix} \mathbf{G}^{c\emptyset} & 0 \\ 0 & \mathbf{G}^{d\emptyset} \end{pmatrix}_{\text{loc}} + \begin{pmatrix} 0 & \mathbf{G}^{c\emptyset} \mathbf{V} \mathbf{G}^{d\emptyset} \\ \mathbf{G}^{d\emptyset} \mathbf{V}^\dagger \mathbf{G}^{c\emptyset} & 0 \end{pmatrix}_{\text{loc}} \quad (5.154)$$

$$+ \left[\begin{pmatrix} \mathbf{G}^{c\emptyset} & 0 \\ 0 & \mathbf{G}^{d\emptyset} \end{pmatrix} \begin{pmatrix} 0 & \mathbf{V} \\ \mathbf{V}^\dagger & 0 \end{pmatrix} \underbrace{\begin{pmatrix} \mathbf{G}^{c\emptyset} & 0 \\ 0 & \mathbf{G}^{d\emptyset} \end{pmatrix} \begin{pmatrix} 0 & \mathbf{V} \\ \mathbf{V}^\dagger & 0 \end{pmatrix}}_{=: \Delta} \begin{pmatrix} \mathcal{G}^c & \mathcal{G}^{cd} \\ \mathcal{G}^{cd} & \mathcal{G}^d \end{pmatrix} \right]_{\text{loc}} \quad (5.155)$$

$$\Delta = \begin{pmatrix} \mathbf{V} \mathbf{G}^{d\emptyset} \mathbf{V}^\dagger & 0 \\ 0 & \mathbf{V}^\dagger \mathbf{G}^{c\emptyset} \mathbf{V} \end{pmatrix} = \begin{pmatrix} \Delta^c & 0 \\ 0 & \Delta^d \end{pmatrix} \quad (5.156)$$

The hybridization \mathbf{V} is local only in d , so Δ^d involves an internal sum over momenta but is still local.

In contrast, Δ^c has external momenta \vec{k} and \vec{k}' with $\vec{k} = \vec{k}'$ due to translation symmetry. Details of this are discussed later and are not relevant right now. The diagonal parts of the Dyson equation can be read-off from above:

$$\mathcal{G}^c = \mathbf{G}^{c\phi} + \mathbf{G}^{c\phi} \Delta^c \mathcal{G}^c \quad \text{with} \quad \Delta^c = \mathbf{V}^\dagger \mathbf{G}^{d\phi} \mathbf{V} \quad (5.157)$$

$$\mathcal{G}^d = \mathbf{G}^{d\phi} + \mathbf{G}^{d\phi} \Delta^d \mathcal{G}^d \quad \text{with} \quad \Delta^d = \mathbf{V} \mathbf{G}^{c\phi} \mathbf{V}^\dagger \quad (5.158)$$

Since we split off the local hybridization, the local impurity is decoupled from the rest of the system and only couples to the rest via the local Dyson equation. This is also a consequence of the self-energy locality DMFT assumption. If the impurity self-energy obtains non-local contributions, the cavity impurity electron will obtain a non-locality that allows for a conversion to c -electrons on remote sites even without local hybridization. In this case, the flavor-diagonal approximation of the local \mathbf{G}^ϕ would break down.

In Section 3.3, a full solution of the Hamiltonian was not presented. It is, however, very similar to the resonant-level model if we assume to have access to the local self-energy. The solution for the impurity can be taken from Eq. (2.44) replacing the free resonant-level Green-function $G^{d(0)}$ by the local, interacting cavity Green-function and the free hybridization function $|V|^2 G^{c(0)}$ by the hybridized cavity Green-function

$$\mathbf{G}^{d\phi}(\omega) = \left(\left[\omega - \varepsilon^d - \mu \right] \mathbb{1} - \Sigma^d(\omega) \right)^{-1} \Rightarrow \mathcal{G}_{\text{loc}}^d(\omega) = \left(\left[\omega - \varepsilon^d - \mu \right] \mathbb{1} - \Delta^d(\omega) - \Sigma^d(\omega) \right)^{-1}. \quad (5.159)$$

The local model is, therefore, just an SIAM with the effective, local conduction-electron Green function $\Delta^d(\omega)$ and hybridization $\mathbb{1}$, implicitly defining the renormalized conduction-electron background. It is important to emphasize this since the hybridization can not always be decoupled from the conduction-electron Green function. Still, we can always solve for $\Delta^d(\omega)$ within DMFT. In the case of a fully local hybridization, the conduction-electron cavity Green function becomes local via $\Delta^d = \mathbf{V}_{\text{loc}} \mathbf{G}_{\text{loc}}^{c\phi} \mathbf{V}_{\text{loc}}^\dagger$ allowing for an interpretation of $\mathbf{G}_{\text{loc}}^{c\phi}$ as the effective, local conduction-electron background¹².

Since this can be solved via a local impurity solver—NCA in our case—we are left with relating the local quantity to the lattice Green function. In order to form a self-consistent set of equations, we need an equation Δ^d in terms of known or computable quantities. The first step towards achieving this is realizing that, once the local impurity self-energy is known, we can solve the system in the same way as we did in the two-band hybridization model (c.f. Sec. 2.3), now allowing for intrinsic structure by promoting objects in flavor-space to matrices of e.g. spin and replacing $\mathbf{G}_{\vec{k}}^{d0}$ by $\mathbf{G}^{d\phi}$ from equation (5.159). The solution for the conduction-electron part is just

$$\mathcal{G}_{\vec{k}}^c = \left(\left[\omega - \varepsilon_{\vec{k}}^c - \mu \right] \mathbb{1} - \Delta_{\vec{k}}^c \right)^{-1} = \left(\left[\omega - \varepsilon_{\vec{k}}^c - \mu \right] \mathbb{1} - \mathbf{V}_{\vec{k}}^\dagger \mathbf{G}_{\text{loc}}^{d\phi} \mathbf{V}_{\vec{k}} \right)^{-1}, \quad (5.160)$$

where the \vec{k} -diagonality is guaranteed by lattice translational symmetry and thus explicitly used here. The cavity Green function $\mathbf{G}_{\text{loc}}^{d\phi}$ can be computed using Eq. (5.158). The quantity $\Delta_{\vec{k}}^c$ is often called

¹² The term *background* is unfortunately not used consistently in literature. Sometimes, the background is defined as the contributions from the full system with the *full* site $i = 0$ removed, sometimes—especially in the case of the PAM—it refers to the local cavity Green function. Both are also sometimes called the *Weiss field* of DMFT.

the conduction-electron self-energy. A few remarks have to be made here. First, it can not be a proper self-energy, which can be immediately seen from the fact that it is non-local, which should not be allowed in our approximation. Stemming from a quadratic term in the Hamiltonian, it could be called the c -electron *hybridization function*. It does, however, contain interactions indirectly via the *local* $\mathbf{G}_{\text{loc}}^{d\phi}$, which does contain the local impurity self-energy. Therefore, the c -electron hybridization function is also a self-energy, containing processes from interactions of the hybridized particles. The interactions purely contributing in the local part and the non-locality stemming from the quadratic part justifies the non-locality of $\Delta_{\vec{k}}^c$ despite the DMFT assumption.

Finally, let's multiply Eq. (5.160) with the local hybridization from left and right and sum over \vec{k} to get

$$\sum_{\vec{k}} \mathbf{V}_{\vec{k}} \mathcal{G}_{\vec{k}}^c \mathbf{V}_{\vec{k}}^\dagger = \sum_{\vec{k}} \mathbf{V}_{\vec{k}} \left(\left[\omega - \varepsilon_{\vec{k}}^c - \mu \right] \mathbb{1} - \Delta_{\vec{k}}^c \right)^{-1} \mathbf{V}_{\vec{k}}^\dagger, \quad (5.161)$$

which is a local quantity $(\mathbf{V} \mathcal{G}^c \mathbf{V}^\dagger)_{\text{loc}}$. Extending Eq. (5.157) in the same way gives

$$\left(\mathbf{V} \mathcal{G}^c \mathbf{V}^\dagger \right)_{\text{loc}} = \left(\mathbf{V} \mathbf{G}^{c\phi} \mathbf{V}^\dagger \right)_{\text{loc}} + \left(\mathbf{V} \mathbf{G}^{c\phi} \mathbf{V}^\dagger \mathbf{G}^{d\phi} \mathbf{V} \mathcal{G}^c \mathbf{V}^\dagger \right)_{\text{loc}} \quad (5.162)$$

$$= \Delta^d + \Delta^d \mathbf{G}_{\text{loc}}^{d\phi} \left(\mathbf{V} \mathcal{G}^c \mathbf{V}^\dagger \right)_{\text{loc}} \quad (5.163)$$

$$\Leftrightarrow \Delta^d = \left(\mathbf{V} \mathcal{G}^c \mathbf{V}^\dagger \right)_{\text{loc}} \cdot \left[\mathbb{1} + \mathbf{G}_{\text{loc}}^{d\phi} \left(\mathbf{V} \mathcal{G}^c \mathbf{V}^\dagger \right)_{\text{loc}} \right]^{-1}, \quad (5.164)$$

closing the self-consistent loop¹³.

The DMFT Loop

Collecting all results from above, the DMFT loop is:

- (0.) Initial guess for Δ_{loc}^d
 1. $\mathcal{G}_{\text{loc}}^d [\Delta_{\text{loc}}^d]$ via a SIAM solver
 2. $\mathbf{G}_{\text{loc}}^{d\phi} = \mathcal{G}^d (1 + \Delta^d \mathcal{G}^d)^{-1}$
 3. $\Delta_{\vec{k}}^c = \mathbf{V}_{\vec{k}} \mathbf{G}_{\text{loc}}^{d\phi} \mathbf{V}_{\vec{k}}^\dagger$
 4. $(\mathbf{V}^\dagger \mathcal{G}^c \mathbf{V})_{\text{loc}} = \sum_{\vec{k}} \mathbf{V}_{\vec{k}}^\dagger \left(\left[\omega - \varepsilon_{\vec{k}}^c - \mu \right] \mathbb{1} - \Delta_{\vec{k}}^c \right)^{-1} \mathbf{V}_{\vec{k}}$
 5. $\Delta^d = \left(\mathbf{V}^\dagger \mathcal{G}^c \mathbf{V} \right)_{\text{loc}} \cdot \left[\mathbb{1} + \mathbf{G}_{\text{loc}}^{d\phi} \left(\mathbf{V}^\dagger \mathcal{G}^c \mathbf{V} \right)_{\text{loc}} \right]^{-1}$
- (6.) Go back to step 1. and repeat until converged.

¹³ All of the above equations can be simplified substantially in the case of a local, scalar hybridization $\mathbf{V}_{\vec{k}} \rightarrow V_0$.

After convergence, the momentum-dependent conduction-electron density of states is just given by Eq. (5.160), and the local density of states is its momentum sum. For the impurities, we can again re-use the T -matrix results from the two-band hybridization model (c.f. Sec. 2.3) just as we did in Eq. (5.160) above, replacing $\mathbf{G}_{\vec{k}}^{d(0)}$ by $\mathbf{G}_{\text{loc}}^{d\phi}$ and respecting the matrix structure in all quantities to get¹⁴

$$\mathcal{G}_{\vec{k}}^d = \mathbf{G}_{\text{loc}}^{d\phi} + \mathbf{G}_{\text{loc}}^{d\phi} \mathbf{V}_{\vec{k}}^\dagger \mathcal{G}_{\vec{k}} \mathbf{V}_{\vec{k}} \mathbf{G}_{\text{loc}}^{d\phi}. \quad (5.165)$$

The momentum-dependence is thus purely generated from the conduction electrons. Summing over \vec{k} and reshaping this into the Dyson-equation (c.f. Appendix C.4) gives precisely Eq. (5.158).

¹⁴ This is allowed since the self-energy is local, restricting the interacting, unhybridized impurity Green function to the be local. Everything else works in an identical way.

Lattice Coherence of CEF States in YbRh_2Si_2

The formation of lattice-coherence in the context of heavy-fermion systems continues to be a topic of interest in strongly correlated systems since its inception in 1975 [51]. As discussed earlier in this thesis (c.f. Sec. 3.5), there is an aspect of competition between localization and de-localization inherent to the topic of Kondo lattices and, therefore, in lattices with localized states, e.g. f -shell. A prototypical example of such a heavy-fermion system is YbRh_2Si_2 , in which the Yb^{3+} ground state configuration is $[\text{Xe}]4f^{13}$, leaving a single hole in the f -shell.

Experiments have revealed many interesting phenomena in YbRh_2Si_2 ; most prominently, it is a heavy-fermion material. The first Kondo temperature¹ was estimated to $T_{K,1} \approx 80 - 100$ K [93] and the $\text{Yb } 4f^{13}$ crystal-field energy difference to the CEF ground state to $\Delta \approx 17, 25, 43$ meV [94]. Below $T_{\text{coh}} \approx 30$ K, which is also the CEF ground-state Kondo temperature $T_{K,0} =: T_K$, lattice coherence can be observed [12]. Around $T_N \approx 65$ mK a phase transition to an antiferromagnetic state was found [93]. This phase is unstable against external magnetic fields and is destroyed at $B_C \approx 60$ mT [93].

In this thesis, I will focus on the lattice coherence and attempt to explain the seemingly odd temperature-dependence of CEF contribution in the scanning tunneling microscopy (STM) spectra in [12].

6.1 Experimental observation of lattice coherence

When investigating heavy-fermion materials with STM, depending on the surface configuration, the voltage- and temperature-dependent differential conductance $g(V, T)$ depends in a non-trivial way on the Green functions of the system under observation. To a first approximation, it is given by the conduction-electron spectrum [12]. Under hybridization between the interacting impurity states with the free conduction electrons, one would typically expect avoided crossing (c.f. e.g. Sec. 2.3) leading to a reduction of itinerant-electron states around crossing points of the impurity- and conduction-electron spectra in momentum space. For low enough temperatures, the Kondo effect generates spectral weight of impurity states around the Fermi energy. Consequently, a dip in the local conduction-electron density of states around the Fermi energy will form in a temperature-dependent way. This was investigated by Ernst et al. in 2011 [12]; the measured differential conductance is shown in Fig. 6.1

¹ In Systems with small CEF splitting, A crossover from a collective Kondo effect of the CEF states to a CEF-resolved Kondo effect can be observed.

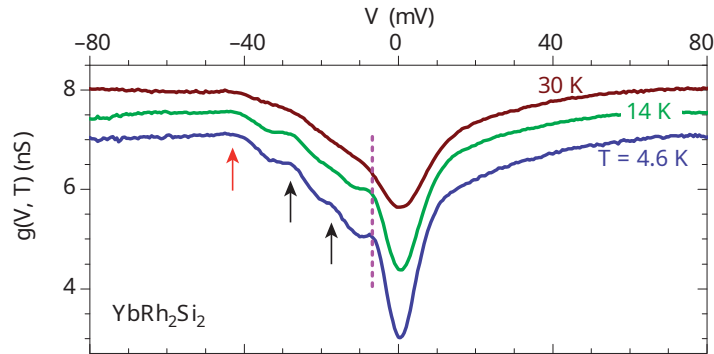
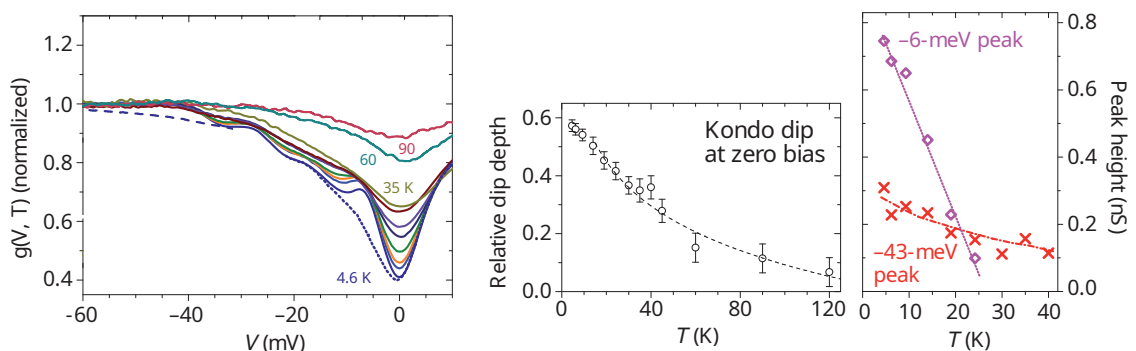


Figure 6.1: STM differential conductance of YbRh_2Si_2 for different temperatures, taken from Fig.2 in [12], cropped, panel label removed. The arrows indicate the expected CEF energies; the dashed line highlights the coherence peak.

(more temperatures are shown in Fig.6.2(a)). First, a clear dip can be seen as the highest temperature in the picture is already much below $T_{K,1}$. For lower temperatures, a peak at $E_C \approx -6$ mV arises next to the dip minimum, which the authors attribute to the formation of lattice coherence. At the same time, additional *peaks* appear at precisely the negative expected CEF energies of $\text{Yb } 4f^{13}$. A series of potential conflicts arise from those observations.

First, if the development of a Kondo peak in the impurity spectrum results in a *dip* in the conduction-electron spectrum, why should the additional CEF peaks in the impurity spectrum result in *peaks*, not *dips*?

Second, what is the relation between the coherence peak at $E_C \approx -6$ mV and the CEF peaks? The temperature dependence of the coherence peak appears to be fundamentally different from the temperature dependence of the dip at zero bias (Fig. 6.2(b)) and the CEF peaks, which can be seen from Fig. 6.2(c). Although the scaling is vastly different, both features emerge at the same temperature. Notably, the Kondo dip at zero bias behaves approximately logarithmic with a tendency to settle at the



(a) Temperature-dependent differential conductance. The dashed line is a guide to the eye.

(b) Temperature-dependent Kondo dip at zero bias.

(c) Comparison of temperature-dependent peak heights.

Figure 6.2: Temperature-dependent features of the STM differential conductance of YbRh_2Si_2 , taken from Fig.2 in [12], cropped, parts removed.

lowest temperatures. In contrast, the coherence peak continues to grow at the lowest temperatures.

In the following sections, I will discuss both questions stated above. First, a minimalistic, microscopic model is constructed to describe the system at hand faithfully. The numerical results, using DMFT with NCA as the impurity solver, are discussed and connected to the experimental results.

6.2 Minimalistic Microscopic Model

In order to construct a faithful model, we first need to determine the states involved in the dynamics. According to Hund's rules, the ground state of the $4f^{13}$ configuration is $J = 7/2$ (c.f. Sec. 4.2.2). The crystal-field splitting is governed by the tetragonal D_{4h} symmetry [93]. Using the analysis discussed in Section 4.3, the ground-state configurations can be identified as four Kramers-doublets. From those arguments, a regular spin- $1/2$ model with CEF states will suffice to give the correct physics. The CEF ground-states of $4f^{12}$ and $4f^{14}$ are expected to be spin-singlets.

Therefore, the periodic Anderson model with CEF states can be used to construct a faithful minimal model for the heavy-fermion physics in the non-ordered phases of YbRh_2Si_2 . In terms of Hubbard operators, it is

$$\begin{aligned}
H_{\text{PAM}}^{\text{YbRh}_2\text{Si}_2} = & H_c + \sum_{i,n,\sigma} \left(\varepsilon^d + \Delta_n \right) |i; f^{13}; n, \sigma\rangle \langle i; f^{13}; n, \sigma| \\
& + \varepsilon^b \sum_i |i; f^{12}\rangle \langle i; f^{12}| + \varepsilon^a \sum_i |i; f^{14}\rangle \langle i; f^{14}| \\
& + \sum_{i,n,\sigma} c_{i\sigma}^\dagger \left(V_n^{(b)} \text{sgn}(\sigma) |i; f^{12}\rangle \langle i; f^{13}; n, -\sigma| \right. \\
& \left. + V_n^{(a)} \text{sgn}(\sigma) |i; f^{13}; n, -\sigma\rangle \langle i; f^{14}| + h.c. \right), \quad (6.1)
\end{aligned}$$

where Δ_n is the microscopic crystal-field splitting of the excited CEF state number $n \in \{1, 2, 3\}$ and the multiplication with $\text{sgn}(\sigma)$ is due to the singlet nature of the excited states². Additionally, the energy difference between the $4f^{13}$ and the two excited states, $4f^{12}$ and $4f^{14}$, was estimated to $E_{13 \rightarrow 12} \approx 2.5$ eV and $E_{13 \rightarrow 14} \approx 1.4$ eV using a local-density approximation with local interactions (LDA+U) [95]. We can, therefore, safely apply the $\varepsilon^d \rightarrow -\infty$ approximation discussed in Section 5.3.7 to the model above. Under this approximation, the Hamiltonian, in terms of auxiliary particles, is

$$\begin{aligned}
H_{\text{PAM}}^{\text{YbRh}_2\text{Si}_2} = & H_c - \sum_{i,n,\sigma} \left(\varepsilon^d + \Delta_n + \lambda \right) f_{i,n\sigma}^\dagger f_{i,n\sigma} \\
& + (\varepsilon^a + \lambda) \sum_i a_i^\dagger a_i \\
& + \sum_{i,n,\sigma} \left(V_n^{(a)} \text{sgn}(\sigma) c_{i\sigma}^\dagger f_{i,n,-\sigma}^\dagger a_i + h.c. \right), \quad (6.2)
\end{aligned}$$

where the additional constant $-\lambda$ has been dropped. Utilizing the $U(1)$ symmetry to shift the energy

² Technically, a factor of $1/\sqrt{2}$ must be included to reproduce the correct Clebsch-Gordan coefficients. It can be absorbed into the hybridization strength.

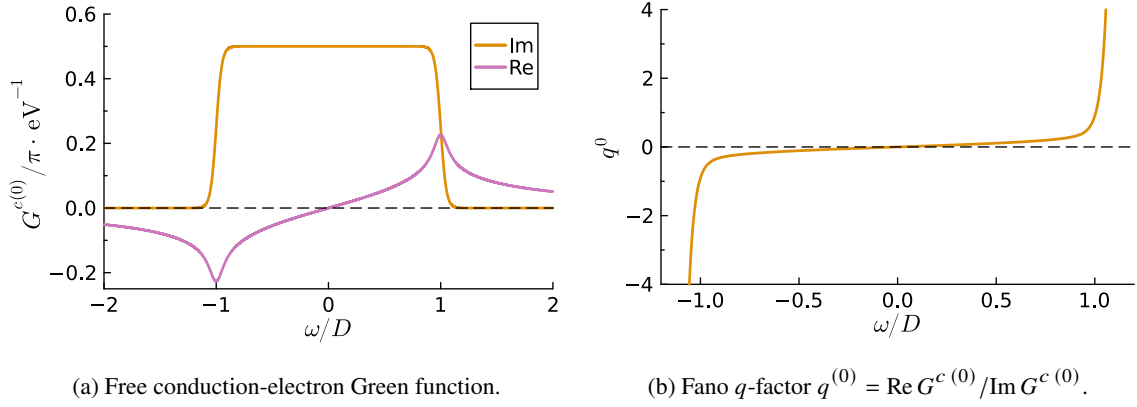


Figure 6.3: Free, model conduction-electron Green function according to Eq. (6.4) using the Kramers-Kronig relation to generate the real part and the q -factor of Eq. (6.6). The presented data is for $s = 2/D$.

ε^a from the boson to the Fermion, the final expression reads

$$\begin{aligned}
 H_{\text{PAM}}^{\text{YbRh}_2\text{Si}_2} = & H_c - \sum_{i,n,\sigma} \left(\tilde{\varepsilon}^d + \Delta_n + \lambda \right) f_{i,n\sigma}^\dagger f_{i,n\sigma} \\
 & + \lambda \sum_i a_i^\dagger a_i \\
 & + \sum_{i,n,\sigma} V_n^{(a)} \text{sgn}(\sigma) c_{i\sigma}^\dagger f_{i,n,-\sigma}^\dagger a_i + h.c. \Big), \quad (6.3)
 \end{aligned}$$

where $\tilde{\varepsilon}^d = \varepsilon^d - \varepsilon^a = E_{13 \rightarrow 14} \approx 1.4$ eV.

The free conduction-electron density of states is approximated by a box of width $2D$ with smooth edges

$$\rho^c(0)(\omega, s) = \{ \tanh[s(\omega + D)] - \tanh[s(\omega - D)] \} / 4D, \quad (6.4)$$

where s controls the sharpness of the flanks in the same way as the inverse temperature β does in the Fermi-Dirac distribution. It is plotted in Fig. 6.3(a) This choice of free DOS is beneficial for investigating the questions mentioned above due to its featureless shape in the region of interest.

The Hamiltonian presented above does not explicitly contain the chemical potential. We can define an effective chemical potential that suffices for the model calculation, coupling directly and exclusively to c , allowing for modeling the filling of the band while keeping the impurity parameters untouched. This filling is only model-related and does *not* reflect the actual filling of conduction-electron bands. Here, it is used exclusively to control the phase between $\text{Im } G^c(\omega)$ and $\text{Re } G^c(\omega)$, as will be discussed in the next section.

Extension of DMFT and NCA for CEF States

Solving this model requires extending the previously derived DMFT and NCA equations by the additional CEF states. The NCA was formulated with a matrix structure in spin-space in mind. It can, therefore, be straightforwardly extended to multiple Kramers-doublet CEF levels. The matrix

structure, as it was used before, still describes spin. Spin flip and transposition work in spin space. Superimposed on that is a CEF-level matrix structure to which those operations don't apply. In fact, since the CEF level only appears in the f -electron, the grand sum³ over the CEF index n has to be taken in Eq. (5.120) for the Boson self-energy. Additionally, Eq. (5.130) for G^d then has to be understood as the impurity part of the T -matrix *and* the object used to generate the impurity spectrum. It is meaningful in the same sense as Hubbard operators generate correct T -matrices and spectra. But since we can *not* generate canonically commuting effective fields in this framework, one should be careful with interpretation and terminology. Most things work as expected, but the objects don't describe the *impurity electron*, but rather the impurity states.

Lastly, the conduction electrons don't have the same quantum numbers as the local impurity states and are, therefore, oblivious to this quantum number. In the same way that makes local scattering fully off-diagonal in \vec{k} -space, the hybridization will make the pseudo-fermion f fully off-diagonal in n while maintaining the σ structure, which is typically diagonal. An argument can be made that different CEF multiplets should not mix *if* the hybridization does not break CEF symmetry, which is what I assume for this model calculation. This has the benefit of reducing the level-repulsion between CEF states, relating the final splittings more closely to the model parameters.

It is generally unclear how much of this off-diagonality should be allowed. Technically, one would need to analyze the different wavefunctions of the CEF eigenstates and calculate the proper \vec{k} -dependent overlap of those with the conduction-electron Wannier functions, resulting in a set of *different* \vec{k} -dependent hybridizations $V_n(\vec{k})$. The local problem utilizes the (matrix) hybridization function $\Delta_{nn'}^d(\omega) = \sum_{\vec{k}\vec{k}'} \mathbf{V}_n(\vec{k}) \mathbf{G}_{\vec{k}\vec{k}'}^{c(0)}(\omega) \mathbf{V}_{n'}^\dagger(\vec{k}')$, which could lead to much smaller off-diagonals in n , if not to full diagonality.

6.3 The Fano-Lineshape in the Conduction-Electron Density of States

When measuring differential conductance with STM in the presence of a magnetic impurity, the spectrum obtains a Fano-lineshape from phase-shift effects due to the scattering [96]. Although being discussed first in the context of single magnetic impurities, the concept can be extended to the lattice case [97]. This is a general feature of *local* T -matrix equations, where the correction to the free DOS is, to first order, given by a Fano-lineshape if the imaginary part of the T -matrix has a sharp feature at the energy of interest. Since this is typically the case in Kondo systems, we can apply it to the situation at hand. The change of the conduction-electron DOS is given by [96]

$$\delta\rho^c(\omega) \propto \left[\rho^{c(0)}(\omega) \right]^2 \frac{2q\epsilon + q^2 - 1}{\epsilon^2 + 1}, \quad (6.5)$$

where $\epsilon = (\omega - \epsilon_K)/T_K$ with the position of the Kondo peak ϵ_K and $q = \text{Re } G^{c(0)A}(\epsilon_K)/\text{Im } G^{c(0)A}(\epsilon_K)$. The correction is strictly negative for $q = 0$, i.e. results in a dip in $\rho^c(\omega) = \rho^{c(0)}(\omega) + \delta\rho^c(\omega)$. The case of $q < 0$ ($q > 0$) results in a peak-dip (dip-peak) structure that eventually turns fully into a peak for $|q| \rightarrow \infty$. A few examples are shown in Fig. 6.4.

This concept can be extended to broader peaks in the T -matrix, although the validity of the approximation is reduced the broader the peak. In this case, one can define a continuous $q \rightarrow q(\omega)$ in

³ The grand sum is the sum over all matrix elements, i.e. $\sum_{ij} M_{ij}$.

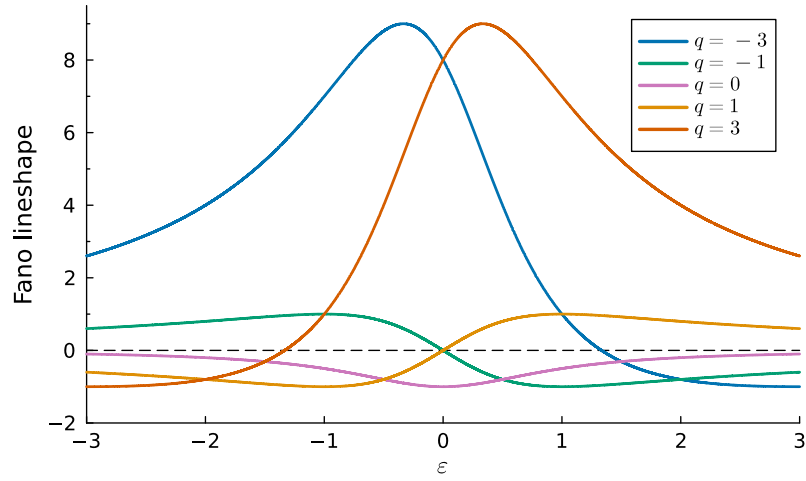


Figure 6.4: Fano lineshape depending on the Fano structure factor q as by the second term in Eq. (6.5).

energy. The primary role of μ in the model is, thus, controlling the q -factor by adjusting the Fermi energy, c.f. Fig. 6.3(b).

Another crucial observation is that this holds in *local* T -matrix equations. In the context of DMFT, the local T -matrix equation (c.f. Eq. (2.49))

$$\mathbf{G}_{\text{loc}}^c(\omega) = \mathbf{G}_{\text{loc}}^{c(0)}(\omega) + \mathbf{G}_{\text{loc}}^{c(0)}(\omega) \mathbf{T}_{\text{loc}}(\omega) \mathbf{G}_{\text{loc}}^{c(0)}(\omega) \quad (6.6)$$

is just

$$\mathbf{G}_{\text{loc}}^c(\omega) = \mathbf{G}_{\text{loc}}^{c\emptyset}(\omega) + \mathbf{G}_{\text{loc}}^{c\emptyset}(\omega) \Delta_{\text{loc}}^c(\omega) \mathbf{G}_{\text{loc}}^{c\emptyset}(\omega). \quad (6.7)$$

The relevant q -factor for determining the lineshape in the context of DMFT is thus given by $q(\omega) = \text{Re} G^{c\emptyset A}(\omega) / \text{Im} G^{c\emptyset A}(\omega)$, which is dynamically generated by the self-consistency loop⁴. The *free* q -factor is plotted in Fig. 6.3(b).

6.4 Numerical Results and Interpretation

In the model calculation, all four CEF states have been taken into account with equal hybridization strength. The parameters of Eq. (6.3) are given in Tab. 6.1.

D	μ	s	$\tilde{\varepsilon}^d$	Δ_1	Δ_2	Δ_3	V^2/D
2 eV	-1.2 eV	10 eV ⁻¹	-1.4 eV	17 meV	25 meV	43 meV	0.074

Table 6.1: Model parameters of Eq. (6.3) used in the numerical calculations.

⁴ This might ultimately be how DMFT generates lattice-coherence and develops Fermi-liquid behavior—a thought to be investigated in future work.

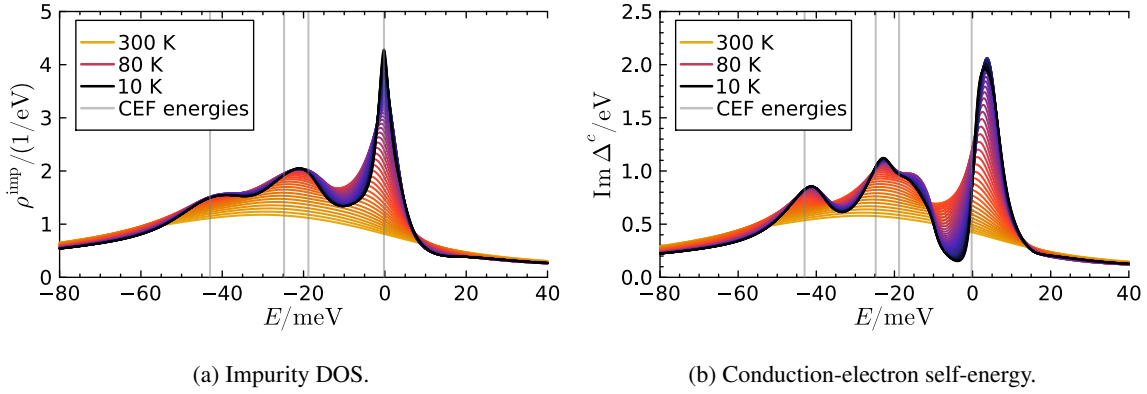


Figure 6.5: Impurity density of states for the YbRh_2Si_2 model and the conduction-electron self-energy Δ^c for different temperatures. Vertical gray lines mark the renormalized CEF energies, c.f. Fig. 6.6(b).

6.4.1 Density of States

The temperature-dependent impurity DOS is shown in Fig. 6.5(a), the $T = 10$ K DOS in Fig. 6.6. Each individual CEF contribution gives a peak at exactly the expected energy *below* the Fermi energy. From multi-orbital (or multi CEF-state) systems, one would expect Kondo peaks to appear at all positive and negative crystal field splittings [98, 99]. As illustrated in Fig. 6.7, virtual transitions starting from the CEF ground state will prevail at zero temperature, thus leading to a Kondo effect. The green, full lines in Fig. 6.7(a) correspond to the second-order process, giving rise to the Kondo effect with an energy difference of zero. The other transition, although also of zero energy, is thermally suppressed due to the depletion of the excited CEF state. Equally, the transition marked with dashed brown lines in Fig. 6.7(b) produces a peak above the Fermi energy, which is thermally suppressed. The full orange lines in Fig. 6.7(b) represent an allowed process, generating a Kondo side-peak below the Fermi energy. Although the energy difference is positive, the spectrum of a system takes energy differences

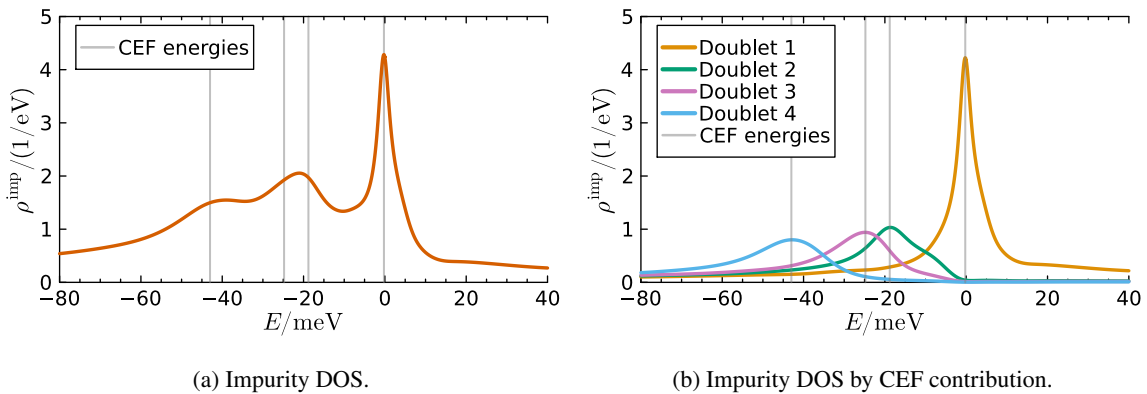


Figure 6.6: Impurity density of states for the YbRh_2Si_2 model at a fixed temperature $T = 10$ K. Vertical gray lines mark the renormalized CEF energies.

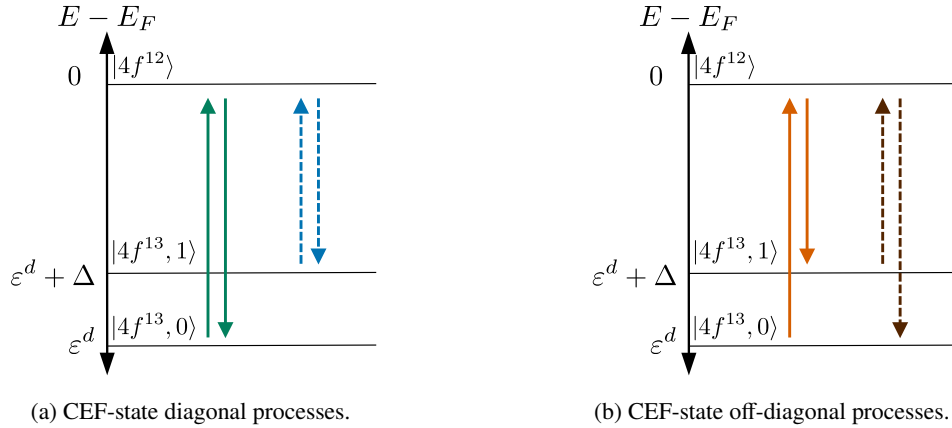


Figure 6.7: Reduced level structure of an Yb^{3+} ion, considering the excited $4f^{12}$ configuration and two CEF states of the $4f^{13}$ valence ground state. Full, colored lines represent contributions to the Kondo effect; dashed lines represent thermally forbidden transitions at zero temperature.

under the removal of a particle. Additions of particles enter with the negative energy⁵. Consequently, peaks below the Fermi energy are *additional* Kondo peaks due to the presence of excited CEF states. Their temperature dependence decreases below the Kondo temperature, whereas the *main* Kondo peak still develops. Peaks above the Fermi energy are strongly suppressed for this set of parameters.

Unfortunately, the individual character of the two lowest-lying CEF states (Fig. 6.6(b)) gets lost in the trace over the contributions, which can be seen in Fig. 6.6(a). Those two contributions merge into a single, larger, and broader peak. In the conduction-electron self-energy (Fig. 6.5(b)), this contribution seems to get disentangled though. Consequently, the conduction electrons get influenced by the individual crystal field states, although not sharply separated.

6.4.2 Conduction-Electron Density of States and q -Factor

The hallmark feature of the experiment lies in the conduction-electron density of states. The numerical results for the density of states at different temperatures are shown in Fig. 6.8. A guide to the eye was added by subtracting a Lorentzian from the free DOS to fit both the dip-depth and the large- $|\omega|$ behavior at the lowest temperature shown. The appearance of a *coherence peak* is nicely visible, and the overall shape matches the experimental data, although some quantitative differences are observable.

First, the *first* Kondo temperature does match the expected result; the DOS suppression is, however, much stronger than in the experiment. There, the DOS is flat at room temperature and only below around $T \approx 100$ K a broad dip develops, c.f. Fig. 6.2(a). Here, at $T = 300$ K, the suppression is already substantial. Second, the coherence peak is very pronounced and starts developing at much larger temperatures. The coherence-peak and Kondo dip positions are offset to the right by approx. 8 meV, their difference is approx. 12 meV, which is double the experimental value of 6 meV. Third, the CEF peak positions are shifted. The first peak is approximately at the correct position; the other two peaks are at lower energies than expected.

In order to investigate the structure further, the peak positions have to be analyzed in the context of

⁵ The same concept but with reversed energies applies to particle-like systems [99].

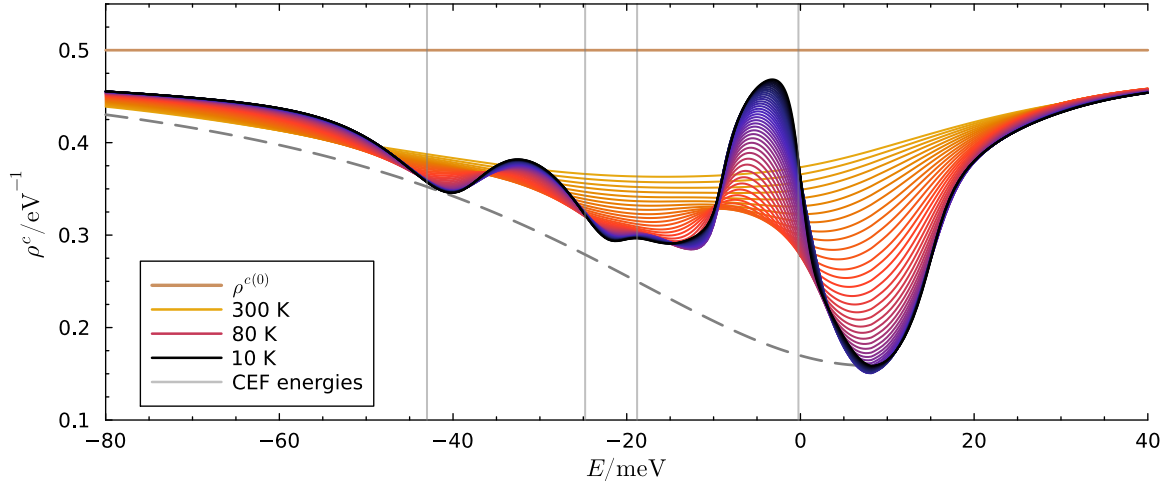


Figure 6.8: Conduction-electron density of states for the YbRh_2Si_2 model for different temperatures. The gray dashed line is a guide to the eye generated from subtracting a Lorentzian from the free conduction-electron density of states. Vertical gray lines mark the renormalized CEF energies, c.f. Fig. 6.6(b).

renormalized CEF states. This can be best seen in the side-by-side comparison in Fig. 6.9. Let's go from right to left. There is a clear asymmetry in the conduction-electron DOS at the position of the first (main) Kondo peak in the impurity DOS. It is, however, not exactly antisymmetric and cannot be directly attributed to a Fano resonance. The origin of this will be discussed in detail in the next section. The first feature generated by an excited CEF state is a clear peak precisely at the position of the first CEF state in the impurity spectrum. Both results are compatible with the experiment.

Next, there is neither a clear peak nor a clear dip in the conduction-electron DOS at the positions of the next two CEF contributions to the impurity DOS. The shown features can possibly be explained by the Fano-lineshape, for which we need to investigate the q -factor, shown in Fig. 6.10(a). Although it does vary largely over the small energy scale of interest, just q alone does not suffice for an analysis. According to Eq. (6.5), the correction is weighted by the conduction-electron DOS, which is the local cavity conduction-electron in DMFT. It was defined as $G_{\text{loc}}^{c\phi} = \mathcal{G}_{\text{loc}}^{c\phi} / (1 + \Delta_{\text{loc}}^c \mathcal{G}_{\text{loc}}^{c\phi})$ and is shown in Fig. 6.10(b). By combining both q -factor and effective DOS and comparing them to the Fano-lineshapes of Fig. 6.4, each individual energy section can be analyzed.

From right to left, we first get a strong peak in the local effective DOS combined with a weakly negative q -factor, resulting in a dip-like structure. Closer to the Fermi energy, the effective DOS approaches a local minimum, and the q -factor approaches $q = -3$, resulting in an increase in the full local DOS, roughly following the lineshape of $\rho_{\text{loc}}^{c\phi}$. This continues up to a local maximum of the DOS below the Fermi energy, which, coupled with an increase of the q -factor to $q = -0.5$ results in a peak-dip contribution, broadening and deforming the coherence peak in the full local DOS when compared to the effective cavity DOS.

Below the energy of the coherence peak, the q -factor varies slowly and is approximately $q = -1$ such that the CEF state contributions get shifted to smaller energies, which explains the discrepancy between the experiment and the presented model calculation. A more intricate modeling of the free conduction-electron DOS or even a \vec{k} -dependent hybridization might be able to remedy this.

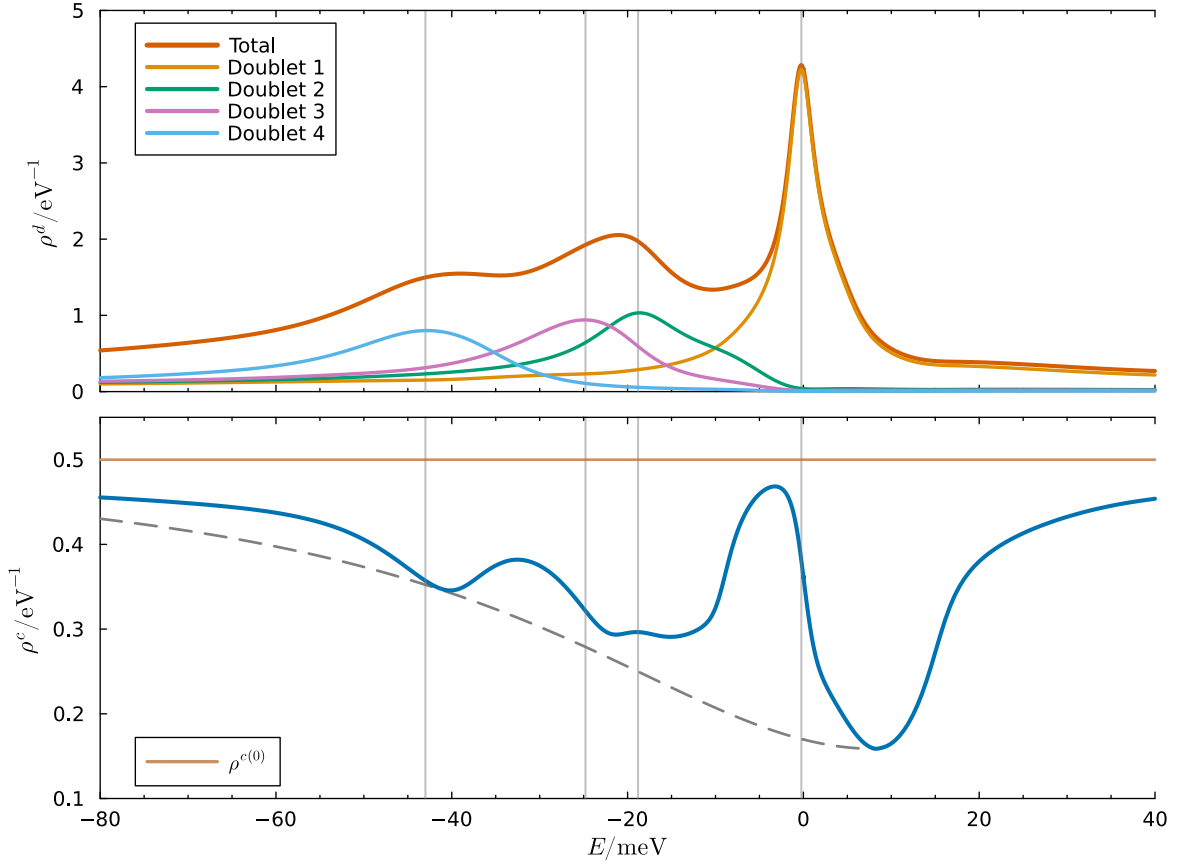
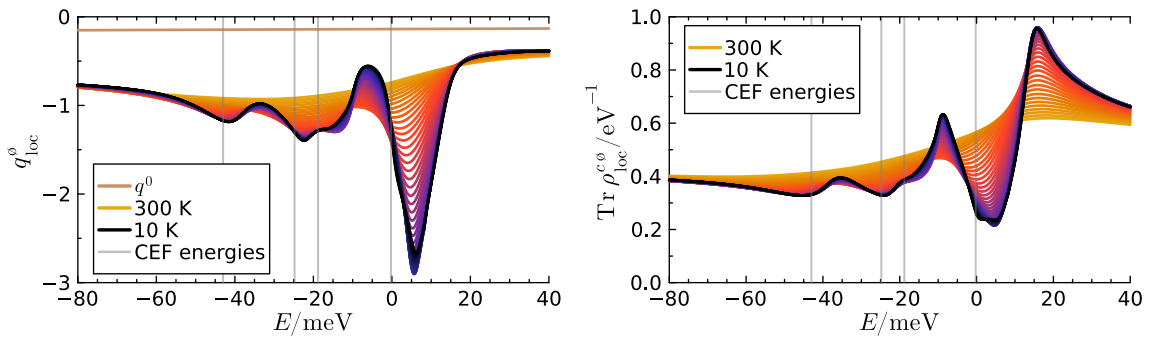


Figure 6.9: Top: Impurity density of states in total and by CEF contribution. Bottom: Conduction-electron density of states for the YbRh_2Si_2 model for $T = 10$ K. The gray dashed line is a guide to the eye generated from subtracting a Lorentzian from the free conduction-electron density of states. Both: Vertical gray lines mark the renormalized CEF energies, c.f. Fig. 6.6(b).

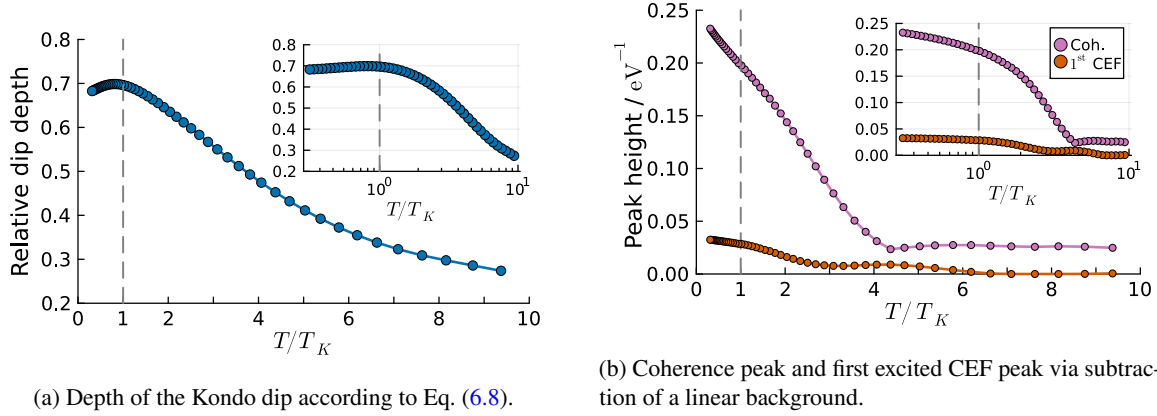


(a) DMFT effective local conduction-electron q -factor.

(b) DMFT effective local conduction-electron DOS.

Figure 6.10: DMFT local-model q -factor and density of states of an effective conduction-electron background. The Green function is defined via $G_{\text{loc}}^{c,0} = \mathcal{G}_{\text{loc}}^{c,0} / (1 + \Delta_{\text{loc}}^c \mathcal{G}_{\text{loc}}^{c,0})$. Vertical gray lines mark the renormalized CEF energies.

6.4.3 Dip Depth and Peak Heights



(a) Depth of the Kondo dip according to Eq. (6.8).

(b) Coherence peak and first excited CEF peak via subtraction of a linear background.

Figure 6.11: Kondo dip and two peak heights of Fig. 6.8. The Kondo temperature $T_K = 32$ K was estimated via the half width at half maximum of the CEF ground-state Kondo peak.

A central feature of the experimental results is the temperature dependence of the different peaks compared to the temperature dependence of the Kondo dip. The latter is shown in Fig. 6.11(a). The data points were extracted from the numerically generated data using the minimum of the conduction-electron DOS in the region $[-30 \text{ meV}, 10 \text{ meV}]$, $\rho^c(\omega_0)$ and the free DOS value at the peak $\rho^c(0)(\omega_0)$. The shown data is

$$[\rho^c(\omega_0, T) - \rho^c(0)(\omega_0)] / \rho^c(0)(\omega_0). \quad (6.8)$$

The dip shows a small region of logarithmic increase around $5T_K$ and banks off around T_K , slightly decreasing below. This behavior is not quite as in the experiment and could stem from the much broader coherence peak influencing the value at the minimum.

Comparing the temperature dependence of the coherence peak and the CEF peak to this is now essential to understanding the underlying physics. For this, a temperature-dependent background has to be subtracted in order to confidently generate peak heights. The method used in [12] can not be used here due to the strong asymmetry. Although a possible alternative, the subtraction of a Lorentzian turns out to be too uncontrolled for a proper analysis. A much simpler but also more robust method is fitting a straight line connecting the flanks of each peak. The peak height is then estimated by subtracting this straight line from the data in the region and taking the maximum. The coherence peak and the first excited CEF peak data extracted in this way are shown in Fig. 6.11(b).

The coherence peak has a much larger total value and grows stronger than the first CEF peak. The latter still grows for small temperatures but with a small slope. The general behavior is compatible with the experiment. However, the experimental data only shows the highest excited CEF peak, which we can not faithfully compare here due to the previously mentioned differences between the model and the experiment.

6.4.4 Spectral Function and Orbitally Selective Lattice Coherence

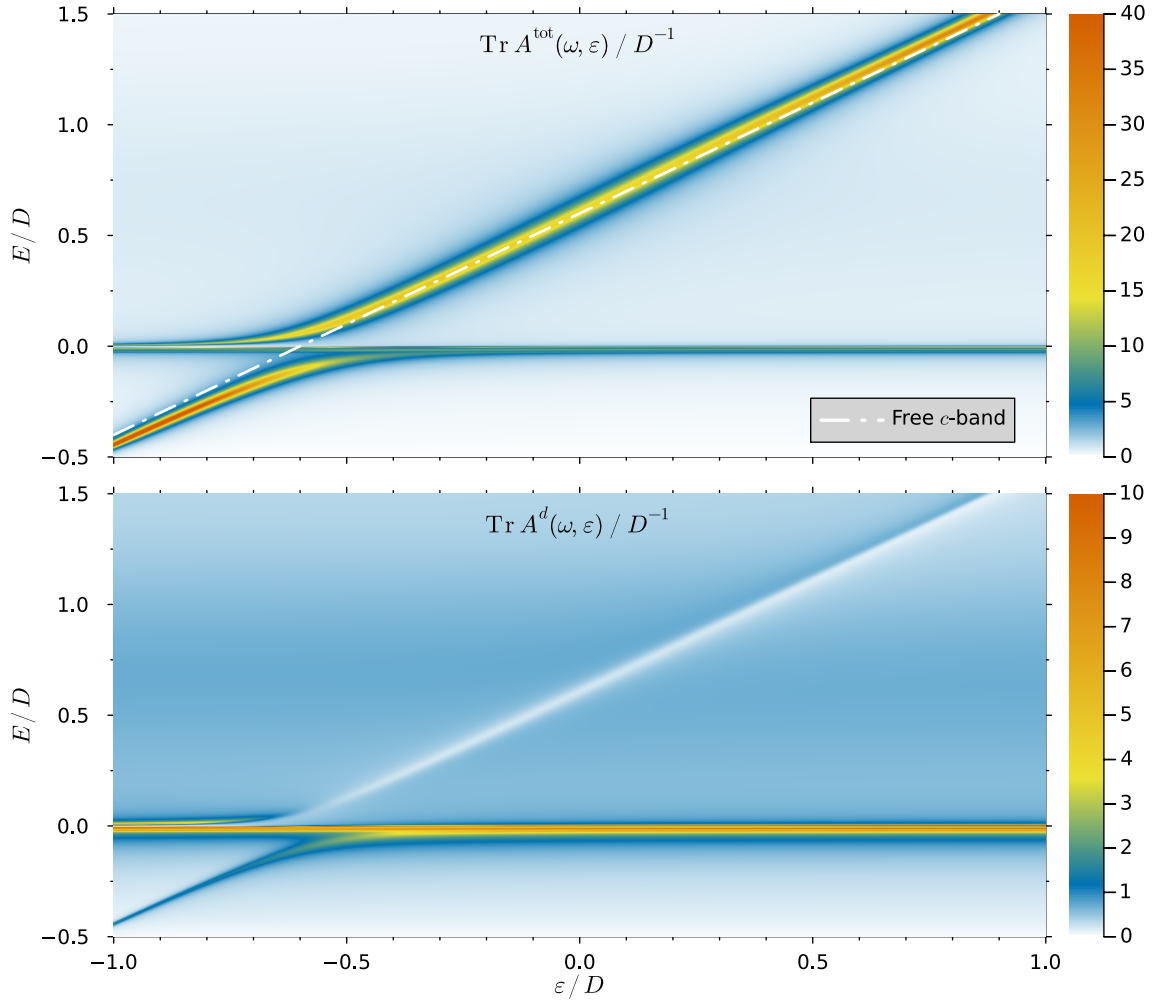


Figure 6.12: Spectral function for the YbRh_2Si_2 model at $T = 10 \text{ K}$ ($T \approx T_K/3$) plotted against the excitation energy and the dispersion ε . The energy is relative to the Fermi energy, including chemical potential. Upper panel: Total spectral function, i.e. $\text{Tr Im } G(\omega, \varepsilon)$. Lower panel: Impurity contribution to the upper panel on a *different* color-code scale to visualize the structure away from the Fermi energy.

Having discussed the similarities and differences between the experiment and the minimalistic model, the question of orbitally-selective lattice coherence can be addressed. For this, let's take a look at the spectral function, i.e. the \vec{k} -dependent spectral density. The model discussed above does not contain information about momenta, only the free density of states. We can, therefore, not investigate the *true* momentum dependence. Equivalently, one can plot the spectral function not against \vec{k} but against ε , which can be translated to momentum via the dispersion. This has the benefit of breaking down the structure to energetics and allowing for an investigation of spectra without knowing the exact \vec{k} -dependence. The spectrum over a wide range of energies is shown in Fig. 6.12.

First, the overall avoided crossing around the Fermi energy can be seen very well. Second, the

impurity contribution shows a clear curvature in parts of its structure, indicating lattice coherence. There is, however, a part that is bent and a part that appears still perfectly flat. This can be further investigated by looking at a small region around the Fermi energy, which is shown in Fig. 6.13. Here,

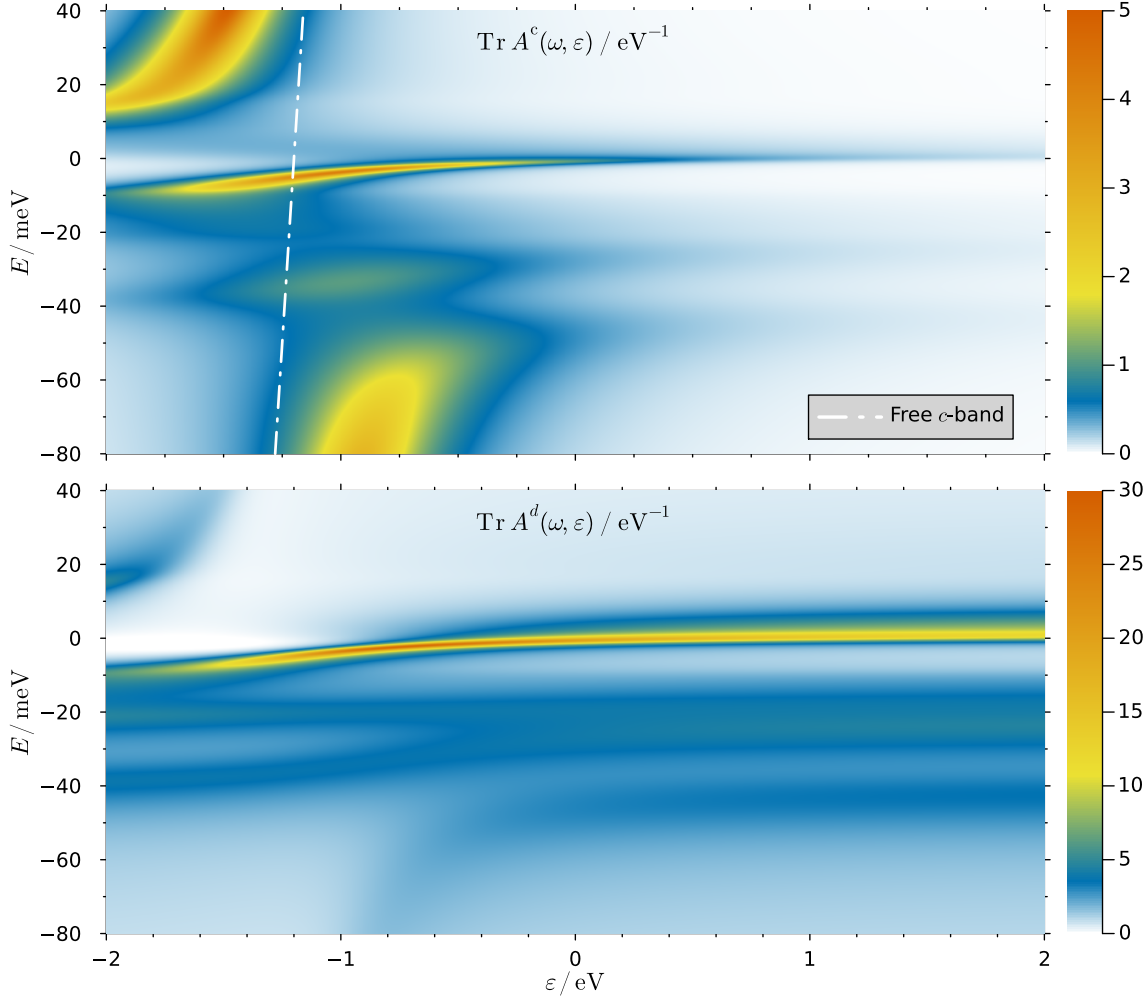


Figure 6.13: Spectral function for the YbRh_2Si_2 model at $T = 10 \text{ K}$ ($T \approx T_K/3$) plotted against the excitation energy and the dispersion ε in a narrow region around the Fermi energy. The energy is relative to the Fermi energy, including chemical potential. Upper panel: Conduction-electron contribution to the spectral function. The dashed-dotted line is the free band. Lower panel: Impurity contribution to the spectral function.

we can find several signatures of lattice coherence. First, the aforementioned avoided crossing, leading to the Kondo dip. Second, a heavy band appears in the conduction electrons *and* the impurities simultaneously, giving rise to the coherence peak in the conduction-electron DOS. Localized impurities would have a flat band⁶—the dominant contribution here is however a heavy, but *curved* band around the Fermi energy. The small peak above -20 meV in the DOS of Fig. 6.8 can be seen very weakly here in the form of a faint partial band.

⁶ For this, compare Fig. 2.8 of the resonant-level model and Fig. 2.9 of the two-band hybridization model.

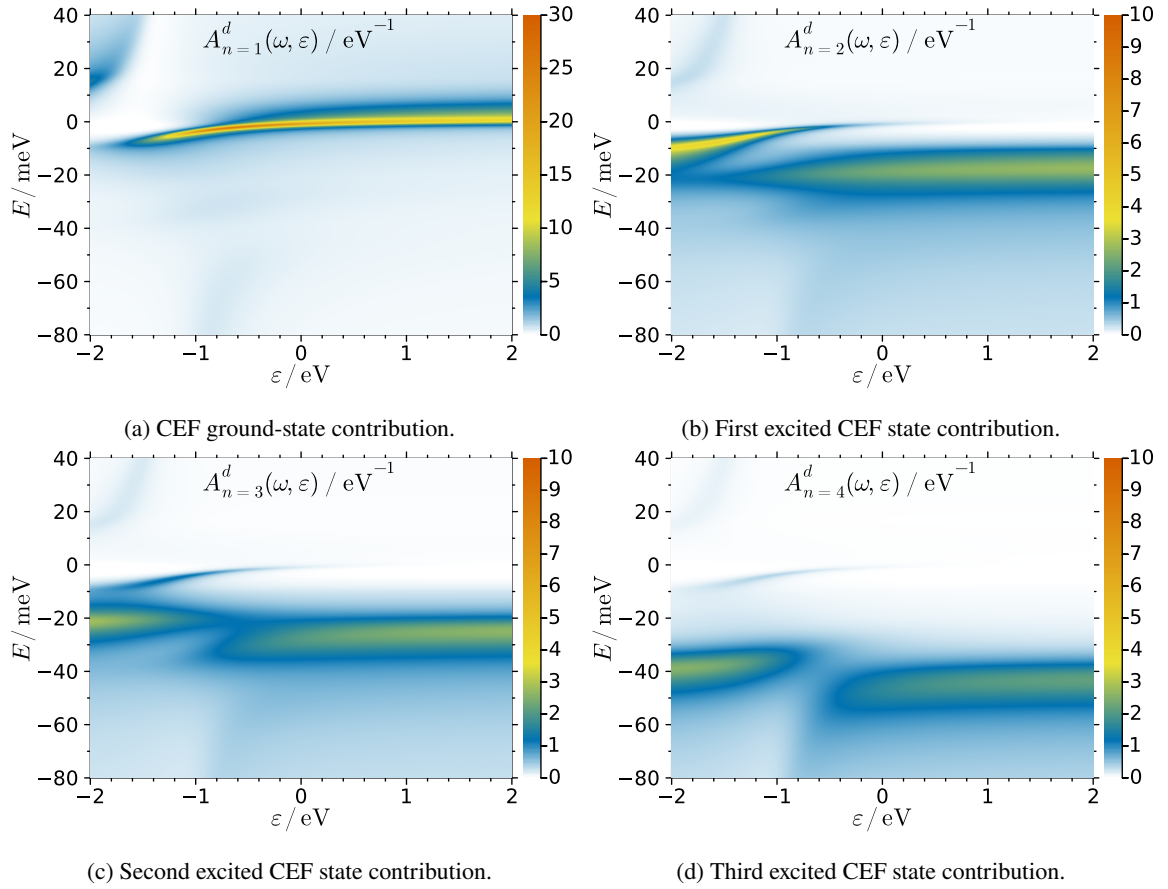


Figure 6.14: Individual Pr 4f CEF-state contribution to the spectral function for the YbRh_2Si_2 model at $T = 10\text{ K}$ ($T \approx T_K/3$) plotted against the excitation energy and the dispersion ε in a narrow region around the Fermi energy. The energy is relative to the Fermi energy, including chemical potential. The color-code scale in (b)-(c) differs from the scale in (a) and other Figures to enhance visibility.

Additionally, there is a reduction of conduction-electron spectral weight just below -20 meV alongside a *flat* band in the impurity spectrum. This can be attributed to the second excited CEF state. Below that, around -35 meV , an increase of spectral weight in the conduction-electron spectrum is encircled by impurity bands. This can be seen as a weak signature of lattice coherence. The final contribution is the lowest-lying, weakly curved band in the conduction electrons and a feint but clearly curved band in the impurities, which can be attributed to the highest excited CEF state.

In order to get a better overview of lattice coherence of different CEF states, each individual contribution is shown in Fig. 6.14. The CEF ground state shows a clear, curved band structure. The first excited state merges with the ground state to extend the band. Hence, the additional peak of this contribution to the DOS in Fig. 6.6(b). The other two contributions show partial traces of lattice coherence, although the band-like structure and curvature are much less pronounced.

6.5 Conclusion

The origin of the experimentally observed peaks inside the broad Kondo dip can be explained by the lattice coherence of individual CEF states in a minimalistic model.

The CEF ground state shows clear lattice coherence, hence a strong coherence peak arises in the local conduction-electron DOS. The first excited CEF state ($n = 2$) merges with the ground-state heavy band, showing a weaker yet clear sign of lattice coherence, resulting in a small peak in the conduction-electron DOS.

The second and third excited CEF states show weak signs of lattice coherence, the contribution to the central heavy band decreasing from $n = 2$ to $n = 4$. The influence on the conduction-electron DOS can be understood more from a Fano-lineshape perspective.

Overall, it appears that the formation of lattice coherence within the DMFT description gives rise to strong fluctuations in the local q -factor of the Fano-lineshape. This phenomenon is worth further investigation and could lead to a deeper understanding of how lattice coherence dynamically forms in heavy-fermion systems.

Despite the quantitative differences between the minimal model and experimental data, there are many qualitative similarities. From here, two routes could be taken. Either improving the fit, which is likely not possible without increasing the complexity, or tuning the parameters away from the experimental values and investigating a more basic, fundamental model.

The non-Fermi liquid behavior in $\text{PrV}_2\text{Al}_{20}$

The discussion so far was concerned with materials that show heavy Fermi liquid (HFL) behavior at low enough temperatures. The main antagonist to this was the Ruderman-Kittel-Kasuya-Yosida (RKKY) interaction, leading to a magnetically ordered state and destroying the HFL phase. Remembering the shape of the Doniach phase diagram in Fig. 3.8, non-Fermi liquid (NFL) behavior at low temperatures would either mean proximity to the quantum-critical point (QCP) or magnetic ordering. When not in the ordered phase, such an NFL shows an unconventional power-law behavior in electrical resistivity, specific heat, magnetic susceptibility, and other thermodynamic and transport quantities. Such a behavior defines the class of *strange metals*.

Although not unheard of ($\beta\text{-YbAlB}_4$ [100]), stoichiometric materials under normal conditions are typically not close enough to a QCP to show a solid NFL phase. This phase is usually accessed by traversing the horizontal axis of the Doniach phase diagram via pressure, doping, or magnetic field, tuning closer to a quantum critical point [100–104]. Enhanced quantum fluctuations were also shown to suppress the Fermi liquid phase, resulting in NFL behavior [105–107].

About a decade ago, indications of two-channel Kondo physics and competing phases were discovered in the so-called 1-2-20 materials¹, mainly $\text{PrT}_2\text{Al}_{20}$ (T=Ti, V). They are special in that they host an *exotic* quadrupolar Kondo effect [109, 110], in which the ground state of the $\text{Pr}^{3+} 4f^2$ state is a non-Kramers doublet with vanishing dipole moment but nonzero quadrupole [110, 111] (and octupole [111, 112]) moment. Here, the twofold quadrupole moment is screened instead of a spin- $1/2$.

The low-temperature behavior varies immensely between the two mentioned materials. While $\text{PrTi}_2\text{Al}_{20}$ shows clear signs of heavy Fermi liquid behavior followed by quadrupole ordering and unconventional superconductivity, $\text{PrV}_2\text{Al}_{20}$ shows non-Fermi liquid behavior, quadrupole order, and superconductivity [113–115], c.f. Fig. 7.1; the latter two at lower temperatures than its counterpart $\text{PrTi}_2\text{Al}_{20}$. Experimental estimation of the quasiparticle masses in both materials gave $m^*/m_e \sim 20$ in $\text{PrTi}_2\text{Al}_{20}$, and ~ 120 in $\text{PrV}_2\text{Al}_{20}$ [13]. Additionally, the appearance of a Kondo peak has been directly observed in photoemission experiments [116].

Gathering all the presented evidence, it might appear that $\text{PrTi}_2\text{Al}_{20}$ sits firmly in the Fermi liquid region of a modified Doniach phase diagram (c.f. Fig.3.8), whereas $\text{PrV}_2\text{Al}_{20}$ would host a weaker coupling (larger effective mass, smaller ordering temperature) and hence would sit closer to a QCP defined by the extrapolated vanishing of the quadrupole-ordered phase. Whilst following from a sound

¹ For a review of 1-2-20 materials, see [108].

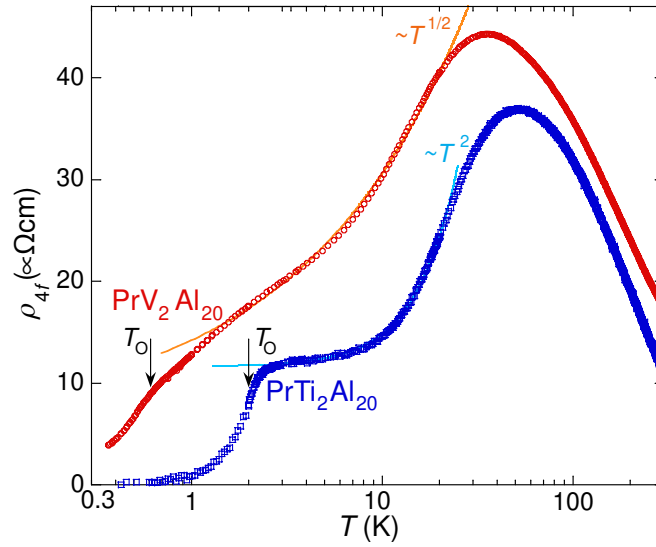


Figure 7.1: Experimentally measured resistivity for $\text{PrV}_2\text{Al}_{20}$ and $\text{PrTi}_2\text{Al}_{20}$ represented by points. The lines illustrate the respective scaling behavior. Taken from [113]; modified (removed text panels and insets)

analysis, it would certainly be a realization of a very rare case, as discussed above. The persistence of the NFL phase over a large temperature range might, however, give hints towards a different interpretation in which the NFL behavior stems from the two-channel Kondo effect.

Following up on the discussion of the quadrupolar Kondo effect, virtual fluctuations with the Kramers doublet ground states of $4f^1$ and $4f^3$ conserve the conduction-electron spin, leading to a realization of the *two-channel* Kondo model in which the two spins act as two individually conserved screening channels for the quadrupole moment (c.f. Fig. 7.2). The notion of a two-channel Kondo effect was pioneered by Nozières and Blandin [58], in which two conduction-electron reservoirs screen the same impurity spin via independently conserved scattering channels. The singlet formation can happen in either channel and, in the case of energetical degeneracy, leads to a twice-degenerate ground state. In contrast to the Nozières Fermi liquid [38], this shows textbook non-Fermi liquid behavior in thermodynamic quantities, like specific heat $C_{\text{imp}}/T \propto -\ln(T/T_K)$, resistivity $\rho \propto \sqrt{T}$, magnetic susceptibility $\chi_{\text{imp}} \propto -\ln(T/T_K)$, predicted by exact solutions via Bethe-Ansatz [117, 118], conformal field-theory [119], and renormalization group [120]. Similarly to the Fermi liquid case, the impurity self-energy vanishes at the Fermi energy, indicating the formation of a bound state. The difference is in the scaling, which is quadratic in temperature and frequency in the Fermi liquid case, and of square-root behavior in the two-channel case.

Similar to the regular Kondo lattice, the two-channel Kondo lattice is not yet exactly solved, and theoretical insight was only gathered in specific cases or under approximations. An intriguing feature of the Kondo lattice is the competition between the Kondo effect, with the tendency to form a heavy Fermi liquid, and the RKKY interaction, with the tendency to induce magnetic order on the impurities. In the two-channel case, the expected non-Fermi liquid behavior and channel order [121, 122] (sometimes called *hastatic order*) are added to the picture.

Hence, the non-Fermi liquid behavior of $\text{PrV}_2\text{Al}_{20}$ could be attributed to the two-channel Kondo effect in the lattice [123].

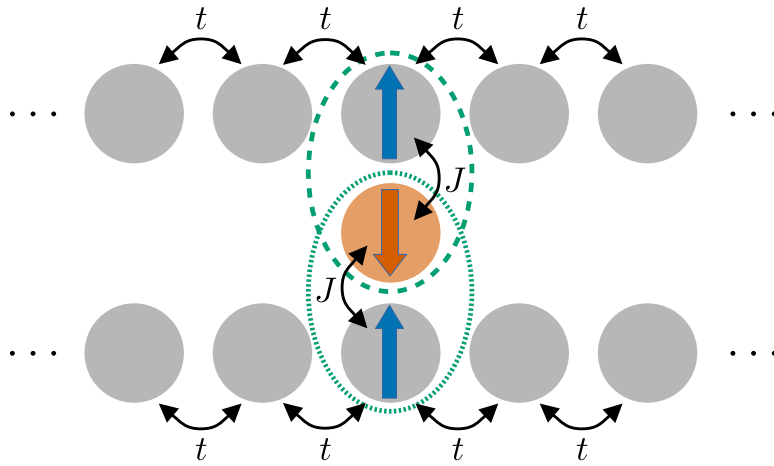


Figure 7.2: Illustration of the two-channel Kondo model. Conduction electrons are represented by gray balls and their spin by blue arrows. The orange ball represents the impurity, with its spin being the orange arrow. The tight-binding nearest neighbor hopping t and the local Kondo coupling J are illustrated via black arrows. Compared to Fig. 3.6, pair formation is degenerate between the two scattering channels. Both possible options are illustrated by green dashed lines.

In this chapter, all the necessary details for setting up an effective model for the Kondo effect in $\text{PrV}_2\text{Al}_{20}$ are presented, supported by DFT results by A. H. Nevidomskyy and F. Gao from Rice University, Houston TX. First, a discussion of the underlying level structure of the Pr^{3+} ion and coupling constants between involved states, including conduction-electrons, is presented. This is followed by a recipe for constructing an effective model for the quadrupolar (two-channel) Kondo effect in terms of a periodic Anderson impurity model with Hubbard operators. Extensions of the previously discussed dynamical mean-field theory and non-crossing approximation are briefly mentioned. Lastly, the numerical results are discussed, and an outlook on future projects is given.

7.1 Crystal Field States of Pr³⁺ in PrV₂Al₂₀

The Kondo effect in PrV₂Al₂₀ will be dominated by the 4*f* electrons of the Pr³⁺ ion, whose valence ground state is the 4*f*² configuration. From there, fluctuations can either happen with the 4*f*¹ or 4*f*³ configurations. As already established in Sec. 4.2.2, the spin-orbit coupled ground state of the 4*f*² configuration is $J = 4$; the ground state for 4*f*¹ is $J = 5/2$, and for 4*f*³ $J = 9/2$. The crystal field point group is T_d , whose double group T'_d can be used to determine the possible CEF states in each valence configuration. They are listed in Eq. (4.15), (4.16), and (4.17). As a reminder, they were

$$\begin{aligned}\Gamma_{J=5/2} &= \Gamma_7 \oplus \Gamma_8 \\ \Gamma_{J=4} &= \Gamma_1 \oplus \Gamma_3 \oplus \Gamma_4 \oplus \Gamma_5 \\ \Gamma_{J=9/2} &= \Gamma_6 \oplus 2\Gamma_8.\end{aligned}$$

The irreps can be interpreted as singlets or triplets in either spin, orbital, or both to gain physical insight. Most importantly, Γ_6 and Γ_7 behave like spin-1/2 states due to their Kramers doublet nature. The non-Kramers Γ_3 doublet, missing a dipole moment, can be understood as a dipole-singlet with a twofold orbital quantum number. Both Γ_4 and Γ_5 behave like dipole-triplets, effectively spin-1 states. The difference between them is the combination of comprising orbitals. Lastly, Γ_1 is a singlet in all possible quantum numbers, and Γ_8 can be understood as a combination of Γ_3 and Γ_6 or Γ_7 , which is exact in the group theoretical sense since $\Gamma_3 \otimes \Gamma_{6/7} = \Gamma_8$. The interpretation in terms of spins and orbitals is not fully true, though, since LS -coupling mixes both quantities into a combined J . Yet, the physical behavior is described correctly.

Determining the CEF ground state is a non-trivial matter. Luckily, the 4*f*² level scheme is approximately known from a comparison of inelastic neutron scattering spectroscopy on PrTi₂Al₂₀ [124], which has the same symmetry and a level scheme of $\Gamma_3 - \Gamma_4 - \Gamma_5 - \Gamma_1$ in ascending energy. For PrV₂Al₂₀, the ground state must also be the Γ_3 state due to the quadrupolar ordering (Γ_4 and Γ_5 are dipole-like, Γ_1 is a singlet). From the appearance of a Schottky anomaly in the specific heat, the energy difference to the first excited CEF state is estimated to $\Delta/k_B \approx 40$ K. This state must be either Γ_4 with a magnetic moment of $0.4\mu_B$ or Γ_5 with $2\mu_B$ [113]. There is evidence promoting Γ_5 as the best candidate due to the larger effective magnetic moment of the high-temperature Curie-Weiss behavior of PrV₂Al₂₀, though it has not been confirmed by direct measurements so far.

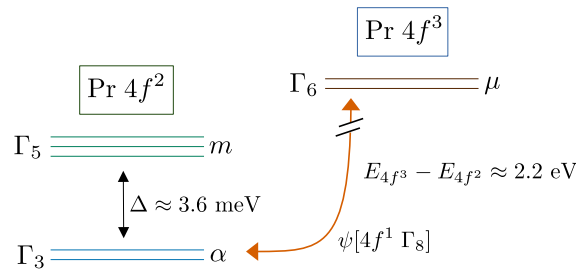


Figure 7.3: Crystal field states involved in the hybridization process of the Pr³⁺ ion in PrV₂Al₂₀. The arrow connecting Γ_3 and Γ_5 indicates the CEF splitting, the arrow connecting the left side to the right side indicates the valence fluctuation to Γ_6 via Γ_8 -projected conduction electrons. As indicated by the broken line, vertical position is in correct order but not to scale.

For the other two cases, symmetry arguments will typically favor the doublets Γ_7 for $4f^1$ and Γ_6 for $4f^3$ as the respective ground states. In previous treatments, the dominant valence fluctuation was often assumed to be between $4f^2 \leftrightarrow 4f^1$. A DFT analysis for PrV₂Al₂₀ has revealed $4f^2 \leftrightarrow 4f^3$ as the dominant fluctuation with an energy difference of $\Delta E_{2\leftrightarrow 3} = E_{4f^3} - E_{4f^2} \approx 2.2$ eV compared to $\Delta E_{2\leftrightarrow 1} \approx 3.8$ eV. Consequently, we shall focus on the $4f^2 \leftrightarrow 4f^3$ fluctuation². This also necessitates using the hole-like NCA as discussed for YbRh₂Si₂ and in Sec. 5.3.7.

A hybridization between Γ_3 and Γ_6 must be of $\Gamma_3 \otimes \Gamma_6 = \Gamma_8$ symmetry. Hence, the conduction electrons of an effective model must be projected onto the local Γ_8 state—this is discussed in more detail in the next section. If we also take Γ_5 into account, the conduction-electron states must be $\Gamma_5 \otimes \Gamma_6 = \Gamma_8 \oplus \Gamma_7$. For simplicity, we will restrict the model to only Γ_8 electrons. The results will qualitatively show the same behavior, which will be discussed at a later point as well.

A particular choice of Clebsch-Gordan coefficients for the $4f^2$ and $4f^1$ states in terms of total angular momentum J states can be found in Appendix E.1.

7.2 An Effective Periodic Anderson Model for PrV₂Al₂₀

The knowledge gathered in the previous section is enough to map out an effective model for the Kondo effect in the alloy. In the simplest case where only the Γ_3 CEF ground state of the Pr $4f^2$ configuration and the Γ_6 doublet in the excited valence configuration $4f^3$ are considered, the impurity part of the Hamiltonian in terms of Hubbard operators is

$$H_{\text{imp}}^{\Gamma_3} = E_{4f^2} \sum_{j,\alpha} |j; 4f^2 \Gamma_3, \alpha\rangle \langle j; 4f^2 \Gamma_3, \alpha| + E_{4f^3} \sum_{j,\mu} |j; 4f^3 \Gamma_6, \mu\rangle \langle j; 4f^3 \Gamma_6, \mu|, \quad (7.1)$$

where j labels Pr sites, α the quadrupolar quantum number of the non-Kramers doublet Γ_3 and μ the spin (channel) quantum number of the Kramers doublet Γ_6 . Energies are taken with respect to the Fermi energy, as always. Conduction electrons are projected onto local Γ_8 states; the hybridization term is, therefore,

$$H_{\text{hyb}}^{\Gamma_3} = \frac{V_0}{\sqrt{2}} \sum_{j\alpha\mu} \text{sgn}(\alpha) |j; 4f^3 \Gamma_6, \mu\rangle \langle j; 4f^2 \Gamma_3, \alpha| \langle j; c \Gamma_8, \tilde{\alpha}, \mu| + h.c., \quad (7.2)$$

where $\tilde{\alpha}$ represents the conjugate pseudospin often also denoted as $-\alpha$. The prefactors of $1/\sqrt{2}$ and $\text{sgn}(\alpha)$ stem from the Clebsch-Gordan coefficients, the latter of which is a matter of definition and could be gauged away. Note that the hybridization in this form conserves both spin μ and pseudospin α at the vertex. The $\text{sgn}(\alpha)$ signals a singlet structure in the pseudospin α . This does not contradict the formulation in [123]; it is a freedom of choice when defining the basis for each individual irrep³. For details about the couplings, see Appendix E.2.

² Note that this choice does not qualitatively influence the behavior at the lowest temperatures; the low-energy effective model is the same Kondo model with a different numerical value of J but the same structure.

³ This comment refers to the $\text{sgn}(\alpha)$ factor. The hybridization in the first arXiv version of [123] is wrongly missing the minus sign in the Γ_8 pseudospin.

If the additional Γ_5 CEF state is taken into account, the model must be extended by

$$H_{\text{imp}}^{\Gamma_5} = (E_{4f^2} + \Delta) \sum_{j,m} |j; 4f^2 \Gamma_5, m\rangle \langle j; 4f^2 \Gamma_5, m| . \quad (7.3)$$

and the appropriate hybridization terms

$$H_{\text{hyb}}^{\Gamma_3} = V_1 \sum_{j\alpha m\mu\mu'} \Xi_{m\mu;\alpha\mu'} |j; 4f^3 \Gamma_6, \mu\rangle \langle j; 4f^2 \Gamma_5, m| \langle j; c \Gamma_8, \alpha, \mu'| + h.c. . \quad (7.4)$$

The factor Ξ contains the non-trivial hybridization structure via Clebsch-Gordan coefficients of the CEF irreps, details of which can be found in Appendix E.2. Essentially, the vertex should conserve dipole moments, and Γ_5 is like a spin-triplet of total spin $S = 1$. The combinations of m , μ and μ' must be chosen such that $\mu = m + \mu'$. Additionally, since Γ_5 does not carry the pseudospin α , an appropriate combination must be taken. Here, a simple average over α suffices. If Γ_4 is added as well, a more detailed analysis using coupling-constant tables for the T'_d group needs to be taken into account.

The impurity states can be represented by auxiliary particles via

$$a_{j,\mu}^\dagger |0\rangle = |j; 4f^3 \Gamma_6, \mu\rangle , \quad (7.5)$$

$$f_{j,\alpha}^\dagger |0\rangle = |j; 4f^2 \Gamma_3, \alpha\rangle , \quad d_{j,m}^\dagger |0\rangle = |j; 4f^2 \Gamma_5, m\rangle , \quad (7.6)$$

$$\hat{Q}_j = \sum_{\alpha} f_{j,\alpha}^\dagger f_{j,\alpha} + \sum_m d_{j,m}^\dagger d_{j,m} + \sum_{\mu} a_{j,\mu}^\dagger a_{j,\mu} . \quad (7.7)$$

Local projected conduction electrons can be represented by ordinary fermionic operators

$$\psi_{j,\alpha\mu} = \sum_{\vec{k}} \sum_{a\sigma} e^{i\vec{k}\cdot\mathbf{R}_j} \Phi_{\alpha\mu;\sigma}^a(\vec{k}) c_{\sigma}^a(\vec{k}) , \quad (7.8)$$

with the transformation matrix Φ and orbitally projected conduction-electrons $c_{\sigma}^a(\vec{k})$, details of which will be the subject of the next section.

For completeness, the Hamiltonian (without the pure conduction-electron part) is then the sum of

$$H_{\text{imp}}^{\Gamma_3} = E_{4f^2} \sum_{j,\alpha} f_{j,\alpha}^\dagger f_{j,\alpha} + E_{4f^3} \sum_{j,\mu} a_{j,\mu}^\dagger a_{j,\mu} , \quad (7.9)$$

$$H_{\text{hyb}}^{\Gamma_3} = \frac{V_0}{\sqrt{2}} \sum_{j\alpha\mu} \text{sgn}(\mu) a_{j,\mu}^\dagger f_{j,\alpha} \psi_{j,-\alpha\mu} + h.c. , \quad (7.10)$$

$$H_{\text{imp}}^{\Gamma_5} = (E_{4f^2} + \Delta) \sum_{j,m} d_{j,m}^\dagger d_{j,m} , \quad (7.11)$$

$$H_{\text{hyb}}^{\Gamma_5} = V_1 \sum_{j\alpha m\mu\mu'} \Xi_{m\mu;\alpha\mu'} a_{j,\mu}^\dagger d_{j,m} \psi_{j,\alpha\mu'} + h.c. , \quad (7.12)$$

and the chemical potential for the auxiliary particles at each site

$$\sum_j \lambda_j (\hat{Q}_j - 1) . \quad (7.13)$$

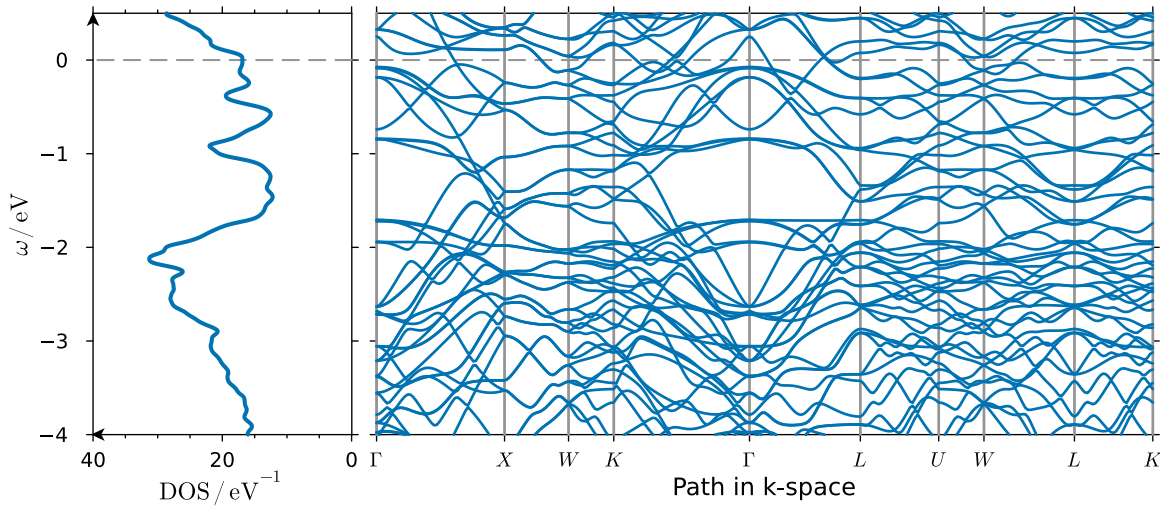


Figure 7.4: Density of states (left) and band structure (right) of the full “open core” ab-initio calculation for $\text{PrV}_2\text{Al}_{20}$ with “frozen” $\text{Pr } 4f^2$ configuration, effectively removing it from the picture.

7.3 Conduction Electrons in the Effective Model

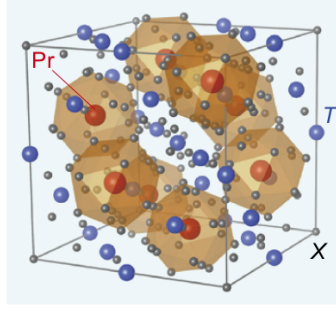
For weakly interacting materials, a faithful band structure can be calculated using ab initio techniques, like the density functional theory⁴ (DFT). Theoretically, knowing the full band structure of a material can be considered beneficial. However, realistic (complex) alloys tend to have a complex band structure. The DFT “open core”⁵ band structure of $\text{PrV}_2\text{Al}_{20}$ is shown in Fig. 7.4; this type of plot is often called *spaghetti plot* for obvious reasons. Many bands cross the Fermi energy, supporting the observation of metallic behavior. The bands shown here each contain a non-trivial mixture of the electronic orbitals of each ion. Due to the necessity of projecting each band onto the local Γ_8 quartet of the Pr ion, the spatial wavefunction of each band must be known in order to calculate the \vec{k} -dependent projection matrix (c.f. Fig. 7.3). Although a tedious process, this can be technically done. Within a dynamical mean-field calculation, though, the inverse transformation has to be applied, and the full set of $\mathcal{O}(100)$ bands would have to be renormalized, each with an individual combination of \vec{k} -dependent transformation matrices. This is numerically not feasible, but luckily, a series of good approximations can be made.

In Kondo systems, only the strongest contribution to the coupling between conduction electrons and impurities determines the ground state. The temperature region in which this is still true depends on the difference in strength. For the local impurity, this is contained in the hybridization function $\Gamma(\omega)$. Finding the dominant contribution to this quantity will allow for the construction of a model with qualitatively correct features but with a much-simplified structure.

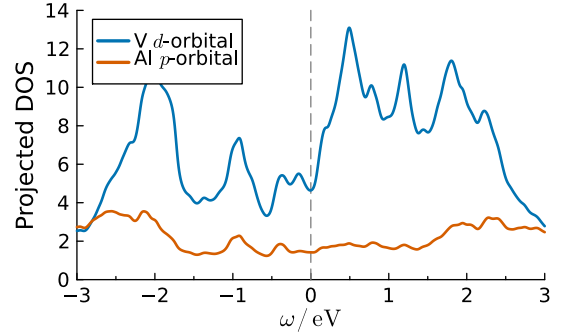
First, conduction electrons in the region of interest (down to ~ -4 eV) will mostly stem from V p -orbitals and Al d -orbitals. The crystal structure is such that the hybridization with Al seems to be

⁴ For a review, see [125]. I will use DFT results in the following, but the method will not be explained in detail since it was not part of my own work, and it’s not essential to the physical context of this thesis.

⁵ Wanting to add a DMFT on top of the DFT later on, the impurity part has to be removed from the dynamics in order to not double-count its contribution. This can be achieved by “freezing” the Pr^{3+} ion to be in the $[\text{Xe}]4f^2$ configuration. More details can be found in section III A of the supplemental material of [123].



(a) Crystal structure (conventional unit cell, coordination number $Z = 8$) of the 1-2-20 materials taken from [108]. Here, red balls represent Pr, blue balls represent $T \in \{\text{V}, \text{Ti}\}$ and gray balls represent Ti. The cells indicated by orange planes connecting Al sites are Frank-Casper cages [126] of 16 Al-atoms surrounding the Pr ion.



(b) Projected density of states (DOS) of V d orbitals and Al p orbitals normalized to the number of Pr neighbors instead of the number of atoms in a unit cell.

dominant due to their large number and close proximity to Pr. This was mainly considered in earlier works [127–129] and often argued to be dominant due to geometrical reasons. We have taken another approach in comparing the density of states at the Fermi energy, which is the main conduction-electron attribute entering the Kondo effect at low temperatures. For this, it has to be understood that V atoms form four distinct sets of fcc-lattices and are arranged in a regular way around each Pr atom. Viewed from any given Pr site, the discrete rotational transformation mapping V atoms of identical distance onto each other also includes atoms from neighboring unit cells. Counting the contributions with appropriate weighting factors results in a much larger (orbitally) projected density of states, which is illustrated in Fig. 7.5(b). Hence, we identify the V orbitals as the main contribution to the hybridization function.

The d -orbitals on each V atom are split by the local D_{3d} point-group symmetry into three irreps: the singlet (ignoring spin) Γ_1^+ irrep⁶ consisting of a d_{z^2} orbital, and two Γ_3^+ doublets $\{d_{xy}, d_{x^2-y^2}\}$ and $\{d_{xz}, d_{x^2-z^2}\}$. The projection onto those states is done on a Green function level with projection weights w given by the DFT

$$G_{\text{eff}}^{c(0)}(\omega, \vec{k}) = \sum_n w_n^a(\vec{k}) G_n^{c(0)}(\omega, \vec{k}), \quad (7.14)$$

where n is the band index, and a is the orbital quantum number; spin has been omitted for readability. This Green function is then projected onto the local Pr Γ_8 states, which is the orbital contribution to the (ground state, i.e. Γ_3) hybridization function

$$\Gamma^0(\omega) = |V_0|^2 \sum_{ka} \Phi^a(\vec{k}) \text{Im}\{\mathbf{G}_{\text{eff}}^{c(0)}\}(\omega, \vec{k}) \Phi^{\dagger a}(\vec{k}) \quad (7.15)$$

up to a prefactor $|V_0|^2$ that is identical between the different contributions but was not calculated within this framework. Details about the transformation matrix (or structure factor) Φ can be found in Appendix E.3. The resulting contribution of each irrep is plotted in Fig. 7.6. The hybridization

⁶ The notation here is extended by a superscript plus, denoting even behavior under inversion; odd behavior is denoted by a superscript minus.

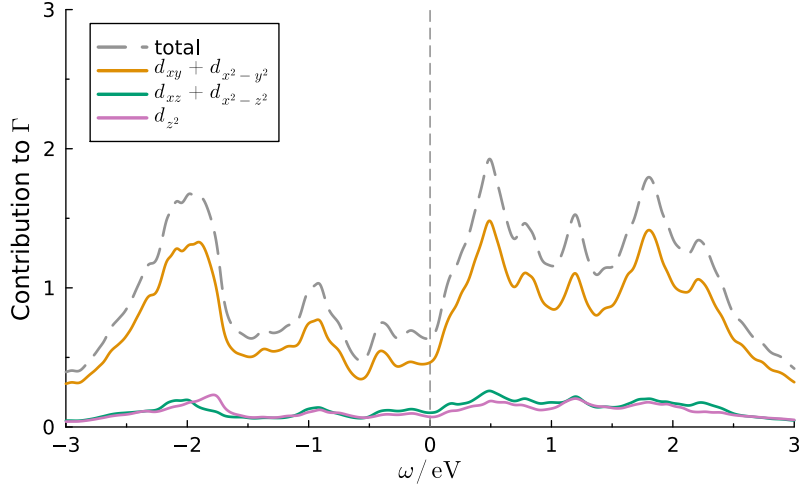


Figure 7.6: Contribution of individual irreps of $V d$ orbitals under D_{3d} symmetry to the hybridization function normalized such that the $\{d_{xy}, d_{x^2-y^2}\}$ integrates to one, maintaining the relative strengths.

function is dominated by the $\{d_{xy}, d_{x^2-y^2}\}$ orbital, allowing for an approximation only including this specific irrep in the model.

7.4 Dynamical Mean-Field Theory and Non-Crossing Approximation for the Model

Having established the full model, the extension of both DMFT and NCA should be briefly discussed.

The free conduction electron part of the model is governed by $G_{\text{eff}}^{c(0)}(\omega, \vec{k})$ and can therefore not be represented in a Hamiltonian formalism. For the DMFT, one can either replicate the full derivation in the path integral formalism (see e.g. [89]) or treat the inverse free Green function as a Schrödinger operator $(\omega - H)$ without going down to the individual field-operator level, which is compatible with the derivation in Sec. 5.4.2. The DMFT equations can then be concisely written as

$$\mathbf{G}^c(i\omega_n) = \sum_{\vec{k}} \frac{1}{\left\{ \mathbf{G}_{\text{eff}}^{c(0)}(i\omega_n, \vec{k}) \right\}^{-1} - \mathbf{\Delta}^c(i\omega_n, \vec{k})}, \quad (7.16)$$

$$\mathbf{G}^{\text{imp}}(i\omega_n) = \frac{1}{i\omega_n - \epsilon^{\text{imp}} - \mathbf{\Delta}^{\text{imp}}(i\omega_n) - \mathbf{\Sigma}(i\omega_n)}, \quad (7.17)$$

with

$$\epsilon^{\text{imp}} = \epsilon \mathbb{1}_{\Gamma_3 \otimes \Gamma_6} \oplus (\epsilon + \Delta) \mathbb{1}_{\Gamma_5 \otimes \Gamma_6}, \quad (7.18)$$

$$\epsilon = E_{4f^2} - E_{4f^3}, \quad (7.19)$$

$$\mathbf{\Delta}^c(i\omega_n, \vec{k}) = \mathbf{V}(\vec{k})^\dagger \frac{1}{i\omega_n - \epsilon^{\text{imp}} - \mathbf{\Sigma}(i\omega_n)} \mathbf{V}(\vec{k}), \quad (7.20)$$

$$\mathbf{V}(\vec{k}) = \left(V_0 \mathbb{1}_{\Gamma_3 \otimes \Gamma_6}, V_1 \Xi \right)^T \Phi(\vec{k}), \quad (7.21)$$

$$\Delta^{\text{imp}}(i\omega_n, \vec{k}) = \sum_{\vec{k}} \mathbf{V}(\vec{k}) \mathbf{G}_{\text{eff}}^c(i\omega_n, \vec{k}) \mathbf{V}^\dagger(\vec{k}), \quad (7.22)$$

where bold quantities are to be understood as matrices in the respective conduction-electron or impurity quantum numbers. Note that the hybridization matrix $\mathbf{V}(\vec{k})$ is a 10×2 matrix at each \vec{k} -point, mapping from effective conduction-electron space (i.e. projected onto a specific set of V d-orbitals) to the impurity space.

The extension of NCA is also straightforward. The new NCA self-energies for the two pseudofermions are

$$\text{Im} \Sigma_{\alpha\alpha'}^{fA}(\omega) = \pi \int_{-\infty}^{\infty} d\varepsilon n_F(\varepsilon) \sum_{\mu\mu'} A_{\mu\mu'}^a(\varepsilon + \omega) \Gamma_{\alpha\mu', \alpha'\mu}^0(\varepsilon), \quad (7.23)$$

$$\text{Im} \Sigma_{m,\alpha}^{dfA}(\omega) = \pi \int_{-\infty}^{\infty} d\varepsilon n_F(\varepsilon) \sum_{\mu\mu'} A_{\mu\mu'}^a(\varepsilon + \omega) \Gamma_{m\mu', \alpha\mu}^{10}(\varepsilon), \quad (7.24)$$

$$\text{Im} \Sigma_{mm'}^{dA}(\omega) = \pi \int_{-\infty}^{\infty} d\varepsilon n_F(\varepsilon) \sum_{\mu\mu'} A_{\mu\mu'}^a(\varepsilon + \omega) \Gamma_{m\mu', m'\mu}^1(\varepsilon), \quad (7.25)$$

$$\text{Im} \Sigma_{\alpha,m}^{fdA}(\omega) = \pi \int_{-\infty}^{\infty} d\varepsilon n_F(\varepsilon) \sum_{\mu\mu'} A_{\mu\mu'}^a(\varepsilon + \omega) \Gamma_{\alpha\mu', m\mu}^{01}(\varepsilon). \quad (7.26)$$

Here, off-diagonal elements between the two pseudofermions are allowed. The expressions for the respective hybridization functions Γ are trivially constructed by attaching Ξ to the left or right of Γ^0 and multiplying with V_1/V_0 . Also, the spin-reflection is absorbed into the definition of Γ , which can further be absorbed into the projection onto Γ_8 states for the Γ_3 hybridization and must then be respected in the additional structure factor Ξ for the Γ_5 hybridization.

The slave-boson self-energy is

$$\begin{aligned} \text{Im} \Sigma_{\mu,\mu'}^{aA}(\omega) = \int_{-\infty}^{\infty} d\varepsilon n_F(-\varepsilon) \left(\sum_{\alpha\alpha'} \Gamma_{\alpha\mu, \alpha'\mu'}^0(\varepsilon) A_{\alpha\alpha'}^f(\omega - \varepsilon) \right. \\ + \sum_{mm'} \Gamma_{m\mu, m'\mu'}^1(\varepsilon) A_{mm'}^d(\omega - \varepsilon) \\ + \sum_{m\alpha} \Gamma_{m\mu, \alpha\mu'}^{10}(\varepsilon) A_{m\alpha}^{df}(\omega - \varepsilon) \\ \left. + \sum_{m\alpha} \Gamma_{\alpha\mu, m\mu'}^{01}(\varepsilon) A_{\alpha m}^{fd}(\omega - \varepsilon) \right). \end{aligned} \quad (7.27)$$

Finally, the impurity spectrum and, equally, the local part of the T -matrix is

$$A_{\alpha\mu,\alpha',\mu'}^{\Gamma_3\Gamma_3}(\omega) = \frac{\int_{-\infty}^{\infty} d\varepsilon' e^{-\beta\varepsilon'} \left\{ A_{\alpha\alpha'}^f(\varepsilon' + \omega) A_{\mu\mu'}^a(\varepsilon') - A_{\alpha\alpha'}^f(\varepsilon') A_{\mu\mu'}^a(\varepsilon' - \omega) \right\}}{\int_{-\infty}^{\infty} d\varepsilon' e^{-\beta\varepsilon'} \left[\sum_{\alpha} A_{\alpha\alpha}^f(\varepsilon') + \sum_m A_{mm}^d(\varepsilon') + \sum_{\mu} A_{\mu\mu}^a(\varepsilon') \right]} \quad (7.28)$$

$$A_{\alpha\mu,m,\mu'}^{\Gamma_3\Gamma_5}(\omega) = \frac{\int_{-\infty}^{\infty} d\varepsilon' e^{-\beta\varepsilon'} \left\{ A_{\alpha m}^{fd}(\varepsilon' + \omega) A_{\mu\mu'}^a(\varepsilon') - A_{\alpha m}^{fd}(\varepsilon') A_{\mu\mu'}^a(\varepsilon' - \omega) \right\}}{\int_{-\infty}^{\infty} d\varepsilon' e^{-\beta\varepsilon'} \left[\sum_{\alpha} A_{\alpha\alpha}^f(\varepsilon') + \sum_m A_{mm}^d(\varepsilon') + \sum_{\mu} A_{\mu\mu}^a(\varepsilon') \right]} \quad (7.29)$$

$$A_{m\mu,m',\mu'}^{\Gamma_5\Gamma_5}(\omega) = \frac{\int_{-\infty}^{\infty} d\varepsilon' e^{-\beta\varepsilon'} \left\{ A_{mm'}^d(\varepsilon' + \omega) A_{\mu\mu'}^a(\varepsilon') - A_{mm'}^d(\varepsilon') A_{\mu\mu'}^a(\varepsilon' - \omega) \right\}}{\int_{-\infty}^{\infty} d\varepsilon' e^{-\beta\varepsilon'} \left[\sum_{\alpha} A_{\alpha\alpha}^f(\varepsilon') + \sum_m A_{mm}^d(\varepsilon') + \sum_{\mu} A_{\mu\mu}^a(\varepsilon') \right]} \quad (7.30)$$

$$A_{m\mu,\alpha,\mu'}^{\Gamma_5\Gamma_3}(\omega) = \frac{\int_{-\infty}^{\infty} d\varepsilon' e^{-\beta\varepsilon'} \left\{ A_{m\alpha}^{df}(\varepsilon' + \omega) A_{\mu\mu'}^a(\varepsilon') - A_{m\alpha}^{df}(\varepsilon') A_{\mu\mu'}^a(\varepsilon' - \omega) \right\}}{\int_{-\infty}^{\infty} d\varepsilon' e^{-\beta\varepsilon'} \left[\sum_{\alpha} A_{\alpha\alpha}^f(\varepsilon') + \sum_m A_{mm}^d(\varepsilon') + \sum_{\mu} A_{\mu\mu}^a(\varepsilon') \right]} \quad (7.31)$$

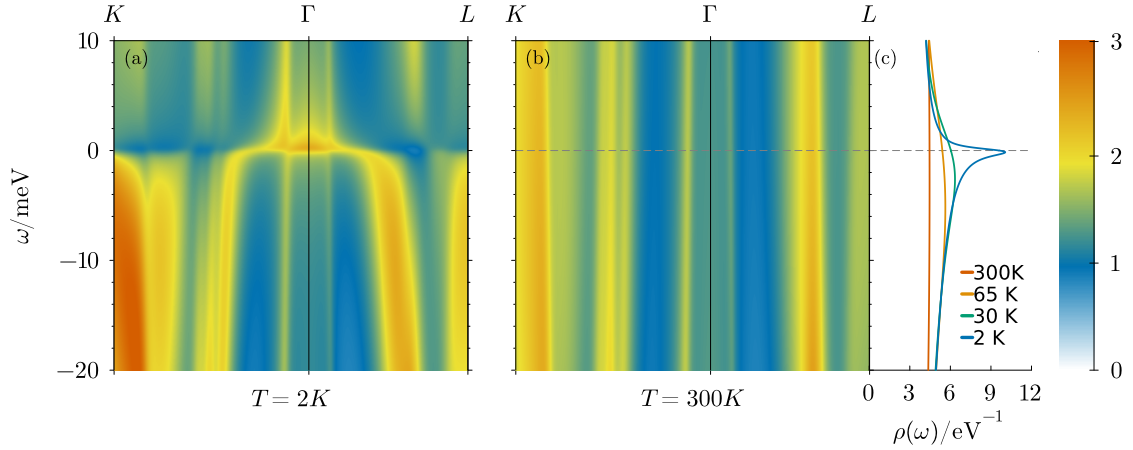


Figure 7.7: Spectrum of the single CEF-state effective model for $\text{PrV}_2\text{Al}_{20}$. Panel (a) shows the total DOS for two different temperatures, for which the spectrum along a path in k -space close to the Γ point is shown in panels (b) and (c).

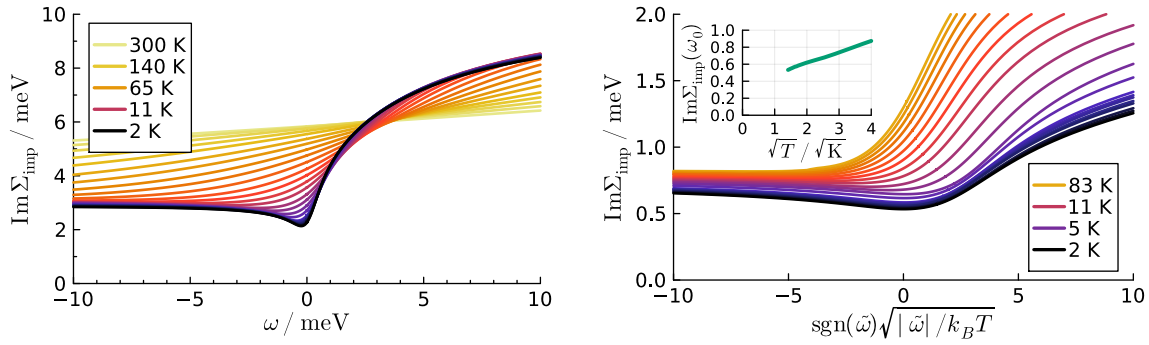
7.5 Results for the Single CEF-State Model

The expected two-channel behavior should be observable in a model containing only the hybridization with the CEF ground state Γ_3 . Hence, let's first consider the previously discussed model with only taking Γ_3 into account. This model only has a single tunable parameter V_0 , which was set such that $|V_0|^2 = 3.4 \text{ eV}^2$, where $|V_0|^2 = 3.0 \text{ eV}^2$ was used just for the magnetic susceptibility⁷. The spectrum of this model for two different temperatures is shown in Fig. 7.7. The figure shows a small region around the Γ -point, where the effect of the hybridization is most pronounced. Due to the small energy range, orders of magnitude smaller than the bandwidth, the projected conduction bands⁸ appear as vertical lines despite their dispersion. The emergence of a heavy band and avoided crossing around the Fermi energy can be clearly observed. Furthermore, the density of states in panel (a) shows first signs of a coherence peak, as discussed in the section about YbRh_2Si_2 . The model successfully achieves the first step: reproducing heavy fermion behavior.

Next, the results must be tested for Fermi liquid or non-Fermi liquid behavior. This can be seen best in the scaling of the local impurity self-energy. If its imaginary part behaves like $\sim \omega^2$ it would be a clear indication of Fermi liquid behavior, whereas $\sim \text{sgn}(\omega)\sqrt{|\omega|}$ is a clear indication of the two-channel Kondo non-Fermi liquid. As can be seen from Fig. 7.8(a) and Fig. 7.8(b), the behavior is that of a non-Fermi liquid which starts to develop around $T = 15 \text{ K}$. A few remarks should be made at this point. Although NCA produces the correct low-energy scaling, frequency dependence, and infrared exponents for a two-channel situation [130], the potential scattering is overestimated, resulting

⁷ Due to the strong hybridization in this model, the numerical calculation of the magnetic susceptibility became uncontrolled and a model with weaker hybridization had to be considered for just this quantity. All other quantities look qualitatively similar between the two models, just with more pronounced non-Fermi liquid behavior in the model with stronger hybridization.

⁸ The figure shows only the spectral weight of the parts considered in the model. The full conduction-electron density of states is much larger. Plotting the full system would not be advisable in the context of our approximations due to a strong underestimation of the impurity influence on the system—all omitted hybridizations for the minimal model are effectively set to zero at the cost of needing adjusted parameters for a faithful description of the material.



(a) Impurity self-energy of the single CEF-state effective model for $\text{PrV}_2\text{Al}_{20}$ for different temperatures.

(b) Impurity self-energy of the single CEF-state effective model for $\text{PrV}_2\text{Al}_{20}$ for different temperatures plotted against the expected square-root scaling function. Here, $\tilde{\omega} = \omega - \omega_0$, where ω_0 is the frequency of the local minimum. The inset shows the value at the minimum in meV against the expected square-root temperature scaling.

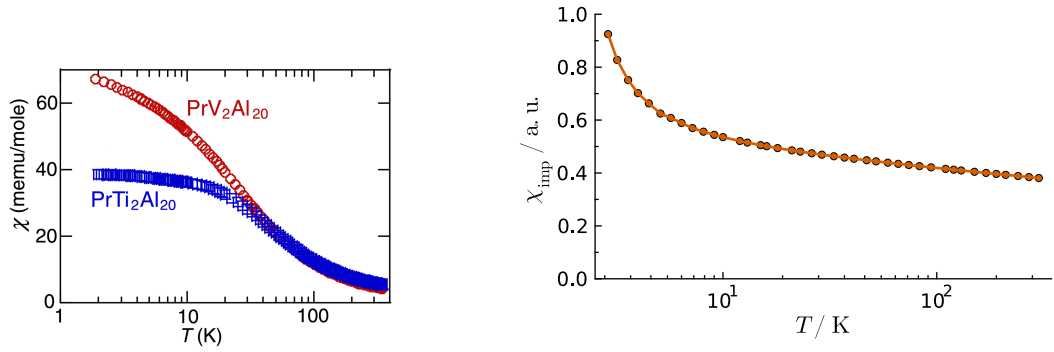
Figure 7.8: Impurity self-energy of the single CEF-state effective model for $\text{PrV}_2\text{Al}_{20}$.

in an offset of the value at the local minimum ω_0 . There is also a small offset of the minimum ω_0 due to strong particle-hole asymmetry, which additionally induces an asymmetric shape. The asymmetry can also be seen in the exact results mentioned above. Additionally, the square-root scaling behavior is strictly true only in a region of order T_K around $\omega = 0$; outside that region, deviations are to be expected and in accordance with exact results. Lastly, at finite temperatures, the region $|\omega| < k_B T$ is *not* guaranteed to show the correct scaling behavior. The constant offset is substantial here, and the non-Fermi liquid behavior sets in at much smaller temperatures than expected. This could be improved by increasing the hybridization prefactor in the model at the cost of numerical stability.

Having established the non-Fermi liquid behavior of $\text{PrV}_2\text{Al}_{20}$ in the context of our model, a comparison of the model's magnetic susceptibility to experimental data reveals a large discrepancy. Details about the numerical treatment of the susceptibility can be found in Appendix E.4. The experimental data, taken from [113], is shown in Fig. 7.9(a). The expected magnetic susceptibility of a two-channel Kondo model is a logarithmic divergence. The numerical data presented in Fig. 7.9(b) shows a weak logarithmic dependence, which crosses over to a different behavior below 3 K. Due to the numerical instability of the susceptibility in this specific case, the hybridization had to be reduced as discussed above. The observed crossover could be a numerical artifact, this possibility was, however, not further investigated due to the clear incompatibility between the model susceptibility and the experiment. The experimental data has a much more complex structure in that it shows the onset of (potentially) logarithmic behavior in the region of $T \approx 300$ K to $T \approx 20$ K and then changes behavior below 20 K, possibly crossing over to a logarithm of different slope⁹. The quadrupole ordering temperature in $\text{PrV}_2\text{Al}_{20}$ is $T_O \approx 2$ K, close to the leftmost point shown in this graph¹⁰. Virtually all previous works have interpreted the behavior below 35 K as a $\chi \sim 1 - \sqrt{T}$ behavior stemming from

⁹ For this, compare also to Fig. 7.12(b).

¹⁰ Intriguingly, the logarithmic behavior seems to persist below the ordering temperature, just with yet another slope, which was shown in a more recent measurement in [131] reproduced in Fig. 7.9(a). This region is not accessible within our approach and, hence, is not discussed further in this thesis.



(a) Experimentally measured impurity susceptibility of $\text{PrTi}_2\text{Al}_{20}$ and $\text{PrV}_2\text{Al}_{20}$ on a logarithmic scale, taken from [113]; modified (removed text panels, rescaled text). (b) Impurity magnetic susceptibility of the single CEF-state effective model for $\text{PrV}_2\text{Al}_{20}$ for different temperatures.

Figure 7.9: Impurity magnetic susceptibility of the single CEF-state model compared to the original experimental data.

the van Vleck susceptibility of the Γ_3 doublet. This is based on the work by Cox and Makivic [132] in which the van Vleck contribution arises from virtual fluctuations between the CEF states Γ_3 and Γ_4 in U^{4+} materials. This provides justification for including the first excited CEF state in the model, which is discussed in the next section.

7.6 Results for the Two CEF-State Model

In the last section, the discussion and comparison with the experiment highlighted the need to include the first excited CEF state in the model. This is furthermore supported by a comparison of scales. Experimentally, non-Fermi liquid behavior is observed below approximately 20 K, where a crossover can be seen in the magnetic susceptibility. The expected crystal field splitting $\Delta/k_B \approx 40$ K introduces a similar temperature scale. Additionally, the intention to compare the magnetic susceptibility in a temperature range comparable to the CEF splitting certainly necessitates the inclusion of this state into the model.

The full model including Γ_5 has three adjustable parameters: V_0 , V_1 , and the microscopic splitting Δ . For simplicity, $V_1 = V_0 = 1.5 \text{ eV}^2$ under the use of the coupling coefficients in Eq. (E.13) in the appendix. As briefly mentioned there, this leads to a strongly enhanced splitting. One might be able to explain this by possible shortcomings of the methods used; this is not further investigated in this thesis. In order to produce the correct final CEF splitting of approximately 40 K, the microscopic parameter must be $\Delta/k_B = -695$ K. This can be avoided by choosing a suitable $V_1 \approx V_0\sqrt{3/2}$, adjusting the free hybridization functions to have the same strength. The results for this alternative case are qualitatively identical.

As before, the first quantity of interest is the spectrum. It is again shown for two different temperatures in Fig. 7.10. The two individual crystal field states are clearly visible but not well separated in k -space. Despite this, lattice coherence can still be identified in the k -dependent spectrum by signs of avoided crossing, as well as in the density of states by the splitting of peaks. Additionally, the excited CEF peaks produce a side-peak below the Fermi energy, similar to the previously discussed case of YbRh_2Si_2 . Two distinct temperature scales can now be identified from the density of states.

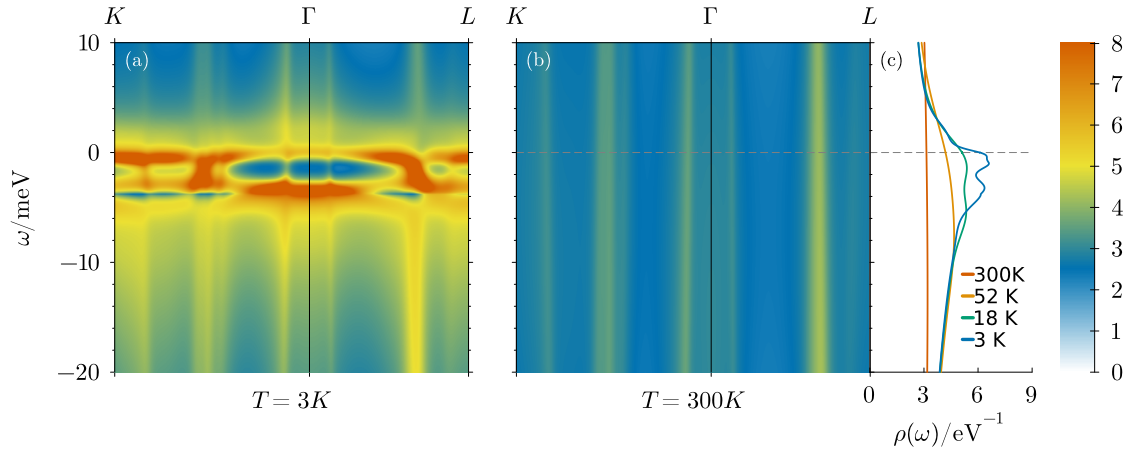


Figure 7.10: Spectrum of the effective model for $\text{PrV}_2\text{Al}_{20}$ including two CEF states. Panel (a) and (b) show the total (model) spectrum along a path in k -space close to the Γ point for $T = 3\text{ K}$ and $T = 300\text{ K}$. Panel (c) shows the total DOS for the same two temperatures.

At temperatures larger than the CEF splitting, only a single broad Kondo peak appears. The onset of this peak at around $T_{K,1} \approx 50\text{ K}$ marks the first Kondo temperature, which is the relevant energy scale for the onset of the Kondo effect in this model. The individual CEF contributions become discernible below around 20 K . Lastly, the ground-state Kondo temperature can be estimated to be around $T_{K,0} \approx 5\text{ K}$. Due to the crossover-like nature of the Kondo effect, first signs of it are usually visible already at higher temperatures.

Next, the Γ_3 component of the impurity self-energy, shown in Fig. 7.11, shows a clear non-Fermi liquid $\sqrt{\omega}$ behavior qualitatively matching exact results for a local two-channel Anderson impurity model [120]. The same discussion as before applies here. This time, the constant offset is much smaller and the square-root behavior more pronounced. Although already visible at the largest shown temperature, the scaling behavior converges below $T_{K,0} \approx 5\text{ K}$.

Finally, the magnetic susceptibility is displayed in Fig. 7.12(a), calculated using the same method as before (c.f. Appendix E.4). The contribution is twofold here. One is the direct contribution from Γ_6 ; the other is the direct contribution from Γ_5 . Since Γ_6 is the excited state and only virtually occupied, its contribution is small and was enhanced in the figure to increase visibility. The—by far—dominant contribution is from Γ_5 directly. At temperatures above the CEF splitting, it *actively* contributes to the magnetic susceptibility due to the direct coupling of the spin-triplet to the magnetic field. This gives rise to the characteristic logarithmic shape of the perturbative onset of the Kondo effect. The dynamics get frozen out below the CEF splitting at a similar temperature scale mentioned in the context of the DOS above. In our model, the susceptibility reaches a local maximum at around 15 K , below which a local minimum just above 10 K is reached. The behavior then shows a crossover to a rising susceptibility, which must be the logarithmic divergence of the ground-state Kondo effect. Unfortunately, the numerical calculation becomes uncontrolled below this point.

Despite the apparent differences between theory and experiment, the overall behavior is reproduced, and bringing it more in line with the experiment would require tuning each individual parameter. This is a time-consuming procedure due to the non-linear cross-dependencies between the parameters, even though only three free parameters are involved.

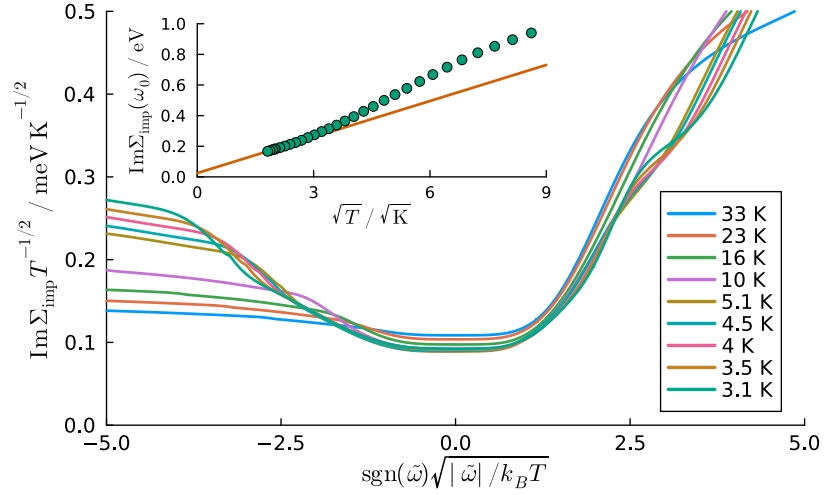
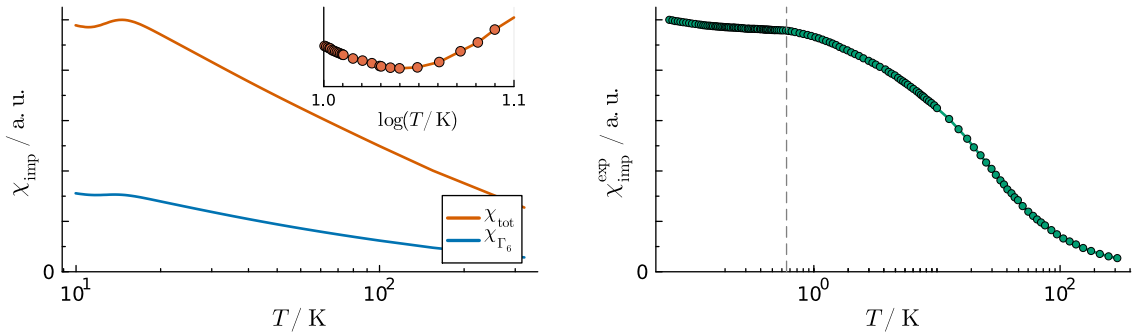


Figure 7.11: Impurity ground-state (Γ_3) self-energy of the effective model for $\text{PrV}_2\text{Al}_{20}$ including two CEF states for different temperatures plotted against the expected square-root scaling function. Here, $\tilde{\omega} = \omega - \omega_0$, where ω_0 is the frequency of the local minimum. The inset shows the value at the minimum in meV against the expected square-root temperature scaling.



(a) Temperature-dependent impurity susceptibility of the effective $\text{PrV}_2\text{Al}_{20}$ model including two CEF states.

(b) Temperature-dependent experimentally measured impurity susceptibility; the gray dashed line marks the quadrupole ordering temperature. Reproduced from [131].

Figure 7.12: Impurity magnetic susceptibility including the excited CEF state in comparison to most recent experimental data.

7.7 Conclusion

The question of whether the non-Fermi liquid behavior of $\text{PrV}_2\text{Al}_{20}$ can be solely attributed to the two-channel Kondo effect was answered affirmatively. A clear non-Fermi liquid behavior can be seen in the local impurity self-energy below a temperature comparable to the experimentally determined onset of NFL behavior in electrical resistivity. Comparing the magnetic susceptibility to the experiment necessitated the inclusion of the first excited CEF state, the Γ_5 triplet, which behaves like a spin-1. Its direct coupling to the magnetic field was shown to give the—by far—dominant contribution to the impurity susceptibility. The excited Γ_6 state alone, although producing a logarithmic divergence due to the two-channel Kondo effect, cannot reproduce the complex structure of the temperature-dependent susceptibility. The inclusion of Γ_5 did not change the non-Fermi liquid behavior of the self-energy qualitatively, as expected.

Despite the apparent differences between the model susceptibility and the experimental results, important features are qualitatively reproduced at comparable temperatures. The temperature dependence of the observed susceptibility was explained by the crossover between two different logarithmic regimes, in contrast to the previously reported $1 - \sqrt{T}$ van Vleck behavior.

Although improving the quantitative similarity between model and experiment would be desirable, the highly non-linear coupling between the involved parameters makes this a time-consuming task. The lack of additional physical insight gained from this procedure starkly contrasts the significant time investment required. Therefore, it is unclear if this will be pursued in future work.

Summary and Outlook

In this thesis, I have presented a comprehensive picture of dynamical effects in heavy-fermion systems in the context of lattice coherence and the non-Fermi liquid behavior of two-channel periodic Anderson lattices.

Beginning with the fundamentals, the quantum theory of particles in periodic potentials was presented in Chapter 2 with special emphasis on the characteristics of localized and de-localized particles. From there, simple models promoting the *competition* between localization and de-localization were discussed: the resonant-level model and a two-band hybridization model.

In Chapter 3, I extended the physical picture of electrons in periodic lattices by discussing the consequences of non-negligible local Coulomb interaction. For this, the electronic Hubbard model was motivated. Strong local interactions and the Pauli principle were argued to increase the spin exchange interaction, directly leading to the *s-d* model of localized spins coupled to itinerant electrons. In this, the Kondo effect was discussed, which successfully explained the experimentally observed resistance minimum in impure metals for the first time. From there, the more general single-impurity Anderson Impurity model (SIAM) was motivated, and its expected spectrum was analyzed. At this point, the dynamical generation of a Kondo peak at the Fermi energy was discussed, giving rise to the dynamical, temperature-dependent generation of a local Nozières Fermi liquid. The chapter concluded by extending the SIAM to the lattice case, resulting in a periodic Anderson model (PAM). Its phase diagram in terms of competing local interactions from the Kondo effect and non-local interactions from the Ruderman-Kittel-Kasuya-Yosida (RKKY) interaction, the *Doniach phase diagram*, was presented, and the emergence of a quantum critical point (QCP) discussed.

Chapter 4 was devoted to bringing the previously discussed models closer to a realistic description of complex matter. There, I presented how a reduction of rotational symmetry leads to the splitting of previously degenerate states. First, the method of coupling angular momenta was laid out in terms of *LS*-coupling, which is the appropriate description in spin-orbit coupled systems. This was followed up by the presentation of Hund's rules as a way of determining the spin-orbit coupled ground state of a given set of electronic states in atoms. Lastly, further reduction of spherical symmetry via the discrete rotational symmetry of the ionic potentials in crystals was discussed in detail. For this, an excursion into group theory led to a series of useful rules for determining the crystal (electric) field (CEF) states of a given ion in a lattice using the irreducible representations of the local point-group symmetry.

Equipped with the tools for constructing realistic models in strongly interacting matter, Chapter 5 explored feasible approaches for solving such models. Although strong interactions are typically

problematic for standard field-theoretical methods, a two-stage process of treating such systems was presented. First, all electronic states were replaced by Hubbard operators, shifting the problem from non-converging perturbation theory to calculating the physical properties of objects with non-canonical commutation relations. This was treated in the second step by introducing auxiliary particles, fixing the commutation relations but extending the Hilbert space to include non-physical states. A solution to this was presented in the projection onto the physical Hilbert space via an auxiliary particle chemical potential. I then proceeded to discuss the non-crossing approximation (NCA) as a conserving approximation for the SIAM with auxiliary particles. Although exact methods for precisely this model exist, NCA is numerically stable, controlled, and can be easily extended to include additional CEF states and multiple scattering channels. It was discussed in detail, owing to the fact that it is the main method used for generating the results presented in this thesis. Finally, the mapping of interacting lattice models onto a local SIAM with a normalized conduction-electron background in the dynamical mean-field theory was motivated and derived, emphasizing the importance of the local impurity solver.

In Chapter 6, the *first main result* of this thesis was presented: an analysis of the lattice coherence of the Yb^{3+} crystal field states in YbRh_2Si_2 . Experimental scanning tunneling microscopy (STM) data for this material intriguingly suggested that a clear scale separation between the perturbative onset of the Kondo effect and lattice coherence of the heavy band can be observed. In addition to the appearance of a coherence peak close to the Fermi energy and *inside* the Kondo dip in conduction electrons, three additional peaks developed at precisely the expected CEF splitting energies. I presented a “minimalistic” periodic Anderson model with a featureless conduction-electron density of states and including all four CEF states of the $\text{Yb}^{3+} 4f^{13}$ configuration. I proceeded to present the model’s numerically calculated spectra and compare them to the experimental results. There, the temperature dependence of the Kondo dip and the coherence peak was qualitatively correctly reproduced. Additionally, the degree of lattice coherence appeared to be decreasing for increasingly large CEF energy, resulting in the first excited CEF state producing a peak at the splitting energy. Higher excited states showed a less clear structure. I discussed potential next steps for this project, where either an improvement in the reproduction of experimental data or more abstraction to aid in understanding the underlying physics can be pursued.

Chapter 7 contained the *second main result*: the non-Fermi liquid behavior in the quadrupolar-Kondo material $\text{PrV}_2\text{Al}_{20}$. In the 1-2-20 materials, clear Fermi liquid behavior was experimentally observed for $\text{PrTi}_2\text{Al}_{20}$, contrasting the non-Fermi liquid behavior and strongly enhanced effective mass observed in $\text{PrV}_2\text{Al}_{20}$. This led to the proposal of close proximity to a quantum critical point in the spirit of the Doniach phase diagram, now with quadrupole- instead of magnetic order. In contrast to this, I presented arguments for an alternative explanation, suggesting that the two-channel nature of the Kondo effect could lead to a non-Fermi liquid phase without the need for proximity to a quantum critical point (QCP). Due to the ground-state degeneracy, single-impurity two-channel systems give rise to a local non-Fermi liquid governed by unconventional power-law behavior of thermodynamic quantities. Assuming this to still hold for the lattice case similar to how Nozières’ Fermi liquid extends to the lattice model, I argued that the observed behavior could be explained by *only* the two-channel Kondo nature of $\text{PrV}_2\text{Al}_{20}$. A more intricate model, including DFT data for the conduction electrons, was set up to explore this possibility. Including only the Γ_3 non-Kramers CEF ground state of the $\text{Pr}^{3+} 4f^2$ configuration was shown to give the desired non-Fermi liquid behavior. However, the magnetic susceptibility and experimentally observed energy scales were not correctly reproduced. To remedy this, an extension of the model via the first excited CEF state, the

Γ_5 triplet, was motivated mainly by the observed energy scales in the magnetic susceptibility. The numerical data for this system showed the same non-Fermi liquid behavior but allowed for a better comparison between experimentally observed and theoretically calculated magnetic susceptibility. As in the previous case, the two possible routes for continuing this project in improving the quantitative compatibility with experimental data or abstraction for a more general physical understanding were presented. The former could be hard to achieve and will likely not provide additional physical insight.

The results presented in this thesis open up several options for future work. The two-channel Kondo effect in lattices is a freshly revived topic due to the observation of “hidden” order in various materials, which may be attributed to higher-order moment ordering. Despite the *non-Fermi liquid* behavior in $\text{PrV}_2\text{Al}_{20}$ being shown to be explainable by the two-channel Kondo effect in lattices, it is not clear how the *Fermi liquid* behavior in “PrTi₂Al₂₀” is to be interpreted in this context. A further analysis of the phase space of two-channel Kondo lattices would be able to provide hints as to which explanation for the observed behavior is more likely. For this, a closer investigation of the strengths and weaknesses of DMFT for such systems would be beneficial.

Combining the two main topics, lattice coherence in two-channel Kondo systems (including CEF states) could be a possible clue in resolving the open questions of 1-2-20 material in special and potentially quadrupolar hidden-order systems in general and might be worth further investigation.

Lattice-Momentum Discretization

Macroscopic samples are usually effectively of infinite size when considering bulk physics. For illustration, consider one spatial dimension. Let's assume we have a one-dimensional lattice with N atoms equally spaced with lattice spacing $\delta r = 1 \text{ \AA}$. The lattice momentum is $p = \hbar k / 2\pi$, where k is the lattice wave vector. Probing matter with photons allows for high precision, so we compare the lattice momentum to the photon momentum $p = \hbar / \lambda$, where \hbar is Planck's constant and λ is the wavelength. Gamma-rays are the highest-energy photons we can produce and typically have $\lambda = 10^{-12} \text{ m}$, so $p = \hbar \cdot 10^{12} \text{ m}^{-1}$. Matching the two, we get $k = 2\pi / \lambda \approx 10^{13} \text{ m}^{-1}$. This is the smallest momentum we can resolve. Therefore, if the discretization is smaller than this, the lattice momentum is effectively continuous. The discretization of k is $\delta k = N / \delta r \propto N \text{ \AA}^{-1} = N 10^{10} \text{ m}^{-1}$, so $N = 10^3$ lattice sites are already enough in this case. That would correspond to a 10 nm sample size.

Simplifying the T -Matrix Equation of the Resonant-Level Model

Let's analyze the T -matrix equation for $G_{\vec{k}\vec{k}}^c$ in terms of advanced Green functions, remembering equation (2.52)

$$G^{(0)}(\omega - i\eta, \varepsilon) = \frac{1}{\omega - \varepsilon - i\eta} \xrightarrow{\eta \rightarrow 0^+} \text{p.v.} \frac{1}{\omega - \varepsilon} + i\pi\delta(\omega - \varepsilon) = G^{(0),A}(\omega - \varepsilon),$$

where $\varepsilon = \varepsilon_{\vec{k}}^c$. The T -matrix equation in terms of real- and imaginary parts, suppressing the superscript A , is

$$\begin{aligned} \text{Im } G_{\vec{k}\vec{k}}^c &= \text{Im } G_{\vec{k}}^{c(0)} \left(1 + |V|^2 \left[2\text{Re } G_{\vec{k}}^{c(0)} \text{Re } G^d - \text{Im } G_{\vec{k}}^{c(0)} \text{Im } G^d \right] \right) \\ &\quad + |V|^2 \text{Re } G_{\vec{k}}^{c(0)} \text{Im } G^d \text{Re } G_{\vec{k}}^{c(0)} \end{aligned} \quad (\text{B.1})$$

The obvious problem is analyzing products of free Green functions' real- and imaginary parts since they are not smooth functions but only strictly defined as a distribution. We can, therefore, work with identities for distributions. Using the identity from Eq. (2.70) one can then argue

$$\int_{-\infty}^{\infty} d\omega G^d(\omega) \left(G^{c(0)}(\omega) \right)^2 = - \int_{-\infty}^{\infty} d\omega G^d(\omega) \frac{dG^{c(0)}(\omega)}{d\omega} \quad (\text{B.2})$$

$$= \int_{-\infty}^{\infty} d\omega \frac{dG^d(\omega)}{d\omega} G^{c(0)}(\omega), \quad (\text{B.3})$$

$$\Rightarrow G^d(\omega) \left(G^{c(0)}(\omega) \right)^2 = \frac{dG^d(\omega)}{d\omega} G^{c(0)}(\omega). \quad (\text{B.4})$$

The T -matrix equation can be expressed linearly in terms of the free \vec{k} -dependent Green function

$$G_{\vec{k}\vec{k}}^c(\omega) = G_{\vec{k}}^{c(0)}(\omega) \left(1 + |V|^2 \frac{dG^d(\omega)}{d\omega} \right), \quad (\text{B.5})$$

with which the norm of the spectral function can be computed straightforwardly.

$$\int_{-\infty}^{\infty} d\omega \operatorname{Im} G_{\vec{k}\vec{k}}^c = \int_{-\infty}^{\infty} d\omega \left(\operatorname{Im} G_{\vec{k}}^{c(0)}(\omega) + |V|^2 \operatorname{Im} G_{\vec{k}}^{c(0)}(\omega) \frac{d}{d\omega} \operatorname{Re} G^d(\omega) + |V|^2 \operatorname{Re} G_{\vec{k}}^{c(0)}(\omega) \frac{d}{d\omega} \operatorname{Im} G^d(\omega) \right) \quad (\text{B.6})$$

$$\int_{-\infty}^{\infty} d\omega \operatorname{Im} G_{\vec{k}}^{c(0)}(\omega) = \int_{-\infty}^{\infty} d\omega \pi \delta(\omega - \varepsilon_{\vec{k}}^c) = \pi \quad (\text{B.7})$$

$$\int_{-\infty}^{\infty} d\omega \operatorname{Im} G_{\vec{k}}^{c(0)}(\omega) \frac{d}{d\omega} \operatorname{Re} G^d(\omega) = \int_{-\infty}^{\infty} d\omega \pi \delta(\omega - \varepsilon_{\vec{k}}^d) \frac{d}{d\omega} \frac{1}{\pi} \text{p.v.} \int_{-\infty}^{\infty} d\nu \frac{\operatorname{Im} G^d(\nu)}{\omega - \nu} \quad (\text{B.8})$$

$$= \frac{d}{d\omega} \text{p.v.} \int_{-\infty}^{\infty} d\nu \frac{\operatorname{Im} G^d(\nu)}{\omega - \nu} \Big|_{\omega=\varepsilon_{\vec{k}}^d} \quad (\text{B.9})$$

$$= \frac{d}{d\varepsilon_{\vec{k}}^c} \text{p.v.} \int_{-\infty}^{\infty} d\nu \frac{\operatorname{Im} G^d(\nu)}{\varepsilon_{\vec{k}}^c - \nu} \quad (\text{B.10})$$

$$\int_{-\infty}^{\infty} d\omega \operatorname{Re} G_{\vec{k}}^{c(0)}(\omega) \frac{d}{d\omega} \operatorname{Im} G^d(\omega) = \text{p.v.} \int_{-\infty}^{\infty} d\omega \frac{1}{\omega - \varepsilon_{\vec{k}}^c} \frac{d}{d\omega} \operatorname{Im} G^d(\omega) \quad (\text{B.11})$$

$$= -\text{p.v.} \int_{-\infty}^{\infty} d\omega \left(\frac{d}{d\omega} \frac{1}{\omega - \varepsilon_{\vec{k}}^c} \right) \operatorname{Im} G^d(\omega) \quad (\text{B.12})$$

$$= -\frac{d}{d\varepsilon_{\vec{k}}^c} \text{p.v.} \int_{-\infty}^{\infty} d\omega \frac{\operatorname{Im} G^d(\omega)}{\omega - \varepsilon_{\vec{k}}^c} \quad (\text{B.13})$$

The two T -matrix terms exactly cancel, and we are left with the spectral function being normalized to unity, since $\operatorname{Im} G_{\vec{k}}^{c(0)}(\omega)$ is normalized to π .

Despite all the massaging and analyzing, computing the \vec{k} -dependent spectral function is numerically not robust. It might appear that employing a finite width η as in Eq. (2.52) should do the trick. The second term in the T -matrix equation does, however, lead to negative values in the spectral function, which is not physical (for fermions). This is even true when breaking down Eq. (B.5) even further. The derivative of $G^d(\omega)$ is

$$\frac{d}{d\omega} \frac{1}{\omega - \varepsilon^d - |V|^2 G_{\text{loc}}^{c(0)}(\omega)} = - \left(1 - |V|^2 \frac{dG_{\text{loc}}^{c(0)}(\omega)}{d\omega} \right) \left(G^d(\omega) \right)^2. \quad (\text{B.14})$$

The final expression for the \vec{k} -dependent Green function is therefore

$$G_{\vec{k}\vec{k}}^c(\omega) = G_{\vec{k}}^{c(0)}(\omega) \left[1 - |V|^2 \left(G^d(\omega) \right)^2 \left(1 - |V|^2 \frac{dG_{\text{loc}}^{c(0)}(\omega)}{d\omega} \right) \right], \quad (\text{B.15})$$

which can be calculated fully analytically (apart from $G^{c(0)}$) for the 1D cubic case.

This, unfortunately, still does not help the numerics. The problem might be the negligence of system size. In an infinite system, the single site should not strongly influence de-localized (lattice-) quantities. This can be reflected in scaling the hybridization $V \rightarrow V/N_s$, where N_s is the number of sites. In this case, the local level will not influence the infinite-size system. Only in spatially restricted regions will the influence appear. Another approach, which turns out to be very fruitful, is restricting the discussion to the scattering phase shift of the conduction electrons, which will not be discussed here. For the sake of argument, let's still look at the numerical result for the T -matrix equation in a 1D-system, which is shown in Fig B.1.

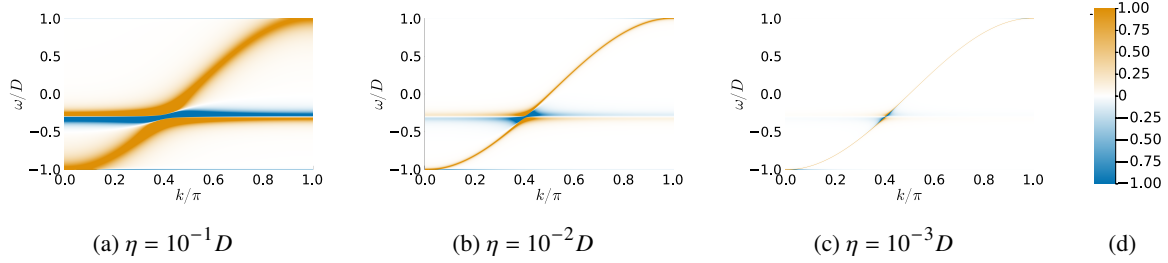


Figure B.1: Conduction-electron spectral function normalized to the free peak height $1/\eta$. Values above 1 and below -1 are cut off for increased visibility.

Transformations, Tricks, and Algorithms

C.1 Integrals over Lorentzians

The normalized Lorentzian of width Γ and position ω_0 is

$$f(\omega) = \frac{1}{\pi} \frac{\Gamma}{(\omega - \omega_0)^2 + \Gamma^2}. \quad (\text{C.1})$$

Its integral can be calculated using a trigonometric substitution:

$$\int_a^b d\omega f(\omega) = \int_a^b d\omega \frac{1}{\pi} \frac{\Gamma}{(\omega - \omega_0)^2 + \Gamma^2} = \frac{1}{\Gamma\pi} \int_a^b d\omega \frac{1}{\left(\frac{\omega - \omega_0}{\Gamma}\right)^2 + 1} \quad \left| \tilde{\omega} = \frac{\omega - \omega_0}{\Gamma} \right. \quad (\text{C.2})$$

$$= \frac{1}{\Gamma\pi} \int_{\frac{a - \omega_0}{\Gamma}}^{\frac{b - \omega_0}{\Gamma}} d\tilde{\omega} \Gamma \frac{1}{\tilde{\omega}^2 + 1} \quad \left| \tilde{\omega} = \tan(x) \right. \quad (\text{C.3})$$

$$= \frac{1}{\pi} \int_{\arctan\left(\frac{a - \omega_0}{\Gamma}\right)}^{\arctan\left(\frac{b - \omega_0}{\Gamma}\right)} dx \frac{1}{\cos^2(x)} \frac{1}{\tan^2(x) + 1} \quad (\text{C.4})$$

$$= \frac{1}{\pi} \int_{\arctan\left(\frac{a - \omega_0}{\Gamma}\right)}^{\arctan\left(\frac{b - \omega_0}{\Gamma}\right)} dx \frac{1}{\cos^2(x) + \sin^2(x)} \quad (\text{C.5})$$

$$= \frac{1}{\pi} \int_{\arctan\left(\frac{a - \omega_0}{\Gamma}\right)}^{\arctan\left(\frac{b - \omega_0}{\Gamma}\right)} dx \quad (\text{C.6})$$

$$\int_a^b d\omega \frac{1}{\pi} \frac{\Gamma}{(\omega - \omega_0)^2 + \Gamma^2} = \frac{1}{\pi} \left[\arctan\left(\frac{b - \omega_0}{\Gamma}\right) - \arctan\left(\frac{a - \omega_0}{\Gamma}\right) \right] \quad (\text{C.7})$$

C.2 Inversion of Tilde Green-Function Matrices

For the so-called tilde representation, generating the inverse Green functions with the correct order in $f(-\omega)$ right away is mandatory since dividing by the Fermi function is not advisable in numerics.

$$\text{Im } G(\omega) = \text{Im } (\omega - \mathcal{H} - \Sigma(\omega))^{-1} = \frac{\text{Im } \Sigma(\omega)}{(\omega - \mathcal{H} - \text{Re } \Sigma(\omega))^2 + (\text{Im } \Sigma(\omega))^2} \quad (\text{C.8})$$

$$\Rightarrow \text{Im } \tilde{G}(\omega) = \frac{\text{Im } \tilde{\Sigma}(\omega)}{(\omega - \mathcal{H} - \text{Re } \Sigma(\omega))^2 + (\text{Im } \Sigma(\omega))^2} \quad (\text{C.9})$$

This method is not easily generalized to matrix Green functions. For this case, the Gauß-Jordan algorithm can be modified to incorporate the correct order in $f(-\omega)$ at every step¹. The core of this algorithm is applying elementary operations to a matrix M to transform it to the identity matrix $\mathbb{1}$ while also applying the same operations to another matrix W , which is just the identity matrix in the beginning. When M becomes the identity, the auxiliary matrix W becomes the inverse of the original M . The algorithm is divided into two parts. First, we want to bring M into an upper triangular shape with the main diagonal only containing ones. All off-diagonal entries can be easily eliminated from this form in a second part. The first part, starting with $k = 1$, is as follows:

1. Normalize the entry M_{kk} to one by dividing the whole row by M_{kk} .
2. For all lines i below k , subtract the k -th line multiplied with M_{ki} from this line.
3. Go to the next k .

The second part, starting with $k = N$, is then:

1. for all lines i above k , subtract the k -th line multiplied with M_{ik} .
2. Go the the next k

When all steps are also applied to the matrix W , where the multiplication weights are still those of the M -matrix, one can extract the imaginary part of the Green function as $\text{Im } W$. To extend this to the tilde representation, one has to keep the imaginary part of both matrices always in the tilde representation. For example, let's look at the first step of the first part. The first entry we want to normalize to one is $M_{11} = \text{Re } M_{11} + i \text{Im } \tilde{M}_{11}$, which would initially be $[G_0^{-1}(\omega)]_{11} - f(-\omega) \tilde{\Sigma}_{11}(\omega) - i \text{Im } \tilde{\Sigma}_{11}(\omega)$. Note how the real part is in the regular representation, whereas the imaginary part is in the tilde representation. The inverse of a complex number z is the complex conjugate divided by the modulus squared $z^{-1} = z^*/|z|^2$. But here, we also have the constraint that only the imaginary part should be in the tilde representation. In a simplified notation, with $a, b \in \mathbb{R}$ and $f^- = f(-\omega)$, this is how one preserves the structure:

$$\frac{(a + i f^- \tilde{b})(a - i f^- \tilde{b})}{a^2 + (f^- \tilde{b})^2} = \frac{a^2 + (f^- \tilde{b})^2 + i f^- (\tilde{b}a - a\tilde{b})}{a^2 + (f^- \tilde{b})^2} = 1 \quad (\text{C.10})$$

¹ I have developed the following algorithm together with Michael Kajan based on the idea of our thesis advisor, Prof. Johann Kroha.

For the other multiplications, it will be

$$a + if^{-}\tilde{b} = (c + if^{-}\tilde{d})(g + if^{-}\tilde{h}) = cg - (f^{-})^2\tilde{d}\tilde{h} + if^{-}(c\tilde{h} + \tilde{d}g), \quad (\text{C.11})$$

$$\Rightarrow a = cg - (f^{-})^2\tilde{d}\tilde{h} \quad \& \quad \tilde{b} = c\tilde{h} + \tilde{d}g. \quad (\text{C.12})$$

Applying this makes it possible to maintain the tilde structure in the imaginary parts always.

C.3 Efficient Calculation of the Cubic Density of States in Arbitrary Dimensions

The density of states is defined as $\rho(\varepsilon) = \sum_{\vec{k}} \delta(\varepsilon - \varepsilon_{\vec{k}})$. Utilizing the continuous version of this relation, the Fourier transform of the density of states can be calculated in an integral representation as

$$\Phi(s) = \int_{-\infty}^{\infty} d\varepsilon e^{is\varepsilon} \rho(\varepsilon) = \int_{-\infty}^{\infty} d\varepsilon e^{is\varepsilon} \int_{-\pi}^{\pi} \frac{d^d k}{(2\pi)^d} \delta(\varepsilon - \varepsilon_{\vec{k}}) \quad (\text{C.13})$$

$$= \int_{-\pi}^{\pi} \frac{d^d k}{(2\pi)^d} e^{-is2t \sum_{i=1}^d \cos k_i} = \left[\int_{-\pi}^{\pi} \frac{dk}{2\pi} e^{-is2t \cos k} \right]^d \quad (\text{C.14})$$

$$= \left[2 \int_0^{\pi} \frac{dk}{2\pi} e^{-is2t \cos k} \right]^d = [J_0(s2t)]^d \quad (\text{C.15})$$

$$= \left[J_0\left(\frac{s2t_*}{\sqrt{2d}}\right) \right]^d, \quad (\text{C.16})$$

with the Bessel function of the first kind J_0 . Here, $t = t_*/\sqrt{2d}$ in the spirit of Section 5.4.1. In the third line, the symmetry in k is used. The power series of the Bessel function can now be utilized together with $(1 + x/d)^d \rightarrow e^x$ for $d \rightarrow \infty$ to relate this expression to a Gaussian curve in Fourier space, which gives a Gaussian density of states in energy space when transformed back:

$$\Phi(s) = \left[1 - \left(\frac{s2t_*}{2\sqrt{2d}}\right) + O\left(\frac{1}{d^2}\right) \right]^d \quad (\text{C.17})$$

$$= \left[1 + \frac{s^2 t_*^2}{2d} + O\left(\frac{1}{d^2}\right) \right]^d \xrightarrow{d \rightarrow \infty} e^{-\frac{s^2 t_*^2}{2}} \quad (\text{C.18})$$

$$\rho(\varepsilon) = \int_{-\infty}^{\infty} \frac{d\varepsilon}{2\pi} e^{-is\varepsilon} \Phi(s) = \frac{1}{2\pi|t_*|} e^{-\frac{\varepsilon^2}{2t_*^2}}. \quad (\text{C.19})$$

Equation (C.15) is also useful for numerically calculating the cubic density of states in arbitrary dimensions. For example, the 1D case has a nice, closed-form solution

$$\rho_{1D}^{c(0)} = \frac{1}{\pi} \frac{\Theta(1 - |\omega/D|)}{\sqrt{1 - (\omega/D)^2}}, \quad (\text{C.20})$$

where $D = 2t$ is the half-bandwidth.

C.4 Transforming Between Local T -Matrices and Self-Energies

Assume we have a full Green function that is either given by a local Dyson equation

$$G = G^0 + G^0 \Sigma G \quad (\text{C.21})$$

and, equivalently, a local T-matrix equation

$$G = G^0 + G^0 T G^0. \quad (\text{C.22})$$

The relation between the two is

$$\Sigma G = T G^0 \quad (\text{C.23})$$

$$\Leftrightarrow \Sigma \left(G^0 + G^0 T G^0 \right) = T G^0 \quad (\text{C.24})$$

$$\Leftrightarrow \Sigma \left(1 + G^0 T \right) G^0 = T G^0 \quad (\text{C.25})$$

$$\Leftrightarrow \Sigma = T \cdot \left(1 + G^0 T \right)^{-1}. \quad (\text{C.26})$$

Alternatively, continuing on Eq. (C.25),

$$\Sigma \left(1 + G^0 T \right) G^0 = T G^0 \quad (\text{C.27})$$

$$\Leftrightarrow \Sigma = \left(1 - \Sigma G^0 \right) T \quad (\text{C.28})$$

$$\Leftrightarrow T = \left(1 - \Sigma G^0 \right)^{-1} \Sigma. \quad (\text{C.29})$$

Expressing $\varepsilon^a \rightarrow \infty$ NCA Equations via $U \rightarrow \infty$ Equations

By modifying the input to the NCA loop ($G^c(0)$), the cases $\varepsilon^a \rightarrow \infty$ and $U \rightarrow \infty$ can be solved by the same set of functions, where the output of the converged NCA (G^d) must be transformed in a simple way to give the appropriate functions. Explicitly, let's first look at the pseudofermion self-energy contributions from Eq. (5.73)

$$\text{Im } \Sigma_1^{fA}(\omega) = \pi \int_{-\infty}^{\infty} d\varepsilon (1 - n_F(\varepsilon)) A^b(\omega - \varepsilon) \sum_{\vec{k}} |V_{\vec{k}}|^2 \mathbf{A}_{\vec{k}\vec{k}}^{c(0)}(\varepsilon),$$

and from Eq. (5.78)

$$\text{Im } \Sigma_2^{fA}(\omega) = \pi \int_{-\infty}^{\infty} d\varepsilon n_F(\varepsilon) A^a(\varepsilon + \omega) \sum_{\vec{k}} |V_{\vec{k}}|^2 \bar{\mathbf{A}}_{\vec{k}\vec{k}}^{c(0)}(\varepsilon).$$

The $U \rightarrow \infty$ NCA only has $\text{Im } \Sigma_1^{fA}$, the $\varepsilon^d \rightarrow -\infty$ case only $\text{Im } \Sigma_2^{fA}$. If we send $\varepsilon \rightarrow -\varepsilon$ in the second equation, we get

$$\text{Im } \Sigma_2^{fA}(\omega) = \pi \int_{-\infty}^{\infty} d\varepsilon (1 - n_F(\varepsilon)) A^a(\omega - \varepsilon) \sum_{\vec{k}} |V_{\vec{k}}|^2 \bar{\mathbf{A}}_{\vec{k}\vec{k}}^{c(0)}(-\varepsilon) \quad (\text{D.1})$$

$$= \pi \int_{-\infty}^{\infty} d\varepsilon (1 - n_F(\varepsilon)) A^a(\omega - \varepsilon) \sum_{\vec{k}} |V_{\vec{k}}|^2 \mathbf{A}_{\vec{k}\vec{k}}^{\text{eff}}(\varepsilon), \quad (\text{D.2})$$

where $\mathbf{A}_{\vec{k}\vec{k}}^{\text{eff}}(\varepsilon) = \bar{\mathbf{A}}_{\vec{k}\vec{k}}^{c(0)}(-\varepsilon)$. Comparing this to the equation for $\text{Im } \Sigma_1^{fA}$ they are of identical structure.

Next, the self-energies for the slave bosons are (Eq. (5.87))

$$\text{Im } \Sigma^b A(\omega) = \pi \int_{-\infty}^{\infty} d\varepsilon n_F(\varepsilon) \sum_{\vec{k}} |V_{\vec{k}}|^2 \text{Tr} \left\{ \mathbf{A}_{\vec{k}\vec{k}}^{c(0)}(\varepsilon) \mathbf{A}^f(\varepsilon + \omega) \right\},$$

and (Eq. (5.96))

$$\text{Im } \Sigma^{aA}(\omega) = \int_{-\infty}^{\infty} d\varepsilon n_F(-\varepsilon) \sum_{\vec{k}} |V_{\vec{k}}|^2 \text{Tr} \left\{ \mathbf{A}_{\vec{k}\vec{k}}^{c(0)}(\varepsilon) \bar{\mathbf{A}}^{fT}(\omega - \varepsilon) \right\}.$$

Sending $\varepsilon \rightarrow -\varepsilon$ in the second equation gives

$$\text{Im } \Sigma^{aA}(\omega) = \int_{-\infty}^{\infty} d\varepsilon n_F(\varepsilon) \sum_{\vec{k}} |V_{\vec{k}}|^2 \text{Tr} \left\{ \mathbf{A}_{\vec{k}\vec{k}}^{c(0)}(-\varepsilon) \bar{\mathbf{A}}^{fT}(\varepsilon + \omega) \right\} \quad (\text{D.3})$$

$$= \int_{-\infty}^{\infty} d\varepsilon n_F(\varepsilon) \sum_{\vec{k}} |V_{\vec{k}}|^2 \text{Tr} \left\{ \bar{\mathbf{A}}_{\vec{k}\vec{k}}^{c(0)}(-\varepsilon) \mathbf{A}^{fT}(\varepsilon + \omega) \right\} \quad (\text{D.4})$$

$$= \int_{-\infty}^{\infty} d\varepsilon n_F(\varepsilon) \sum_{\vec{k}} |V_{\vec{k}}|^2 \text{Tr} \left\{ \mathbf{A}_{\vec{k}\vec{k}}^{\text{eff}}(\varepsilon) \mathbf{A}^{fT}(\varepsilon + \omega) \right\}, \quad (\text{D.5})$$

with the same definition for $\mathbf{A}_{\vec{k}\vec{k}}^{\text{eff}}(\varepsilon)$ from and in the second line, the identity

$$\sum_{\sigma\sigma'} A_{\sigma'\sigma} B_{-\sigma',-\sigma} \stackrel{\bar{\sigma}=-\sigma}{\bar{\sigma}'=-\sigma'} \sum_{\bar{\sigma}\bar{\sigma}'} A_{-\bar{\sigma}',-\bar{\sigma}} B_{\bar{\sigma}'\bar{\sigma}} \quad (\text{D.6})$$

$$\Rightarrow \text{Tr} \left\{ \mathbf{A}_{\vec{k}\vec{k}}^{c(0)}(-\varepsilon) \bar{\mathbf{A}}^{fT}(\varepsilon + \omega) \right\} = \text{Tr} \left\{ \bar{\mathbf{A}}_{\vec{k}\vec{k}}^{c(0)}(-\varepsilon) \mathbf{A}^{fT}(\varepsilon + \omega) \right\} \quad (\text{D.7})$$

was used. The transposed could also be transferred to the other side if desired. This is identical to the equation for $\text{Im } \Sigma^{bA}(\omega)$ apart from taking the transpose of the pseudofermion matrix.

Lastly, the impurity Green function contributions from Eq. (5.60) and (5.62) are

$$\text{Im } \mathbf{G}_1^{dA}(\omega) = \pi \frac{\int_{-\infty}^{\infty} d\varepsilon e^{-\beta\varepsilon} (1 + e^{-\beta\omega}) \mathbf{A}^f(\varepsilon + \omega) A^b(\varepsilon)}{\int_{-\infty}^{\infty} d\varepsilon e^{-\beta\varepsilon} \left[A^b(\varepsilon) + A^a(\varepsilon) + \sum_{\sigma} A_{\sigma\sigma}^f(\varepsilon) \right]},$$

and

$$\text{Im } \mathbf{G}_2^{dA}(\omega) = \pi \frac{\int_{-\infty}^{\infty} d\varepsilon e^{-\beta\varepsilon} (1 + e^{\beta\omega}) \bar{\mathbf{A}}^f(\varepsilon - \omega) A^a(\varepsilon)}{\int_{-\infty}^{\infty} d\varepsilon e^{-\beta\varepsilon} \left[A^b(\varepsilon) + A^a(\varepsilon) + \sum_{\sigma} A_{\sigma\sigma}^f(\varepsilon) \right]}.$$

Since the matrix structure stems directly from the pseudofermions, the equation for $\text{Im } \bar{\mathbf{G}}_2^{dA}(-\omega)$ is identical to the equation for $\text{Im } \mathbf{G}_1^{dA}(\omega)$ with just a being replaced by b .

Before finalizing the set of operations necessary for using the same equations, we must identify the

parameters that enter the Hamiltonian. For this, we take Eq. (5.140) and substitute $\tilde{\mu} = -\mu$ such that

$$\begin{aligned}
H_{\text{SIAM}}^{\varepsilon^b \rightarrow \infty} &= \sum_{\vec{k}, \sigma} \left(\varepsilon_{\vec{k}}^c - \tilde{\mu} \right) c_{\vec{k}\sigma}^\dagger c_{\vec{k}\sigma} + \sum_{\sigma} \left(\tilde{\varepsilon}^a - \tilde{\mu} + \lambda \right) f_{\sigma}^\dagger f_{\sigma} + (\lambda) a^\dagger a \\
&+ \sum_{\vec{k}, \sigma} \left(V_{\vec{k}} \operatorname{sgn}(\sigma) c_{\vec{k}\sigma}^\dagger f_{\vec{\sigma}}^\dagger a + h.c. \right) - \lambda.
\end{aligned} \tag{D.8}$$

We, therefore, have a microscopic parameter $\tilde{\varepsilon}^a$ for the double-occupation peak position and $\tilde{\mu}$ as the chemical potential, which acts with a different sign in the conduction electrons. It can be understood as controlling the hole-filling like the regular chemical potential controls the particle-filling. To avoid confusion, we shall define all quantities explicitly with the chemical potential.

The following recipe can, therefore, be used to solve the case of omitting b with equations of the case where a is omitted:

1. Start with the set of equations for the $U \rightarrow \infty$ case, i.e. without a .
2. Instead of using $\varepsilon^d - \mu$, use $\tilde{\varepsilon}^a - \tilde{\mu}$.
3. Explicitly including the chemical potential, Instead of using $\mathbf{A}_{\vec{k}\vec{k}}^{c(0)}(\varepsilon - \mu)$ in the self-energy equations, use the spin-flipped energy-mirrored $\mathbf{A}_{\vec{k}\vec{k}}^{\text{eff}}(\varepsilon + \tilde{\mu}) = \bar{\mathbf{A}}_{\vec{k}\vec{k}}^{c(0)}(-(\varepsilon - \tilde{\mu}))$.
4. In the slave-boson self-energy, instead of using $\mathbf{A}^f(\varepsilon + \omega)$, use the transpose $\mathbf{A}^{fT}(\varepsilon + \omega)$.
5. After convergence, calculate $\operatorname{Im} \mathbf{G}^{dA}(\omega)$, flip the spin and invert the energy $\operatorname{Im} \bar{\mathbf{G}}^{dA}(-\omega)$. The result is the impurity spectrum for the $\varepsilon^b \rightarrow \infty$ case.

Details of the PrV₂Al₂₀ Model

E.1 Representation of Selected CEF States in Total Angular Momentum States for PrV₂Al₂₀

This is reproduced from section VI of the supplemental material of [123] with minor modifications.

The experimentally determined CEF ground state of the Pr²⁺ ion is the Γ_3 doublet of the cubic T_d point group. Hund's rules for the $4f^2$ configuration state that the spin-orbit coupled ground state is a $J = 4$ state, whose m_J states provide a basis in which the CEF states can be expressed [133].

The index $\alpha = \pm$, dubbed isospin, enumerates the non-Kramers $|4f^2, \Gamma_3\alpha\rangle$ states:

$$|\Gamma_3-\rangle = \frac{1}{\sqrt{2}} (|+2\rangle + |-2\rangle) \quad (\text{E.1})$$

$$|\Gamma_3+\rangle = \frac{1}{2\sqrt{6}} \left(\sqrt{7} [|+4\rangle + |-4\rangle] - \sqrt{10} |0\rangle \right). \quad (\text{E.2})$$

Additionally, first excited CEF state is the Γ_5 triplet, whose states $|4f^2 \Gamma_5, m\rangle$ with $m \in \{-1, 0, 1\}$ are

$$|\Gamma_5, \pm\rangle = \pm \frac{1}{4\sqrt{2}} \left(\sqrt{7} |\pm 3\rangle - |\mp 1\rangle \right) \quad (\text{E.3})$$

$$|\Gamma_5, 0\rangle = \frac{1}{\sqrt{2}} \left(|+2\rangle - |-2\rangle \right). \quad (\text{E.4})$$

In the same manner, the $4f^1$ states mediating the valence fluctuations can be expressed in their Hund's rule ground state of $J = 5/2$. Here, we only consider The Γ_8 quartet, which is given by

$$|\Gamma_8^{+7/4}\rangle = \frac{1}{\sqrt{6}} \left(\sqrt{5} |\pm 5/2\rangle + |\mp 3/2\rangle \right) \quad (\text{E.5})$$

$$|\Gamma_8^{-7/4}\rangle = |\pm 1/2\rangle. \quad (\text{E.6})$$

E.2 CEF Multiplet Hybridization Matrix Elements

This is reproduced from section **VII** of the supplemental material of [123] with minor modifications.

The CEF ground state of the $4f^2$ transforms as Γ_3 , the ground state of $4f^3$ likely as Γ_6 irreps of the T_d group. A hybridization term connecting $4f^2$ and $4f^3$ should, therefore, transform as $\Gamma_6 \otimes \Gamma_3 = \Gamma_8$. Conduction electrons mediating this transition are to be projected onto the local Γ_8 quartet. Excited CEF levels of $4f^2$ will be frozen out exponentially at low temperatures. One expects this hybridization to be most important for the discussion of the two-channel quadrupolar Kondo physics in PrV₂Al₂₀. As discussed in section 7.6, however, we also need to include the first excited $4f^2$ CEF level to investigate the magnetic susceptibility faithfully. The associated irrep is Γ_5 and transforms like a spin-triplet, labeled by the index m . The corresponding hybridization term transforms as $\Gamma_6 \otimes \Gamma_5 = \Gamma_7 \oplus \Gamma_8$, requiring an additional Γ_7 doublet on the conduction-electron side. By choosing a basis for Γ_8 that trivializes the hybridization with Γ_3 we get a non-trivial hybridization with Γ_5 . This could be mitigated by choosing an appropriate $\Gamma_7 \oplus \Gamma_8$ basis for this hybridization separately at the cost of having two different projected conduction-electron fields: ψ in Eq. (7.8) and ψ' given by a modified \vec{k} -dependent structure factor. This increases the DMFT complexity and numerical cost significantly, which is why we chose to stay in the original basis.

In an effort to simplify the model and in the context of the main interest of this thesis, we take the conduction electrons to transform as the Γ_8 quartet, neglecting the Γ_7 part on the right-hand side of $\Gamma_6 \otimes \Gamma_5 = \Gamma_7 \oplus \Gamma_8$. Since we describe the symmetries of the local Pr 4f orbitals faithfully, this does not change any of our conclusions.

Once additional CEF levels are taken into account, one needs to consider relative phases and hybridization strengths carefully. The matrix elements we use are calculated from dipole-moment conservation and an appropriate combination of states using Clebsch-Gordan coefficients. For the Γ_3 ground state, we have local hybridization terms of the structure $f_\alpha^\dagger a_\mu \psi_{\alpha'\mu'}^\dagger$. If we take f_α^\dagger as the target state, we first need to particle-hole-transform *with spin- and quadrupole-moment flipped* in the conduction electrons $\psi_{\alpha\mu}^\dagger \rightarrow \zeta_{-\alpha-\mu}$, resulting in a hybridization $f_\alpha^\dagger a_\mu \zeta_{\alpha'\mu'}$. Since α is conserved in the scattering, we immediately get $\alpha = \alpha'$. The dipole moment must vanish in order for it to transform as a scalar, indicating that conduction-electron holes and slave bosons must form a spin singlet. We therefore get

$$H_{\text{hyb,loc}}^{\Gamma_3} = V_0 \sum_{\alpha} f_{\alpha}^{\dagger} \frac{1}{\sqrt{2}} \left(a_{\uparrow} \zeta_{\alpha\downarrow} - a_{\downarrow} \zeta_{\alpha\uparrow} \right) + h.c. \quad (\text{E.7})$$

$$= \frac{V_0}{\sqrt{2}} \sum_{\alpha} \text{sgn}(\mu) f_{\alpha}^{\dagger} a_{\mu} \zeta_{\alpha-\mu} + h.c. \quad (\text{E.8})$$

$$= \frac{V_0}{\sqrt{2}} \sum_{\alpha} \text{sgn}(\mu) f_{\alpha}^{\dagger} a_{\mu} \psi_{-\alpha\mu}^{\dagger} + h.c. \quad (\text{E.9})$$

The conjugation (spin- and quadrupole flip) of quantum numbers in the particle-hole transformation was necessary to make sure the Hamiltonian conserves spin and quadrupole moment in both representations. This is needed since we *only transform the conduction electrons* and not the whole Hamiltonian.

For the excited state, which transforms like a spin-triplet, we have to apply the same logic. First, the hybridization term is $d_m^\dagger a_\mu \psi_{\alpha\mu'}^\dagger \rightarrow d_m^\dagger a_\mu \zeta_{\alpha\mu'}$ with $\psi_{\alpha\mu}^\dagger \rightarrow \zeta_{-\alpha-\mu}$ as before. Here, $m \in \{-1, 0, 1\}$. We need to combine the spins of a and ζ to a triplet. The local hybridization contribution of Γ_5 to the

Hamiltonian is therefore

$$H_{\text{hyb,loc}}^{\Gamma_5} = V_1 \sum_{\alpha} \eta_{\alpha} \left[d_0^{\dagger} \frac{1}{\sqrt{2}} (a_{\uparrow} \zeta_{\alpha\downarrow} + a_{\downarrow} \zeta_{\alpha\uparrow}) + d_{+1}^{\dagger} a_{\uparrow} \zeta_{\alpha\uparrow} + d_{-1}^{\dagger} a_{\downarrow} \zeta_{\alpha\downarrow} \right] + h.c. \quad (\text{E.10})$$

The factor η_{α} has to be determined to match the right-side quadrupole moment with the quadrupole moment of Γ_5 . This will generally lead to a superposition. Since it really is a superposition and not a combination of quadrupole moments of two particles, a reasonable approach would be to define η_{α} such that $\sum_{\alpha} |\eta_{\alpha}|^2 = 1$. The simplest choice is $\eta_{+} = \eta_{-}$, with which we get $\eta_{\alpha} = 1/\sqrt{2}$, resulting in

$$H_{\text{hyb,loc}}^{\Gamma_5} = \frac{V_1}{\sqrt{2}} \sum_{\alpha} \left[d_0^{\dagger} \frac{1}{\sqrt{2}} (a_{\uparrow} \zeta_{\alpha\downarrow} + a_{\downarrow} \zeta_{\alpha\uparrow}) + d_{+1}^{\dagger} a_{\uparrow} \zeta_{\alpha\uparrow} + d_{-1}^{\dagger} a_{\downarrow} \zeta_{\alpha\downarrow} \right] + h.c. \quad (\text{E.11})$$

With this choice of prefactors, setting $V_1 = V_0$ results in identical local hybridization function strengths for Γ_3 and Γ_5 .

Additionally to what was discussed before, one can also modify the prefactors such that the hybridization transforms like a scalar, which can be achieved by understanding the operators ξ and a combined as a spin-1 operator ζ , combining d and the ζ -hole (with flipped spin) $\tilde{\zeta}$ to a total spin zero such that

$$H_{\text{hyb,loc}}^{\Gamma_5} = \frac{V_1}{\sqrt{6}} \sum_{\alpha} \eta_{\alpha} \left(d_{+1}^{\dagger} \tilde{\zeta}_{\alpha,-1}^{\dagger} + d_{-1}^{\dagger} \tilde{\zeta}_{\alpha,+1}^{\dagger} - d_0^{\dagger} \tilde{\zeta}_{\alpha,0}^{\dagger} \right) + h.c., \quad (\text{E.12})$$

or, substituting everything back,

$$H_{\text{hyb,loc}}^{\Gamma_5} = \frac{V_1}{\sqrt{3}} \sum_{\alpha} \eta_{\alpha} \left[d_{+1}^{\dagger} a_{\uparrow} \psi_{\alpha\downarrow}^{\dagger} + d_{-1}^{\dagger} a_{\downarrow} \psi_{\alpha\uparrow}^{\dagger} - d_0^{\dagger} \frac{1}{\sqrt{2}} (a_{\uparrow} \psi_{\alpha\uparrow}^{\dagger} + a_{\downarrow} \psi_{\alpha\downarrow}^{\dagger}) \right] + h.c.. \quad (\text{E.13})$$

When setting $V_1 = V_0 \sqrt{3/2}$, this is identical to the previous case with the exception of a minus sign in front of the $m = 0$ term, which turns out to be insignificant in our calculation. We found that numerically, an imbalance between the two induces a much larger CEF splitting than the experimental results [113] suggest. This has to be mitigated via a modified bare splitting in the Hamiltonian.

Generally, we could also have an imbalance between the two quadrupole momenta, e.g. $\eta_{-} = 0$. This is reflected by the fact that $\Gamma_6 \otimes \Gamma_8 = \Gamma_3 \oplus \Gamma_4 \oplus \Gamma_5$. Forming a dipole singlet on the left side leaves a quadrupole moment unpaired, resulting in the Γ_3 doublet. When forming a spin triplet on the other hand, the quadrupole moment is still not paired. Now, the right-hand side needs to have a threefold spin-1 quantum number in addition to the twofold quadrupole orientation. One can imagine the most extreme case in which each quadrupole moment orientation is individually attached to a triplet, resulting in two potentially different triplets, which is reflected in the appearance of the Γ_4 and Γ_5 triplets on the right. Only considering one of the triplets potentially induces an imbalance between the two quadrupole moments, resulting in a splitting at all temperatures. Since this is unphysical, we

stick to an α -symmetric Γ_5 coupling. One could remedy this by also considering Γ_4 , which is beyond the scope of this thesis.

E.3 Details of the Structure factor

This is reproduced from section **II** of the supplemental material of [123] with minor modifications.

The effective conduction electrons in our model are given by a projection of all bands onto V d orbitals. The hybridization is, however, mediated by those electrons projected onto Γ_8 states at the location of the Pr atom. For this, the overlap of the orbital Wannier functions at each V site has to be calculated, resulting in a \vec{k} -dependent structure factor $\Phi(\vec{k})$.

The real-space hybridization structure factor is

$$\Phi_{\alpha\mu;\sigma}^a(\mathbf{R}_j - \mathbf{r}_i) = \langle \text{Pr } \Gamma_8^{\delta}; j\alpha\mu | \text{V}; ia\sigma \rangle. \quad (\text{E.14})$$

Here, j labels the Pr position \mathbf{R}_j and i the V position \mathbf{r}_i . Additionally, $\alpha = \pm$ and $\mu = \uparrow, \downarrow$ are the Γ_8 quantum numbers, a and σ represent V orbital and spin quantum numbers. Note that the structure factor only depends on the distance $\mathbf{R}_j - \mathbf{r}_i$ and its Fourier transform is diagonal in momentum space. The structure factor in \vec{k} -space,

$$\Phi_{\alpha\mu;\sigma}^a(\vec{k}) = \sum_{i,j} e^{-i\vec{k}(\mathbf{R}_j - \mathbf{r}_i)} \Phi_{\alpha\mu;\sigma}^a(\mathbf{R}_j - \mathbf{r}_i), \quad (\text{E.15})$$

does not depend on \mathbf{R}_j anymore. The Pr position is, however explicitly treated in the projection, which reads,

$$\psi_{j,\alpha\mu} = \sum_i \sum_{a,\sigma} \Phi_{\alpha\mu;\sigma}^a(\mathbf{R}_j - \mathbf{r}_i) c_{\sigma}^a(\mathbf{r}_i) \quad (\text{E.16})$$

$$= \sum_{\vec{k}, \vec{k}', i} \sum_{a,\sigma} e^{i\vec{k}(\mathbf{R}_j - \mathbf{r}_i)} \Phi_{\alpha\mu;\sigma}^a(\vec{k}) e^{i\vec{k}'\mathbf{r}_i} c_{\sigma}^a(\vec{k}') \quad (\text{E.17})$$

$$= \sum_{\vec{k}} \sum_{a,\sigma} e^{i\vec{k}\mathbf{R}_j} \Phi_{\alpha\mu;\sigma}^a(\vec{k}) c_{\sigma}^a(\vec{k}). \quad (\text{E.18})$$

For convenience, we define a matrix $\Phi_j^a(\vec{k})$ as

$$\left[\Phi_j^a(\vec{k}) \right]_{\alpha\mu;\sigma} := \Phi_{j\alpha\mu;\sigma}^a(\vec{k}) := e^{i\vec{k}\mathbf{R}_j} \Phi_{\alpha\mu;\sigma}^a(\vec{k}). \quad (\text{E.19})$$

Only two orbitals $a \in \{d_{xy}, d_{x^2-y^2}\} =: \mathcal{D}$ are considered, as discussed in section 7.3. Due to the local nature of DMFT, we only need to consider \mathbf{R}_j in a single unit cell, and due to the two Pr atoms being crystallographically identical, we only take one of them (\mathbf{R}_1) into account. Additionally, we are unable to resolve the two degenerate orbitals and the individual V sub-lattices within DFT and, therefore, sum over them. In order to numerically calculate this \vec{k} -dependent structure factor, the position vectors of all structure-factor relevant atoms are needed.

There are 4 V atoms per primitive unit cell. The lattice basis vectors are

$$\mathbf{a}_1 = \frac{1}{2} \begin{pmatrix} 0 \\ a \\ a \end{pmatrix}, \quad \mathbf{a}_2 = \frac{1}{2} \begin{pmatrix} a \\ 0 \\ a \end{pmatrix}, \quad \mathbf{a}_3 = \frac{1}{2} \begin{pmatrix} a \\ a \\ 0 \end{pmatrix}. \quad (\text{E.20})$$

In the basis of those, the coordinates of V atoms are

$$\begin{aligned} \mathbf{v}_{\text{red}} &= \frac{1}{2} \begin{pmatrix} 0 \\ 1 \\ 1 \end{pmatrix}, & \mathbf{v}_{\text{green}} &= \frac{1}{2} \begin{pmatrix} 1 \\ 0 \\ 1 \end{pmatrix}, \\ \mathbf{v}_{\text{blue}} &= \frac{1}{2} \begin{pmatrix} 1 \\ 1 \\ 0 \end{pmatrix}, & \mathbf{v}_{\text{yellow}} &= \frac{1}{2} \begin{pmatrix} 1 \\ 1 \\ 1 \end{pmatrix}, \end{aligned}$$

and those of the two Pr atoms are

$$\mathbf{R}_1 = \frac{1}{8} \begin{pmatrix} 1 \\ 1 \\ 1 \end{pmatrix}, \quad \mathbf{R}_2 = \frac{1}{8} \begin{pmatrix} 7 \\ 7 \\ 7 \end{pmatrix}.$$

As explained before, we only take the Pr atom at \mathbf{R}_1 into account. It has 12 neighboring V atoms, three V atoms for each fcc sub-lattice $l \in \{1, 2, 3, 4\}$ or equivalently {Red, Green, Blue, Yellow}. Each of those three V atoms is then labeled by $l_s \in \{1, 2, 3\}$. Their position vectors \mathbf{r}_{l,l_s} are listed below.

$$\begin{aligned} \mathbf{r}_{1,1} &= \frac{1}{2} \begin{pmatrix} 0 \\ 1 \\ 1 \end{pmatrix} & \mathbf{r}_{1,2} &= \frac{1}{2} \begin{pmatrix} 0 \\ 1 \\ -1 \end{pmatrix} & \mathbf{r}_{1,3} &= \frac{1}{2} \begin{pmatrix} 0 \\ -1 \\ 1 \end{pmatrix} \\ \mathbf{r}_{2,1} &= \frac{1}{2} \begin{pmatrix} 1 \\ 0 \\ 1 \end{pmatrix} & \mathbf{r}_{2,2} &= \frac{1}{2} \begin{pmatrix} 1 \\ 0 \\ -1 \end{pmatrix} & \mathbf{r}_{2,3} &= \frac{1}{2} \begin{pmatrix} -1 \\ 0 \\ 1 \end{pmatrix} \\ \mathbf{r}_{3,1} &= \frac{1}{2} \begin{pmatrix} 1 \\ 1 \\ 0 \end{pmatrix} & \mathbf{r}_{3,2} &= \frac{1}{2} \begin{pmatrix} 1 \\ -1 \\ 0 \end{pmatrix} & \mathbf{r}_{3,3} &= \frac{1}{2} \begin{pmatrix} -1 \\ 1 \\ 0 \end{pmatrix} \\ \mathbf{r}_{4,1} &= \frac{1}{2} \begin{pmatrix} -1 \\ 1 \\ 1 \end{pmatrix} & \mathbf{r}_{4,2} &= \frac{1}{2} \begin{pmatrix} 1 \\ -1 \\ 1 \end{pmatrix} & \mathbf{r}_{4,3} &= \frac{1}{2} \begin{pmatrix} 1 \\ 1 \\ -1 \end{pmatrix} \end{aligned}$$

We only consider the contribution of those 12 atoms, them being the nearest neighbors of Pr.

Collecting everything above, the final expression for the structure factor reads,

$$\left[\Phi_j(\vec{k}) \right]_{\alpha\mu;\sigma} = e^{i\vec{k}\mathbf{R}_j} \sum_{a \in \mathcal{D}} \Phi_{\alpha\mu;\sigma}^a(\vec{k}), \quad (\text{E.21})$$

$$\Phi_{\alpha\mu;\sigma}^a(\vec{k}) = \sum_{l,l_s} e^{-i\vec{k}(\mathbf{R}_1 - \mathbf{r}_{l,l_s})} \Phi_{\alpha\mu;\sigma}^a(\mathbf{R}_j - \mathbf{r}_{l,l_s}), \quad (\text{E.22})$$

which is the structure factor used in the numerical calculations. Note that the second line is just the Fourier transform in the reduced set of contributing V atoms, projected onto a single Pr atom.

E.4 Details about the Numerical Treatment of the Magnetic Susceptibility

In order to extract the magnetic susceptibility, a magnetic field is coupled to the model via a Zeeman term in all dipole-bearing quantities

$$\begin{aligned}
 H_{\text{mag}} = & g_c B \sum_{n,\sigma,\vec{k}} \text{sgn}(\sigma) c_{n,\sigma}^\dagger(\vec{k}) c_{n,\sigma}(\vec{k}) \\
 & + g_d B \sum_{j,m} m d_{j,m}^\dagger d_{j,m} \\
 & + g_a B \sum_{j,\mu} \text{sgn}(\mu) a_{j,\mu}^\dagger a_{j,\mu}.
 \end{aligned} \tag{E.23}$$

The relative coupling constants are given by the Landé factors, which can be extracted for the CEF states via a simple calculation [133]. They are

$$g_c = 2, \tag{E.24}$$

$$g_d = 2, \tag{E.25}$$

$$g_a = -5/2. \tag{E.26}$$

Only coupling of linear orders in the external magnetic field B is taken into account. Hence, Γ_3 does not couple directly. From this, the magnetization of each particle species (locally) is proportional to the occupation number imbalance $n_+ - n_-$, where plus and minus refer to the dipole moment orientation. This method automatically includes all vertex corrections induced by the field and is, therefore, preferable to the diagrammatic evaluation of linear-response theory.

The external magnetic field is chosen to be small enough to sit firmly in the linear response regime, smaller than the Kondo temperature, and large enough not to have the data dominated by numerical noise. Due to the increased numerical complexity and necessary precision, susceptibility calculations with this method tend to converge worse than the bare models.

More details, including a comparison of the parameter dependence of the susceptibility, can be found in section **IX** of the supplemental material of [123].

Bibliography

- [1] L. D. Landau, *The Theory of a Fermi Liquid*, **30** (1956) 1058, *J. Exp. Theor. Phys.* **3**, 920 (1956) (cit. on p. 1).
- [2] J. Kondo, *Resistance Minimum in Dilute Magnetic Alloys*, en, *Progress of Theoretical Physics* **32** (1964) 37, ISSN: 0033-068X, 1347-4081, URL: <https://academic.oup.com/ptp/article-lookup/doi/10.1143/PTP.32.37> (visited on 03/14/2024) (cit. on pp. 1, 38, 39).
- [3] M. A. Ruderman and C. Kittel, *Indirect Exchange Coupling of Nuclear Magnetic Moments by Conduction Electrons*, en, *Physical Review* **96** (1954) 99, ISSN: 0031-899X, URL: <https://link.aps.org/doi/10.1103/PhysRev.96.99> (visited on 05/14/2024) (cit. on pp. 1, 46).
- [4] T. Kasuya, *A Theory of Metallic Ferro- and Antiferromagnetism on Zener's Model*, en, *Progress of Theoretical Physics* **16** (1956) 45, ISSN: 0033-068X, URL: <https://academic.oup.com/ptp/article-lookup/doi/10.1143/PTP.16.45> (visited on 05/14/2024) (cit. on pp. 1, 39, 46).
- [5] K. Yosida, *Magnetic Properties of Cu-Mn Alloys*, en, *Physical Review* **106** (1957) 893, ISSN: 0031-899X, URL: <https://link.aps.org/doi/10.1103/PhysRev.106.893> (visited on 05/14/2024) (cit. on pp. 1, 39, 46).
- [6] S. Doniach, *The Kondo lattice and weak antiferromagnetism*, en, *Physica B+C* **91** (1977) 231, ISSN: 03784363, URL: <https://linkinghub.elsevier.com/retrieve/pii/0378436377901905> (visited on 05/20/2024) (cit. on pp. 2, 3, 47).
- [7] R. Settai, T. Takeuchi, and Y. Ōnuki, *Recent Advances in Ce-Based Heavy-Fermion Superconductivity and Fermi Surface Properties*, en, *Journal of the Physical Society of Japan* **76** (2007) 051003, ISSN: 0031-9015, 1347-4073, URL: <https://journals.jps.jp/doi/10.1143/JPSJ.76.051003> (visited on 06/05/2024) (cit. on p. 2).

- [8] M. W. McElfresh et al., *Effect of high pressure on the electrical resistivity of the heavy-fermion compound UBe 13*, en, *Physical Review B* **42** (1990) 6062, ISSN: 0163-1829, 1095-3795, URL: <https://link.aps.org/doi/10.1103/PhysRevB.42.6062> (visited on 06/05/2024) (cit. on p. 2).
- [9] J. D. Thompson and Z. Fisk, *Kondo-lattice – mixed-valence resistance scaling in heavy-fermion CeCu 6 under pressure*, en, *Physical Review B* **31** (1985) 389, ISSN: 0163-1829, URL: <https://link.aps.org/doi/10.1103/PhysRevB.31.389> (visited on 06/05/2024) (cit. on p. 2).
- [10] G. R. Stewart, *Heavy-fermion systems*, en, *Reviews of Modern Physics* **56** (1984) 755, ISSN: 0034-6861, URL: <https://link.aps.org/doi/10.1103/RevModPhys.56.755> (visited on 06/05/2024) (cit. on p. 2).
- [11] H. Kang, K. Haule, G. Kotliar, P. Coleman, and J.-H. Shim, *Energy scales of the doped Anderson lattice model*, en, *Physical Review B* **99** (2019) 165115, ISSN: 2469-9950, 2469-9969, URL: <https://link.aps.org/doi/10.1103/PhysRevB.99.165115> (visited on 02/27/2023) (cit. on p. 2).
- [12] S. Ernst et al., *Emerging local Kondo screening and spatial coherence in the heavy-fermion metal YbRh2Si2*, *Nature* **474** (2011) 362, ISSN: 0028-0836, 1476-4687, URL: <http://www.nature.com/articles/nature10148> (visited on 03/21/2023) (cit. on pp. 2, 101, 102, 111).
- [13] Y. Shimura et al., *Field-induced quadrupolar quantum criticality in PrV₂Al₂₀*, *Phys. Rev. B* **91** (2015) 241102, ISSN: 1098-0121, 1550-235X, URL: <https://link.aps.org/doi/10.1103/PhysRevB.91.241102> (visited on 01/01/2019) (cit. on pp. 3, 117).
- [14] F. Bloch, *über die Quantenmechanik der Elektronen in Kristallgittern*, *Zeitschrift für Physik* **52** (1929) 555, ISSN: 1434-6001, 1434-601X, URL: <http://link.springer.com/10.1007/BF01339455> (visited on 03/25/2024) (cit. on p. 7).
- [15] C. Kittel, *Introduction to solid state physics*, 8th ed, Hoboken, NJ: Wiley, 2005, ISBN: 978-0-471-41526-8 (cit. on p. 7).
- [16] *Wannier function*, URL: https://en.wikipedia.org/wiki/Wannier_function (visited on 03/27/2024) (cit. on p. 7).
- [17] N. W. Ashcroft and N. D. Mermin, *Solid state physics*, Fort Worth Philadelphia San Diego [etc.]: Saunders college publ, 1976, ISBN: 978-0-03-083993-1 (cit. on p. 7).
- [18] H. Föll, *Semiconductors I*, 2019, URL: https://www.tf.uni-kiel.de/matwis/amat/semi_en/kap_2/basics/m2_1_2.html (visited on 03/26/2024) (cit. on p. 8).

-
- [19] G. H. Wannier, *The Structure of Electronic Excitation Levels in Insulating Crystals*, *Physical Review* **52** (1937) 191, ISSN: 0031-899X, URL: <https://link.aps.org/doi/10.1103/PhysRev.52.191> (visited on 03/27/2024) (cit. on p. 10).
- [20] J. C. Slater and G. F. Koster, *Simplified LCAO Method for the Periodic Potential Problem*, *Physical Review* **94** (1954) 1498, ISSN: 0031-899X, URL: <https://link.aps.org/doi/10.1103/PhysRev.94.1498> (visited on 03/27/2024) (cit. on p. 11).
- [21] R. d. L. Kronig and W. G. Penney, *Quantum mechanics of electrons in crystal lattices*, en, *Proceedings of the Royal Society of London. Series A, Containing Papers of a Mathematical and Physical Character* **130** (1931) 499, ISSN: 0950-1207, 2053-9150, URL: <https://royalsocietypublishing.org/doi/10.1098/rspa.1931.0019> (visited on 05/25/2024) (cit. on p. 12).
- [22] J. Schmalian, *Lecture notes in Theory of Condensed Matter II*, 2018, URL: https://www.tkm.kit.edu/downloads/ss2018_tkm2 (cit. on p. 15).
- [23] G. P. Curbera, S. Okada, and W. J. Ricker, *Inversion and extension of the finite Hilbert transform on $(-1,1)$* , *Annali di Matematica Pura ed Applicata (1923 -)* **198** (2019) 1835, This was the best reference that I could find on the matter, the results that I use are likely already established for a long time., ISSN: 0373-3114, 1618-1891, URL: <http://link.springer.com/10.1007/s10231-019-00837-w> (visited on 05/02/2024) (cit. on p. 18).
- [24] A. C. Hewson, *Kondo Problem to Heavy Fermions*, OCLC: 958551621, Cambridge, GBR: Cambridge University Press, 2009, ISBN: 978-0-511-47075-2 (cit. on pp. 21, 40–42, 45).
- [25] A. Sumiyama et al., *Coherent Kondo State in a Dense Kondo Substance: $Ce_xLa_{1-x}Cu_6$* , *Journal of the Physical Society of Japan* **55** (1986) 1294, ISSN: 0031-9015, 1347-4073, URL: <http://journals.jps.jp/doi/10.1143/JPSJ.55.1294> (visited on 04/10/2024) (cit. on p. 30).
- [26] J. Hubbard, *Electron correlations in narrow energy bands*, *Proceedings of the Royal Society of London. Series A. Mathematical and Physical Sciences* **276** (1963) 238, Publisher: The Royal Society London, ISSN: 0080-4630, URL: <https://royalsocietypublishing.org/doi/10.1098/rspa.1963.0204> (visited on 12/15/2022) (cit. on pp. 31, 33).
- [27] J. Hubbard, *Electron correlations in narrow energy bands. II. The degenerate band case*, *Proceedings of the Royal Society of London. Series A. Mathematical and Physical Sciences* **277** (1964) 237, ISSN: 0080-4630, 2053-9169, URL: <https://royalsocietypublishing.org/doi/10.1098/rspa.1964.0019> (visited on 05/14/2024) (cit. on pp. 31, 32).

- [28] E. C. Stoner, *Collective electron ferromagnetism*, *Proceedings of the Royal Society of London. Series A. Mathematical and Physical Sciences* **165** (1938) 372, ISSN: 0080-4630, 2053-9169, URL: <https://royalsocietypublishing.org/doi/10.1098/rspa.1938.0066> (visited on 05/14/2024) (cit. on p. 31).
- [29] K. A. Chao, J. Spalek, and A. M. Oleś, *Canonical perturbation expansion of the Hubbard model*, *Physical Review B* **18** (1978) 3453, ISSN: 0163-1829, URL: <https://link.aps.org/doi/10.1103/PhysRevB.18.3453> (visited on 06/05/2024) (cit. on p. 31).
- [30] P. W. Anderson, *New Approach to the Theory of Superexchange Interactions*, *Physical Review* **115** (1959) 2, ISSN: 0031-899X, URL: <https://link.aps.org/doi/10.1103/PhysRev.115.2> (visited on 06/05/2024) (cit. on p. 31).
- [31] G. Kotliar and A. E. Ruckenstein, *New Functional Integral Approach to Strongly Correlated Fermi Systems: The Gutzwiller Approximation as a Saddle Point*, *Physical Review Letters* **57** (1986) 1362, ISSN: 0031-9007, URL: <https://link.aps.org/doi/10.1103/PhysRevLett.57.1362> (visited on 06/05/2024) (cit. on p. 32).
- [32] P. W. Anderson, *Localized Magnetic States in Metals*, en, *Physical Review* **124** (1961) 41, ISSN: 0031-899X, URL: <https://link.aps.org/doi/10.1103/PhysRev.124.41> (visited on 11/21/2023) (cit. on p. 33).
- [33] A. Georges, *The beauty of impurities: Two revivals of Friedel's virtual bound-state concept*, en, *Comptes Rendus. Physique* **17** (2015) 430, ISSN: 1878-1535, URL: <https://comptes-rendus.academie-sciences.fr/physique/articles/10.1016/j.crhy.2015.12.005/> (visited on 05/20/2024) (cit. on p. 34).
- [34] H. Lehmann, *Über Eigenschaften von Ausbreitungsfunktionen und Renormierungskonstanten quantisierter Felder*, de, *Il Nuovo Cimento* **11** (1954) 342, ISSN: 0029-6341, 1827-6121, URL: <http://link.springer.com/10.1007/BF02783624> (visited on 05/19/2024) (cit. on p. 34).
- [35] H. Suhl, *Dispersion Theory of the Kondo Effect*, *Physical Review* **138** (1965) A515, ISSN: 0031-899X, URL: <https://link.aps.org/doi/10.1103/PhysRev.138.A515> (visited on 05/20/2024) (cit. on p. 38).
- [36] Y. Nagaoka, *Self-Consistent Treatment of Kondo's Effect in Dilute Alloys*, *Physical Review* **138** (1965) A1112, ISSN: 0031-899X, URL: <https://link.aps.org/doi/10.1103/PhysRev.138.A1112> (visited on 05/20/2024) (cit. on p. 38).

-
- [37] A. A. Abrikosov, *Electron scattering on magnetic impurities in metals and anomalous resistivity effects*, *Physics Physique Fizika* **2** (1965) 5, ISSN: 0554-128X, URL: <https://link.aps.org/doi/10.1103/PhysicsPhysiqueFizika.2.5> (visited on 05/20/2024) (cit. on pp. 38, 45, 47, 66, 70).
- [38] P. Nozières, *A fermi-liquid description of the Kondo problem at low temperatures*, *Journal of Low Temperature Physics* **17** (1974) 31, ISSN: 0022-2291, 1573-7357, URL: <http://link.springer.com/10.1007/BF00654541> (visited on 05/16/2024) (cit. on pp. 38, 46, 118).
- [39] C. Mora, C. P. Moca, J. Von Delft, and G. Zaránd, *Fermi-liquid theory for the single-impurity Anderson model*, *Physical Review B* **92** (2015) 075120, ISSN: 1098-0121, 1550-235X, URL: <https://link.aps.org/doi/10.1103/PhysRevB.92.075120> (visited on 05/20/2024) (cit. on p. 38).
- [40] J. R. Schrieffer and P. A. Wolff, *Relation between the Anderson and Kondo Hamiltonians*, *Physical Review* **149** (1966) 491, ISSN: 0031-899X, URL: <https://link.aps.org/doi/10.1103/PhysRev.149.491> (visited on 01/12/2024) (cit. on pp. 38, 40).
- [41] W. De Haas and G. Van Den Berg, *The electrical resistance of gold and silver at low temperatures*, *Physica* **3** (1936) 440, ISSN: 00318914, URL: <https://linkinghub.elsevier.com/retrieve/pii/S0031891436800093> (visited on 05/15/2024) (cit. on p. 39).
- [42] J. Friedel, *XIV. The distribution of electrons round impurities in monovalent metals*, en, *The London, Edinburgh, and Dublin Philosophical Magazine and Journal of Science* **43** (1952) 153, ISSN: 1941-5982, 1941-5990, URL: <http://www.tandfonline.com/doi/abs/10.1080/14786440208561086> (visited on 05/14/2024) (cit. on p. 39).
- [43] C. Zener, *Interaction Between the d Shells in the Transition Metals*, en, *Physical Review* **81** (1951) 440, ISSN: 0031-899X, URL: <https://link.aps.org/doi/10.1103/PhysRev.81.440> (visited on 05/14/2024) (cit. on p. 39).
- [44] Wikipedia, *Boltzmann equation* — *Wikipedia, The Free Encyclopedia*, <http://en.wikipedia.org/w/index.php?title=Boltzmann%20equation&oldid=1208664401>, [Online; accessed 16-May-2024], 2024 (cit. on p. 41).
- [45] P. W. Anderson, *A poor man's derivation of scaling laws for the Kondo problem*, *Journal of Physics C: Solid State Physics* **3** (1970) 2436, ISSN: 0022-3719, URL: <https://iopscience.iop.org/article/10.1088/0022-3719/3/12/008> (visited on 05/16/2024) (cit. on p. 46).

- [46] K. Yamada, *Perturbation Expansion for the Anderson Hamiltonian. II*, *Progress of Theoretical Physics* **53** (1975) 970, ISSN: 0033-068X, 1347-4081, URL: <https://academic.oup.com/ptp/article-lookup/doi/10.1143/PTP.53.970> (visited on 05/16/2024) (cit. on p. 46).
- [47] T. A. Costi, A. C. Hewson, and V. Zlatic, *Transport coefficients of the Anderson model via the numerical renormalization group*, *Journal of Physics: Condensed Matter* **6** (1994) 2519, ISSN: 0953-8984, 1361-648X, URL: <https://iopscience.iop.org/article/10.1088/0953-8984/6/13/013> (visited on 05/16/2024) (cit. on p. 46).
- [48] O. Újsághy, J. Kroha, L. Szunyogh, and A. Zawadowski, “Theory of Scanning Tunneling Spectroscopy of Kondo Ions on Metal Surfaces”, *Kondo Effect and Dephasing in Low-Dimensional Metallic Systems*, ed. by V. Chandrasekhar, C. Van Haesendonck, and A. Zawadowski, Dordrecht: Springer Netherlands, 2001 245, ISBN: 978-94-010-0427-5, URL: https://doi.org/10.1007/978-94-010-0427-5_34 (cit. on p. 46).
- [49] P. Coleman, *Introduction to Many-Body Physics*, 1st ed., Cambridge University Press, 2015, ISBN: 978-0-521-86488-6, URL: <https://www.cambridge.org/core/product/identifier/9781139020916/type/book> (visited on 05/16/2024) (cit. on pp. 46, 47, 75).
- [50] F. Steglich and S. Wirth, *Foundations of heavy-fermion superconductivity: lattice Kondo effect and Mott physics*, *Reports on Progress in Physics* **79** (2016) 084502, ISSN: 0034-4885, 1361-6633, URL: <https://iopscience.iop.org/article/10.1088/0034-4885/79/8/084502> (visited on 05/24/2024) (cit. on p. 46).
- [51] K. Andres, J. E. Graebner, and H. R. Ott, *4f-Virtual-Bound-State Formation in CeAl₃ at Low Temperatures*, en, *Physical Review Letters* **35** (1975) 1779, ISSN: 0031-9007, URL: <https://link.aps.org/doi/10.1103/PhysRevLett.35.1779> (visited on 05/20/2024) (cit. on pp. 46, 101).
- [52] F. Steglich et al., *Superconductivity in the Presence of Strong Pauli Paramagnetism: Ce Cu₂ Si₂*, en, *Physical Review Letters* **43** (1979) 1892, ISSN: 0031-9007, URL: <https://link.aps.org/doi/10.1103/PhysRevLett.43.1892> (visited on 05/20/2024) (cit. on p. 46).
- [53] J. Kroha, “Interplay of Kondo Effect and RKKY Interaction”, *The Physics of Correlated Insulators, Metals, and Superconductors: lecture notes of the Autumn School on Correlated Electrons 2017: at Forschungszentrum Jülich, 25-29 September 2017*, ed. by E. Pavarini et al., Schriften des Forschungszentrums Jülich. Reihe Modeling and Simulation Band 7, Meeting Name: Autumn School on Correlated Electrons, Jülich: Forschungszentrum, Zentralbibliothek, 2017 12.1, ISBN: 978-3-95806-224-5 (cit. on p. 47).

-
- [54] S. Doniach, “Phase Diagram for the Kondo Lattice”, en, *Valence Instabilities and Related Narrow-Band Phenomena*, ed. by R. D. Parks, Boston, MA: Springer US, 1977 169, ISBN: 978-1-4615-8816-0, URL: http://link.springer.com/10.1007/978-1-4615-8816-0_15 (visited on 05/20/2024) (cit. on p. 47).
- [55] N. F. Mott, *Rare-earth compounds with mixed valencies*, en, *Philosophical Magazine* **30** (1974) 403, ISSN: 0031-8086, URL: <http://www.tandfonline.com/doi/abs/10.1080/14786439808206566> (visited on 05/20/2024) (cit. on p. 47).
- [56] K. Miyake, S. Schmitt-Rink, and C. M. Varma, *Spin-fluctuation-mediated even-parity pairing in heavy-fermion superconductors*, en, *Physical Review B* **34** (1986) 6554, ISSN: 0163-1829, URL: <https://link.aps.org/doi/10.1103/PhysRevB.34.6554> (visited on 05/20/2024) (cit. on p. 47).
- [57] D. J. Scalapino, E. Loh, and J. E. Hirsch, *d-wave pairing near a spin-density-wave instability*, en, *Physical Review B* **34** (1986) 8190, ISSN: 0163-1829, URL: <https://link.aps.org/doi/10.1103/PhysRevB.34.8190> (visited on 05/20/2024) (cit. on p. 47).
- [58] P. Nozières and A. Blandin, *Kondo effect in real metals*, *Journal de Physique* **41** (1980) 193, ISSN: 0302-0738, URL: <http://www.edpsciences.org/10.1051/jphys:01980004103019300> (visited on 07/17/2023) (cit. on pp. 47, 118).
- [59] J. M. Luttinger and J. C. Ward, *Ground-State Energy of a Many-Fermion System. II*, *Physical Review* **118** (1960) 1417, ISSN: 0031-899X, URL: <https://link.aps.org/doi/10.1103/PhysRev.118.1417> (visited on 05/21/2024) (cit. on pp. 48, 72).
- [60] J. M. Luttinger, *Fermi Surface and Some Simple Equilibrium Properties of a System of Interacting Fermions*, *Physical Review* **119** (1960) 1153, ISSN: 0031-899X, URL: <https://link.aps.org/doi/10.1103/PhysRev.119.1153> (visited on 05/21/2024) (cit. on p. 48).
- [61] H. Shishido, R. Settai, H. Harima, and Y. Ōnuki, *A Drastic Change of the Fermi Surface at a Critical Pressure in CeRhIn₅: dHvA Study under Pressure*, *Journal of the Physical Society of Japan* **74** (2005) 1103, ISSN: 0031-9015, 1347-4073, URL: <https://journals.jps.jp/doi/10.1143/JPSJ.74.1103> (visited on 05/21/2024) (cit. on p. 49).
- [62] H. J. Leder and B. Mühlischlegel, *Susceptibility and specific heat of intermediate valence compounds studied in mean-field theory of a periodic anderson model*, en, *Zeitschrift für Physik B Condensed Matter and Quanta* **29** (1978) 341, ISSN: 0340-224X, 1434-6036, URL: <http://link.springer.com/10.1007/BF01324031> (visited on 05/21/2024) (cit. on p. 49).

- [63] M. S. Dresselhaus, G. Dresselhaus, and A. Jorio, *Group theory: application to the physics of condensed matter*, OCLC: ocn150354198, Berlin: Springer-Verlag, 2008, ISBN: 978-3-540-32897-1 (cit. on pp. 56, 57, 60).
- [64] M. I. Aroyo, A. Kirov, C. Capillas, J. M. Perez-Mato, and H. Wondratschek, *Bilbao Crystallographic Server. II. Representations of crystallographic point groups and space groups*, *Acta Crystallographica Section A Foundations of Crystallography* **62** (2006) 115, ISSN: 0108-7673, URL: <https://scripts.iucr.org/cgi-bin/paper?S0108767305040286> (visited on 06/01/2024) (cit. on pp. 59, 63).
- [65] G. F. Koster, ed., *Properties of the thirty-two point groups*, eng, 3. printing, Cambridge, Mass: M.I.T. Pr, 1969, ISBN: 978-0-262-11010-5 (cit. on pp. 59, 61).
- [66] R. Winkler, *Introduction to Group Theory, Revised edition (2015)*, 2011, URL: <https://www.niu.edu/rwinkler/teaching/group-11/> (cit. on pp. 62, 63).
- [67] S. E. Barnes, *New method for the Anderson model*, *Journal of Physics F: Metal Physics* **6** (1976) 1375, ISSN: 0305-4608, URL: <https://iopscience.iop.org/article/10.1088/0305-4608/6/7/018> (visited on 05/23/2024) (cit. on pp. 65, 66, 70).
- [68] S. E. Barnes, *New method for the Anderson model. II. The $U=0$ limit*, en, *Journal of Physics F: Metal Physics* **7** (1977) 2637, ISSN: 0305-4608, URL: <https://dx.doi.org/10.1088/0305-4608/7/12/022> (visited on 02/14/2023) (cit. on pp. 65, 66, 70).
- [69] Y. Kuramoto, *Self-consistent perturbation theory for dynamics of valence fluctuations*, *Zeitschrift für Physik B Condensed Matter* **53** (1983) 37, ISSN: 1431-584X, URL: <https://doi.org/10.1007/BF01578246> (visited on 02/14/2023) (cit. on pp. 65, 74).
- [70] Y. Kuramoto and E. Müller-Hartmann, *Analytic results on dynamics of the degenerate Anderson model*, *Journal of Magnetism and Magnetic Materials* **52** (1985) 122, ISSN: 03048853, URL: <https://linkinghub.elsevier.com/retrieve/pii/0304885385902367> (visited on 06/07/2024) (cit. on pp. 65, 74).
- [71] N. E. Bickers, D. L. Cox, and J. W. Wilkins, *Self-consistent large- N expansion for normal-state properties of dilute magnetic alloys*, *Physical Review B* **36** (1987) 2036, ISSN: 0163-1829, URL: <https://link.aps.org/doi/10.1103/PhysRevB.36.2036> (visited on 06/07/2024) (cit. on pp. 65, 74).
- [72] H. A. Kramers, “Théorie générale de la rotation paramagnétique dans les cristaux”, French, *Proceedings Koninklijke Akademie van Wetenschappen*, vol. 33, 1930 959 (cit. on p. 69).

-
- [73] E. P. Wigner, “Über die Operation der Zeitumkehr in der Quantenmechanik”, en, *The Collected Works of Eugene Paul Wigner*, ed. by A. S. Wightman, Berlin, Heidelberg: Springer Berlin Heidelberg, 1993 213, ISBN: 978-3-662-02781-3, URL: http://link.springer.com/10.1007/978-3-662-02781-3_15 (visited on 06/05/2024) (cit. on p. 69).
- [74] R. Eder, “The Variational Cluster Approximation”, eng, *Emergent phenomena in correlated matter: lecture notes of the Autumn School Correlated Electrons 2013: at Forschungszentrum Jülich, 23-27 September 2013*, ed. by E. Pavarini, E. Koch, U. Schollwöck, Institute for Advanced Simulation, and German Research School for Simulation Sciences, Schriften des Forschungszentrums Jülich. Reihe Modeling and Simulation Band 3, Meeting Name: Autumn School Correlated Electrons, Jülich: Forschungszentrum, Zentralbibliothek, 2013 4.1, ISBN: 978-3-89336-884-6 (cit. on p. 72).
- [75] J. M. Cornwall, R. Jackiw, and E. Tomboulis, *Effective action for composite operators*, en, *Physical Review D* **10** (1974) 2428, ISSN: 0556-2821, URL: <https://link.aps.org/doi/10.1103/PhysRevD.10.2428> (visited on 05/26/2024) (cit. on p. 72).
- [76] J. Kroha and P. Wölfle, *Fermi and Non-Fermi Liquid Behavior in Quantum Impurity Systems: Conserving Slave Boson Theory*, tech. rep., 1998 (cit. on pp. 74, 88).
- [77] G. Baym and L. P. Kadanoff, *Conservation Laws and Correlation Functions*, en, *Physical Review* **124** (1961) 287, ISSN: 0031-899X, URL: <https://link.aps.org/doi/10.1103/PhysRev.124.287> (visited on 05/26/2024) (cit. on p. 74).
- [78] H. A. Kramers, “La diffusion de la lumière par les atomes”, *Atti del Congresso Internazionale dei Fisici*, vol. 2, English translation in Ter Haar D, 1998 Master of Modern Physics: The Scientific Contributions of H. A. Kramers (Princeton University Press) Appendix D, Como-Pavia-Roma, 1927 545 (cit. on p. 79).
- [79] R. De L. Kronig, *On the Theory of Dispersion of X-Rays*, *Journal of the Optical Society of America* **12** (1926) 547, ISSN: 0030-3941, URL: <https://opg.optica.org/abstract.cfm?URI=josa-12-6-547> (visited on 05/27/2024) (cit. on p. 79).
- [80] D. L. Cox and A. Zawadowski, *Exotic Kondo Effects in Metals: Magnetic Ions in a Crystalline Electric Field and Tunneling Centers*, arXiv:cond-mat/9704103, 1997, URL: <http://arxiv.org/abs/cond-mat/9704103> (visited on 12/16/2022) (cit. on p. 91).
- [81] D. G. Anderson, *Iterative Procedures for Nonlinear Integral Equations*, en, *Journal of the ACM* **12** (1965) 547, ISSN: 0004-5411, 1557-735X, URL: <https://dl.acm.org/doi/10.1145/321296.321305> (visited on 05/27/2024) (cit. on p. 91).

- [82] K. Haule, S. Kirchner, J. Kroha, and P. Wölfle, *Anderson impurity model at finite Coulomb interaction U : Generalized noncrossing approximation*, *Physical Review B* **64** (2001) 155111, ISSN: 0163-1829, 1095-3795, URL: <https://link.aps.org/doi/10.1103/PhysRevB.64.155111> (visited on 02/15/2023) (cit. on p. 92).
- [83] A. Georges and G. Kotliar, *Hubbard model in infinite dimensions*, *Physical Review B* **45** (1992) 6479, Publisher: American Physical Society, URL: <https://link.aps.org/doi/10.1103/PhysRevB.45.6479> (visited on 02/14/2023) (cit. on p. 94).
- [84] W. Metzner and D. Vollhardt, *Correlated Lattice Fermions in $d = \infty$ Dimensions*, *Physical Review Letters* **62** (1989) 324, ISSN: 0031-9007, URL: <https://link.aps.org/doi/10.1103/PhysRevLett.62.324> (visited on 05/28/2024) (cit. on p. 94).
- [85] P. Weiss, *L'hypothèse du champ moléculaire et la propriété ferromagnétique*, *Journal de Physique Théorique et Appliquée* **6** (1907) 661, ISSN: 0368-3893, URL: <http://www.edpsciences.org/10.1051/jphysap:019070060066100> (visited on 05/28/2024) (cit. on p. 94).
- [86] D. Vollhardt, “Dynamical Mean-Field Approach for Strongly Correlated Materials”, *The LDA+DMFT approach to strongly correlated materials: lecture notes of the Autumn School 2011 Hands-on LDA+DMFT: at Forschungszentrum Jülich, 4-7 October 2011*, ed. by E. Pavarini et al., Schriften des Forschungszentrums Jülich. Reihe Modeling and Simulation Band 1, Meeting Name: Autumn School Hands-on LDA+DMFT, Jülich: Forschungszentrum Jülich, Zentralbibliothek, Verl, 2011 1.1, ISBN: 978-3-89336-734-4 (cit. on p. 94).
- [87] M. Kollar, “Introduction to Dynamical Mean-Field Theory”, *The LDA+DMFT approach to strongly correlated materials: lecture notes of the Autumn School 2011 Hands-on LDA+DMFT: at Forschungszentrum Jülich, 4-7 October 2011*, ed. by E. Pavarini et al., Schriften des Forschungszentrums Jülich. Reihe Modeling and Simulation Band 1, Meeting Name: Autumn School Hands-on LDA+DMFT, Jülich: Forschungszentrum Jülich, Zentralbibliothek, Verl, 2011 5.1, ISBN: 978-3-89336-734-4 (cit. on p. 94).
- [88] J. Kroha, personal communication, 2019 (cit. on p. 95).
- [89] A. Georges, G. Kotliar, W. Krauth, and M. J. Rozenberg, *Dynamical mean-field theory of strongly correlated fermion systems and the limit of infinite dimensions*, tech. rep., 1996 (cit. on pp. 95, 125).
- [90] G. Kotliar et al., *Electronic structure calculations with dynamical mean-field theory*, *Reviews of Modern Physics* **78** (2006) 865, ISSN: 00346861 (cit. on p. 95).
- [91] V. Turkowski, *Dynamical mean-field theory for strongly correlated materials*, Cham: Springer, 2021, ISBN: 978-3-030-64903-6 (cit. on p. 95).

-
- [92] P. Coleman, *I N expansion for the Kondo lattice*, *Physical Review B* **28** (1983) 5255, ISSN: 0163-1829, URL: <https://link.aps.org/doi/10.1103/PhysRevB.28.5255> (visited on 05/21/2024) (cit. on p. 95).
- [93] O. Trovarelli et al., *Yb Rh₂ Si₂ : Pronounced Non-Fermi-Liquid Effects above a Low-Lying Magnetic Phase Transition*, *Physical Review Letters* **85** (2000) 626, ISSN: 0031-9007, 1079-7114, URL: <https://link.aps.org/doi/10.1103/PhysRevLett.85.626> (visited on 01/09/2024) (cit. on pp. 101, 103).
- [94] O. Stockert et al., *Crystalline electric field excitations of the non-Fermi-liquid*, *Physica B: Condensed Matter* **378-380** (2006) 157, ISSN: 09214526, URL: <https://linkinghub.elsevier.com/retrieve/pii/S0921452606000640> (visited on 01/09/2024) (cit. on p. 101).
- [95] G. A. Wigger et al., *Electronic band structure and Kondo coupling in Yb Rh₂ Si₂*, *Physical Review B* **76** (2007) 035106, ISSN: 1098-0121, 1550-235X, URL: <https://link.aps.org/doi/10.1103/PhysRevB.76.035106> (visited on 01/09/2024) (cit. on p. 103).
- [96] O. Újsághy, J. Kroha, L. Szunyogh, and A. Zawadowski, *Theory of the Fano Resonance in the STM Tunneling Density of States due to a Single Kondo Impurity*, *Physical Review Letters* **85** (2000) 2557, ISSN: 0031-9007, 1079-7114, URL: <https://link.aps.org/doi/10.1103/PhysRevLett.85.2557> (visited on 03/28/2023) (cit. on p. 105).
- [97] P. Wölfle, Y. Dubi, and A. V. Balatsky, *Tunneling into Clean Heavy Fermion Compounds: Origin of the Fano Line Shape*, *Physical Review Letters* **105** (2010) 246401, ISSN: 0031-9007, 1079-7114, URL: <https://link.aps.org/doi/10.1103/PhysRevLett.105.246401> (visited on 08/11/2023) (cit. on p. 105).
- [98] F. Reinert et al., *Temperature Dependence of the Kondo Resonance and Its Satellites in CeCu₂Si₂*, *Physical Review Letters* **87** (2001) 106401, ISSN: 0031-9007, 1079-7114, URL: <https://link.aps.org/doi/10.1103/PhysRevLett.87.106401> (visited on 06/16/2023) (cit. on p. 107).
- [99] J. Kroha et al., *Structure and transport in multi-orbital Kondo systems*, *Physica E: Low-dimensional Systems and Nanostructures, 23rd International Conference on Low Temperature Physics (LT23)* **18** (2003) 69, ISSN: 1386-9477, URL: <https://www.sciencedirect.com/science/article/pii/S1386947702009773> (visited on 01/18/2023) (cit. on pp. 107, 108).
- [100] Y. Matsumoto et al., *Quantum Criticality Without Tuning in the Mixed Valence Compound β -YbAlB₄*, *Science* **331** (2011) 316, URL: <https://www.science.org/doi/10.1126/science.1197531> (visited on 09/28/2022) (cit. on p. 117).

- [101] H. v. Löhneysen, *Non-Fermi-liquid behaviour in the heavy-fermion system*, *J. Phys.: Condens. Matter* **8** (1996) 9689, ISSN: 0953-8984, URL: <https://doi.org/10.1088/0953-8984/8/48/003> (visited on 09/28/2022) (cit. on p. 117).
- [102] J. Paglione et al., *Field-induced quantum critical point in CeCoIn₅*, *Phys. Rev. Lett.* **91** (2003) 246405, URL: <https://link.aps.org/doi/10.1103/PhysRevLett.91.246405> (visited on 09/28/2022) (cit. on p. 117).
- [103] J. Custers et al., *The break-up of heavy electrons at a quantum critical point*, *Nature* **424** (2003) 524, ISSN: 1476-4687, URL: <https://www.nature.com/articles/nature01774> (visited on 09/28/2022) (cit. on p. 117).
- [104] P. Gegenwart, Q. Si, and F. Steglich, *Quantum criticality in heavy-fermion metals*, *Nature Phys* **4** (2008) 186, ISSN: 1745-2481, URL: <https://www.nature.com/articles/nphys892> (visited on 09/28/2022) (cit. on p. 117).
- [105] Q. Si, S. Rabello, K. Ingersent, and J. L. Smith, *Locally critical quantum phase transitions in strongly correlated metals*, *Nature* **413** (2001) 804, ISSN: 0028-0836, 1476-4687, URL: <https://www.nature.com/articles/35101507> (visited on 06/15/2023) (cit. on p. 117).
- [106] P. Coleman, C. Pépin, Q. Si, and R. Ramazashvili, *How do Fermi liquids get heavy and die?*, *Journal of Physics: Condensed Matter* **13** (2001) R723, ISSN: 0953-8984, 1361-648X, URL: <https://iopscience.iop.org/article/10.1088/0953-8984/13/35/202> (visited on 06/15/2023) (cit. on p. 117).
- [107] T. Senthil, M. Vojta, and S. Sachdev, *Weak magnetism and non-Fermi liquids near heavy-fermion critical points*, *Phys. Rev. B* **69** (2004) 035111, ISSN: 1098-0121, 1550-235X, URL: <https://link.aps.org/doi/10.1103/PhysRevB.69.035111> (visited on 06/15/2023) (cit. on p. 117).
- [108] T. Onimaru and H. Kusunose, *Exotic quadrupolar phenomena in non-Kramers doublet systems - The cases of PrT₂Zn₂₀ (T = Ir, Rh) and PrT₂Al₂₀ (T = V, Ti)*, *Journal of the Physical Society of Japan* **85** (2016), Publisher: Physical Society of Japan, ISSN: 13474073 (cit. on pp. 117, 124).
- [109] D. L. Cox, *Quadrupolar Kondo effect in uranium heavy-electron materials?*, *Phys. Rev. Lett.* **59** (1987) 1240, ISSN: 0031-9007, URL: <https://link.aps.org/doi/10.1103/PhysRevLett.59.1240> (visited on 01/01/2019) (cit. on p. 117).

-
- [110] D. L. Cox and A. Zawadowski, *Exotic Kondo effects in metals: Magnetic ions in a crystalline electric field and tunnelling centres*, *Advances in Physics* **47** (1998) 599, ISSN: 0001-8732, 1460-6976, URL: <http://www.tandfonline.com/doi/abs/10.1080/000187398243500> (visited on 01/01/2019) (cit. on p. 117).
- [111] K. Hattori and H. Tsunetsugu, *Antiferro Quadrupole Orders in Non-Kramers Doublet Systems*, *Journal of the Physical Society of Japan* **83** (2014) 034709, ISSN: 0031-9015, 1347-4073, URL: <http://journals.jps.jp/doi/10.7566/JPSJ.83.034709> (visited on 01/01/2019) (cit. on p. 117).
- [112] K. Hattori and H. Tsunetsugu, *Classical Monte Carlo Study for Antiferro Quadrupole Orders in a Diamond Lattice*, *Journal of the Physical Society of Japan* **85** (2016) 094001, ISSN: 0031-9015, 1347-4073, URL: <http://journals.jps.jp/doi/10.7566/JPSJ.85.094001> (visited on 01/01/2019) (cit. on p. 117).
- [113] A. Sakai and S. Nakatsuji, *Kondo effects and multipolar order in the cubic PrTr₂Al₂₀ (Tr = Ti, V)*, *Journal of the Physical Society of Japan* **80** (2011), arXiv: 1104.4167, ISSN: 00319015 (cit. on pp. 117, 118, 120, 129, 130, 155).
- [114] A. Sakai, K. Kuga, and S. Nakatsuji, *Superconductivity in the Ferroquadrupolar State in the Quadrupolar Kondo Lattice PrTi₂Al₂₀*, *Journal of the Physical Society of Japan* **81** (2012) 083702, ISSN: 0031-9015, 1347-4073, URL: <http://journals.jps.jp/doi/10.1143/JPSJ.81.083702> (visited on 06/05/2024) (cit. on p. 117).
- [115] M. Tsujimoto, Y. Matsumoto, T. Tomita, A. Sakai, and S. Nakatsuji, *Heavy-Fermion Superconductivity in the Quadrupole Ordered State of PrV₂Al₂₀*, *Physical Review Letters* **113** (2014) 267001, ISSN: 0031-9007, 1079-7114, URL: <https://link.aps.org/doi/10.1103/PhysRevLett.113.267001> (visited on 04/05/2023) (cit. on p. 117).
- [116] M. Matsunami et al., *Kondo resonance in PrTi₂Al₂₀ : Photoemission spectroscopy and single-impurity Anderson model calculations*, *Phys. Rev.B* **84** (2011) 193101, ISSN: 1098-0121, 1550-235X, URL: <https://link.aps.org/doi/10.1103/PhysRevB.84.193101> (visited on 01/01/2019) (cit. on p. 117).
- [117] A. M. Tsvelick and P. B. Wiegmann, *Exact solution of the multichannel Kondo problem, scaling, and integrability*, *Journal of Statistical Physics* **38** (1985) 125, ISSN: 0022-4715, 1572-9613, URL: <http://link.springer.com/10.1007/BF01017853> (visited on 01/12/2024) (cit. on p. 118).

- [118] P. D. Sacramento and P. Schlottmann, *Thermodynamics of the n -channel Kondo model for general n and impurity spin S in a magnetic field*, *Journal of Physics: Condensed Matter* **3** (1991) 9687, ISSN: 0953-8984, 1361-648X, URL: <https://iopscience.iop.org/article/10.1088/0953-8984/3/48/010> (visited on 07/14/2023) (cit. on p. 118).
- [119] I. Affleck and A. W. W. Ludwig, *Exact conformal-field-theory results on the multichannel Kondo effect: Single-fermion Green's function, self-energy, and resistivity*, *Physical Review B* **48** (1993) 7297, ISSN: 0163-1829, 1095-3795, URL: <https://link.aps.org/doi/10.1103/PhysRevB.48.7297> (visited on 04/05/2023) (cit. on p. 118).
- [120] F. B. Anders, *Renormalization-group approach to spectral properties of the two-channel Anderson impurity model*, *Physical Review B* **71** (2005) 121101, ISSN: 1098-0121, 1550-235X, URL: <https://link.aps.org/doi/10.1103/PhysRevB.71.121101> (visited on 02/23/2023) (cit. on pp. 118, 131).
- [121] P. Chandra, P. Coleman, and R. Flint, *Hastatic order in the heavy-fermion compound URu₂Si₂*, *Nature* **493** (2013) 621, ISSN: 0028-0836, 1476-4687, URL: <https://www.nature.com/articles/nature11820> (visited on 06/05/2024) (cit. on p. 118).
- [122] R. Eder and P. Wróbel, *Channel order in the two-channel Kondo lattice*, *Physical Review B* **105** (2022) 125133, ISSN: 2469-9950, 2469-9969, URL: <https://link.aps.org/doi/10.1103/PhysRevB.105.125133> (visited on 06/05/2024) (cit. on p. 118).
- [123] M. Lenk, F. Gao, J. Kroha, and A. H. Nevidomskyy, *Strange-metal behavior without fine tuning in PrV₂Al₂₀*, *Physical Review Research* **6** (2024) L042008, Licensed under CC BY 4.0: <http://creativecommons.org/licenses/by/4.0/>, ISSN: 2643-1564, URL: <https://link.aps.org/doi/10.1103/PhysRevResearch.6.L042008> (visited on 10/17/2024) (cit. on pp. 118, 121, 123, 153, 154, 156, 158).
- [124] T. J. Sato et al., *Ferroquadrupolar ordering in PrTi₂Al₂₀*, *Physical Review B* **86** (2012) 184419, ISSN: 1098-0121, 1550-235X, URL: <https://link.aps.org/doi/10.1103/PhysRevB.86.184419> (visited on 06/05/2024) (cit. on p. 120).
- [125] R. O. Jones, *Density functional theory: Its origins, rise to prominence, and future*, en, *Reviews of Modern Physics* **87** (2015) 897, ISSN: 0034-6861, 1539-0756, URL: <https://link.aps.org/doi/10.1103/RevModPhys.87.897> (visited on 06/05/2024) (cit. on p. 123).
- [126] F. C. Frank and J. S. Kasper, *Complex alloy structures regarded as sphere packings. I. Definitions and basic principles*, *Acta Crystallographica* **11** (1958) 184, ISSN: 0365110X,

-
- URL: <https://scripts.iucr.org/cgi-bin/paper?S0365110X58000487> (visited on 06/06/2024) (cit. on p. 124).
- [127] J. S. Van Dyke, G. Zhang, and R. Flint, *Field-induced ferrohastatic phase in cubic non-Kramers doublet systems*, *Physical Review B* **100** (2019), ISSN: 2469-9969, URL: <http://dx.doi.org/10.1103/PhysRevB.100.205122> (cit. on p. 124).
- [128] A. S. Patri, I. Khait, and Y. B. Kim, *Emergent non-Fermi-liquid phenomena in multipolar quantum impurity systems*, *Phys. Rev. Research* **2** (2020) 013257, ISSN: 2643-1564, URL: <https://link.aps.org/doi/10.1103/PhysRevResearch.2.013257> (visited on 06/06/2023) (cit. on p. 124).
- [129] S. Han, D. J. Schultz, and Y. B. Kim, *Non-Fermi liquid behavior and quantum criticality in cubic heavy fermion systems with non-Kramers multipolar local moments*, *Phys. Rev. B* **106** (2022) 155155, ISSN: 2469-9950, 2469-9969, URL: <https://link.aps.org/doi/10.1103/PhysRevB.106.155155> (visited on 06/06/2023) (cit. on p. 124).
- [130] D. L. Cox and A. E. Ruckenstein, *Spin-flavor separation and non-Fermi-liquid behavior in the multichannel Kondo problem: A large- N approach*, *Phys. Rev. Lett.* **71** (1993) 1613, Publisher: American Physical Society, URL: <https://link.aps.org/doi/10.1103/PhysRevLett.71.1613> (visited on 02/15/2023) (cit. on p. 128).
- [131] K. Araki et al., “Magnetization and Specific Heat of the Cage Compound $\text{PrV}_2\text{Al}_{20}$ ”, *Proceedings of the International Conference on Strongly Correlated Electron Systems (SCES2013)*, Tokyo, Japan: Journal of the Physical Society of Japan, 2014, ISBN: 978-4-89027-104-7, URL: <http://journals.jps.jp/doi/10.7566/JPSCP.3.011093> (visited on 06/27/2023) (cit. on pp. 129, 132).
- [132] D. L. Cox and M. Makivic, *Phenomenology of two channel Kondo alloys and compounds*, *Physica B: Condensed Matter* **199-200** (1994) 391, ISSN: 0921-4526, URL: <https://www.sciencedirect.com/science/article/pii/0921452694918481> (visited on 02/23/2023) (cit. on p. 130).
- [133] H. Kusunose and H. Ikeda, *Interplay of crystal field structures with f^2 configuration to heavy fermions*, *Journal of the Physical Society of Japan* **74** (2005) 405, ISSN: 00319015 (cit. on pp. 153, 158).

List of Figures

2.1	Illustration of the filling of bands. The shaded area represents the Fermi distribution function, gray areas are fully filled, white areas are unfilled. Full horizontal lines represent bands, the dashed horizontal line indicates the Fermi energy. Blue circles illustrate states in bands, filled blue circles signal an occupied state. The vertical distance between bands represents excitation energies. Orange arrows highlight a selection of possible transitions.	6
2.2	Dispersion of a free particle folded into the first Brillouin zone.	13
2.3	Dispersion and DOS of a 1D tight-binding lattice.	17
2.4	Occupation of the resonant level for $T = 0$ according to Eq. (2.57).	18
2.5	Resonant-level density of states.	19
2.6	Local DOS of a 1D tight-binding lattice.	20
2.7	Trace of the DOS of a 1D tight-binding lattice.	22
2.8	Illustration of a resonant-level model's expected lattice-momentum dependent spectrum. The resonant-level density of states is exactly reproduced at each momentum since it is perfectly localized. As discussed in the text, the conduction-electron band is modeled as just the free band. The free band was approximated by a Lorentzian of width $\eta/D = 10^{-3}$. The color corresponds approximately to strength, but the normalization is not meaningful due to the problems discussed in the text. The color bar, therefore, remains unlabeled. Here, k is dimensionless via the lattice constant $a = 1$	23
2.9	Spectral function of the 1D two-band hybridization model for two different V , where $\varepsilon_k^c = -\cos(k)$ and $\varepsilon^d = -0.3$. The coloring represents the flavor of the eigenvector in terms of c - and d electrons. Here, k is dimensionless via the lattice constant $a = 1$	25
2.10	Spectral function of the two-band hybridization model for two sets of parameters a and V , where $\varepsilon_k^c = -\cos(k)$, $\varepsilon_k^d = \kappa \cdot \varepsilon_k^c + \varepsilon_0^d$, and $\varepsilon_0^d = -0.3 D$. The coloring represents the flavor of the eigenvector in terms of c - and d electrons. The grey dashed lines in (b) are at the predicted gap edges $\omega = \pm V $. Here, k is dimensionless via the lattice constant $a = 1$	26
2.11	Density of states of the 1D two-band hybridization model for two different V , where $\varepsilon_k^c = -\cos(k)$ and $\varepsilon^d = -0.3$	28
3.1	Resistivity measurement on $\text{Ce}_x \text{La}_{1-x} \text{Cu}_6$ with varying Cerium concentration, extracted from [25]. The lines are of increasing Ce concentration from top to bottom. A low concentration leads to the expected results for dilute magnetic impurities, whereas a large concentration leads to Fermi liquid behavior.	30

3.2	Illustration of the impurity level-scheme in the SIAM. The corresponding energies are the level-energies, <i>not</i> the single-particle excitations. Energies are given in reference to the Fermi energy.	35
3.3	Sketch of the impurity spectral function in the single-impurity Anderson model with $\Gamma/D = 0.1$, $\varepsilon^d/D = -0.2$, and $U/D = 0.6$	35
3.4	Exemplary $T = 0$ and $\Gamma/D = 1$ impurity occupation according to Eq. (3.14) with $U/D = 10$. Thick dashed lines represent the positions of the two Lorentzian peaks in the spectrum; thin dashed lines are a guide to the eye.	36
3.5	Sketch of the impurity spectral function in the single-impurity Anderson model with $\Gamma/D = 0.1$, $\varepsilon^d/D = -0.2$, and $U/D = 0.6$ including the Kondo peak.	37
3.6	Sketch of one component of the localized spin singlet in the Kondo model. The conduction-electron hopping in this picture is assumed to be between nearest neighbors.	38
3.7	Measured resistance of various gold-wire samples by W.J. De Haas and G.H. Van Den Berg in 1936. Plots taken from [41].	39
3.8	Modernized sketch of the Doniach phase diagram [6] inspired by its renditions in [49] and [53]. The blue curve is the critical temperature of magnetic ordering via RKKY-interaction; the blue region below it shows the magnetically ordered (MO) phase. The orange curve is the Kondo temperature for the crossover to the heavy Fermi liquid, which is the colored region below it. The regions are separated by a quantum-critical point (QCP), denoted by a dashed gray line.	47
3.9	Two-band hybridization model from Section 2.3 with $(\varepsilon^d - E_F)/D = 0.05$ and $V/D = 0.1$. The free conduction-electron dispersion is shown as an orange dashed-dotted line, the dotted gray line is the Fermi energy, and the gray and green dashed lines correspond to the free and renormalized Fermi momenta.	49
5.1	Illustration of the variation of a Green function in terms of Feynman diagrams, taken from [74]. The missing line comes from the factoring out of the variation δG	72
5.2	Simplified Feynman rules for the single-impurity Anderson model with auxiliary particles, c.f. Eq. (5.31).	74
5.3	Diagrammatic representation of the Luttinger-Ward functional for the SIAM in terms of auxiliary particles with the convention of quantum numbers associated with the creation operator appearing first, those associated with the annihilation operator second.	74
5.4	Diagrammatic representation of the conduction electron self-energy. The incoming and outgoing lines are just shown for bookmarking of the conserved quantities.	75
5.5	Contour for evaluating the Matsubara-sum in the conduction-electron self-energy. Curly lines visualize the branch cuts of the respective Green functions. Bosonic Matsubara frequencies are shown as blue dots.	76
5.6	Diagrammatic representation of the pseudofermion self-energy.	80
5.7	Contour for evaluating the Matsubara-sum in the pseudofermion self-energy. Curly lines visualize branch cuts of the respective Green functions. Bosonic Matsubara frequencies are shown as blue dots.	81
5.8	Diagrammatic representation of the slave-boson b self-energy.	83
5.9	Contour for evaluating the Matsubara sum in the slave-boson self-energy. Curly lines visualize branch cuts of the respective Green functions. Fermionic Matsubara frequencies are shown as red dots.	84

5.10	Diagrammatic representation of the slave-boson a self-energy.	85
5.11	Different schematic Feynman diagrams for the non-local self-energy discussion. Diagrams no. 3 and 4 are valid self-energy diagrams, whereas 1 and 2 are not. Lines represent full Green functions; blobs represent diagram insertions.	95
6.1	STM differential conductance of YbRh_2Si_2 for different temperatures, taken from Fig.2 in [12], cropped, panel label removed. The arrows indicate the expected CEF energies; the dashed line highlights the <i>coherence peak</i>	102
6.2	Temperature-dependent features of the STM differential conductance of YbRh_2Si_2 , taken from Fig.2 in [12], cropped, parts removed.	102
6.3	Free, model conduction-electron Green function according to Eq. (6.4) using the Kramers-Kronig relation to generate the real part and the q -factor of Eq. (6.6). The presented data is for $s = 2/D$	104
6.4	Fano lineshape depending on the Fano structure factor q as by the second term in Eq. (6.5).	106
6.5	Impurity density of states for the YbRh_2Si_2 model and the conduction-electron self-energy Δ^c for different temperatures. Vertical gray lines mark the renormalized CEF energies, c.f. Fig. 6.6(b).	107
6.6	Impurity density of states for the YbRh_2Si_2 model at a fixed temperature $T = 10$ K. Vertical gray lines mark the renormalized CEF energies.	107
6.7	Reduced level structure of an Yb^{3+} ion, considering the excited $4f^{12}$ configuration and two CEF states of the $4f^{13}$ valence ground state. Full, colored lines represent contributions to the Kondo effect; dashed lines represent thermally forbidden transitions at zero temperature.	108
6.8	Conduction-electron density of states for the YbRh_2Si_2 model for different temperatures. The gray dashed line is a guide to the eye generated from subtracting a Lorentzian from the free conduction-electron density of states. Vertical gray lines mark the renormalized CEF energies, c.f. Fig. 6.6(b).	109
6.9	Top: Impurity density of states in total and by CEF contribution. Bottom: Conduction-electron density of states for the YbRh_2Si_2 model for $T = 10$ K. The gray dashed line is a guide to the eye generated from subtracting a Lorentzian from the free conduction-electron density of states. Both: Vertical gray lines mark the renormalized CEF energies, c.f. Fig. 6.6(b).	110
6.10	DMFT local-model q -factor and density of states of an effective conduction-electron background. The Green function is defined via $G_{\text{loc}}^{c\emptyset} = \mathcal{G}_{\text{loc}}^{c\emptyset} / (1 + \Delta_{\text{loc}}^c \mathcal{G}_{\text{loc}}^{c\emptyset})$. Vertical gray lines mark the renormalized CEF energies.	110
6.11	Kondo dip and two peak heights of Fig. 6.8. The Kondo temperature $T_K = 32$ K was estimated via the half width at half maximum of the CEF ground-state Kondo peak.	111
6.12	Spectral function for the YbRh_2Si_2 model at $T = 10$ K ($T \approx T_K/3$) plotted against the excitation energy and the dispersion ε . The energy is relative to the Fermi energy, including chemical potential. Upper panel: Total spectral function, i.e. $\text{Tr Im } G(\omega, \varepsilon)$. Lower panel: Impurity contribution to the upper panel on a <i>different</i> color-code scale to visualize the structure away from the Fermi energy.	112

6.13	Spectral function for the YbRh_2Si_2 model at $T = 10 \text{ K}$ ($T \approx T_K/3$) plotted against the excitation energy and the dispersion ε in a narrow region around the Fermi energy. The energy is relative to the Fermi energy, including chemical potential. Upper panel: Conduction-electron contribution to the spectral function. The dashed-dotted line is the free band. Lower panel: Impurity contribution to the spectral function.	113
6.14	Individual Pr $4f$ CEF-state contribution to the spectral function for the YbRh_2Si_2 model at $T = 10 \text{ K}$ ($T \approx T_K/3$) plotted against the excitation energy and the dispersion ε in a narrow region around the Fermi energy. The energy is relative to the Fermi energy, including chemical potential. The color-code scale in (b)-(c) differs from the scale in (a) and other Figures to enhance visibility.	114
7.1	Experimentally measured resistivity for $\text{PrV}_2\text{Al}_{20}$ and $\text{PrTi}_2\text{Al}_{20}$ represented by points. The lines illustrate the respective scaling behavior. Taken from [113]; modified (removed text panels and insets)	118
7.2	Illustration of the two-channel Kondo model. Conduction electrons are represented by gray balls and their spin by blue arrows. The orange ball represents the impurity, with its spin being the orange arrow. The tight-binding nearest neighbor hopping t and the local Kondo coupling J are illustrated via black arrows. Compared to Fig. 3.6, pair formation is degenerate between the two scattering channels. Both possible options are illustrated by green dashed lines.	119
7.3	Crystal field states involved in the hybridization process of the Pr^{3+} ion in $\text{PrV}_2\text{Al}_{20}$. The arrow connecting Γ_3 and Γ_5 indicates the CEF splitting, the arrow connecting the left side to the right side indicates the valence fluctuation to Γ_6 via Γ_8 -projected conduction electrons. As indicated by the broken line, vertical position is in correct order but not to scale.	120
7.4	Density of states (left) and band structure (right) of the full “open core” ab-initio calculation for $\text{PrV}_2\text{Al}_{20}$ with “frozen” Pr $4f^2$ configuration, effectively removing it from the picture.	123
7.6	Contribution of individual irreps of V d orbitals under D_{3d} symmetry to the hybridization function normalized such that the $\{d_{xy}, d_{x^2-y^2}\}$ integrates to one, maintaining the relative strengths.	125
7.7	Spectrum of the single CEF-state effective model for $\text{PrV}_2\text{Al}_{20}$. Panel (a) shows the total DOS for two different temperatures, for which the spectrum along a path in \vec{k} -space close to the Γ point is shown in panels (b) and (c).	128
7.8	Impurity self-energy of the single CEF-state effective model for $\text{PrV}_2\text{Al}_{20}$	129
7.9	Impurity magnetic susceptibility of the single CEF-state model compared to the original experimental data.	130
7.10	Spectrum of the effective model for $\text{PrV}_2\text{Al}_{20}$ including two CEF states. Panel (a) and (b) show the total (model) spectrum along a path in k -space close to the Γ point for $T = 3 \text{ K}$ and $T = 300 \text{ K}$. Panel (c) shows the total DOS for the same two temperatures.	131
7.11	Impurity ground-state (Γ_3) self-energy of the effective model for $\text{PrV}_2\text{Al}_{20}$ including two CEF states for different temperatures plotted against the expected square-root scaling function. Here, $\tilde{\omega} = \omega - \omega_0$, where ω_0 is the frequency of the local minimum. The inset shows the value at the minimum in meV against the expected square-root temperature scaling.	132

7.12 Impurity magnetic susceptibility including the excited CEF state in comparison to most recent experimental data. 132

B.1 Conduction-electron spectral function normalized to the free peak height $1/\eta$. Values above 1 and below -1 are cut off for increased visibility. 143

List of Tables

4.1	Character table of the point group C_4 . Top left is the group designation, the rest of the first row are the conjugacy classes, and the rest of the first column are the irreducible representations.	59
4.2	Character table for the T'_d double group. Integers in front of classes label the number of members in a class. The last three classes are additions to the point group T_d . The classes of T_d are: the identity E , threefold rotations C_3 , twofold rotations C_2 , improper fourfold rotations S_4 (rotation followed by a reflection in a perpendicular plane), and the reflection in a diagonal plane σ_d (the plane parallel to the symmetry axis but arranged in a specific way, which is not relevant to us here).	61
4.3	Character of irreducible representations of $SO(3)$ under the classes of T'_d . Although σ_d and $\bar{\sigma}_d$ are conjugate in T'_d , they lead to different character for some irreps of $SO(3)$, so they have to be split up for the orthogonality.	61
6.1	Model parameters of Eq. (6.3) used in the numerical calculations.	106